The Influence of Laser Relative Intensity Noise on Space-Based Heterodyne Interferometers – from the LISA Pathfinder to the LISA Mission

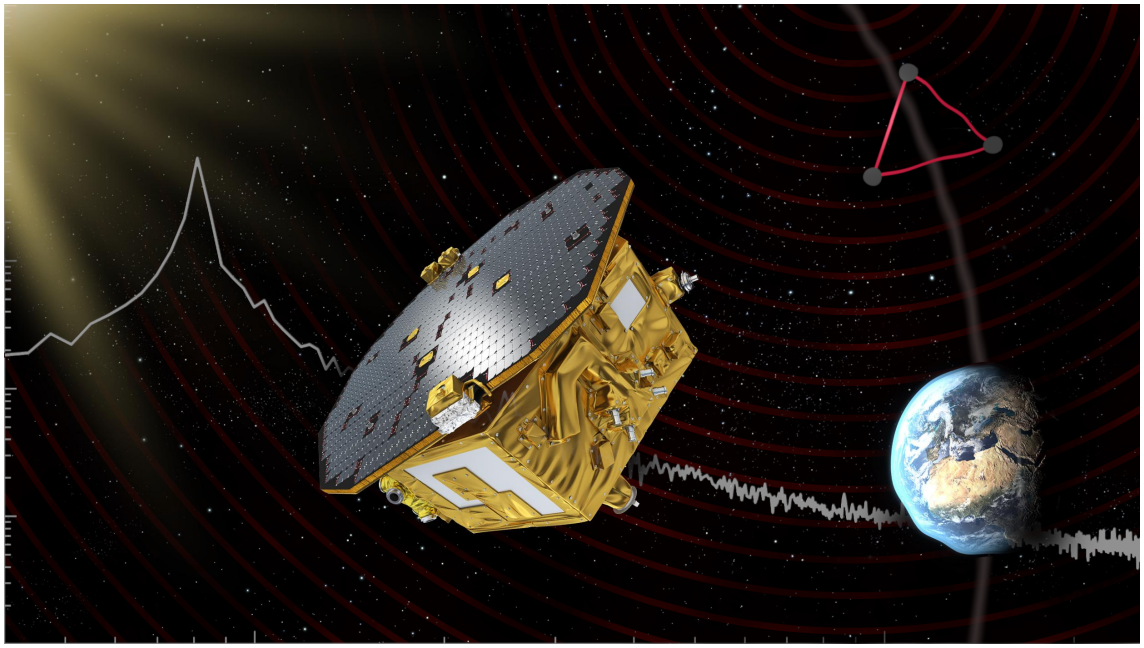

Dissertation
Lennart Wissel
2024

MAX-PLANCK-INSTITUT
FÜR GRAVITATIONSPHYSIK
(Albert-Einstein-Institut)

Leibniz
Forschungs-
Schule

Image on cover:	Illustration of LISA and LISA Pathfinder and RIN (not to scale) by Lennart Wissel
Background used:	LISA Pathfinder with Sun and Earth by ESA – C. Carreau
RIN measurement:	Provided by S. Barke

The Influence of Laser Relative Intensity Noise on Space-Based Heterodyne Interferometers – from the LISA Pathfinder to the LISA Mission

Dissertation

Von der QUEST-Leibniz-Forschungsschule
der Gottfried Wilhelm Leibniz Universität Hannover
zur Erlangung des akademischen Grades

Doktor der Naturwissenschaften
– Dr. rer. nat. –

genehmigte Dissertation von

M. Sc. Lennart Wissel

2024

Referent:	Apl. Prof. Dr. Gerhard Heinzel Max Planck Institut für Gravitationsphysik, Leibniz Universität Hannover
Korreferent:	Prof. Dr. Karsten Danzmann Max Planck Institut für Gravitationsphysik, Leibniz Universität Hannover
Korreferent:	Prof. Dr. William Joseph Weber Dipartimento di Fisica, Universitá di Trento
Tag der Promotion:	22.03.2024

Abstract

In recent years, scientists have established the new field of Gravitational Wave (GW) astronomy through direct measurements of spacetime perturbations. These are caused by GWs originating from accelerating astrophysical objects and have been observed in ground-based interferometers, confirming predictions made by Albert Einstein more than 100 years ago. The Laser Interferometer Space Antenna (LISA) mission, led by the European Space Agency (ESA) with a planned launch in the mid-2030s, will detect such waves in the 0.1 mHz – 1 Hz frequency band in space for the first time. It will measure their induced distance changes between free-falling Test Masses (TMs), which are shielded inside three separate Spacecraft (SC), as optical pathlength fluctuations with pm precision through heterodyne interferometry. Going to space offers many advantages and overcomes typical limitations of ground-based detectors. It allows the possibility of using longer interferometer arms, thus reducing the required displacement sensitivity, while naturally avoiding noise sources present on Earth. It does, however, bring its own technical challenges.

This thesis addresses one of these challenges: the influence of measurement noise originating from the lasers' power instabilities, a problem known as Relative Intensity Noise (RIN). While it is also present in ground-based detectors, the mission architecture, with its complex heterodyne interferometry, provides a unique problem. RIN inevitably reduces the ability to resolve GW signals. It is necessary to identify, characterize, understand, model, and mitigate its effect to a level that allows the achievement of the desired scientific objectives. Therefore, this research investigates RIN to phase coupling in the readout of balanced and unbalanced heterodyne interferometers and its influence on space missions. A significant result is the detailed understanding of RIN contributions from the heterodyne frequency ("1f-RIN") and its first harmonic ("2f-RIN") to the interferometric phase readout, including possible mitigation strategies using correlated subtractions. The study derives the couplings theoretically and generally, studies common-mode rejection properties, performs simulations and analyzes measurements from the technology demonstrator mission LISA Pathfinder (LPF), before projecting the results onto LISA.

LPF was launched in 2015 to prove the feasibility of the TMs free-fall control and interferometric readout due to the complexity of LISA. With its unique design and performance, LPF was an unprecedented laboratory in space. It contained the first sub-pm interferometer in space to measure the distance variations between two TMs. In analyzing the whole mission performance with respect to the optical readout, this work finds that it achieved a residual sensor noise of $32.0^{+2.4}_{-1.7}\mathrm{fm}/\sqrt{\mathrm{Hz}}$ at frequencies above 200 mHz along its

main measurement axis. The residual angular Differential Wavefront Sensing (DWS) noise was in the order of $100\,\mathrm{prad}/\sqrt{\mathrm{Hz}}$ (at similar frequencies). This work further reports on the characterization of noise couplings and incorporates their contribution to the overall LPF noise model, which is verified from low to high interferometric contrasts. As part of this noise budget, the mission provided valuable data for testing the RIN model. Due to its correlation properties, RIN impacts the readout of longitudinal and angular degrees of freedom. In this thesis, the coupling of RIN in those readout channels is analyzed, and its influence during the whole mission is modeled. From dedicated experiments it follows that the contribution was not above $2.4\,\mathrm{fm}/\sqrt{\mathrm{Hz}}$ (assumed white, excluding radiation pressure effects), for nominal mission operations and that the 2f-RIN components were dominating the 1f-RIN terms. The RIN model constitutes an important contribution to the overall understanding of a very stable and reliable readout system.

With the knowledge gained from LPF, this thesis shows to what level RIN needs to be mitigated regarding the more complex LISA, setting requirements on the laser power instabilities of $3 \times 10^{-8}\,\mathrm{Hz}^{-1/2}$ between (3 to 60) MHz, such that it does not significantly reduce the ability to detect GWs. Since RIN in LISA has a unique correlation imprint, its impact on the essential frequency noise reduction algorithm called Time-Delay Interferometry (TDI) is important to understand. For this reason, the propagation of RIN in the mission constellation is simulated for all laser locking topologies, together with the transfer function through TDI. It shows that efficient balanced detection reduces the coupling from a significant contribution of $8.7\,\mathrm{pm}/\sqrt{\mathrm{Hz}}$ (as white in-band noise) per inter-SC interferometer to a much less problematic sub-$1\,\mathrm{pm}/\sqrt{\mathrm{Hz}}$ level, and, that simple models can be derived that describe a practically uncorrelated behavior, independent of the locking scheme.

Keywords: Laser interferometry, Relative Intensity Noise, LISA Pathfinder, LISA

Acknowledgments

Over the last years, my conviction has grown that science essentially thrives thanks to the people behind it, their curiosity, and their warm-hearted openness. My time at the Albert Einstein Institute (AEI) was imbued with kindness during the ups and downs that culminated in this thesis, which would not have been possible without the generosity and support of many friends, colleagues, and a big team behind the scenes at the institute and in my life.

My biggest thanks goes to the whole LPF and LISA team here at the AEI (and also worldwide!). I was welcomed with outspoken friendliness and sincerity and had the privilege to join just in time to witness the launch of the LPF mission. What a treat!

You all have contributed to the ongoing success of the mission(s) and the institute. Thank you, Gerhard Heinzel and Martin Hewitson, for the supervision and help going down as many rabbit holes as we liked. You have always had another helpful idea, a new perspective, or brilliant insight, even though many projects require your attention. I learned a lot from our discussions and your humility in all of this.

This is also true for Nikolaos Karnesis, Heather Audley, Michael Born, Natalia Korsakova, Brigitte Kaune, Andreas Wittchen, Gudrun Wanner, Sarah Paczkowski and Marie-Sophie Hartig. We have researched, hiked, cooked, discussed, listened, danced, played, and traveled from Scotland to Italy together, shared despair and laughter. You have been the best team, office mates, and friends I could have wished for!

I am very grateful that our institute director, Karsten Danzmann, has created this excellent place where people matter and we are encouraged to really delve into our chosen topics, backed by a superb infrastructure. Many people here have supported me with small and big things. I would not have been as happy without Kirsten Labove (thanks for the cakes!), Konrad Mors (and our IT!), Jens Reiche and Ines Klein (and our human resources department!). I have fond memories of group hikes with the LISA group, game nights, soccer tournaments, night shifts for PhD hats and Christmas parties with the whole institute.

Sincere gratitude goes to my PhD committee for their time and effort. Your curiosity and view on science has helped me to remember the bigger picture, especially when there was yet another roadblock on the way.

The quality of this work has been improved thanks to all the proofreaders and co-authors of the publications. Thank you Sarah, Marie, Gudrun, Martin, Malte, Michael, Andi,

Brigitte, Dave, Martin, Thomas, Olaf and Jean-Baptiste for all your help. All remaining mistakes are, of course, my own (as this thesis is still AI free ;-)).

My dear family and all my friends have always encouraged and supported me. I wish to express my deepest gratitude to all of you for always believing in me and because you are wonderful human beings. Thank you!

Hannover, in January 2024
Lennart Wissel

A brief personal note

My first encounter with the subject of general relativity and GWs was during a fascinating lecture by a former AEI scientist when I was still at school. He used the famous "ant on an apple" analogy for geodesics in curved spacetime, which sparked my curiosity. Ever since, metaphorical models have aided my understanding of nature's complexity and helped build this thesis. It is mind-boggling that we can now "listen" to our universe's gravitational "sound" or measure distances equivalent to measuring the distance to the nearest star to an accuracy smaller than a human hair [2]. We are building and controlling physics laboratories in our solar system at incredible locations (see picture with correct scaling on the first page of part I). And, we are using (as an analogy slightly more modest) toy models in the form of simple yellow foam cubes to understand experiments related to free falling gold-platinum TMs during such missions. The dimensions covered from galactic objects to femtometer measurements in space are astonishing.

While nature's phenomena on the smallest scales are well described by the theories of quantum physics, the large-scale effects and structures of our universe are governed by gravitation, which is described in Albert Einstein's theory of general relativity. However, in 1916, when he predicted that perturbations in the metric of spacetime can be caused by waves propagating with the speed of light through the universe, it was hard to imagine that they would ever be measured because of their very weak interaction with matter [3, 4].

At that time, it was impossible to predict the development of laser technology and the invention of optical interferometers, which has now progressed for over 70 years. These new experimental tools changed what was thinkable and inspired research regarding GW detection – a field originally established by resonant-mass detectors [5]. My mind is intrigued that a virus's weight must (and can) be measured over long timescales as a metaphor to explain what is needed to detect GWs in space.

The simple idea that light itself, with its constant speed (in vacuum), provides the perfect ruler to measure distance variations by comparing travel time differences between photons bouncing off reference mirrors was instrumental to the first direct detection of GWs from a binary black hole system by the Laser Interferometer Gravitational-Wave Observatory (LIGO) interferometers in 2015 [6]. This achievement confirmed decades of research and was later awarded with the Nobel Prize in 2017 for Rainer Weiss, Barry Barish and Kip Thorne. As all of this happened during our "own" LPF mission in preparation

for LISA, me and my colleagues directly experienced the excitement and progression in the field.

The ongoing observations of GWs have opened a new "window to the universe". They inform us about the most energetic events in space, impacting the very structure of spacetime, encoded in their signatures. Figuratively speaking, scientists, engineers and data analysts have developed this new, unique ability, or sense, to "listen" to the universe – right at a time when I was just joining the field as a fascinated witness. These new developments drastically deepen our understanding of cosmology and astrophysics, which previously relied on electromagnetic, neutrino, or cosmic ray observations.

This thesis is only one of many small contributions by a worldwide scientific community that, in the end, will make the now adopted[1] LISA mission possible. Here, the introductory sections give an overview to motivate the research for space-based GW detectors and the subject of this thesis, which the reader, like myself, hopefully finds helpful.

[1] LISA has been approved by ESA's Science Programme Committee on 25.01.2024, see https://www.esa.int/Science_Exploration/Space_Science/Capturing_the_ripples_of_spacetime_LISA_gets_go-ahead

Contents

List of Figures

List of Tables

List of Acronyms

ADC Analogue to Digital Convertor

AEI Albert Einstein Institute

AOM Acousto-Optic Modulator

ASD Amplitude Spectral Density

BS Beamsplitter

BH92 Blackmann-Harris-92

DFACS Drag-Free and Attitude Control System

DFT Discrete Fourier transform

DMU Data Management Unit

DPLL Digital Phase-Locked Loop

DOF Degree-of-Freedom

DRS Disturbance Reduction System

DWS Differential Wavefront Sensing

ESA European Space Agency

ESOC European Space Operations Centre

ET Einstein Telescope

FPGA Field Programmable Gate Array

GRS Gravitational Reference Sensor

GW Gravitational Wave

IABG Industrieanlagen-Betriebsgesellschaft mbH

IDL Interferometer Data Log

ISI Inter-Spacecraft Interferometer

LCU Laser Control Unit

LIGO Laser Interferometer Gravitational-Wave Observatory

LISA Laser Interferometer Space Antenna

LMU Laser Modulation Unit

LPF LISA Pathfinder

LPSD Logarithmic Frequency Axis Power Spectral Density

MAD Median Absolute Deviation

MOSA Moving Optical Sub-Assembly

NCO Numerically Controlled Oscillator

NPRO Non-Planar Ring Oscillator

OB Optical Bench

OBI Optical Bench Interferometer

OMS Optical Metrology System

OPD Optical Pathlength Difference

PD Photodiode

PLL Phase Locked Loop

PM Phasemeter

PPS Pulse Per Second

PSD Power Spectral Density

PZT Piezo-electric Transducer

QPD Quadrant Photodiode

RF Radio Frequency

RFI Reference Interferometer

RIN Relative Intensity Noise

RLU Reference Laser Unit

RMS Root Mean Square

RPN Relative Power Noise

SBDFT Single-Bin Discrete Fourier Transform

SC Spacecraft

SNR Signal to Noise Ratio

SVN Small Vector Noise

TDI Time-Delay Interferometry

TM Test Mass

TMI Test Mass Interferometer

TTL Tilt-To-Length

Part I

Introduction

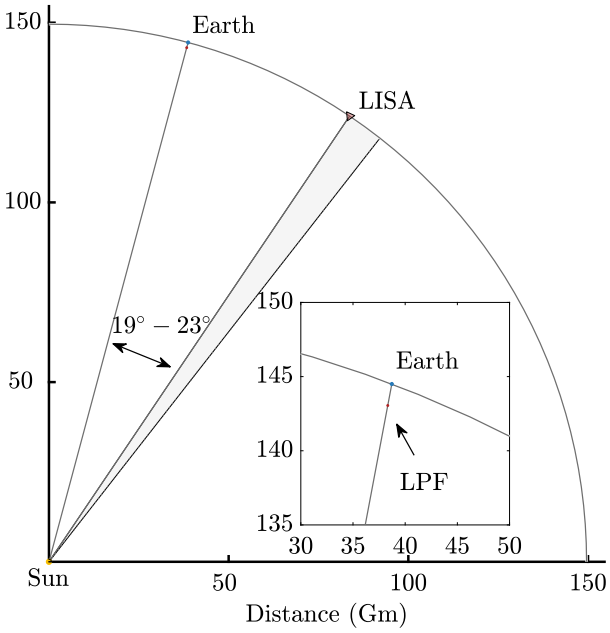

Chapter 1
Overview

This thesis consists of six parts.

Part I contains the introduction and describes the scientific scope regarding GWs, their detection in space, and the influence of measurement noises. Here, the problem of RIN is introduced. It also gives an overview of the LPF and LISA missions, as needed for the main parts. It is partially based on publications [P1–P4] as indicated in the sections.

Part II describes the RIN to phase coupling theoretically and derives relations that estimate the resulting noise levels. It also covers the common-mode rejection properties and shows simulations of these predictions. This part stems from the article [P1]: "Relative-Intensity-Noise Coupling in Heterodyne Interferometers", by Wissel *et al.*

Part III presents a detailed analysis of the RIN contribution to the overall performance of the LPF mission. It characterizes the essential interferometric measurement system aboard the SC and highlights specific experiments. This part is based on the articles [P2]: "Sensor Noise in LISA Pathfinder: In-Flight Performance of the Optical Test Mass Readout", and [P3]: "Sensor noise in LISA Pathfinder: An extensive in-flight review of the angular and longitudinal interferometric measurement system", by the LPF collaboration (with the author of this thesis being the first corresponding author).

Part IV transfers the research from parts II and III to the LISA mission architecture. It analyzes the possible RIN contributions theoretically and summarizes simulation results for the whole constellation. The RIN induced phase error is also propagated through the important TDI algorithm for various laser locking configurations. This part is from the article [P4]: "Influence of Laser Relative-Intensity Noise on the Laser Interferometer Space Antenna", by Wissel *et al.*

In part V, a summary of the results and conclusions is given together with ideas for future research.

The appendix in part VI gives more details on balanced detection and lists the experiments and timespans used in the LPF sensitivity analysis.

Chapter 2
Regarding gravitation

2.1 Gravitational Waves

In his theory of general relativity, Albert Einstein describes the structure of spacetime and its interaction with matter through the Einstein field equations. Here, contrary to Newton's immediate action at a distance, local changes in the gravitational field cannot act instantaneously everywhere. Instead, they propagate in the form of GWs with the speed of light and transport energy through the universe. Visually, GWs are often referred to as "ripples in the fabric of spacetime" [7].

Famously, the three fundamental principles that Einstein used were, (1) that locally, geodesics appear straight (with the free fall of objects as their natural state of motion), (2) that space tells matter how to move, and (3) that matter tells space how to curve [8]. Therefore, gravitation becomes a property of the curvature of space, which influences the objects following their geodesics within.

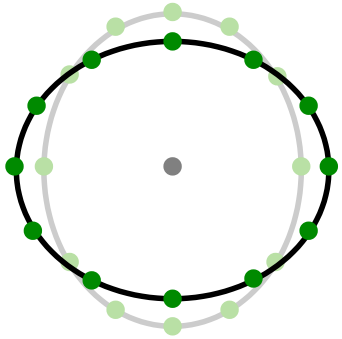

Figure 2.1 The effect of a linearly polarized GW on a ring of (spherical) TMs with respect to a central TM and orthogonal propagation. The distances are continuously stretched and squeezed (or vice-versa) while the GW is passing through.

A key property of every accelerated system of masses is the radiation of gravitational energy in the form of waves throughout spacetime, with some analogy to accelerated electromagnetic charges. If space is curved by a mass resting at a certain point, it must also change if the mass is accelerating away. However, no gravitational dipole radiation exists since there are no negative masses. GWs are radiated from the quadrupole moment of the mass distribution, meaning that even a single spinning mass with any given asymmetry produces GWs. Especially interesting are systems with two masses orbiting each other because they emit GWs converted from their kinetic energy, see for example the first indirectly observed GW through the discovery of a pulsar in a binary system from Hulse and Taylor in 1974, leading to the publication from Weisberg and Taylor in 1981 [9, 10]. This loss of energy constantly reduces their separation until a

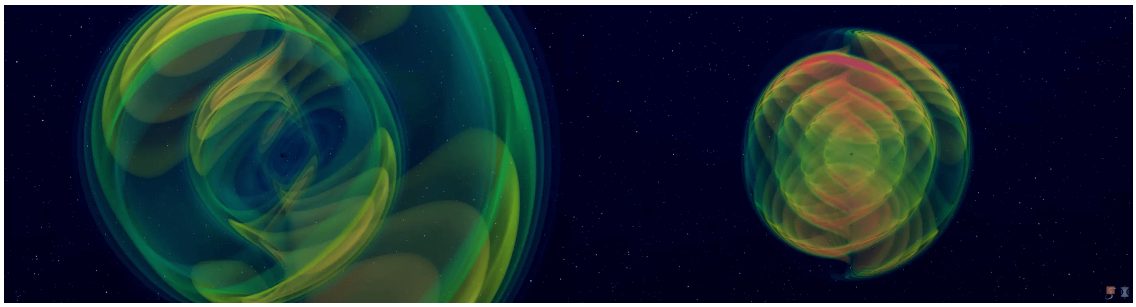

Figure 2.2 A simulation that shows the merger of two asymmetric black holes with 8 and 30 solar masses each. This leads to higher harmonics in the GW signal. Image from [12].

final merger event occurs. They produce very characteristic waveforms from their late inspiral, merger, and ring-down phases that can be compared against simulated waveforms calculated from general relativity [11].

Generally, any change in gravitation manifests (or can be imagined) in the relative acceleration of nearby TMs by a change in their separation, since their geodesics are no longer parallel in the new curvature of space, as indicated in figure 2.1 for a GW passing through a ring of such TMs. GWs have an alternating contraction and expansion effect on this ring, so their separation changes periodically. They are transversal and have states of linear and (by linear combination) circular polarization. The orthogonal linear states are called "+" (plus) and "x" (cross), the latter due to the 45° rotation in its influence relative to the "+" orientation. This behavior motivates the typical "L" shape of most terrestrial interferometric detectors with two perpendicular measurement arms, in which laser light travel time differences, induced by the passing GWs, are compared. This is explained in more detail in section 2.3.

The effect of a violent astrophysical event that causes strong changes in the curvature of space, as illustrated for an unequal mass binary black hole merger in figure 2.2, can be described (far away from the source) as a small perturbation in a, at any other time, flat local spacetime metric. Since the Nobel Prize winning first direct discovery of two merging black holes by the LIGO detectors in 2015 [6] (a merger event with black holes of about 29 and 36 solar masses respectively, generating a 62 solar mass black hole, while emitting the energy of 3 solar masses in form of GWs), these variations are routinely being detected with terrestrial observatories, and the future LISA mission will detect them for the first time in space.

When GWs arrive at the ground-based detectors, the strength (amplitude or dimensionless strain h) of their induced metrical perturbations is typically very small and in the order of $h \sim \Delta L/L \sim 10^{-21}$, even though their peak gravitational luminosity can easily reach 10^{49} W at the source [6]. ΔL is the absolute change in distance over the measurement length L. For ground-based detectors with $L \sim (3 \text{ to } 4)$ km, this means that the gravitational signals required to be resolvable correspond to length changes of about 10^{-18} m, which

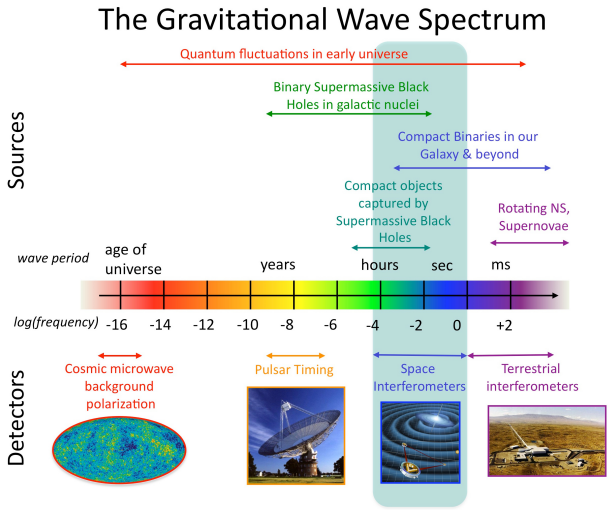

Figure 2.3 The gravitational wave spectrum from [17]. Shown are cosmological and astrophysical objects causing GWs at different wave frequencies. Various detectors are required to detect their signals, similar to the electromagnetic spectrum. This thesis focuses on space interferometers like the LISA mission.

is technologically very challenging [6, 13]. Nowadays, the detectors are approaching a sensitivity of $10^{-20}\,\mathrm{m}/\sqrt{\mathrm{Hz}}$ at a few hundred Hz. For roughly equivalent space-based detectors with much larger arm-length L in the order of Gm, this only requires to be sensitive for length changes ΔL in the order of pm.

2.2 Gravitational Wave sources

As mentioned above, GWs, arriving at Earth far away from the source, have typically very small amplitudes and thus their effects on spacetime are tiny. Therefore, only the more violent astrophysical events associated with stellar-mass objects and above cause perturbations strong enough to be observable. Currently, the vast majority of measured signals belongs to binary black hole mergers with tens of solar masses [14]. These GWs from merging black holes with varying mass ranges allow insights into their origin and the general structure of galaxies and the universe. They provide a new measure of distance, allow to test general relativity, and to investigate formation scenarios while yielding statistics on populations [15].

However, black holes are not the only source of observable GWs. The first detection of a $\sim 100\,\mathrm{s}$ signal of a binary neutron star inspiral allowed a very successful electromagnetic follow-up campaign, which verified that GWs are indeed traveling at the speed of light, by observing a short gamma-ray burst less than 2 s after the merger occurred with the Fermi observatory. It was further possible to set restrictions on the neutron stars equation of state and to confirm theories about the origin of heavy elements such as gold from the merger [16].

In general, while the amplitude of the GW signal reveals the distance to the source, the frequency and its time derivative are influenced by the collective mass of the system.

Heavier objects are moving at slower velocities in larger systems, thus producing GWs at lower frequencies and longer wavelengths. Due to the response of detectors depending on their arm-length, technological constraints and the influence of noise on the sensitivity at different frequencies, various detectors are needed to observe sources overa broad frequency band, as highlighted in the following and shown in figure 2.3.

Fast spinning neutron stars or even supernovae are expected to produce GWs up to kHz frequencies. More compact binary objects can be observed at the end of the inspiral and merger phase in the band between approximately (10 to 2000) Hz by terrestrial observatories [18]. These types of detectors use sophisticated Michelson interferometers to detect mergers from binary black holes and binary neutron stars.

Massive black hole binaries in the range of about (10^4 to 10^7) solar masses generate GWs that are crossing the mHz regime with wavelengths of thousands of kilometers (far before merger due to their long orbital period), requiring space-based observatories such as LISA with longer arm-lengths than possible on Earth. A large volume of compact galactic binary systems in our own Milky Way will be visible via space interferometry years before merger (and potentially later crossing into the terrestrial frequency band). These white dwarfs, neutron stars and stellar-origin black holes constitute one of the main study objectives of the LISA mission, with up to 25 000 individually resolvable galactic binaries expected [19]. Furthermore, the many research prospects with regards to LISA are stated as the study of the formation and evolution of those compact binaries, the origin and history of black holes across cosmic ages, the understanding of dense nuclear clusters with extreme mass ratio inspirals (which produce very complicated waveforms [20]), investigations into the astrophysics of stellar origin black holes, the estimation of the expansion rate of the universe, and the understanding of the stochastic GW background.

At the very low nHz frequencies, pulsar timing arrays search for remnants from supermassive black hole mergers. They try to identify slow variations in the arrival times from multiple pulsar observations in different sky locations due to the influence of GWs with arrays of radio-telescopes across the Earth. Pulsars are spinning neutron stars that are periodically emitting radio pulses with very stable timings. Recently, in an article analyzing 15 years of the NANOGrav pulsar timing array dataset, strong evidence for a stochastic GW background originating from a population of supermassive black hole binaries has been successfully identified [21].

2.3 Detecting Gravitational Waves with laser interferometers

The fundamental principle of GW detection with laser interferometers is identical for all currently operational ground-based and future space-based observatories. It is depicted in figure 2.4 with its typical “L” shaped Michelson configuration as used in ground-based

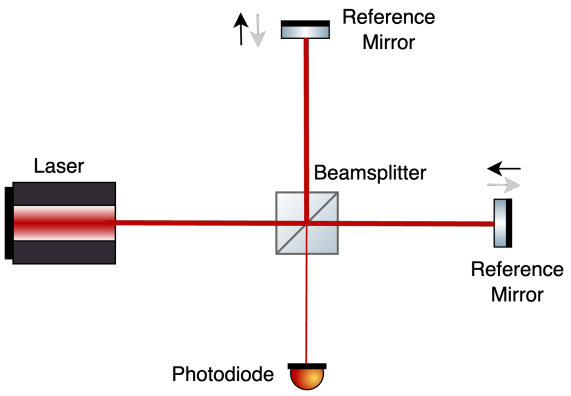

Figure 2.4 Typical simplified Michelson configuration of a GW observatory. The laser light is split at a Beamsplitter (BS) and propagates through different arm-lengths due to the effect of a GW passing through the detector. The Photodiode (PD) records the interference pattern of the two beams after recombining them at the BS. The detected power is modulated by the (weak) GW interaction. Many different noises make this measurement in reality very challenging [22].

facilities. The detector has two arms which allow to measure light travel time differences (from a coherent laser source) in one arm compared to the other. The time dependent strain of a GW passing through the detector creates a change in space perpendicular to the propagation axis. A linearly ("+") polarized wave orthogonal to the two detector arms leads to an elongation in one arm while compressing the other arm.

The light beams between the BS and reference mirror points (e.g. TMs) collect more or less phase, depending on the arm they are propagating in. The interference pattern on the PD changes due to the time dependent strain of the GW that is passing through the arms, thus translating the GW wave directly into a detectable change in power. An important advantage of laser light is the magnification of the travel time difference by the frequency of the beams, which is typically in the order of THz, making it easier to measure the resulting phase changes. For this type of equal arm-length configuration, any fluctuations in the laser beam itself such as frequency noise is highly correlated between the two arms and subtracts to a large degree upon interference, while the GW signals are differential (except for a precise 45° propagation or "x"-polarized wave with respect to the arms) and remain visible.

Not only is this measurement principle very similar for ground and space-based observatories (except for very unequal arm-lengths in space), but also the fundamental challenges that restrict their sensitivities are comparable. Both types need to isolate their reference TMs from stray forces that could mimic real GW signals, and they need to minimize any noises in the required high-precision displacement readouts that track the separation of the TMs. However, the precise implementations and technical complications differ. The distinctions between space and ground-based detectors are mainly due to their environments, and their arm-lengths.

A typical observatory on Earth is using homodyne detection in an highly upgraded and stabilized Michelson interferometer. Homodyne detection implies that the laser light in the two interferometer arms is at the same frequency upon interference, creating a constant signal on the PDs, that only changes when, for example, a GW passes through. The arm-lengths are in the order of a few km.

For space-based interferometers other modes of operation are required. The differential time measurement in a Michelson-like configuration is precisely timed by the coherent light itself, which is a practical feature of ground-based detectors. This design is not possible for space-based interferometers with arm lengths of millions of km due to beam divergence and the resulting loss of optical power at the distant SC. It requires a transponder scheme with another laser beam being actively transmitted back, mimicking the reference mirror reflection. Then, correlating independent measurements needs highly stable time references due to the timing precision required to compare photon arrival times in the different arms. Furthermore, space-based interferometers are not in a rigid configuration and subject to Doppler shifts due to their orbital dynamics, that lead naturally to a time-varying PD signal, which also contains the GW signals encoded as phase shifts. This measurement principle, the so called heterodyne interferometry, is presented in detail in chapter 6.

Coincident characteristic detections at multiple interferometers, only delayed due to their separation by the GW travel time (which is equal to the speed of light), give high confidence in measuring a true signal. Considering only terrestrial observatories, sky-localization by triangulation is already improving constantly due to an evolving network of detectors (LIGO at Livingston and Hanford in the US, Virgo near Pisa in Italy, KAGRA in Japan, the planned LIGO-India, and GEO600 near Hannover in Germany). With more and more ground-based detectors becoming available, the prospect of a worldwide detector network with multi-messenger follow-up observations in the electromagnetic spectrum has already become reality [23, 24]. The catalog of confirmed mergers is growing steadily, as can be seen by the 94 observations published to date [14], covering the "O1" – "O3" measurement campaigns. Currently, the observational period "O4" of the terrestrial LIGO, VIRGO and KAGRA observatories is running until the end of the year. This already very prolific state of affairs will only improve with the commissioning of LISA.

In general, laser interferometers have been well-established as the key technology to measure GWs. The next generation of terrestrial detectors will address technical noise sources, for example, by lowering thermal noise couplings at the mirror coatings and suspensions and by including frequency-dependent squeezing to reduce quantum noise, as has been recently demonstrated [25]. One prime example is the Einstein Telescope (ET), currently being designed as an underground facility with longer arm-lengths of 10 km in a triangular configuration, incorporating many advanced technologies [26].

The main focus of this thesis is on space interferometry, and the prospects of space-based GW observatories are detailed in the next chapter.

Chapter 3

Going to space: Toward the Laser Interferometer Space Antenna

Ground-based detectors are limited at the high frequencies (hundreds of Hz) by quantum effects such as shot-noise, while at lower frequencies (around a few Hz) their sensitivity is dominated by seismic fluctuations, the influence of the local gravity field due to the environment, thermal noise, and quantum radiation pressure noise.

However, especially at low frequencies from 10^{-4} Hz up to 1 Hz a large number of interesting GW sources are expected (see figure 2.3), whose detections would allow to investigate the evolution from the early universe to the formation processes of stars. To improve sensitivity at these frequencies, the limiting environmental effects are "easily" resolved by constructing a very large and quiet GW observatory in space. This provides the possibility to use arms with millions of km which improves the sensitivity for very long wavelengths. Due to the much longer arms, the interferometric displacement sensitivity required for a comparable GW strain sensitivity of ground based detectors is relaxed by about a factor of a million [24].

Many merger events visible in ground-based detectors will be seen much earlier from space during their inspiral phase until enough kinetic energy has been radiated away and the orbital frequency reaches a few hundred Hertz. Different observations with space-based and ground-based detectors, electromagnetic telescopes, and neutrino detections will foster research through combined multi-messenger astronomy.

While ground-based detectors are largely restricted by noise in their sensitivity and measure currently up to a few events per week, space-based detectors will likely be dominated by a large number of resolvable signals, requiring new data analysis methods such as simultaneous global fits of the whole data set, see [27].

This completely new type of detector is planned to launch in the next decade and has a long conceptual history. An introduction to LISA and its precursor mission LPF is presented in the following sections. They also highlight system details relevant for the subsequent parts of this thesis.

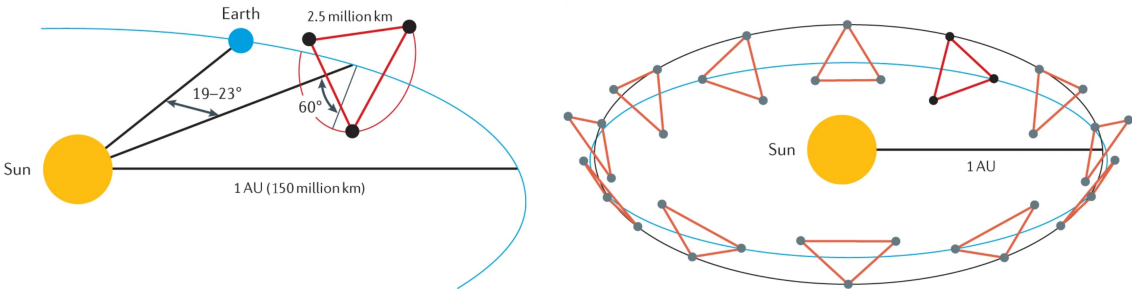

Figure 3.1 The LISA constellation shown here in an Earth-trailing heliocentric orbit with its three sensitive arms (left). The three SC follow a cartwheel formation and orbit around the sun within a year (right). Image modified and not to scale, courtesy of the LISA consortium.

3.1 LISA

Please note that this section has been published in [P4] in collaboration with the co-authors.

LISA is an ESA led future space mission to be launched in the mid 2030s, that will detect GWs in the range from 0.1 mHz – 1 Hz, aiming at the observational gap between pulsar timing arrays, which are targeting very low frequencies, and the ground-based detectors sensitive toward higher frequencies [19, 28].

As depicted in figure 3.1, the mission consists of a constellation of three identical SC, each of which follows a heliocentric orbit at similar distance to the Sun as the Earth, such that the whole constellation forms an almost equilateral triangle either leading or trailing our planet with an angular separation of (19 to 23)° [24].

Each SC hosts two free-falling TMs, which are shielded inside the SCs from external disturbances and act as geodesic reference points for the GW detection. Laser beams are exchanged between the SCs across the 2.5 Gm arms of the constellation (called "links"), tracking the distance variations between the TMs.

Due to orbital dynamics, the frequencies of the inter-SC lasers will be subject to Doppler shifts in the MHz band, such that the interferometers will detect heterodyne frequencies with a bandwidth of about (5 to 25) MHz. Distance fluctuations between the SC and the TMs housed within them will be encoded as phase fluctuations in these MHz beatnotes, which the LISA PMs will be able to resolve with μ-cycle precision, corresponding to a design sensitivity of $\sim$ pm/$\sqrt{\text{Hz}}$ in the measurement band.

This ultra precise measurement will enable LISA to simultaneously detect and characterize tens of thousands of gravitational-wave sources, potentially answering many open questions in astrophysics, cosmology and fundamental physics, see part I, and [19].

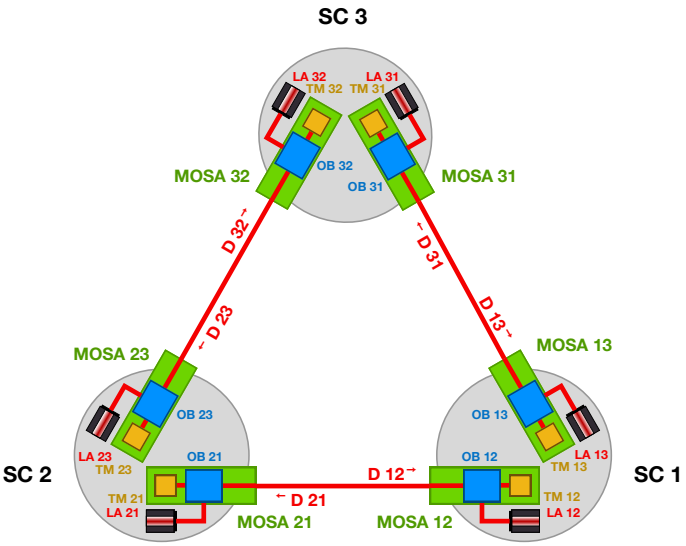

Figure 3.2 Simplified overview of the LISA triangular constellation with the naming conventions as used here. Delays are denoted D_{ij}; Moving Optical Sub-Assembly $(\text{MOSA})_{ij}$; Optical Bench $(\text{OB})_{ij}$; lasers are called LA_{ij}. Reprint from [P4, 29, 30].

In figure 3.2, a schematic of the constellation with the commonly used nomenclature is shown. The main measurement is the "virtual" TM-to-TM measurement along one LISA arm. For technical reasons (e.g., beam divergence over millions of kilometers leading to very weak beam powers, straylight effects and optical design), no direct TM-to-TM measurements are possible. Therefore, we use the "split-interferometry" setup, in which three optical measurements are combined to reconstruct the desired quantity: the local TM-to-local SC measurement, the local SC-to-distant SC measurement, and the distant SC-to-distant TM measurement.

All components need to be stable within the measurement band during the mission, which implies that the optics need to be constructed on an ultra-stable OB and tested to not only withstand the forces acting during launch, but also for the long duration of about ten years in space and resist any spurious radiation propagating through the SC.

The Amplitude Spectral Density (ASD) requirement for the total single TM-to-TM link metrology noise is

$$S_{\text{IFO}}^{1/2} \leq 10 \frac{\text{pm}}{\sqrt{\text{Hz}}} \cdot \sqrt{1 + \left(\frac{2\,\text{mHz}}{f}\right)^4}. \tag{3.1}$$

Here the square root factor allows for a relaxation towards lower frequencies, where acceleration noise becomes dominant and testing is difficult [19].

The lasers have an output power of 2 W at 1064 nm [19], and are stabilized on a cavity. A total of six lasers are powering 18 interferometers, and enable the TM-to-TM measurement by linear combinations. Per SC, there are two MOSAs among other units, each attached to a laser source (named "LA_{ij}"), see figure 3.3. They host three interferometers:

- one inter-SC interferometer (ISI) containing the GW signals,

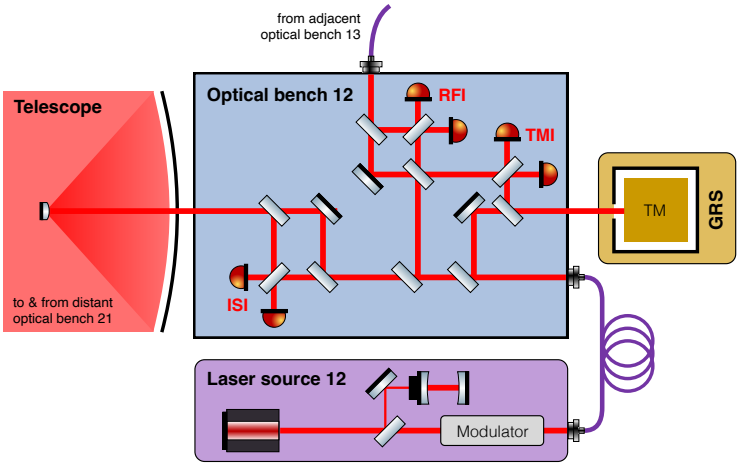

Figure 3.3 Schematic of one LISA MOSA. A telescope collects the light from the distant SC and interferes it with the local beam. The local laser is also interfered with the laser from the adjacent MOSA on the same SC in the local TMIs and RFIs. The GRS controls the TM relative to the SC in the suspended degrees of freedom. Reprint from [P4, 30].

- one TM-to-SC interferometer (TMI), used to monitor the reference points in this split interferometry setup with respect to the local SC, and
- one reference interferometer (RFI), used for laser locking and reduction of common noise.

Between the two SC of one LISA arm, there are two symmetric laser links. Due to divergence of the Gaussian output beam, the laser power reduces drastically over the 2.5 Gm propagation distance to a few hundreds pW at the receiving SC; it is then interfered with a local mW beam. The laser beams will carry additional modulation sidebands used for clock synchronization, ranging information and data transfer, which further reduce the available power in the main carrier-to-carrier beat signal to about 81 % [19, 31].

The two adjacent MOSAs exchange their laser light via fiber backlinks as indicated in figure 3.3. To reduce backscatter, the powers guided into the fibers are also relatively small (in the order of mW to nW). Thus, the out-coupled beams are interfered with beams a few orders of magnitude stronger, such that the beam power ratio in any interferometer is far from unity. Note that, even though the two local interferometers between each MOSA on a single SC mix the same two laser beams (i.e., measure the same absolute beat frequency), they have their power ratios inverted due to the fiber transfer. This is relevant for the local scaling of the RIN to phase couplings, as will be considered later in part IV.

In every interferometer, two beams interfere at a recombination BS. Subsequent PDs measure their impinging time-varying power. The two output ports of each of these BS are used to apply balanced detection to the (naturally π-shifted) signals, which allows us to subtract both ports to reduce noises (like certain RIN components as described later), while maintaining the signal information (see also parts II and VI).

The phase measurement is performed by dedicated Digital Phase-Locked Loops (DPLLs) [32, 33], as depicted in figure 3.4. The loops are able to track the time-varying beatnote over many MHz and measure the phase with μ-cycle precision. It resembles a typical

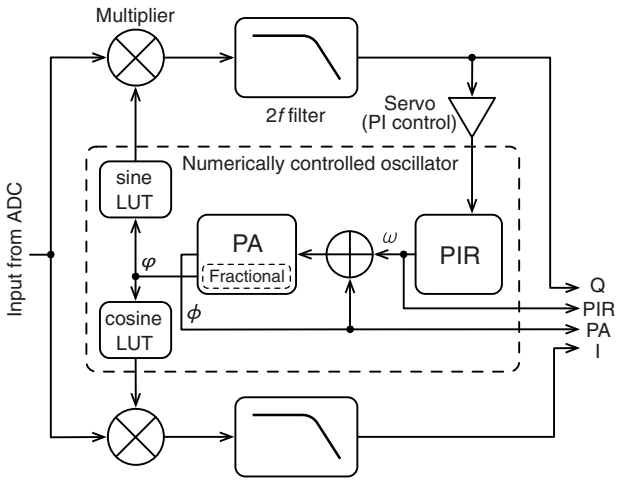

Figure 3.4 Schematic of a DPLL in LISA. The input time series from the ADC is mixed with the sine from an NCO, which represents a closed control loop with the down-mixed instantaneous frequency as its error signal. The DPLL is able to follow the input frequency (even for time-varying heterodyne frequencies) within its bandwidth and accumulates the total phase of the input, which is the desired phase measurement. PA phase accumulator; PIR phase-increment register; LUT look-up table; PI proportional-integral. Image reprinted from [33].

I/Q-demodulation scheme, but is all performed digitally and uses a control loop on the Q quadrature as an error signal for an Numerically Controlled Oscillator (NCO) to track the variable incoming signal frequency for the mixing process.

Due to its complexity, a precursor mission, LPF, had to demonstrate the feasibility of many parts of the system, especially the sufficient free-fall of the TMs [P5, P6], including the local interferometry inside each SC, which was performing beyond expectations with approximately $30\,\mathrm{fm}/\sqrt{\mathrm{Hz}}$ sensitivity at frequencies where the interferometry was limiting [P2, P3]. LPF is described in the next section.

Further, the inter-SC interferometry has been partially demonstrated with the GRACE-FO mission. It had similar characteristics in terms of laser noise, Doppler shifts and envisaged light powers, but with "only" one laser link of about 200 km, reaching $1\,\mathrm{nm}/\sqrt{\mathrm{Hz}}$ sensitivity above 100 mHz [34].

However, LISA presents a number of unique technical challenges. Similar to GRACE-FO, the raw readout of the inter-satellite interferometers of LISA will be dominated by laser frequency noise, which does not immediately cancel (as it would in a perfect Michelson interferometer), due to the time-varying and unequal arms of the constellation. Contrary to GRACE-FO, LISA will make use of the post processing technique Time-Delay Interferometry (TDI), in which multiple interferometric readouts are combined with the appropriate delays to suppress the dominant noise sources, such as laser frequency noise [35]. TDI and further techniques, together with strict requirements that are placed on the subsystems and lasers, will ensure that LISA reaches its sensitivity goal.

Different noises propagate through TDI with various transfer functions [36], depending on their characteristics, such that evaluating the final performance of LISA requires detailed studies for all performance relevant noise sources. A thorough analysis of the RIN coupling in LISA is given in part IV.

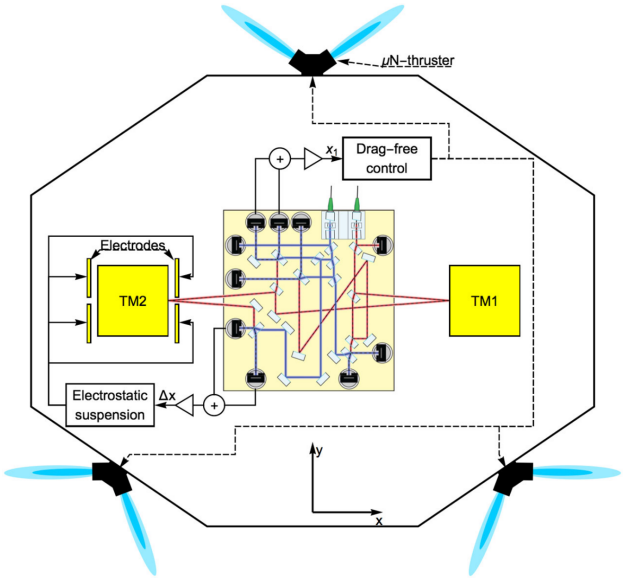

Figure 3.5 Functional schematic showing the nominal mode of operation of LPF. TM1 is freely moving along its geodesic trajectory. The SC and TM2 are forced to follow by measuring the path variations of TM1 and applying subsequent actuation forces and torques via the Drag-Free and Attitude Control System (DFACS) loop. A more detailed description is given in the text. This image is a reprint from [P5].

At the time of submitting this dissertation, LISA has been successfully adopted by ESA and is now moving into the industrialization phases, which constitutes a major milestone for the mission.

3.2 LISA Pathfinder

Please note that this section is using some content from [P2, P3] that was written in collaboration with the co-authors.

ESA's LPF mission (launched from Kourou, French Guiana, on December 3, 2015, on a VEGA rocket, and ended after an extension on July 18, 2017, by telecommand from ESOC, Darmstadt) was designed to prove that the technology needed for LISA is feasible. In particular it proved that the TMs could be placed in free fall with sufficiently low residual acceleration noise [P5, P6].

The mission consisted of a single SC, as shown in figure 3.5. It was operated in a very quiet and stable Lissajous orbit around the Earth-Sun Lagrange point L1, about 1.5 million km from the Earth and at a nearly constant separation and orientation with respect to the Sun. This led to a very stable thermal and mechanical environment, better than what is possible to achieve on Earth.

It contained two free falling TMs, each inside an electrode housing located in a small vacuum chamber. The position and orientation of both TMs along several degrees of freedom was continuously monitored by the OMS, the high precision interferometric

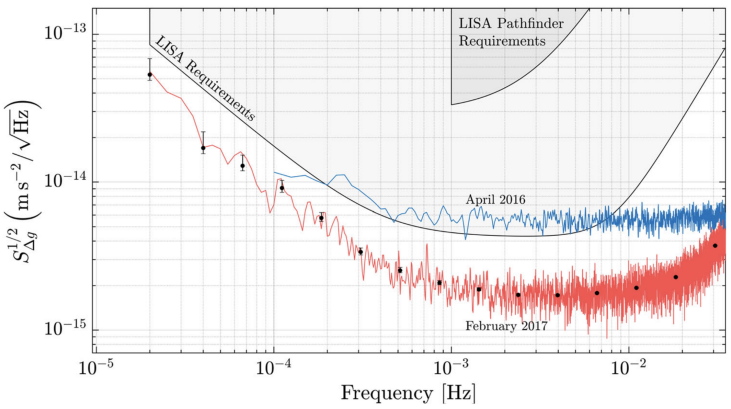

Figure 3.6 The main results of the LPF mission highlighting its great success. Shown are the ASDs of the residual differential acceleration between the free falling TMs. The results from February 2017 were better than what is required for LISA. This plot is copied from the publication [P6].

readout system. The sensitivity analysis of this subsystem is subject of this thesis in part III, with particular focus on RIN.

In science operations, the SC operated in a "drag-free" state where one TM (TM1 in figure 3.5) was allowed to freely follow its inertial path and the SC was forced to follow accordingly. The second "suspended" TM was forced to follow the inertial TM by electrostatic actuation. The SC used the signals from the OMS to sense its own movement relative to the inertial mass, and used these signals as one set of inputs to the DFACS. This system controlled 15 degrees of freedom of the relative position and attitude of the SC and TMs through firing micro-Newton thrusters attached to the SC and acting on the TMs through electrostatic forces (shown for TM2 in figure 3.5).

LPF's target was to achieve a differential acceleration noise between its two TMs within a factor of 10 of the LISA requirement. As figure 3.6 shows, the mission exceeded its goal and demonstrated even better performance than the level of free fall required for LISA.

The OMS comprised 4 interferometers (their entirety called Optical Bench Interferometer (OBI)), which were needed in order to achieve the high precision readout: the so-called Reference-, Frequency-, X1-, and X12-interferometers, see figure 3.7. They allowed to directly measure six degrees of freedom, namely

- the variations in separation of the two TMs, x_{12},
- the variation in separation of the first TM to the OB, x_1,
- the corresponding pitch $\phi_{12} = \phi_2 - \phi_1$ via DWS,
- and yaw angle $\eta_{12} = \eta_2 - \eta_1$ (which are differential tilts between the TMs),
- as well as ϕ_1, and
- η_1 (which are relative tilts of TM1 to the OB).

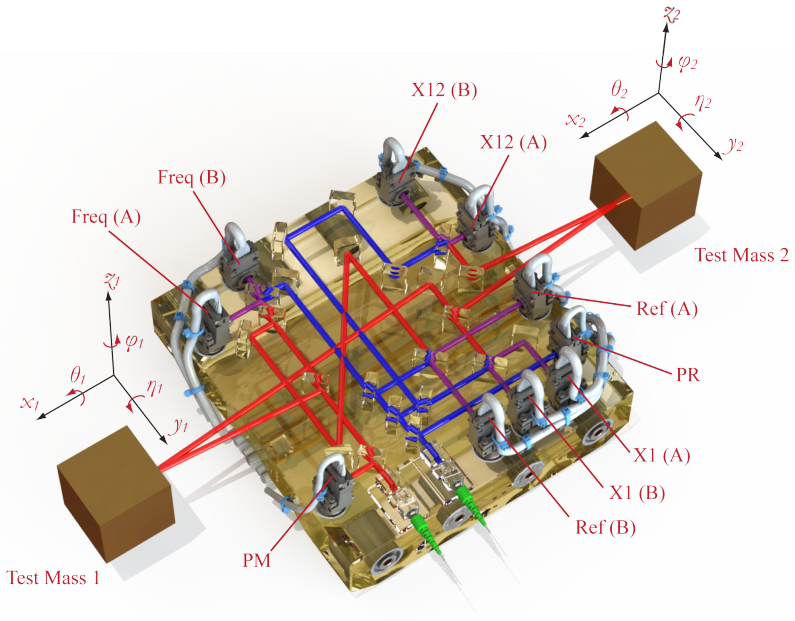

Figure 3.7 A rendering of the OBI highlighting the four interferometers (X12, X1, Ref. and Freq.). The reference beam is blue, the measurement beam red, and combined beams purple. Also shown are the TMs and their associated coordinate frames. This image is a reprint from [P3], provided by the LPF collaboration.

Linear combinations of these measurements (performed with Quadrant Photodiodes (QPDs)) provided the position and orientation of the second TM with respect to the OB, x_2, ϕ_2 and η_2. The "raw" measurements in radian were scaled to TM motion, and to TM angles using DWS calibration factors from electrical to optical phase of order $5000\,\mathrm{rad_{el.}/rad_{opt.}}$, which were determined on ground (see later in this section).

In the *Reference interferometer*, both beams were routed entirely within the OB, without reflection at the TMs. The beams' optical pathlengths were equal by design so that the Reference interferometer sensed common mode noise sources that all interferometers were subject to, such as differential phase changes originating from the optical fibers or modulators. The Reference interferometer signal (x_R) was therefore subtracted from all other longitudinal interferometer readout signals to obtain clean measurements.

In the *Frequency interferometer* both beams were again routed entirely within the OB, however the optical pathlengths were intentionally unequal by $(38.2 \pm 0.1)\,\mathrm{cm}$ [37], which enhanced the coupling of laser frequency noise. The phase readout signal of this interferometer had the Reference signal subtracted and was then used in a digital control loop to stabilize the laser frequency (see [38]).

In the *X1-interferometer*, the measurement beam (indicated in red in figure 3.7) reflected from TM1 before recombining with its reference beam (blue beam in figure 3.7) to give x_1.

On-board processing formed

$$o_1 = \frac{\lambda}{4\pi\cos(\alpha)}(x_1 - x_R), \tag{3.2}$$

the displacement between the free falling TM1 and the OB. λ is the wavelength of the laser. The parameter $\alpha \approx 4.5°$ corrects for the angle of incidence on the TMs and the factor 2 in front of 2π is due to the double path change when a TM moves. Without the scaling factors, we call the quantities "raw" measurements; namely o_1^{raw}, (and see below) o_{12}^{raw}. This interferometer readout was dominated by SC motion, since the OB was rigidly connected to the SC. Similarly, the angular DWS signals η_1^{raw} and ϕ_1^{raw} were processed from pairs of top-bottom and left-right quadrant phase differences. The calibration for DWS is given at the end of this section.

In the *X12-interferometer*, the measurement beam reflected from both TMs before being recombined with its reference beam. The on-board computer calculated

$$o_{12} = -\frac{\lambda}{4\pi\cos(\alpha)}(x_{12} - x_R), \tag{3.3}$$

to get a signal that sensed differential displacement between both TMs (strongly suppressing any SC motion) and was therefore the main scientific readout signal in LPF. Similarly formed (as in X1) were differential in-plane and out-of-plane angular readouts ϕ_{12}^{raw} and η_{12}^{raw} from pairs of quadrant combinations.

The OMS measured the TM to TM displacement (o_{12}) with a requirement of

$$S_{\text{OMS}}^{1/2}(f) \leq 9\,\frac{\text{pm}}{\sqrt{\text{Hz}}}\sqrt{1 + \left(\frac{3\,\text{mHz}}{f}\right)^4}, \tag{3.4}$$

over a frequency range of (1 to 30) mHz. This is a relaxation of the sensitivity which will be required for the LISA Test Mass Interferometer (TMI) by approximately one order of magnitude (not to be confused with the total LISA single link requirement in equation (3.1)). The LPF OMS is directly comparable with the TMI, since there a similar low-noise, multi degree of freedom readout is key to reaching the desired sensitivity.

The requirement for the measurement noise of ϕ_{12}, η_{12}, ϕ_1 and η_1 was $20\,\text{nrad}/\sqrt{\text{Hz}} \times \text{NSF}(f)$, with the identical $\text{NSF}(f) = \sqrt{1 + (3\,\text{mHz}/f)^4}$, which is the noise shape function adapted to the expected cross-over between force noise induced TM motion and interferometric sensing noise. The required measurement band was also (1 to 30) mHz, [39, 40].

The OMS further comprised not only the OBI, but also the Reference Laser Unit (RLU), the Laser Modulation Unit (LMU), the Laser Control Unit (LCU), the PM, and the Data Management Unit (DMU) [42–44]. A schematic of the system is shown in figure 3.8.

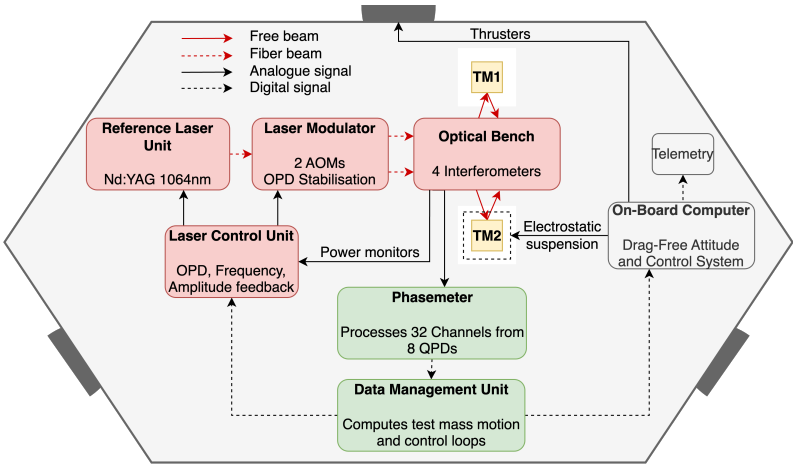

Figure 3.8 A functional overview of the OMS and its subsystems. The electrode housing around TM1 is not shown. Modified reprint from [P3], based on [41].

The OBI consisted of a $20 \times 21.2 \times 4.5\,\mathrm{cm}$ OB made of Zerodur (a glass ceramic) onto which the optical components were hydroxide-catalysis bonded [45]. The OBI was located between the two vacuum chambers housing the TMs, and it was rigidly connected to the SC. Onto the OB, all BSs, mirrors and PDs of the laser interferometers were bonded. The laser light in the OBI was produced in the reference laser unit from a Nd:YAG non-planar ring oscillator that provided about 35 mW of single-mode light at $\lambda = 1064\,\mathrm{nm}$. This light was fiber coupled into the laser modulator unit, where the beam was split by a 50/50 BS and each beam was then frequency shifted by an acousto-optic modulator by about 80 MHz, such that a relative frequency shift of $f_1 - f_2 = f_{\mathrm{het}} = 1\,\mathrm{kHz}$ was generated to enable heterodyne interferometry.

From the laser modulator unit, the light was then delivered via optical fibers to the OBI (indicated by the two green fiber connectors in figure 3.7). On the OB, the beam paths were split into 4 different interferometers and finally detected by 8 QPDs. About 2.4 mW was reflected off TM1, and 1.2 mW off TM2. The signals were processed by two hot-redundant PM units, which performed Single-Bin Discrete Fourier Transforms (SBDFTs) [P3, 43] and passed data at a sampling frequency of 100 Hz to the DMU. Within the PM, the digitized photocurrents or voltages, U_i, were further processed by a Field Programmable Gate Array (FPGA) that performed the SBDFT. For each segment of $N_{\mathrm{FFT}} = 500$ samples (10 ms and thus 10 cycles at 1 kHz), it computed the three quantities

$$y_{\mathrm{DC}} = \frac{1}{N_{\mathrm{FFT}}} \sum_{i=0}^{N_{\mathrm{FFT}}-1} U_i \tag{3.5}$$

$$y_{\mathrm{Re}} = \frac{2}{N_{\mathrm{FFT}}} \sum_{i=0}^{N_{\mathrm{FFT}}-1} U_i \cos(\omega_{\mathrm{het}} t_i) \tag{3.6}$$

$$y_{\mathrm{Im}} = \frac{2}{N_{\mathrm{FFT}}} \sum_{i=0}^{N_{\mathrm{FFT}}-1} U_i \sin(\omega_{\mathrm{het}} t_i) \tag{3.7}$$

and auxiliary diagnostic quantities (the actual processing was using unsigned integer arithmetic) [46]. From these, the longitudinal and angular signals were formed by linear combinations and the resulting phases computed via $\arctan(y_{\mathrm{Im}}/y_{\mathrm{Re}})$, followed by a phase-tracking algorithm to remove phase wraps of 2π. The scaling from raw phase to TM motion was then applied as described above. An exact processing overview is given in [41].

The factors determined on-ground for calibrating the raw DWS sensing to TM angles were

$$g_1 = (-0.202 \pm 0.004) \times 10^{-3}\,\mathrm{rad/rad}, \tag{3.8}$$
$$g_2 = (0.209 \pm 0.004) \times 10^{-3}\,\mathrm{rad/rad}, \tag{3.9}$$
$$g_3 = (-0.175 \pm 0.006) \times 10^{-3}\,\mathrm{rad/rad}, \tag{3.10}$$
$$g_4 = (-0.189 \pm 0.003) \times 10^{-3}\,\mathrm{rad/rad}, \tag{3.11}$$
$$g_5 = (0.188 \pm 0.007) \times 10^{-3}\,\mathrm{rad/rad}, \tag{3.12}$$
$$g_6 = (-0.193 \pm 0.004) \times 10^{-3}\,\mathrm{rad/rad}, \tag{3.13}$$

with the uncertainties originating from the measurements with approximately 2 % errors, recalculated for the in-flight coefficients. These were applied in the following way:

$$\phi_1 = g_1 \phi_1^{\mathrm{raw}}, \tag{3.14}$$
$$\eta_1 = g_2 \eta_1^{\mathrm{raw}}, \tag{3.15}$$
$$\phi_2 = g_3 \phi_1^{\mathrm{raw}} + g_4 \phi_{12}^{\mathrm{raw}}, \tag{3.16}$$
$$\eta_2 = g_5 \eta_1^{\mathrm{raw}} + g_6 \eta_{12}^{\mathrm{raw}}. \tag{3.17}$$

The measurements were downsampled to 10 Hz and sent to the on-board computer for use in the SC and TM control, and telemetered as science output data down to Earth.

Moreover, the power of each beam was sensed by a dedicated power PD. Their signals were used in an analogue control loop for fast laser amplitude stabilization.

Chapter 4

Introducing RIN

4.1 Laser noise contributions

While lasers are generally very good at producing coherent light at a central carrier frequency, they exhibit different kinds of noises, namely phase (or frequency) and intensity noise, both from technical imperfections and quantum interactions. Since those reduce the signal-to-noise ratio in interferometric phase measurements, they are ideally mitigated with sophisticated methods to a level required for GW detection. There are, however, firm limitations in the possible suppression due to the Heisenberg principle, which states that the phase and amplitude quadrature of a coherent state of laser light cannot be measured with arbitrary accuracy. The introduction of squeezing technology has improved sensitivity for ground-based detectors below the standard quantum limit by redistributing the uncertainty from one quadrature (quantum shot-noise) to another (quantum radiation pressure noise) [47]. This method is, however, not possible for space-based detectors due to their significant optical losses. LISA is operating with classical light. Locally (without considering frequency noise), it is limited by shot-noise at its Inter-Spacecraft Interferometer (ISI) arising from the statistical distribution of photons arriving at the detector (whose resulting phase noise scales inversely with the arriving beam power of a few hundred pW).

On the one hand, phase or frequency noise directly causes uncertainty in the phase readout. It is inherently present due to imperfect sinusoidal carriers of single-mode lasers. However, similar direct phase noise also appears due to numerous other effects, such as optical path length variations or straylight couplings. The fluctuations in the carrier frequencies of the LISA lasers magnify via the huge armlength mismatches (up to 35 000 km due to orbital motion, [48]) and constitute the primary noise problem. It masks the sensitivity by about eight orders of magnitude above the requirement for GW detection and drives the necessity for TDI, which reduces its influence drastically, as explained later in part IV. A typical mitigation strategy for frequency noise is to stabilize it with a stable reference cavity, which constitutes an optical resonator with a small bandwidth for a given mode.

On the other hand, stochastic processes also influence the electrical field amplitudes of lasers. The so-called laser intensity noise describes the fluctuations in the beams' intensity (or power) and originates from excess photon noise. It leads to photon radiation

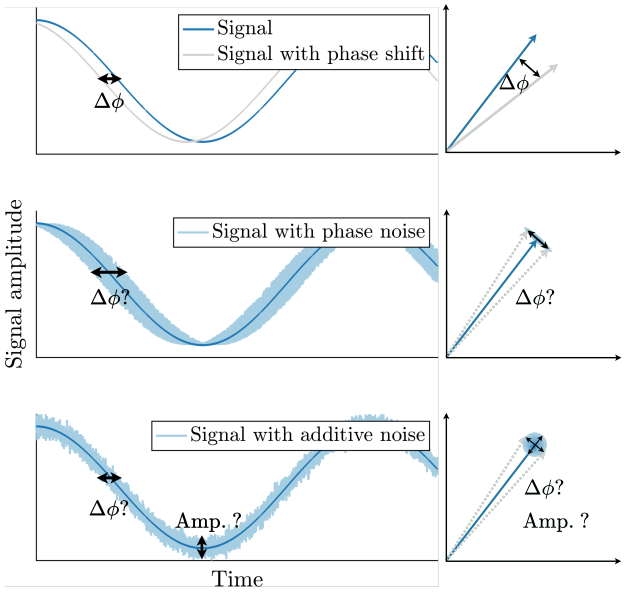

Figure 4.1 Illustration of the influence of noise on a signal. Top panel: Ideal phase shifted signal measurement without noise. Middle panel: Direct phase noise included in the signal phase. Bottom panel: Additive noise causing both amplitude and phase noise. The right column depicts another representation with phase and amplitude quadrature. RIN causes (among radiation pressure noise) intensity noise that belongs to the last category.

pressure noise on the TMs, but also comprises an additive noise, which, unfortunately, adds uncertainty to the main signal phase readout. Active power control schemes are usually implemented to mitigate its influence, e.g. using a power pick-off and subsequent feedback loop to act on the laser pump current. However, the relative shot-noise of the in-loop beam used to measure the power in such methods limits the possible reduction. New concepts for active power stabilization using optical springs have recently been demonstrated in ground-based laboratories to circumvent this limitation [49]. Passive schemes as in [50] use optomechanical cavities at cryogenic temperatures in the kHz band and are therefore not easily adaptable for LISA. For space missions in general, the MHz heterodyne frequencies and noisy thrusters may be limiting for such ideas.

The influence of phase and intensity noise in a heterodyne measurement with regards to a given signal is illustrated in figure 4.1. Contrary to a homodyne readout, the readout contains a time-varying sinusoidal signal term that includes the desired phase information. A detailed review of heterodyne interferometry is given in chapter 6. While ideally, changes in the phase of the beatnote can be tracked immediately (top panel), the noise in real-world systems adds some ambiguity to the determination. A pure phase noise (middle panel) only acts on the phase quadrature of the signal, whereas additive (sometimes called "vector") noise (bottom panel) adds uncertainty in both the amplitude and phase quadrature. This can be interpreted as if a random, constantly changing vector in both length and angle is added to the signal phasor, perturbing the measurement. Using the phasor representation, a pure phase shift is described by multiplication with a simple complex exponential that contains the phase shift. Further, direct phase noise can be represented by two phasors that, to first order for small perturbations, do not influence the length of the signal phasor. In general, however, two such sideband phasors will change both the amplitude and phase

of the signal phasor (last panel). Additive stochastic noise can be described by such random phasors as will be used later in part II for the RIN to phase coupling derivation. More noise may then require a longer averaging duration to reach a certain measurement precision. This is problematic for tracking fast changes in the signal (relative to the averaging time needed).

This thesis mainly investigates RIN coupling that belongs to the last category. The graphical representation in figure 4.1 of noise in the phasor picture motivates the theoretical derivation given in chapter 7.

4.2 RIN definition

Please note that this section contains parts from my publication [P1].

The total noise measured in a laser power spectrum can be attributed to different noise processes. They are typically described by shot-noise from the quantized nature of the light field and its detection process, thermal or electronic noise from the PDs and subsequent transimpedance amplifier stages, and excess photon noise.

The latter (excess photon noise) is usually referred to as RIN and results from the unintentional beating of various spectral components with random phases in the laser process, mainly photons interfering due to stimulated and spontaneous emission, and due to technical noise couplings, for example from the shot-noise in the pump diode current.

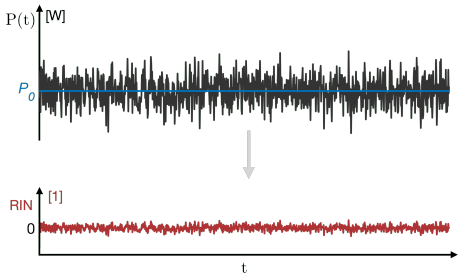

Figure 4.2 RIN time-series. It is calculated from laser intensity fluctuations normalized by their mean.

This thesis focuses on the effects of technical laser RIN. It is a measure of intensity noise, which is typically normalized to the average intensity (or to the power, therefore sometimes also called Relative Power Noise (RPN)). Figure 4.2 depicts a time-series representation. The spectral shape is generally not flat, as shown in figure 4.3, but may be approximated by white noise for small enough frequency bands, e.g. around a certain signal.

RIN, denoted $r(t)$ in the following, is measured from the beam power $P(t)$ with excess photon noise δP, and represents a multiplicative noise source with respect to the mean intensity (or power):

$$r(t) \coloneqq \delta P / \overline{P(t)}, \tag{4.1a}$$

$$\Rightarrow \quad \delta P = r \cdot \overline{P(t)} \tag{4.1b}$$

$$\Rightarrow \quad \overline{P(t)} + \delta P = \overline{P(t)}(1 + r), \tag{4.1c}$$

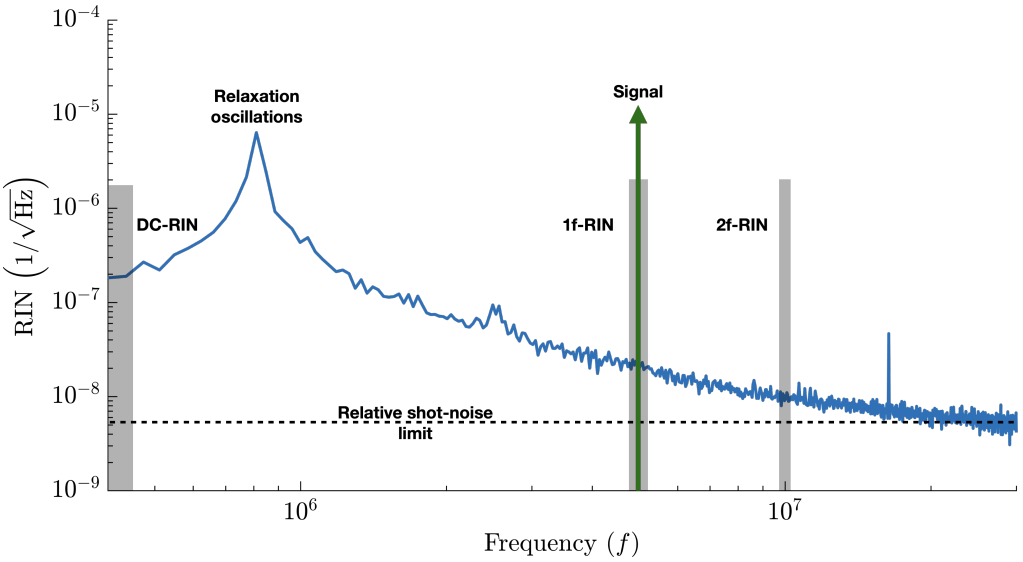

Figure 4.3 RIN measurement (provided by S. Barke) of a 1064 nm non-planar ring oscillator (NPRO) laser. For illustration purposes some areas have been marked as described in the text, and an arbitrary signal has been added to fix the position of the 1f-RIN and 2f-RIN bands.

where the bar denotes the mean or average power of the beam. The last equation shows how RIN is modeled in the theoretical derivation in part II.

RIN is usually expressed as a spectral density in units $\text{Hz}^{-1/2}$, as can be seen in figure 4.3. Typical Non-Planar Ring Oscillator (NPRO) lasers can be stabilized to operate around or below $10^{-4}\,\text{Hz}^{-1/2}$ at mHz and $10^{-8}\,\text{Hz}^{-1/2}$ at MHz frequencies (see, for example, [P3, 51]). A RIN spectrum typically has a peak (also visible in figure 4.3) that is due to relaxation oscillations originating from dynamics between the laser gain and the intracavity power. At higher frequencies, it saturates at the relative shot noise limit for the beam power used in the measurement. The relative level of shot-noise in a RIN measurement is proportional to the inverse average power and thus increases for low light intensities.

To mitigate the effect of RIN perturbations the beam power is typically stabilized before propagating it through the interferometer, and remaining excess noise on the PDs is often removed by applying a balanced detection scheme utilizing two interferometer output ports, as described earlier [P3, 52].

This thesis reports on the well-known "1f-RIN" (the contribution of RIN from near the heterodyne frequency) and derives coupling relations and its common mode rejection properties. A less known "2f-RIN" coupling mechanism (the contribution of RIN from near twice the heterodyne frequency) to the phase measurement that contributes noise even in a balanced heterodyne interferometer is also analyzed (see marked areas in figure 4.3). Furthermore, this work highlights simulations and experiments that were performed to explore these effects in LPF and in LISA.

Part II

Laser RIN coupling

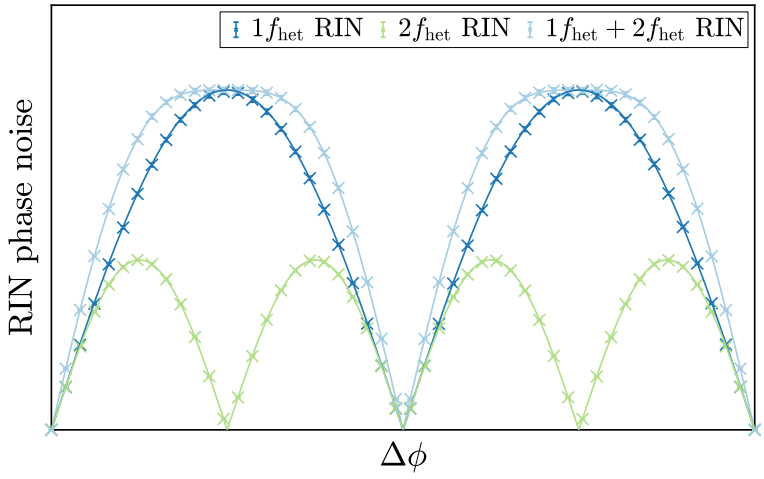

Chapter 5

Overview

Please note that this part has mostly been published in [P1].

An introduction to RIN has been given in chapter 4. This chapter gives an overview of the following theoretical sections and an executive summary of the main results. To set the scope, a review of the typical heterodyne equations is given in chapter 6. The modeling and derivation of the resulting phase noise is described in chapter 7 in great detail, followed by computational simulations in chapter 8 that verify the theoretical predictions.

For a brief summary, the main RIN to phase coupling features are the following: RIN r is defined as fluctuations of the laser power divided by its mean value, i.e. $r = \delta P/\overline{P}$. It causes phase noise in optical heterodyne interferometers and there are two (first order) distinct coupling mechanisms:

- purely additive "1f-RIN" effects from around the heterodyne frequency and
- multiplicative (non-linear) "2f-RIN" effects from around twice the heterodyne frequency (that can also be treated as additive noise after Taylor expansion).

The 1f- and 2f-RIN have distinct coupling mechanisms and contribute uncorrelated phase noise (since they are usually far apart in frequency) and thus need to be summed quadratically (when considered in amplitude units of noise, as opposed to power).

For completeness it should be mentioned that there is also "DC-RIN" (sometimes called "0f-RIN") originating from the same multiplicative mechanism as the 2f-RIN, that, mathematically to first and second order, only causes pure amplitude modulation and no phase noise in the demodulation process. DC-RIN does, however, generally lead to in-band acceleration noise on TMs via radiation pressure (not covered in this thesis, see section 18.3). The latter mechanism is well understood from the LPF mission. However, during electrical ground testing at the AEI with prototype hardware for the LISA PM, a small DC-RIN coupling was observed with a coupling factor in the order of 10^{-3} [53]. This is still under investigation.

5.1 Main aspects of 1f-RIN coupling

1f-RIN describes the coupling of RIN from around the heterodyne frequency. The resulting phase noise depends on beam powers, BS coefficients and the heterodyne efficiency (contrast) and subtracts with balanced detection. It scales approximately with 1/contrast and can be magnified by power mismatches between the two beams. The 1f-RIN common mode rejection shows a sinusoidal behavior with respect to the relative phase (e.g. between TM- and Reference interferometers, thus visible via the TM position). In this case, if the phase difference can be kept close to zero, the coupling is further reduced (after balanced detection) depending on the matching of the involved beam powers.

5.2 Main aspects of 2f-RIN coupling

2f-RIN describes the coupling of RIN from *twice* the heterodyne frequency. Here, the resulting phase noise is *independent* of beam powers and contrast. Unfortunately, it does *not* subtract with balanced detection since it is in-phase with the signal. It is roughly a factor contrast/2 smaller than the corresponding 1f-RIN term for equal beam powers. The 2f-RIN common mode rejection shows sinusoidal behavior with respect to *twice* the relative phase (e.g. typical noise dependency on TM position similar to 1f-RIN). In this case, if the phase difference can be kept close to zero, the coupling is minimized (*no* dependency on the power ratio).

Chapter 6
Review of Heterodyne Interferometry

The well-known relations for a heterodyne interferometer with two output ports A, B, can be derived assuming two Gaussian beams, $\boldsymbol{E}_\mathrm{m}, \boldsymbol{E}_\mathrm{r}$, propagating through a beamsplitter onto two photodiodes, one per output port, as depicted in figure 6.1.

Two beams with a difference frequency $f_\mathrm{het} = f_1 - f_2 \equiv f_\mathrm{m} - f_\mathrm{r}$, $(f_\mathrm{m} > f_\mathrm{r})$ are brought to interference using a BS. The resulting phase signal that corresponds to the arm length difference, $m - r$, is measured in both output ports, A and B, with PDs, which see the signal with a π phase shift between them due to energy conservation at the BS. In this case, f_m corresponds to the measurement beam with a time-varying phase (the observable of interest being the distance change of the TMs), while the propagation path of f_r is assumed constant and termed the reference beam. The term 'balanced detection' refers to the subtraction of the measurements occurring in PD A and PD B to reduce common noise.

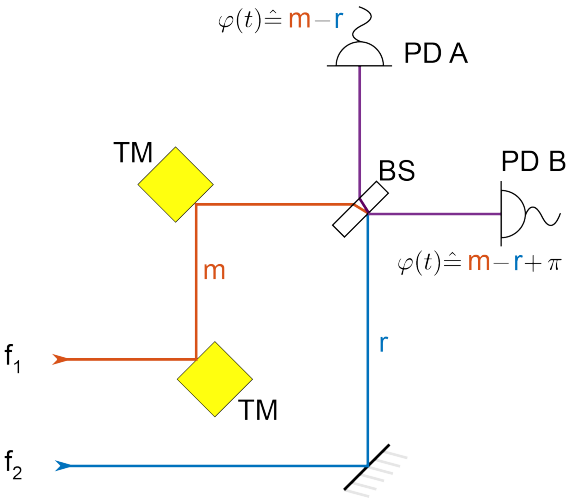

Figure 6.1 Simplified Mach-Zehnder heterodyne interferometer with two TMs. Modified reprint from [P1].

The beams are assumed to be well aligned when hitting the detectors and for simplicity it is assumed that both beams travel (locally) in the z direction at all times. In fact, the propagation direction of the beams is tilted by 90° after reflection of the beamsplitter, but we neglect any offsets or imperfections in the optical path and perform the calculation for parallel beams.

The mathematical description for two beams (denoted m for measurement, r for reference beam with indices $k = \{\mathrm{m}, \mathrm{r}\}$) assumes propagation through vacuum and travel times t_k when arriving at the detector:

$$\boldsymbol{E}_\mathrm{m} = \mathrm{Re}\left\{\boldsymbol{e}_p a_\mathrm{m}(x, y, t - t_\mathrm{m}) e^{i\left(\omega_\mathrm{m}(t-t_\mathrm{m})\right)}\right\}, \tag{6.1a}$$

$$\boldsymbol{E}_\mathrm{r} = \mathrm{Re}\Big\{\boldsymbol{e}_p a_\mathrm{r}(x,y,t-t_\mathrm{r})e^{i\left(\omega_\mathrm{r}(t-t_\mathrm{r})\right)}\Big\}, \tag{6.1b}$$

with unity polarization vectors $\mathbf{e}_p$ and $\mathbf{e}_p \perp \mathbf{e}_z$, position and time dependent amplitudes $a_{\mathrm{m,r}}(x,y,t) \in \mathbb{C}$ and optical frequencies $\omega_k = 2\pi f_k$, $f_\mathrm{m} = f_\mathrm{r} + f_\mathrm{het}$. As usual we drop the $\mathrm{Re}\{\cdot\}$ in the following and implicitly assume it for measurable quantities like the electrical field.

Typically, f_het is much smaller than $f_{\mathrm{m,r}}$, which leads to a slowly varying heterodyne beatnote, while the faster frequencies are averaged away through the detection process. This is implicitly assumed when taking the absolute square (see the following calculations). Constant factors are absorbed in $a_{\mathrm{m,r}}$ such that $|a_{\mathrm{m,r}}|^2$ represents an intensity with units Wm^{-2}. The detectors are assumed to be located at an equivalent local $z = 0$ point in each arm.

We assume a light travel time, t_c, that is common to both beams, and a slowly time-varying differential time, t_d, that we attribute to $\boldsymbol{E}_\mathrm{m}$ in the sense that the runtime difference of the beams is $t_\mathrm{m} - t_\mathrm{r} = (t_c + t_d) - t_c = t_d$, which translates to a slowly time-varying differential phase. This light travel time difference between the beams is magnified by a large optical carrier frequency, as given by $\phi_d = \omega_\mathrm{m} t_d$.

We drop the polarization vector, $\boldsymbol{e}_p$, since both beams are assumed to have identical polarization, perpendicular to the plane of incidence of the recombination BS and the detector surface.

The properties of a lossless BS are usually described by amplitude reflection and transmission coefficients, ρ, $\tau \in \mathbb{C}$, $\rho^2 + \tau^2 = 1$ which are used in a unitary coupling matrix, $\boldsymbol{M}$, such that

$$\boldsymbol{M} = \begin{pmatrix} \rho & i\tau \\ i\tau & \rho \end{pmatrix} \text{ or } \boldsymbol{M} = \begin{pmatrix} \rho & \tau \\ \tau & -\rho \end{pmatrix}. \tag{6.2}$$

The optical intensities impinging on the PDs in ports A and B can then be calculated by squaring the amplitudes $(E_\mathrm{A}, E_\mathrm{B})^\top = \boldsymbol{M} \cdot (E_\mathrm{m}, E_\mathrm{r})^\top$,

$$\begin{aligned} |E_\mathrm{A}|^2 &= |\rho E_\mathrm{m} + \tau E_\mathrm{r}|^2 \\ &= \rho^2 |E_\mathrm{m}|^2 + \tau^2 |E_\mathrm{r}|^2 + 2\rho\tau\,\mathrm{Re}[E_\mathrm{m} E_\mathrm{r}^*], \end{aligned} \tag{6.3a}$$

$$\begin{aligned} |E_\mathrm{B}|^2 &= |\tau E_\mathrm{m} - \rho E_\mathrm{r}|^2 \\ &= \tau^2 |E_\mathrm{m}|^2 + \rho^2 |E_\mathrm{r}|^2 - 2\rho\tau\,\mathrm{Re}[E_\mathrm{m} E_\mathrm{r}^*], \end{aligned} \tag{6.3b}$$

using * to indicate complex conjugation and the fact that $z + z^* = 2\,\mathrm{Re}(z)$.

To describe the detected optical powers, $P_{A,B}$, one has to integrate over the PD surface, S, such that $P_{A,B} = \int |E_{A,B}|^2 \,\mathrm{d}S$.

The first terms of equation (6.3) yield the single beam powers:

$$P_\mathrm{m} = \int \mathrm{d}S(\rho^2|E_\mathrm{m}|^2 + \tau^2|E_\mathrm{m}|^2) = \int \mathrm{d}S|E_\mathrm{m}|^2, \tag{6.4a}$$

$$P_\mathrm{r} = \int \mathrm{d}S(\tau^2|E_\mathrm{r}|^2 + \rho^2|E_\mathrm{r}|^2) = \int \mathrm{d}S|E_\mathrm{r}|^2 \tag{6.4b}$$

for the measurement and for the reference beam ($S \gg$ beam diameter).

The integration of the last terms, assuming normalized beam amplitudes $A_k(x,y) \coloneqq a_k/\sqrt{P_k(t)}$ (again constant factors absorbed in a_k), gives

$$\begin{aligned}
&\pm 2\rho\tau \int \mathrm{d}S\ \mathrm{Re}[E_\mathrm{m}E_\mathrm{r}^*] \\
&= \pm\, 2\rho\tau\sqrt{P_\mathrm{m}P_\mathrm{r}}\,\mathrm{Re}\left[e^{i(\omega_\mathrm{m}(t-t_\mathrm{m})-\omega_\mathrm{r}(t-t_\mathrm{r}))}\int \mathrm{d}S\, A_\mathrm{m}A_\mathrm{r}^*\right] \\
&= \pm\, 2\rho\tau\sqrt{\eta_\mathrm{het}P_\mathrm{m}P_\mathrm{r}}\cos(\omega_\mathrm{het}t - \phi_d - \phi_c - \phi_\mathrm{het}),
\end{aligned} \tag{6.5}$$

with $\omega_\mathrm{het} = \omega_\mathrm{m} - \omega_\mathrm{r}$ and $\phi_c = \omega_\mathrm{het}t_c$. In the last step, we make use of the so-called overlap integral, σ, of the two beams (see [54]), arising from beam geometry:

$$\sigma = \int \mathrm{d}S\, A_\mathrm{m}A_\mathrm{r}^* =: \sqrt{\eta_\mathrm{het}}e^{i\phi_\mathrm{het}}, \tag{6.6}$$

which can be separated into a magnitude factor, $\eta_\mathrm{het} = |\sigma|^2$, and a phase contribution, $\phi_\mathrm{het} = \arg(\sigma)$, to the signal. The amplitude contribution is called the heterodyne efficiency. The additional phase contribution due to the spatial wave front properties is added as a phase factor, which, in general, can be different between the two output ports. We further neglect any time-dependence of the beam geometries.

As a result we arrive at the well known heterodyne equations with $P_\mathrm{m,r} = P_\mathrm{m,r}(t - t_\mathrm{m,r})$:

$$P_\mathrm{A} = \rho^2P_\mathrm{m} + \tau^2P_\mathrm{r} + 2\rho\tau\sqrt{\eta_\mathrm{het,A}P_\mathrm{m}P_\mathrm{r}}\cdot B_\mathrm{A}, \tag{6.7a}$$

$$P_\mathrm{B} = \tau^2P_\mathrm{m} + \rho^2P_\mathrm{r} - 2\rho\tau\sqrt{\eta_\mathrm{het,B}P_\mathrm{m}P_\mathrm{r}}\cdot B_\mathrm{B}, \tag{6.7b}$$

with the beat term, $B_{A,B}$, oscillating at the heterodyne frequency, f_het,

$$\begin{aligned}
B_\mathrm{A,B} &= \cos\Big(\omega_\mathrm{het}t - \phi_d - \phi_c - \phi_\mathrm{het,A,B}\Big) \\
&=: \cos\Big(\omega_\mathrm{het}t - \varphi_\mathrm{A,B}\Big).
\end{aligned} \tag{6.8}$$

In the last step we merge the geometric phase, ϕ_het, with ϕ_d and the typically constant ϕ_c phase into an effective detected phase signal $\varphi_\mathrm{A,B} = \phi_c + \phi_d + \phi_\mathrm{het,A,B}$.

To simplify the following sections, we assume no differential losses in the detection process on the PDs and neglect differences in the overlap integral between the two ports, so that $\phi_{\mathrm{het},A,B} = \phi_\mathrm{het}$, $\eta_{\mathrm{het},A,B} = \eta_\mathrm{het}$, $\varphi = \varphi_{A,B}$, $B_{A,B} = B$.

Note that the interferometer contrast can be computed as

$$\text{Contrast}_\text{A} = C_\text{A} = \frac{2\rho\tau\sqrt{\eta_{\text{het,A}} P_\text{m} P_\text{r}}}{\rho^2 P_\text{m} + \tau^2 P_\text{r}}, \tag{6.9a}$$

$$\text{Contrast}_\text{B} = C_\text{B} = \frac{2\rho\tau\sqrt{\eta_{\text{het,B}} P_\text{m} P_\text{r}}}{\tau^2 P_\text{m} + \rho^2 P_\text{r}}. \tag{6.9b}$$

Equation (6.7) contains two DC terms each, depending on the transmitted and reflected powers, and one signal term per output port, the latter with different signs. This allows to compute the so-called *balanced detection* signal. It is realized by forming the difference between the powers of the two complementary output ports, $\Delta P \coloneqq (P_\text{A} - P_\text{B})/2$, which reduces excess noise (e.g., certain components of RIN). Ideally for this purpose, $\rho^2 = \tau^2 = 1/2$ with a perfect 50/50 BS.

After interfering and detecting the beams, there are different ways to extract the phase information, for example using Phase Locked Loops (PLLs) [55] or a SBDFTs, see section 3.2. The latter can be seen as an practical example used aboard LPF. In a continuous case, the signal can be extracted by a Fourier analysis of the form

$$F = \frac{1}{\pi}\int_0^{2\pi} \Delta P e^{i2\pi f_\text{het} t} d(2\pi f_\text{het} t), \tag{6.10}$$

$$\Rightarrow \varphi = \arg(F) = \arctan\left(\frac{\text{Im}(F)}{\text{Re}(F)}\right). \tag{6.11}$$

However, the last equation is only exactly true in the absence of phase noise. How this changes when RIN is introduced in the system will be discussed in the following.

Chapter 7

RIN to phase coupling

Based on the previous chapter that reviews the detection equations for heterodyne interferometry, one can derive the RIN to phase coupling relations.

In the following, all powers P_k are assumed to be long term mean values (we refrain from using the extra bar on $\overline{P}$) and only the RIN itself carries the time dependence. Therefore, we introduce RIN denoted by $r_{\mathrm{m,r}}(t)$ in the beam powers as

$$P_\mathrm{m} \to P_\mathrm{m}(1 + r_\mathrm{m}(t - t_\mathrm{m})), \tag{7.1a}$$
$$P_\mathrm{r} \to P_\mathrm{r}(1 + r_\mathrm{r}(t - t_\mathrm{r})). \tag{7.1b}$$

Note: One can also derive RIN directly from an amplitude noise, n, of the electric field amplitudes in the form $a(t) = \overline{a}(1 + n)$, as introduced in equation (6.1). Then $|a(t)|^2 = \overline{a}^2(1 + n)^2 \approx \overline{a}^2(1 + 2n) \approx \overline{P}(1 + r)$, so the above definition matches with RIN $r \approx 2n$, neglecting the small n^2 term.

Inserting the RIN terms into equation (6.7) (and hiding the time dependency in the same manner, since $P_i(t)$ only appears in multiplication with $r_i(t)$) yields

$$\begin{aligned} P_\mathrm{A} &= \rho^2 P_\mathrm{m} + \tau^2 P_\mathrm{r} + \rho^2 P_\mathrm{m} r_\mathrm{m} + \tau^2 P_\mathrm{r} r_\mathrm{r} \\ &\quad + 2\rho\tau\sqrt{\eta_\mathrm{het} P_\mathrm{m}(1 + r_\mathrm{m}) P_\mathrm{r}(1 + r_\mathrm{r})}\cos(\omega_\mathrm{het} t - \varphi), \end{aligned} \tag{7.2a}$$
$$\begin{aligned} P_\mathrm{B} &= \tau^2 P_\mathrm{m} + \rho^2 P_\mathrm{r} + \tau^2 P_\mathrm{m} r_\mathrm{m} + \rho^2 P_\mathrm{r} r_\mathrm{r} \\ &\quad - 2\rho\tau\sqrt{\eta_\mathrm{het} P_\mathrm{m}(1 + r_\mathrm{m}) P_\mathrm{r}(1 + r_\mathrm{r})}\cos(\omega_\mathrm{het} t - \varphi). \end{aligned} \tag{7.2b}$$

Factors of constant power are neglected in the following, since they do not add direct phase noise. Further, we simplify by using $r_{\mathrm{m,r}} \ll 1$ so that $\sqrt{(1 + r_\mathrm{m})(1 + r_\mathrm{r})} = \sqrt{1 + r_\mathrm{m} + r_\mathrm{r} + r_\mathrm{m} r_\mathrm{r}} \approx \sqrt{1 + r_\mathrm{m} + r_\mathrm{r}} \approx 1 + \frac{r_\mathrm{m} + r_\mathrm{r}}{2}$, yielding the simplified detection equations

$$\begin{aligned} P_\mathrm{A} = &\underbrace{\rho^2 P_\mathrm{m} r_\mathrm{m} + \tau^2 P_\mathrm{r} r_\mathrm{r}}_{\text{1f-RIN, port A}} \underbrace{+(r_\mathrm{m} + r_\mathrm{r})\rho\tau\sqrt{\eta_\mathrm{het} P_\mathrm{m} P_\mathrm{r}}\cos(\omega_\mathrm{het} t - \varphi)}_{\text{2f-RIN, port A}} \\ &\underbrace{+2\rho\tau\sqrt{\eta_\mathrm{het} P_\mathrm{m} P_\mathrm{r}}\cos(\omega_\mathrm{het} t - \varphi)}_{\text{Signal, port A}}, \end{aligned} \tag{7.3a}$$

$$P_{\mathrm{B}} = \underbrace{\tau^2 P_{\mathrm{m}} r_{\mathrm{m}} + \rho^2 P_{\mathrm{r}} r_{\mathrm{r}}}_{\text{1f-RIN, port B}} \underbrace{-(r_{\mathrm{m}} + r_{\mathrm{r}})\rho\tau\sqrt{\eta_{\mathrm{het}} P_{\mathrm{m}} P_{\mathrm{r}}}\cos(\omega_{\mathrm{het}} t - \varphi)}_{\text{2f-RIN, port B}}$$
$$\underbrace{-2\rho\tau\sqrt{\eta_{\mathrm{het}} P_{\mathrm{m}} P_{\mathrm{r}}}\cos(\omega_{\mathrm{het}} t - \varphi)}_{\text{Signal, port B}}\,. \tag{7.3b}$$

At this point, we can already make important observations: Firstly, the term called 1f-RIN appears with the same sign in both output ports, and is approximately the same for well matched 50/50 BSs. Therefore, this term can be suppressed with the balanced detection process defined above. Secondly, the term called 2f-RIN appears with the same phasing as the signal (and with half its amplitude) in both output ports and therefore *cannot* be reduced by balanced detection. Thirdly, the sum of equally labeled terms (sum of 1f- or 2f-RIN terms, respectively) that contain either r_{m} or r_{r} has to be performed linearly if the RIN is correlated between the two beams, and quadratically for uncorrelated RIN in the two beams (with regards to their noise spectral densities). However, 1f-RIN and 2f-RIN terms are always considered uncorrelated between each other, since they occur at different frequencies and the noise in a small band is typically approximately white. Lastly, we see that all these noise contributions have been approximated as additive noise (phasors) to the main signal.

A very important aspect is that a PM is only sensitive in a narrow band around f_{het}, because the phase demodulation in equation (6.10) can be interpreted as a narrow filter around f_{het}. Therefore, only additive components in a limited bandwidth around the heterodyne frequency can cause phase noise.

7.1 The additive channel: 1f-RIN

When we consider the Fourier spectrum, we see that the terms labeled "1f-RIN" are only scaled by constant factors. Therefore these terms contribute RIN from near $1f_{\mathrm{het}}$, since higher or lower frequency components are filtered out through the demodulation process.

Note: The time delay t_k included in the measurement beam also affects 1f-RIN (at f_{het}), but since it is scaled by f_{het} instead of f_{m} or f_{r}, with $f_{\mathrm{het}} \ll f_{\mathrm{m}}$, we neglect it here and assume good correlation at the detector if RIN between the two beams was correlated at the start. For very large scale interferometers like LISA, different laser sources have to be used. However, even if the same laser could be realized, significant light travel time differences along the arms would still require post processing such as TDI, which creates correlated measurements, such that this assumption also holds.

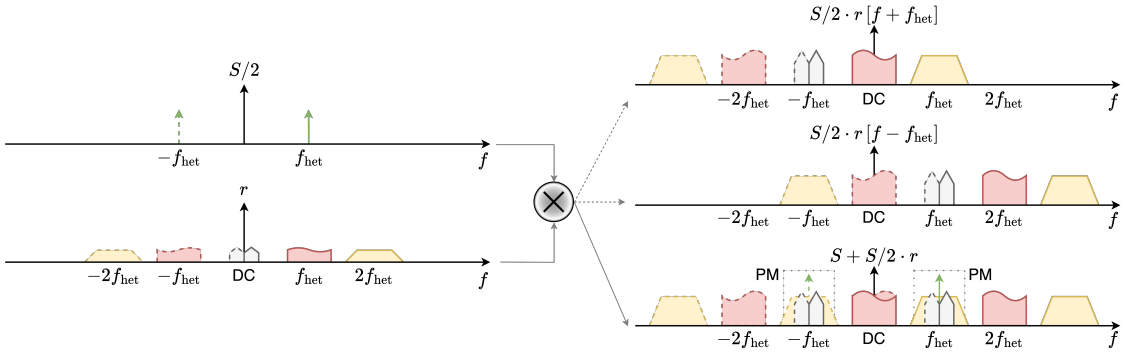

Figure 7.1 Schematic illustrating the "2f-RIN" terms in equation (7.3) showing spectral mixing of (half) the signal beat term (first row) with RIN (second row). A real valued signal has conjugate symmetry in its Fourier transform, which is indicated by the negative frequency range. As shown in equation (7.4), half of the noise power is shifted downwards (third row), while the other half is upconverted (fourth row). The total resulting spectrum (last row) is again conjugate symmetric. Therefore, RIN components from both $2f_{\text{het}} \pm \epsilon$ and $0 \pm \epsilon$ (near DC) end up in the PM bandwidth. However, the DC components consist of conjugate phasors at $f_{\text{het}} \pm \epsilon$, meaning they only contribute amplitude noise and no direct phase noise. Modified reprint from [P1].

7.2 The multiplicative channel: DC-RIN and 2f-RIN

The terms labeled "2f-RIN" behave differently since they carry the same sign as the signal. Moreover, they have an interesting frequency mixing property: They consist of the RIN itself ($r_{\text{m}} + r_{\text{r}}$), which is then multiplied by half the heterodyne term. That heterodyne term has a frequency component at f_{het}. From Fourier analysis it follows for $r_k(t)$ with Fourier representation $\tilde{r}_k(f)$ that (see [52])

$$\begin{aligned} G_k(f) &:= \int r_k \cos(2\pi f_{\text{het}} t) e^{-i2\pi f t}\,\mathrm{d}t \\ &= \frac{1}{2}\left[\tilde{r}_k(f - f_{\text{het}}) + \tilde{r}_k(f + f_{\text{het}})\right]. \end{aligned} \tag{7.4}$$

From equation (7.4) we see that the only possible coupling frequencies are small offset frequencies to DC, named ϵ, and those around twice the heterodyne frequency, $f \approx \{0 + \epsilon,\, 2f_{\text{het}}\}$, because only such frequencies result in components near f_{het} in the resulting spectrum (that is conjugate symmetric, since r_k has only real values):

$$G(0 + \epsilon) = \frac{1}{2}\left[\tilde{r}_k(\epsilon - f_{\text{het}}) + \tilde{r}_k(\epsilon + f_{\text{het}})\right], \tag{7.5a}$$

$$G(2f_{\text{het}}) = \frac{1}{2}\left[\tilde{r}_k(f_{\text{het}}) + \tilde{r}_k(3f_{\text{het}})\right]. \tag{7.5b}$$

This up- and downconversion is depicted in figure 7.1.

To investigate the DC terms further, we look at one specific RIN component at frequency ϵ with (long term average) amplitude r and a stochastic phase ψ, represented by $R = r\cos(2\pi\epsilon t - \psi)$. We perform a similar operation as it occurs in equation (7.3) by adding and multiplying a general signal $S = s\cos(2\pi f_{\mathrm{het}} t - \varphi)$ to demonstrate the effect:

$$\begin{aligned} S + \frac{RS}{2} &= S + \frac{rs}{4}\Big[\cos\big(2\pi(f_{\mathrm{het}} - \epsilon)t - \varphi + \psi\big) + \cos\big(2\pi(f_{\mathrm{het}} + \epsilon)t - \varphi - \psi\big)\Big] \\ &= \underbrace{\left(1 + \frac{r}{2}\cos(2\pi\epsilon t - \psi)\right)}_{\text{Amplitude modulation}} s\cos(2\pi f_{\mathrm{het}} t - \varphi). \end{aligned} \tag{7.6}$$

We conclude that RIN from near DC results in conjugate phasors around the heterodyne frequency. These phasors can only cause direct amplitude modulation of the signal and therefore do not contribute additive phase noise.

With that in mind, only the spectral contribution from $2f_{\mathrm{het}}$ remains relevant. With $G(2f_{\mathrm{het}})$ it is clear that half of the RIN amplitude at $2f_{\mathrm{het}}$ is downmixed to f_{het} causing phase noise, while the other (non relevant) half is upconverted to $3f_{\mathrm{het}}$, which is not measured by the PM. The resulting scaling for 2f-RIN (meaning $r_{\mathrm{m,r}}$ near $2f_{\mathrm{het}}$) in port A and B is therefore

$$\text{2f-RIN}_{\mathrm{A,B}} = \pm\frac{r_{\mathrm{m}} + r_{\mathrm{r}}}{2}\rho\tau\sqrt{\eta_{\mathrm{het}} P_{\mathrm{m}} P_{\mathrm{r}}}. \tag{7.7}$$

In conclusion, the only relevant terms causing RIN to phase coupling at the PDs are

$$P_{\mathrm{A}} = \underbrace{\rho^2 P_{\mathrm{m}} r_{\mathrm{m}} + \tau^2 P_{\mathrm{r}} r_{\mathrm{r}}}_{\text{1f-RIN, port A}} + \underbrace{\frac{r_{\mathrm{m}} + r_{\mathrm{r}}}{2}\rho\tau\sqrt{\eta_{\mathrm{het}} P_{\mathrm{m}} P_{\mathrm{r}}}}_{\text{2f-RIN, port A}} \underbrace{+2\rho\tau\sqrt{\eta_{\mathrm{het}} P_{\mathrm{m}} P_{\mathrm{r}}}\cos(2\pi f_{\mathrm{het}} t - \varphi)}_{\text{Signal, port A}},$$

$$P_{\mathrm{B}} = \underbrace{\tau^2 P_{\mathrm{m}} r_{\mathrm{m}} + \rho^2 P_{\mathrm{r}} r_{\mathrm{r}}}_{\text{1f-RIN, port B}} - \underbrace{\frac{r_{\mathrm{m}} + r_{\mathrm{r}}}{2}\rho\tau\sqrt{\eta_{\mathrm{het}} P_{\mathrm{m}} P_{\mathrm{r}}}}_{\text{2f-RIN, port B}} \underbrace{-2\rho\tau\sqrt{\eta_{\mathrm{het}} P_{\mathrm{m}} P_{\mathrm{r}}}\cos(2\pi f_{\mathrm{het}} t - \varphi)}_{\text{Signal, port B}}.$$

It is important to note that for 1f-RIN, $r_k = r_k(f_{\mathrm{het}})$, and for 2f-RIN, $r_k = r_k(2f_{\mathrm{het}})$.

We can already learn from these equations that the coupling coefficient for 2f-RIN is roughly half the 1f-RIN coefficient for equal beam powers, 50/50 BS and high contrast ($\eta_{\mathrm{het}} \approx 1$).

In the following sections we derive the phase noise arising from 1f- and 2f-RIN components, since the phase usually comprises the main observable of interest (as opposed to, e.g., the induced noise current).

We assume that the RIN spectrum is at least uncorrelated between frequencies as far apart as at least $\approx f_{\mathrm{het}}$ and thus we can discuss 1f- and 2f-RIN couplings separately. The total noise is then the quadratic sum of both 1f- and 2f-RIN contributions.

We also develop formulas addressing the subtraction of a common mode reference phase, which allows the finding of a working point that minimizes the coupling for both 1f- and 2f-RIN experimentally.

7.3 RIN modeling approach

In general, if the noise in the two beams is differential or uncorrelated RIN we write $r_{\mathrm{m}}(t) \neq r_{\mathrm{r}}(t)$. If only one laser source has been used it can only be caused by processes after the beams are split up (e.g., due to large differential time delays or modulations), or, if two separate light sources have been used. Otherwise, if $r_{\mathrm{m}} = r_{\mathrm{r}}$, it is called common mode or correlated RIN. This defines whether both $r_{\mathrm{m,r}}$ realizations are independent, adding them quadratically, or whether they are coherent, adding them linearly.

We begin to model the effect of RIN to phase coupling with a formal white noise Fourier series approach, because in a small band around the heterodyne frequency RIN is usually almost flat. While this can be used to derive the additional phase noise, we found it easier to simplify the calculations with phasor components. We formulate the full expression here and describe the second approach in the following section, which utilizes only two specific components of the Fourier series approach.

A narrow band white noise representation consists of $2p$ sine waves around a center frequency f_c with independent, instantaneous random amplitudes, c_i, and phases, ψ_i. This center frequency could be either $f_c = f_{\mathrm{het}}$ or $f_c = 2f_{\mathrm{het}}$. The amplitudes are given by $c_i = (2\tilde{r}_i^2 \Delta f)^{1/2}$ and are separated in frequency by $\Delta f \to 0\,\mathrm{Hz}$ as described in [56]. $\tilde{r}^2$ refers to the Power Spectral Density (PSD) of the noise. Hence, this approach gives

$$r_{\mathrm{m,r}}(t, f_c) = \sum_{\substack{i=-p,\\ i\neq 0}}^{p} c_i \cos(2\pi(f_c + i\Delta f)t - \psi_i), \tag{7.9}$$

with uniformly distributed random phase angles ψ_i in $(0, 2\pi)$. The total noise power is $\langle r_{\mathrm{m,r}}^2 \rangle = 2p\Delta f \tilde{r}^2 = 2B\tilde{r}^2$, because for white noise all $\tilde{r}_i$ converge to the same value for large enough sample sizes. The bandwidth $2B$ represents in a typical PM readout the output sampling frequency of the phase measurement.

In the following section we show how one can simplify this approach.

7.4 Phase noise from additive vector noise

To simplify the calculations we utilize complex phasors to describe the general coupling mechanism of an additive vector (noise), as sketched in figure 7.2, and apply it to RIN to phase coupling afterwards. This is an adapted version of what can be found in [57]. A signal phasor, S, at frequency $\omega_s = 2\pi f_s$ and a small additive phasor, V, with frequency $\omega_v = 2\pi(f_s + \epsilon)$, is given by

$$S = s e^{i(\omega_s t + \phi_s)}, \quad V = v e^{i(\omega_v t + \phi_v)}, \tag{7.10}$$

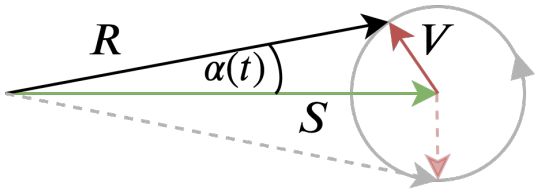

Figure 7.2 Additive unwanted vectors, V, cause a phase deviation, α, in the observable of interest, which is the phase of the signal, S. Reprint from [P1].

which results in a phasor

$$R = S + V = re^{i(\omega_s t + \phi_r(t))}, \tag{7.11}$$

with

$$r^2 = s^2 + v^2 + 2sv\cos(2\pi\epsilon t + \phi_s - \phi_v), \tag{7.12a}$$

$$\phi_r = \arg\left(e^{i\phi_s} + \frac{v}{s}e^{i(2\pi\epsilon t + \phi_v)}\right). \tag{7.12b}$$

We are interested in the phase variations of ϕ_s, called α, due to the presence of V:

$$\phi_r = \arg\left(e^{i\phi_s}\left(1 + \frac{v}{s}e^{i(2\pi\epsilon t + \phi_v - \phi_s)}\right)\right) = \phi_s + \underbrace{\arg\left(1 + \frac{v}{s}e^{i(2\pi\epsilon t + \phi_v - \phi_s))}\right)}_{=\alpha}. \tag{7.13}$$

Therefore, the phase deviations, α, are given by

$$\alpha = \arg\left(1 + \frac{v}{s}e^{i(2\pi\epsilon t + \phi_v - \phi_s))}\right), \tag{7.14a}$$

$$= \arctan\left(\frac{\mathrm{Im}[1 + \ldots]}{\mathrm{Re}[1 + \ldots]}\right), \tag{7.14b}$$

$$= \arctan\left(\frac{\frac{v}{s}\sin(2\pi\epsilon t + \phi_v - \phi_s)}{1 + \frac{v}{s}\cos(2\pi\epsilon t + \phi_v - \phi_s)}\right), \tag{7.14c}$$

$$\approx \frac{v}{s}\sin\left(2\pi\epsilon t + \phi_v - \phi_s\right), \tag{7.14d}$$

where we assume in the last step that the offending phasor, V, has a much smaller amplitude than S, i.e., $v \ll s$. figure 7.3 shows the resulting phase deviations. The variance or squared Root Mean Square (RMS) value is $\alpha^2_{\mathrm{RMS}} = \frac{v^2}{2s^2}$.

We can immediately extend this result for a phasor at a frequency $f_s - \epsilon$. Such a phasor would end up at $-\epsilon$ in the resulting phase spectrum, and be folded to $+\epsilon$ in a typical one-sided spectral calculation. This is important for the notion of band-limited noise around the signal, as it is present in real measurement systems. There, both sides of the signal contain a certain level of noise, that is uncorrelated between each other.

Using these considerations, we model the noise as follows: We assume band-limited, white noise with a PSD value $n_0(f)$ and total noise power $NP = \int_B n_0(f)df \approx 2n_0B$, equally distributed left and right of the signal, see figure 7.4 top panel.

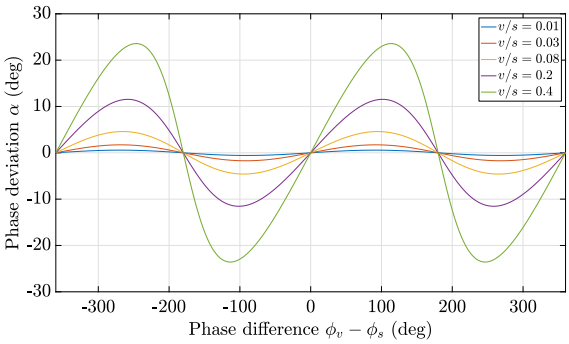

Figure 7.3 Phase deviation in the signal phase for varying amplitude ratios of the signal and "noise" phasor with the non-approximated phase formula. This shows visually that the small vector noise approximation is valid below percentage level amplitude rations. Reprint from [P1]. Based on a plot from H. Halloin.

We already showed in the previous calculation, that noise at a frequency $f_s \pm \epsilon$ ends up at frequency ϵ in the one-sided phase spectrum. Therefore we can represent the noise for one particular frequency on the left and right side of the signal by sine phasors $N_{1,2}$ with the white noise amplitude n_0 in a band of $b = 1\,\mathrm{Hz}$. Both sine representations follow a uniform random phase distribution, since they represent uncorrelated noise:

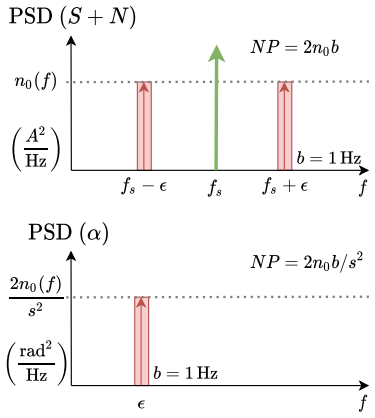

Figure 7.4 Modeling additive white noise. Reprint from [P1].

$$N_{1,2} = \sqrt{2n_0b}\cos(\omega_{1,2}t + \psi_{1,2}), \tag{7.15}$$

with $\omega_{1,2} = 2\pi(f_s \pm \epsilon)$ and equal noise power $N^2_{1,2,\mathrm{rms}} = n_0 b$. So, the total noise power measured in a PSD of the resulting phase at frequency ϵ would be $N^2_{1,\mathrm{RMS}} + N^2_{2,\mathrm{RMS}} = 2n_0b = 2N^2_{1,2,\mathrm{RMS}}$. figure 7.4 (bottom panel) shows a graphical representation of this.

We can simplify this even further and use only one single sine representation for both left and right phasors with additional scaling, since their noise power ends up at the same frequency. This leads to a single noise vector

$$N = \sqrt{2}\sqrt{2n_0b}\cos(2\pi(f_s + \epsilon)t + \psi), \tag{7.16}$$

with a RMS value of $N^2_{\mathrm{RMS}} = 2n_0b$. In the end, this is true for all frequencies in a bandwidth, B, that defines the sampling frequency of the output phase signal. Therefore, it is enough to propagate a general noise amplitude in this way to describe the whole resulting phase spectrum over the bandwidth B.

We can now describe the resulting phase noise from a general additive white noise process using equation (7.14d): A signal S with amplitude s and an additive small noise N with amplitude $\sqrt{2}\sqrt{2n_0b}$ at frequencies $f_s \pm \epsilon$ will lead to phase deviations of the form

$$\alpha \approx \frac{\sqrt{2}\sqrt{2n_0b}}{s}\sin(2\pi\epsilon t + \psi - \phi_s). \tag{7.17}$$

Calculating the variance we find

$$\alpha_{\mathrm{RMS}}^2 = \frac{2n_0 b}{s^2}, \tag{7.18}$$

which can be given in units of an ASD by dividing by $b = 1\,\mathrm{Hz}$ and taking the square root:

$$\tilde{\alpha} = \frac{\sqrt{2}\sqrt{n_0}}{s}. \tag{7.19}$$

This result is true for any frequency, ϵ. Therefore the frequency dependence was dropped and the result describes the whole output spectrum (for white noise).

This marks an important result for additive vector noise. Since $s/\sqrt{2}$ represents the signal RMS value, for an approximately white noise source around a strong carrier signal we can calculate the resulting phase noise ASD $\tilde{\alpha}$ with the following general formula

$$\tilde{\alpha} = \frac{\text{Noise ASD}}{\text{Signal RMS}}, \quad \left[\frac{\mathrm{rad}}{\sqrt{\mathrm{Hz}}}\right]. \tag{7.20}$$

This equation can also be independently verified using, e.g., a model of a SBDFT PM. For the RIN terms in equation (7.8) the signal RMS is given by $\rho\tau\sqrt{2\eta_{\mathrm{het,A,B}}P_{\mathrm{m}}P_{\mathrm{r}}}$. In the following, we calculate the phase noise, $\tilde{\alpha}$, for different 1f- and 2f-RIN scenarios.

Please note that a very similar derivation can be used to derive the resulting amplitude noise from a small vector on a signal, see appendix A.

7.5 1f-RIN phase coupling relations

In this section, we look at RIN at frequency $r_k = r_k\,(1f_{\mathrm{het}})$. For each output port, the 1f-RIN has a differently scaled component due to the BS parameters and power levels. Therefore, the formula for port B can be found by exchanging ρ and τ.

From equations (7.8) and (7.20) it follows immediately that, for *correlated RIN* (i.e., $r_{\mathrm{m}} = r_{\mathrm{r}} = r$), the resulting phase noise in port A is given by

$$\begin{aligned}\tilde{\alpha}_{\mathrm{1f,A}} &= \frac{\rho^2 P_{\mathrm{m}}\tilde{r}_{\mathrm{m}} + \tau^2 P_{\mathrm{r}}\tilde{r}_{\mathrm{r}}}{\rho\tau\sqrt{2\eta_{\mathrm{het}}P_{\mathrm{m}}P_{\mathrm{r}}}} \\ &= \frac{\rho^2 P_{\mathrm{m}} + \tau^2 P_{\mathrm{r}}}{\rho\tau\sqrt{2\eta_{\mathrm{het}}P_{\mathrm{m}}P_{\mathrm{r}}}}\tilde{r}\,(1f_{\mathrm{het}}) = \frac{\sqrt{2}\cdot\tilde{r}\,(1f_{\mathrm{het}})}{C_{\mathrm{A}}},\end{aligned} \tag{7.21}$$

and for port B

$$\tilde{\alpha}_{\mathrm{1f,B}} = \frac{\tau^2 P_{\mathrm{m}} + \rho^2 P_{\mathrm{r}}}{\rho\tau\sqrt{2\eta_{\mathrm{het}}P_{\mathrm{m}}P_{\mathrm{r}}}}\tilde{r}\,(1f_{\mathrm{het}}) = \frac{\sqrt{2}\cdot\tilde{r}\,(1f_{\mathrm{het}})}{C_{\mathrm{B}}}. \tag{7.22}$$

However, for *uncorrelated RIN*, i.e., $r_\mathrm{m} \neq r_\mathrm{r}$, the addition has to be performed quadratically, giving for port A

$$\tilde{\alpha}_\mathrm{1f,A} = \frac{\sqrt{(\rho^2 P_\mathrm{m}\tilde{r}_\mathrm{m})^2 + (\tau^2 P_\mathrm{r}\tilde{r}_\mathrm{r})^2}}{\rho\tau\sqrt{2\eta_\mathrm{het} P_\mathrm{m} P_\mathrm{r}}} \tag{7.23}$$

$$\approx \frac{\sqrt{(\rho^2 P_\mathrm{m})^2 + (\tau^2 P_\mathrm{r})^2}}{\rho\tau\sqrt{2\eta_\mathrm{het} P_\mathrm{m} P_\mathrm{r}}}\tilde{r}\,(1f_\mathrm{het})\,, \text{ if } \tilde{r}_\mathrm{m} \approx \tilde{r}_\mathrm{r} \tag{7.24}$$

and for port B

$$\tilde{\alpha}_\mathrm{1f,B} = \frac{\sqrt{(\tau^2 P_\mathrm{m}\tilde{r}_\mathrm{m})^2 + (\rho^2 P_\mathrm{r}\tilde{r}_\mathrm{r})^2}}{\rho\tau\sqrt{2\eta_\mathrm{het} P_\mathrm{m} P_\mathrm{r}}} \tag{7.25}$$

$$\approx \frac{\sqrt{(\tau^2 P_\mathrm{m})^2 + (\rho^2 P_\mathrm{r})^2}}{\rho\tau\sqrt{2\eta_\mathrm{het} P_\mathrm{m} P_\mathrm{r}}}\tilde{r}\,(1f_\mathrm{het})\,, \text{ if } \tilde{r}_\mathrm{m} \approx \tilde{r}_\mathrm{r}. \tag{7.26}$$

Another interesting case appears if one of the beams has much higher intensity, e.g. $P_\mathrm{r} \gg P_\mathrm{m}$ while the RIN levels are somewhat comparable, $r_\mathrm{m} \approx r_\mathrm{r}$. Then we get for *correlated and uncorrelated* RIN respectively:

$$\tilde{\alpha}_\mathrm{1f,A} = \frac{\tau}{\rho}\sqrt{\frac{P_\mathrm{r}}{2\eta_\mathrm{het} P_\mathrm{m}}}\tilde{r}_\mathrm{r}\,(1f_\mathrm{het})\,, \quad \text{if } P_\mathrm{r} \gg P_\mathrm{m}, \tag{7.27a}$$

$$\tilde{\alpha}_\mathrm{1f,B} = \frac{\rho}{\tau}\sqrt{\frac{P_\mathrm{r}}{2\eta_\mathrm{het} P_\mathrm{m}}}\tilde{r}_\mathrm{r}\,(1f_\mathrm{het})\,, \quad \text{if } P_\mathrm{r} \gg P_\mathrm{m}. \tag{7.27b}$$

In this case the phase noise is dominated by RIN from the more powerful beam.

7.6 1f-RIN coupling relations after balanced detection

A more extensive treatment of balanced detection is given in appendix C.

Here, the simplified approach assumes identical processing and heterodyne efficiencies in the detection chains in port A and B, and only allows a mismatch in the BS parameters and beam powers. We gain an improvement in the signal to noise ratio, since the signal is measured twice and added, while the noise is subtracted. As mentioned before, 2f-RIN is not reduced and only the resulting 1f-RIN is affected by balanced detection.

The phase noise for *correlated* RIN after balanced detection is

$$\tilde{\alpha}_{1f,\Delta P} = \frac{\left|P_\mathrm{m}(\rho^2 - \tau^2) + P_\mathrm{r}(\tau^2 - \rho^2)\right|}{\rho\tau\sqrt{8\eta_\mathrm{het} P_\mathrm{m} P_\mathrm{r}}}\tilde{r}\,(1f_\mathrm{het})\,, \tag{7.28a}$$

and for *uncorrelated* RIN

$$\tilde{\alpha}_{1f,\Delta P} = \frac{\sqrt{P_\mathrm{m}^2\tilde{r}_\mathrm{m}^2(\rho^2 - \tau^2)^2 + P_\mathrm{r}^2\tilde{r}_\mathrm{r}^2(\tau^2 - \rho^2)^2}}{\rho\tau\sqrt{8\eta_\mathrm{het} P_\mathrm{m} P_\mathrm{r}}} \tag{7.29a}$$

$$\approx \frac{\sqrt{P_\mathrm{m}^2(\rho^2-\tau^2)^2 + P_\mathrm{r}^2(\tau^2-\rho^2)^2}}{\rho\tau\sqrt{8\eta_\mathrm{het}P_\mathrm{m}P_\mathrm{r}}}\tilde{r}\,(1f_\mathrm{het})\,, \quad \text{if } \tilde{r}_\mathrm{m} \approx \tilde{r}_\mathrm{r}. \tag{7.29b}$$

We see that the resulting phase noise is minimized for $\rho^2 = \tau^2$ (or $P_\mathrm{m} = P_\mathrm{r}$ when rearranging the terms). If that is the case, RIN is distributed equally in both ports and thus can be canceled to a large degree.

In the case that $P_\mathrm{r} \gg P_\mathrm{m}$ we find, for *correlated and uncorrelated* RIN, that

$$\tilde{\alpha}_{1f,\Delta P} = \left|\frac{\tau}{\rho} - \frac{\rho}{\tau}\right| \sqrt{\frac{P_\mathrm{r}}{8\eta_\mathrm{het}P_\mathrm{m}}}\tilde{r}_\mathrm{r}\,(1f_\mathrm{het})\,. \tag{7.30}$$

7.7 1f-RIN common mode subtraction

When subtracting another interferometric measurement that shares (some) of the same RIN, the subtraction can minimize the resulting phase noise. This is a technique for reducing common mode noises, typically implemented by a fixed beam "reference" interferometer. Note that we assume negligible time differences between interferometers (assuring high correlation).

Since the 1f-RIN coupling depends on beam powers, heterodyne efficiencies and BS coefficients, the general formula is not very compact. We derive a complete functional expression and simplify afterwards for common use-cases. In this section, we assume no differential time delay effects.

We denote the two interferometers involved by the subscript $n \in \{1, 2\}$.

According to equation (7.16) we can represent 1f-RIN by one component at $f_\mathrm{het} + \epsilon$ as in

$$r_{n,k} = 2\sqrt{r_{n,k}^2 b}\cos\Big(2\pi(f_\mathrm{het}+\epsilon)t - \psi_{n,k}\Big), \tag{7.31}$$

where $r_{n,k} = r_{n,k}\,(1f_\mathrm{het})$.

This term is scaled in the two interferometers by the following factors (see equation (7.8)): $\rho_n^2 P_{n,\mathrm{m}}$, $\tau_n^2 P_{n,\mathrm{m}}$, $\rho_n^2 P_{n,\mathrm{r}}$, $\tau_n^2 P_{n,\mathrm{r}}$. Without loss of generality, we restrict ourselves to the case that only port A is used per interferometer (otherwise ρ and τ need to be exchanged appropriately):

$$r_{n,\mathrm{m}} = 2\rho_n^2 P_{n,\mathrm{m}}\sqrt{r_{n,\mathrm{m}}^2 b}\cos\Big(2\pi(f_{\mathrm{het},n}+\epsilon)t + \psi_{n,\mathrm{m}}\Big), \tag{7.32a}$$

$$r_{n,\mathrm{r}} = 2\tau_n^2 P_{n,\mathrm{r}}\sqrt{r_{n,\mathrm{r}}^2 b}\cos\Big(2\pi(f_{\mathrm{het},n}+\epsilon)t + \psi_{n,\mathrm{r}}\Big). \tag{7.32b}$$

The signal amplitude is

$$s_n = 2\rho_n\tau_n\sqrt{\eta_{\mathrm{het},n}P_{n,\mathrm{m}}P_{n,\mathrm{r}}}, \tag{7.33}$$

and the signal phase is summarized by $-\varphi_n$. The resulting functional phase noise equations follow from equation (7.17); they are

$$\alpha_{n,\mathrm{m}} = \frac{\rho_n}{\tau_n} P_{n,\mathrm{m}} \sqrt{\frac{r_{n,\mathrm{m}}^2 b}{\eta_{\mathrm{het},n} P_{n,\mathrm{m}} P_{n,\mathrm{r}}}} \sin(2\pi\epsilon t - \psi_{n,\mathrm{m}} + \varphi_n), \tag{7.34a}$$

$$\alpha_{n,\mathrm{r}} = \frac{\tau_n}{\rho_n} P_{n,\mathrm{r}} \sqrt{\frac{r_{n,\mathrm{r}}^2 b}{\eta_{\mathrm{het},n} P_{n,\mathrm{m}} P_{n,\mathrm{r}}}} \sin(2\pi\epsilon t - \psi_{n,\mathrm{r}} + \varphi_n). \tag{7.34b}$$

To abbreviate we define

$$g_{n,\mathrm{m}} \coloneqq \frac{\rho_n}{\tau_n} P_{n,\mathrm{m}} \sqrt{\frac{r_{n,\mathrm{m}}^2 b}{\eta_{\mathrm{het},n} P_{n,\mathrm{m}} P_{n,\mathrm{r}}}}, \tag{7.35a}$$

$$g_{n,\mathrm{r}} \coloneqq \frac{\tau_n}{\rho_n} P_{n,\mathrm{r}} \sqrt{\frac{r_{n,\mathrm{r}}^2 b}{\eta_{\mathrm{het},n} P_{n,m} P_{n,\mathrm{r}}}}. \tag{7.35b}$$

The general total phase noise after subtraction is

$$\alpha_{\mathrm{tot}} = \alpha_{1,\mathrm{m}} + \alpha_{1,\mathrm{r}} - (\alpha_{2,\mathrm{m}} + \alpha_{2,\mathrm{r}}), \tag{7.36}$$

whose terms have to be added quadratically for all uncorrelated noise terms, and linearly for all correlated terms.

To derive some practically useful equations, we introduce the following cases: In the first two, we assume that the mean power levels per beam are somewhat identical across the interferometers ($P_{1,\mathrm{m}} \approx P_{2,\mathrm{m}} = P_{\mathrm{m}}$, $P_{1,\mathrm{r}} \approx P_{2,\mathrm{r}} = P_{\mathrm{r}}$, but not necessarily $P_{\mathrm{m}} = P_{\mathrm{r}}$), that both recombination BS are 50/50, $\rho/\tau = \rho_n/\tau_n \approx \tau_n/\rho_n$, and $\eta_{\mathrm{het},n} \approx \eta_{\mathrm{het}}$, and differentiate then between (i) all beams sharing the same *correlated RIN* and (ii) pairwise *uncorrelated RIN*. In a third case (iii) we allow more variations between the interferometers, implying that the RIN cannot be fully subtracted.

The first case (i) is described by $r_{1,k} = r_{2,k} = r, \psi_{1,k} = \psi_{2,k} = \psi$, leading to

$$\begin{aligned}
&\alpha_{1,k} - \alpha_{2,k} \\
&\quad = g_{1,k} \left[\sin(2\pi\epsilon t - \psi + \varphi_1) - \sin(2\pi\epsilon t - \psi + \varphi_2)\right] \\
&\quad = 2 g_{1,k} \cos\left(2\pi\epsilon t - \psi + \frac{\varphi_1 + \varphi_2}{2}\right) \sin\left(\frac{\varphi_1 - \varphi_2}{2}\right).
\end{aligned} \tag{7.37}$$

Setting $k = \mathrm{m}$ and $k = \mathrm{r}$ and adding both cases (in accordance to equation (7.36)) describes an ASD after taking the RMS and dividing by $\sqrt{b}$ for each frequency ϵ. Therefore it follows for white, *correlated RIN* that

$$\tilde{\alpha}_{\mathrm{tot}} = \frac{\sqrt{2}(P_{\mathrm{m}} + P_{\mathrm{r}})}{\sqrt{\eta_{\mathrm{het}} P_{\mathrm{m}} P_{\mathrm{r}}}} \tilde{r}\,(1 f_{\mathrm{het}}) \left|\sin\left(\frac{\varphi_1 - \varphi_2}{2}\right)\right|. \tag{7.38}$$

The second case (ii) also features the same scaling factors across the interferometers, but *uncorrelated RIN* between the measurement and reference beams. This gives

$$\begin{aligned}\alpha_{\mathrm{tot}} &= g_{n,\mathrm{m}}\left[\sin(2\pi\epsilon t - \psi_{\mathrm{m}} + \varphi_1) - \sin(2\pi\epsilon t - \psi_{\mathrm{m}} + \varphi_2)\right] \\ &\quad + g_{n,\mathrm{r}}\left[\sin(2\pi\epsilon t - \psi_{\mathrm{r}} + \varphi_1) - \sin(2\pi\epsilon t - \psi_{\mathrm{r}} + \varphi_2)\right] \\ &= 2\Bigg[g_{n,\mathrm{m}}\cos\left(2\pi\epsilon t - \psi_{\mathrm{m}} + \frac{\varphi_1+\varphi_2}{2}\right) \\ &\quad + g_{n,\mathrm{r}}\cos\left(2\pi\epsilon t - \psi_{\mathrm{r}} + \frac{\varphi_1+\varphi_2}{2}\right)\Bigg]\sin\left(\frac{\varphi_1-\varphi_2}{2}\right). \end{aligned} \tag{7.39}$$

In terms of an ASD it takes the form

$$\tilde{\alpha}_{\mathrm{tot}} = \sqrt{\frac{2\left(P_{\mathrm{m}}^2\tilde{r}_{\mathrm{m}}^2 + P_{\mathrm{r}}^2\tilde{r}_{\mathrm{r}}^2\right)}{\eta_{\mathrm{het}}P_{\mathrm{m}}P_{\mathrm{r}}}}\left|\sin\left(\frac{\varphi_1-\varphi_2}{2}\right)\right|, \tag{7.40}$$

which simplifies further if $\tilde{r}_{\mathrm{m}} \approx \tilde{r}_{\mathrm{r}} = \tilde{r}$ to

$$\tilde{\alpha}_{\mathrm{tot}} = \sqrt{\frac{2\left(P_{\mathrm{m}}^2 + P_{\mathrm{r}}^2\right)}{\eta_{\mathrm{het}}P_{\mathrm{m}}P_{\mathrm{r}}}}\tilde{r}\,(1f_{\mathrm{het}})\left|\sin\left(\frac{\varphi_1-\varphi_2}{2}\right)\right|. \tag{7.41}$$

We see that even without balanced detection, the effect of 1f-RIN can be nulled by subtracting a common RIN reference phase with the same interferometric operating point.

An experimentally relevant case is case (iii), where full RIN subtraction is not possible. Here we allow variations of the form $g_{2,\mathrm{m}} = (1+\delta_{\mathrm{m}})g_{1,\mathrm{m}}$, $g_{2,\mathrm{r}} = (1+\delta_{\mathrm{r}})g_{1,\mathrm{r}}$ between the interferometric ports. It is expected that the resulting maximum represents the sum of the individual coupling terms per interferometer, while the minimal coupling does not reduce to zero, but is rather limited by the difference of the induced phase noise per interferometer.

We use the following general approach to calculate the mean squared noise (after some algebra, similar to derivations above)

$$\begin{aligned}&\left\langle\left[a\sin(x+y) - a(1+\delta)\sin(x+z)\right]^2\right\rangle \\ &\quad = \left\langle a^2\right\rangle\left[\frac{\delta^2}{2} + (2+2\delta)\sin\left(\frac{y-z}{2}\right)^2\right], \end{aligned} \tag{7.42}$$

where we have assumed that x carries a random-time dependence (as in $x = 2\pi\epsilon t - \psi$) and consider $y = \varphi_1$, $z = \varphi_2$ as static for the time-scale of the averaging process. The RIN is hidden in a, which relates to the power noise per signal strength in the respective interferometer (i.e., the $g_{n,k}$).

If we assume in case (iii) *uncorrelated RIN*, we set either $a = g_{1,\mathrm{m}}$ or $a = g_{2,\mathrm{m}}$ and add the resulting mean squared terms from equation (6.3) (we drop the averaging symbols), giving

$$\alpha_{\mathrm{tot}}^2 = g_{1,\mathrm{m}}^2 \frac{\delta_{\mathrm{m}}^2}{2} + g_{1,\mathrm{r}}^2 \frac{\delta_{\mathrm{r}}^2}{2} + \left[g_{1,\mathrm{m}}^2(2+2\delta_{\mathrm{m}}) + g_{1,\mathrm{r}}^2(2+2\delta_{\mathrm{r}})\right] \sin\left(\frac{\varphi_1 - \varphi_2}{2}\right)^2. \tag{7.43}$$

Now we can see, that even for phase-matched interferometers ($\varphi_1 = \varphi_2$) phase noise remains due to the amplitude mismatch as expected.

In terms of an ASD, for the remaining noise we get at the minimum (assuming division by $\sqrt{b}$)

$$\begin{aligned}\tilde{\alpha}_{\mathrm{tot,min}} &= \sqrt{g_{1,\mathrm{m}}^2 \frac{\delta_{\mathrm{m}}^2}{2} + g_{1,\mathrm{r}}^2 \frac{\delta_{\mathrm{r}}^2}{2}} \\ &= \frac{1}{\sqrt{2\eta_{\mathrm{het},1}}} \sqrt{\frac{\rho_1^2}{\tau_1^2}\frac{P_{1,\mathrm{m}}}{P_{1,\mathrm{r}}}\delta_{\mathrm{m}}^2 \tilde{r}_{\mathrm{m}}^2 + \frac{\tau_1^2}{\rho_1^2}\frac{P_{1,\mathrm{r}}}{P_{1,\mathrm{m}}}\delta_{\mathrm{r}}^2 \tilde{r}_{\mathrm{r}}^2}.\end{aligned} \tag{7.44}$$

Looking at case (iii) and assuming *correlated RIN* we have to consider cross terms between $r_{\mathrm{m}} = r_{\mathrm{r}} = r$. The mean squared expression is

$$\begin{aligned}\alpha_{\mathrm{tot}}^2 = {} & g_{1,\mathrm{m}}^2 \frac{\delta_{\mathrm{m}}^2}{2} + g_{1,\mathrm{r}}^2 \frac{\delta_{\mathrm{r}}^2}{2} + g_{1,\mathrm{m}} g_{1,\mathrm{r}} \delta_{\mathrm{m}} \delta_{\mathrm{r}} \\ & + \Big[4 g_{1,\mathrm{m}} g_{1,\mathrm{r}} + 2 g_{1,\mathrm{m}} g_{1,\mathrm{r}}(\delta_{\mathrm{m}} + \delta_{\mathrm{r}}) \\ & + g_{1,\mathrm{m}}^2(2+2\delta_{\mathrm{m}}) + g_{1,\mathrm{r}}^2(2+2\delta_{\mathrm{r}})\Big] \sin\left(\frac{\varphi_1 - \varphi_2}{2}\right)^2.\end{aligned} \tag{7.45}$$

Unsurprisingly, the minimum here is larger due to the cross terms. The minimal noise ASD becomes

$$\begin{aligned}\tilde{\alpha}_{\mathrm{tot,min}} &= \frac{1}{\sqrt{2}} \left(g_{1,\mathrm{m}}\delta_{\mathrm{m}} + g_{1,\mathrm{r}}\delta_{\mathrm{r}}\right) \\ &= \frac{\frac{\rho_1}{\tau_1} P_{1,\mathrm{m}}\delta_{\mathrm{m}} + \frac{\tau_1}{\rho_1} P_{1,\mathrm{r}}\delta_{\mathrm{r}}}{\sqrt{2\eta_{\mathrm{het},1} P_{1,\mathrm{m}} P_{1,\mathrm{r}}}} \tilde{r}(1 f_{\mathrm{het}}).\end{aligned} \tag{7.46}$$

7.8 2f-RIN coupling relations

This section deals with the downconverted RIN from twice the heterodyne frequency, $\tilde{r}_k = \tilde{r}_k\,(2 f_{\mathrm{het}})$. Using both equations (7.8) and (7.20) we see that the resulting phase noise is independent of powers and contrasts. It only depends on the RIN level.

Correlated RIN with $r_\mathrm{m} = r_\mathrm{r} = r$ couples via

$$\tilde{\alpha}_\mathrm{2f,A} = \frac{\tilde{r}_\mathrm{m} + \tilde{r}_\mathrm{r}}{\sqrt{8}} = \frac{1}{\sqrt{2}}\tilde{r}\left(2f_\mathrm{het}\right), \tag{7.47}$$

while *uncorrelated RIN* ($r_\mathrm{m} \neq r_\mathrm{r}$) follows

$$\tilde{\alpha}_\mathrm{2f,A} = \frac{\sqrt{\tilde{r}_\mathrm{m}^2 + \tilde{r}_\mathrm{r}^2}}{\sqrt{8}} \approx \frac{1}{2}\tilde{r}\left(2f_\mathrm{het}\right), \text{ if } \tilde{r}_\mathrm{m} \approx \tilde{r}_\mathrm{r} = \tilde{r}. \tag{7.48}$$

7.9 2f-RIN common mode subtraction

In the 2f-RIN common mode subtraction, the derivations are more compact compared to the 1f-RIN case, since the parameter space is reduced to correlation assumptions. Again, we use functional expressions with both amplitude and phase.

Like for the 1f-RIN case, we assume two interferometers, labeled by the additional subscript $n \in \{1, 2\}$. We look at one specific frequency component ϵ near $2f_\mathrm{het}$.

Following equation (7.16) we find the form

$$r_{n,k} = 2\sqrt{r_{n,k}^2 b}\cos\Big(2\pi(2f_\mathrm{het} + \epsilon)t - \psi_{n,k}\Big). \tag{7.49}$$

According to equation (7.3) this is multiplied by $\rho\tau\sqrt{\eta_{\mathrm{het},n}P_{n,\mathrm{m}}P_{n,\mathrm{r}}}\cos(2\pi f_\mathrm{het}t - \varphi_n)$. As mentioned before, only the component downmixed to near $1f_\mathrm{het}$ couples through the PM, leaving

$$r_{n,k} = \rho\tau\sqrt{\eta_{\mathrm{het},n}P_{n,\mathrm{m}}P_{n,\mathrm{r}}}\sqrt{r_{n,k}^2 b}\cos\Big(2\pi(f_\mathrm{het} + \epsilon)t - \psi_{n,k} + \varphi_n\Big). \tag{7.50}$$

Therefore, using equations (7.17) and (7.33), we find the functional form of the resulting phase noise

$$\alpha_{n,k} = \frac{\sqrt{r_{n,k}^2 b}}{2}\sin\Big(2\pi\epsilon t - \psi_{n,k} + 2\varphi_n\Big). \tag{7.51}$$

Subtracting both interferometers yields

$$\alpha_\mathrm{tot} = \alpha_{1,\mathrm{m}} + \alpha_{1,\mathrm{r}} - \left(\alpha_{2,\mathrm{m}} + \alpha_{2,\mathrm{r}}\right). \tag{7.52}$$

Now there are four possible RIN realizations. We restrict our analysis to two practical cases: All beams have identical (correlated and same level) RIN (i), and pairwise identical RIN (ii).

First, we assume that all four beams share the same *correlated RIN* with small enough light travel time differences, such that $r_{1,k} = r_{2,k} = r, \psi_{1,k} = \psi_{2,k} = \psi$, resulting in

$$\alpha_\mathrm{tot} = \sqrt{r^2 b}\Big[\sin(2\pi\epsilon t - \psi + 2\varphi_1) - \sin(2\pi\epsilon t - \psi + 2\varphi_2)\Big]$$

$$= 2\sqrt{r^2 b}\cos(2\pi\epsilon t - \psi + \varphi_1 + \varphi_2)\sin(\varphi_1 - \varphi_2). \tag{7.53}$$

By taking the RMS and dividing by $\sqrt{b}$ we arrive at the corresponding amplitude spectral density,

$$\tilde{\alpha}_{\mathrm{tot}}(2f_{\mathrm{het}}) = \sqrt{2}\cdot\tilde{r}(2f_{\mathrm{het}})\,|\sin(\varphi_1 - \varphi_2)|, \tag{7.54}$$

which depends on the relative phase difference of the two interferometers, thus allowing to null the effect of 2f-RIN by adjusting the interferometric operating points.

For the second case, we simplify the formula assuming RIN is *uncorrelated* between the measurement and reference beams, but that the beams are shared in both interferometers. Again, we neglect travel time differences. This leads to $r_{1,\mathrm{m}} = r_{2,\mathrm{m}} = r_{\mathrm{m}}$, $\psi_{1,m} = \psi_{2,m} = \psi_{\mathrm{m}}$ and $\tilde{r}_{1,\mathrm{r}} = \tilde{r}_{2,r} = \tilde{r}_{\mathrm{r}}$, $\psi_{1,\mathrm{r}} = \psi_{2,\mathrm{r}} = \psi_{\mathrm{r}}$.

Then,

$$\begin{aligned}
\alpha_{\mathrm{tot}} &= \frac{\sqrt{r_{\mathrm{m}}^2 b}}{2}\Big[\sin(2\pi\epsilon t - \psi_{\mathrm{m}} + 2\varphi_1) - \sin(2\pi\epsilon t - \psi_{\mathrm{m}} + 2\varphi_2)\Big] \\
&\quad + \frac{\sqrt{r_{\mathrm{r}}^2 b}}{2}\Big[\sin(2\pi\epsilon t - \psi_{\mathrm{r}} + 2\varphi_1) - \sin(2\pi\epsilon t - \psi_{\mathrm{r}} + 2\varphi_2)\Big] \\
&= \Big[\sqrt{r_{\mathrm{m}}^2 b}\cos(2\pi\epsilon t - \psi_{\mathrm{m}} + \varphi_1 + \varphi_2) + \sqrt{r_{\mathrm{r}}^2 b}\cos(2\pi\epsilon t - \psi_{\mathrm{r}} + \varphi_1 + \varphi_2)\Big] \\
&\quad \cdot \sin(\varphi_1 - \varphi_2).
\end{aligned} \tag{7.55}$$

We find an amplitude spectral density of

$$\tilde{\alpha}_{\mathrm{tot}}(2f_{\mathrm{het}}) = \frac{\sqrt{\tilde{r}_{\mathrm{m}}^2 + \tilde{r}_{\mathrm{r}}^2}}{\sqrt{2}}|\sin(\varphi_1 - \varphi_2)|. \tag{7.56}$$

Assuming that the simple case that $\tilde{r}_{\mathrm{m}} \approx \tilde{r}_{\mathrm{r}} = \tilde{r}$ we arrive at

$$\tilde{\alpha}_{\mathrm{tot}}(2f_{\mathrm{het}}) = \tilde{r}(2f_{\mathrm{het}})\,|\sin(\varphi_1 - \varphi_2)|. \tag{7.57}$$

7.10 Overview of simplified RIN coupling relations

Using the previously derived equations we summarize a few selected and simplified RIN to phase coupling relations in table 7.1 with the following assumptions: The recombination BS has an equal splitting ratio of 50 % : 50 %. The band-limited white RIN can be correlated or uncorrelated between the beams, representing, for example, whether one (correlated) laser source or two (uncorrelated) laser sources have been used. When used, a common reference phase (e.g. from a reference interferometer) is assumed to have the same power levels, RIN contributions and contrast (quantities labeled $\varphi - \varphi_R$). *Please note that this is not true for LISA.*

Measured quantity	**1f-RIN phase noise** $\left[\mathrm{rad/Hz^{1/2}}\right]$	**2f-RIN phase noise** $\left[\mathrm{rad/Hz^{1/2}}\right]$
φ [corr. RIN: $r_\mathrm{m} = r_\mathrm{r}$]	$\frac{P_\mathrm{m}+P_\mathrm{r}}{\sqrt{2\eta_\mathrm{het}P_\mathrm{m}P_\mathrm{r}}}\tilde{r}\,(1f_\mathrm{het})$	$\frac{1}{\sqrt{2}}\tilde{r}\,(2f_\mathrm{het})$
φ [uncorr. RIN: $r_\mathrm{m} \approx r_\mathrm{r}$]	$\sqrt{\frac{P_\mathrm{m}^2+P_\mathrm{r}^2}{2\eta_\mathrm{het}P_\mathrm{m}P_\mathrm{r}}}\tilde{r}\,(1f_\mathrm{het})$	$\frac{1}{2}\tilde{r}\,(2f_\mathrm{het})$
$\varphi - \varphi_R$ [corr. RIN: $r_\mathrm{m} = r_\mathrm{r}$]	$\frac{\sqrt{2}(P_\mathrm{m}+P_\mathrm{r})}{\sqrt{\eta_\mathrm{het}P_\mathrm{m}P_\mathrm{r}}}\tilde{r}\,(1f_\mathrm{het})\left\lvert\sin\left(\frac{\varphi-\varphi_R}{2}\right)\right\rvert$	$\sqrt{2}\tilde{r}\,(2f_\mathrm{het})\,\lvert\sin(\varphi-\varphi_R)\rvert$
$\varphi - \varphi_R$ [uncorr. RIN: $r_\mathrm{m} \approx r_\mathrm{r}$]	$\sqrt{\frac{2\left(P_\mathrm{m}^2+P_\mathrm{r}^2\right)}{\eta_\mathrm{het}P_\mathrm{m}P_\mathrm{r}}}\tilde{r}\,(1f_\mathrm{het})\left\lvert\sin\left(\frac{\varphi-\varphi_R}{2}\right)\right\rvert$	$\tilde{r}\,(2f_\mathrm{het})\,\lvert\sin(\varphi-\varphi_R)\rvert$

Table 7.1 Summary of the simplified RIN to phase coupling relations for a 50/50 recombination BS and band-limited white RIN. The indices m and r refer to the measurement and reference beam, respectively. $P_\mathrm{m,r}$ are the beam powers, while the RIN ASD values are described by $\tilde{r}\,(1, 2\cdot f_\mathrm{het})$. RIN can appear correlated (corr.) or uncorrelated (uncorr.) in the measured quantity, depending on the experimental configuration. For uncorrelated RIN its magnitude is assumed to have approximately the same value per beam, $\tilde{r}_\mathrm{m} \approx \tilde{r}_\mathrm{r}$. When a reference phase is subtracted, the beam power and RIN levels in the reference interferometer are assumed to be identical in φ and φ_R. The total phase noise caused by RIN is given by the $2f_\mathrm{het}$ column alone if perfect balanced detection is used. However, in the case of unbalanced detection the $1f_\mathrm{het}$ and the $2f_\mathrm{het}$ terms have to be added quadratically. Reprint from [P1].

These relations show the coupling magnitude with individual contributions from $1f_\mathrm{het}$ and $2f_\mathrm{het}$. For uncorrelated RIN, approximately the same level $\tilde{r}_\mathrm{m} \approx \tilde{r}_\mathrm{r}$ is assumed.

It can be seen that the $2f_\mathrm{het}$ terms, which appear regardless of balanced detection, only depend on constant factors and are independent of the beam powers. For $1f_\mathrm{het}$ this is not the case and there is a dependence on the beam powers. It follows that with matched beam powers, $P_\mathrm{m} = P_\mathrm{r}$, and equal splitting at the recombination BS, the $1f_\mathrm{het}$ contribution is a factor 2 higher than the $2f_\mathrm{het}$ contribution across all cases. However, the phase noise from 1f-RIN is magnified for imperfectly matched beam powers. This emphasizes the importance of balanced detection in precision metrology.

A rather typical scenario is the subtraction of a reference phase with common mode RIN. Here it can be seen that the error follows a sinusoidal pattern, depending on the relative phase relation. For $2f_\mathrm{het}$ the coupling strength becomes zero, if the two signals are in phase, and it becomes maximal for 90 ° out of phase signals. For $1f_\mathrm{het}$ the coupling also disappears if the signals are in phase, but the maximal coupling is reached for 180 ° out of phase signals. While 1f-RIN is well under control via balanced detection, this allows the minimizing of the $2f_\mathrm{het}$ contribution under certain circumstances, for example with perfectly aligned beams (i.e., a DWS offset of = 0 rad) or vanishing TM offsets in a LISA- or LPF-like measurement configuration.

Chapter 8
RIN Simulations

Various simulations have been performed to verify the theoretical results stated in table 7.1. A simulator resembling the LPF style heterodyne PM readout system as described in part I was developed and used to verify the theoretical derivations described above. In part IV, more complex simulations in accordance to the LISA mission are shown.

A schematic of the simulation is shown in figure 8.1. The interfering beam powers, as they are disturbed by broadband white RIN of strength $\tilde{r}$, are propagated with a sampling frequency of 50 kHz into SBDFTs with a Discrete Fourier transform (DFT) length of 500 samples at the heterodyne frequency of 1 kHz, generating a time-series phase output signal with a sampling frequency of 100 Hz.

Any light travel time delay on the RIN has been neglected in the simulation, since we assume $f_{\mathrm{m}} \approx 300\,\mathrm{THz} \gg f_{\mathrm{het}} = 1\,\mathrm{kHz}$ and closely matched pathlengths in the interferometers. The resulting noise is measured numerically, yielding an average phase noise ASD value.

Different filters and noise realizations have been tested to verify the scenarios with both correlated and uncorrelated input noise for balanced and unbalanced detection. The common mode phase subtraction has been tested by simulating an additional reference interferometer signal that is subtracted from the main measurement. To simulate two different laser sources two independent noise realizations with the same average noise spectral density have been used.

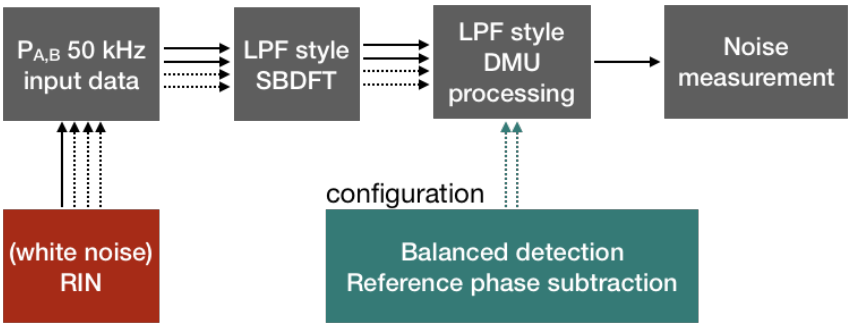

Figure 8.1 Overview of the LPF type RIN simulator used to verify the theoretical results. Dashed lines mark optional input, for example for simulating different correlations and multiple beams.

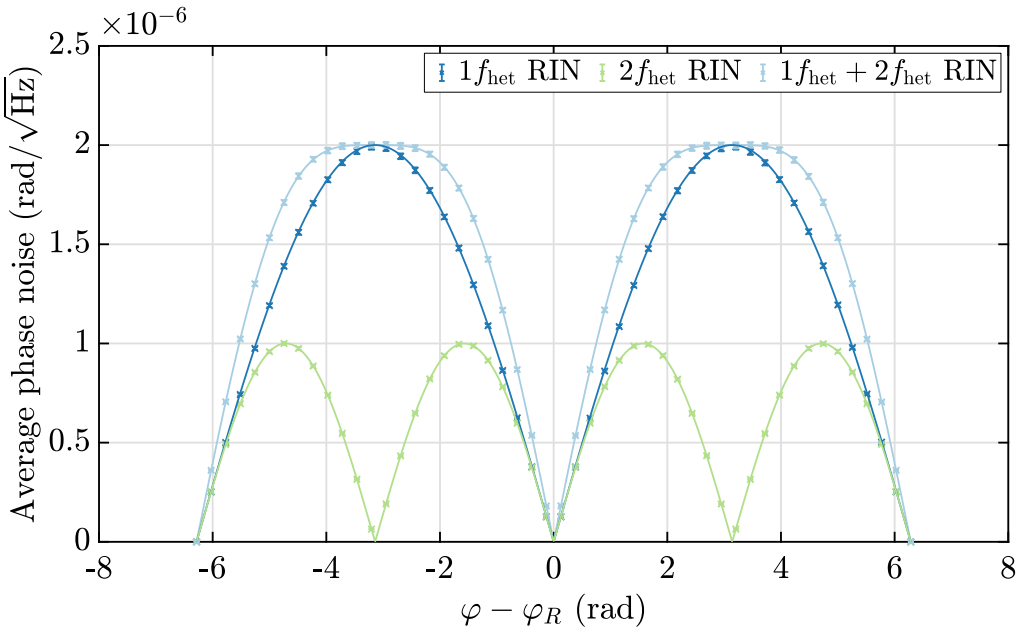

Figure 8.2 Dependence of RIN to phase coupling on the differential phase between two interferometric measurements that share the same RIN. Simulation (crosses) and theory expectation (solid lines) are in agreement. A detailed description is given in the text. Reprint from [P1].

Figure 8.2 shows the theoretical predictions (solid lines) and the numerical results (crosses) of the phase readout for the unbalanced, the balanced and the $1f_{\mathrm{het}}$ band-limited white noise case after reference phase subtraction (see table 7.1, last row). If balanced detection is used, only the $2f_{\mathrm{het}}$ contribution causes phase disturbances, as can be seen by the green bottom trace. If only noise around $1f_{\mathrm{het}}$ is present, the coupling increases while the sinusoidal period doubles (blue trace in the middle). If only one output port is used or if balanced detection is inactive, both contributions have to be considered, which is shown by the light blue top curve, which corresponds to a quadratic addition of the $1f_{\mathrm{het}}$ and $2f_{\mathrm{het}}$ RIN terms. Both $1f_{\mathrm{het}}$ and $2f_{\mathrm{het}}$ terms together recover the unbalanced simulation.

To separate the effect of $1f_{\mathrm{het}}$, a high order bandpass filter has been used to suppress the $2f_{\mathrm{het}}$ component to a large degree. In all three cases two independent noise sources, averaged over 100 runs have been used, representing two lasers with comparable properties. The average beam powers are kept identical at 1 mW with an input RIN ASD at an average level of $1 \times 10^{-6}\,\mathrm{Hz}^{-1/2}$. A second interferometer is simulated as a reference interferometer, which allows the subtraction of its phase, leading to a sinusoidal noise dependence on the relative phase. The properties of the reference interferometer are identical to the measurement interferometer, except for a zero phase offset. RIN was correlated in the measurement and the reference interferometers, but uncorrelated between the measurement and reference beams.

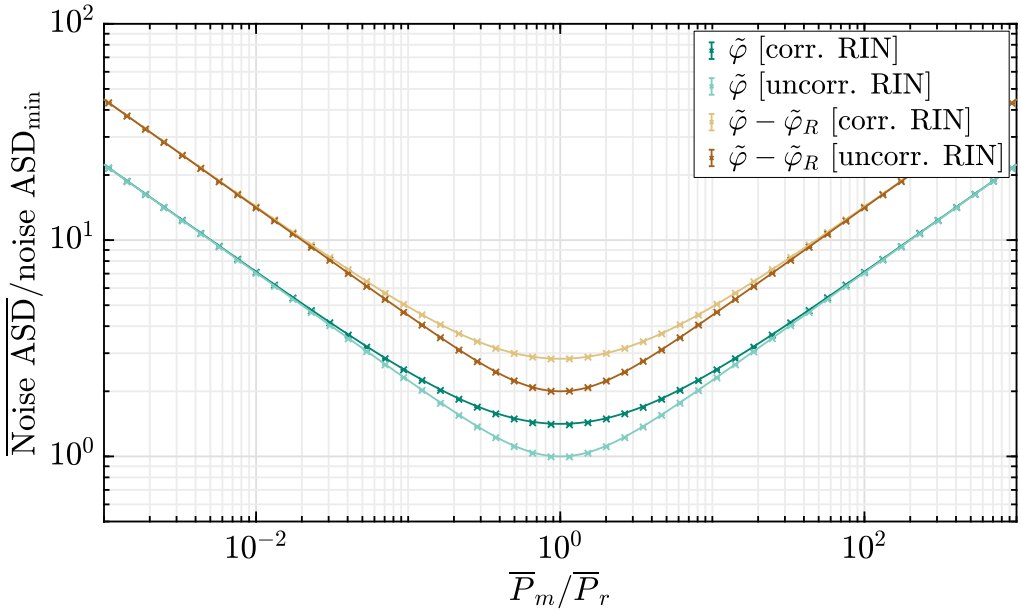

Figure 8.3 Coefficients of $1f_{\text{het}}$ RIN to phase coupling for different beam powers, normalized to the minimal coupling. Simulation (crosses) and theory expectation (solid lines), evaluated at maximal coupling strength (sine factor equal to 1), and in the phase subtraction case for equal RIN levels between the two beams. A detailed description is given in the text. This plot has previously been published in [P1].

Figure 8.3 shows the error magnification for all derived $1f_{\text{het}}$ coupling coefficients (see table 7.1, column $1f_{\text{het}}$ phase noise) as given by theory (solid lines) and simulation (crosses) for various input beam powers. The inputs are expressed with respect to the beam power ratio and the output is normalized by the minimal coupling strength of the smallest coupling (φ uncorr. RIN), which is reached when both beam powers are matched. The $2f_{\text{het}}$ coupling is suppressed in this plot, since it does not depend on the power levels. It can be seen that, for unequally matched beam powers, the $1f_{\text{het}}$ contribution may increase by orders of magnitude if imperfect or no balanced detection is applied. The symmetry and magnitude as given by the formulas is recovered. As expected, the maximal ratio between the correlated and uncorrelated cases is given by a factor of $\sqrt{2}$. The two cases with a reference phase subtraction have been calculated with a phase difference between measurement interferometer and reference interferometer of exactly π to only record the maximal coupling coefficient. Every simulation is generated from new noise seeds, and for each point 50 averages have been used.

It should be noted that the phase demodulation processing affects the noise spectrum with its gain function. The exact transfer coefficient depends on the signal path and can be found by integrating the total noise power that is effectively propagating.

Part III

LISA Pathfinder

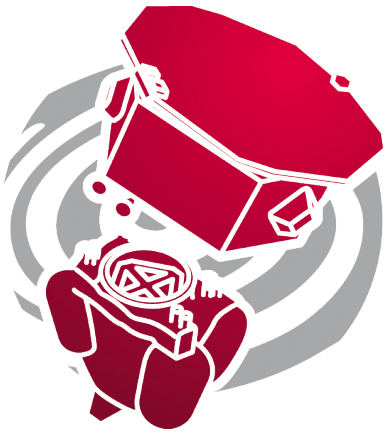

Chapter 9
In-flight behavior

Please note that chapters 9 to 12 comprise most contents in exact wording from [P2, P3] (constituting contributions by the author of this thesis in collaboration with the LPF OMS team, especially with S. Paczkowski, G. Wanner, D. Robertson, M.-S. Hartig, M. Hewitson, and G. Heinzel).

This part covers the in-flight noise modeling and sensitivity analysis of the LPF OMS in the following chapters, including the RIN contributions theoretically described in the previous chapters. It also highlights findings from specific RIN experiments in chapter 13.

9.1 General observations

In general, the OMS exhibited exceptionally stable performance throughout the mission with $32.0^{+2.4}_{-1.7}\mathrm{fm}/\sqrt{\mathrm{Hz}}$ sensitivity above 200 Hz along x (as presented in [P2]), and an angular sensitivity regarding TM rotations as good as $100\,\mathrm{prad}/\sqrt{\mathrm{Hz}}$ (as presented in [P3]), substantially better than its requirements.

The interferometer was first turned on during commissioning (13th January 2016) with still caged TMs and hence large beam misalignment. The propulsion module was also still attached to the SC at this time, resulting in a varying thermal environment under vibrational stress. Nevertheless, the OMS immediately demonstrated full functionality and noise levels well below $10\,\mathrm{pm}/\sqrt{\mathrm{Hz}}$ at a frequency range between (1 to 1000) mHz, despite having a contrast of only 0.6 % in the X12 interferometer, limited by misalignment of the beams with the TMs in their "launch locked" positions.

The TMs were released during commissioning on 15./16.02.2016; a few days later they were aligned and dynamically controlled by DFACS using the interferometer signals. A contrast of around 99 % in X12 and 98.5 % in X1 was immediately achieved (see figure 9.1) and science operations started on March 1st 2016. LPF maintained a similar OMS performance throughout the whole mission.

This long-term stability of the OMS was particularly impressive and has relevance to the approximately six times longer LISA mission. Overall, the operational duty cycle of the OMS, measured in terms of laser and PM functionality, between launch in December

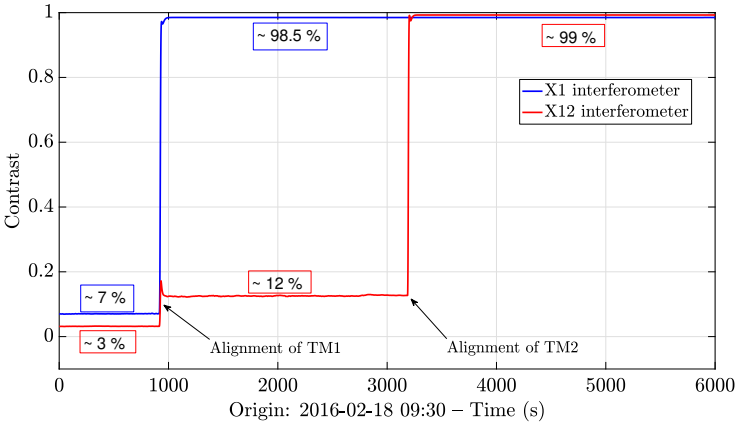

Figure 9.1 Contrasts during TM alignment. The TMs were previously released and here aligned using electrostatic actuation, which improved the contrast considerably; best achieved in ground testing was ∼93 % using aligned mirrors. This behavior underlines the built quality of the OMS. Reprint from [P3], based on a plot from M. Hewitson/G. Heinzel.

2015 and the end of the mission extension in July 2017 reached 99.4 %, demonstrating the system's reliability. To determine this number, we chose the measured contrast in the reference interferometer above 85 % as a parameter to indicate that these two units are operating well. This choice was made because the reference interferometer measurement is unaffected during a large number of maneuvers and this level of contrast can only be reached if both beams are operational and well centered on the PDs. In addition, the ADC utilization parameters used for this computation are a result of the PM and thus the availability of reasonable data indicates it was operating. We defined the mission duration to begin with the beginning of nominal operations on March, 1st 2016 at 08:00 UTC and to end on July, 1st 2017 at 08:00 UTC.

A general observation regarding the laser power stability (RIN) can also be made. It stayed within requirements and was not the limiting noise source, as far as we were able to estimate from indirect measurements (see chapter 11). Further detailed analyses of the very stable performance is given in [P3], including OB stability, PD degradation due to cosmic radiation, contamination and beam polarization, which is outside the scope of this thesis.

In the following, characteristic observations and the noise model to describe the OMS sensitivity are given. Our understanding of the system explains most of the sensing noise as combination of noise sources associated with the laser (frequency noise, intensity noise, shot-noise) and noise sources associated with the phase measurement system (quantization noise, electronic noise). The overall model also contains indirect contributions from Tilt-To-Length (TTL) coupling and Brownian force noise.

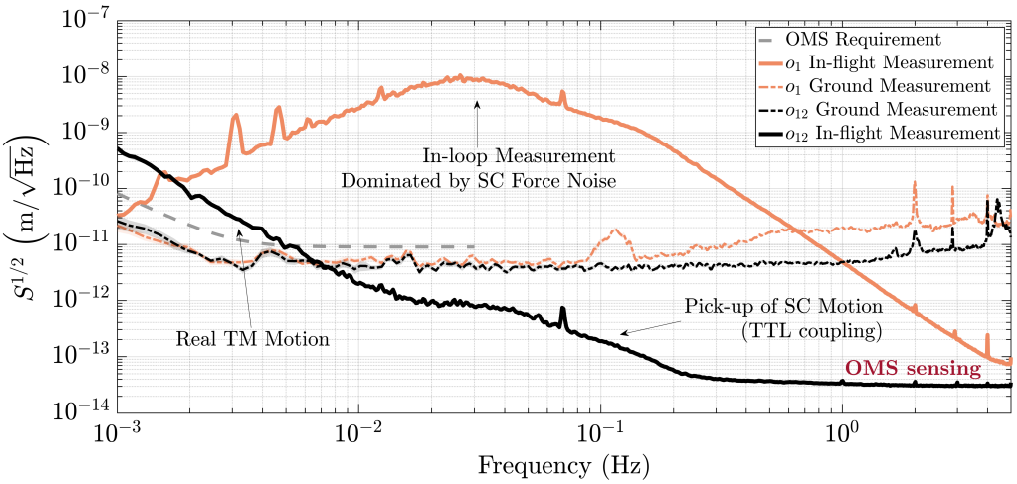

Figure 9.2 Comparison of o_1 and o_{12} on-ground and in-flight. On-ground, the data is comparable below the requirement. The in-flight measurement of $o_{12} < 200\,\text{mHz}$ is dominated by cross-coupling from spacecraft jitter and real TM motion (see section 10.3.2 and figure 11.1). At higher frequencies, the noise is significantly below the ground data and OMS sensing noise is dominating (marked in red). The in-flight o_1 readout is an in-loop measurement to control the SC. It is dominated by force noise on the SC. Figure produced using the Logarithmic Frequency Axis Power Spectral Density (LPSD) algorithm [58] (1000 frequencies, 100 averages) with 66.1 % overlapping BH92 windows [59]. Reprint from [P3].

9.2 Typical spectra and comparison with ground measurements

In this section, we look at some typical noise measurements of the longitudinal and angular measurements and compare those to data from the pre-flight ground test campaign.

9.2.1 Description of the data

The in-flight measurements for these examples were taken in March 2016 during the first two days of mission operations (2016-03-01 08:05 - 2016-03-03 00:00 UTC), just after the commissioning phase was completed. The on-ground measurements were taken more than 4 years earlier during the "on-station thermal test" campaign at Industrieanlagen-Betriebsgesellschaft mbH (IABG) in Ottobrunn from 2011-10-26 – 2011-11-06, during the hot (used for angular DWS data below) and cold (used for the longitudinal data here) test phase with temperatures of between approximately (9.5 to 30.5) °C. The spectral densities of the longitudinal readouts o_{12} and o_1 are shown in figure 9.2, expressed as an ASD. We give one measurement from on-ground tests and one from in-flight data, respectively, compared to the overall requirement of the OMS. Similarly, figure 9.3 shows the corresponding DWS comparison.

9.2.2 Description of o_{12}

The in-flight o_{12} measurement of the relative x displacement of two TMs represents an "in-loop" sensor, used by DFACS to control the TM2 electrostatic force along x to maintain constant TM separation. However, its unity gain frequency is around 1 mHz and has negligible effect on the data shown, especially on the sensor noise dominated high frequencies.

We note that in general the sensing noise at those mHz frequencies cannot be measured but only estimated and bounded by upper limits. As visible, the measured o_{12} displacement exceeds the optical metrology requirement at such frequencies less than 5 mHz, but this can most likely be attributed to true TM motion, since the sensor is designed to detect real distance fluctuations.

In addition, we provide measurements for mechanically fixed TMs by the Gravitational Reference Sensor (GRS) "grabbing positioning release" system during flight. These are shown along x in figure 11.6 and figure 11.7, while the angular DWS is presented in figure 11.8. This data suggest that also the in-flight noise at frequencies as low as 1 mHz is consistent with the level observed at higher frequencies.

For the data between (20 to 200) mHz we attribute the excess noise to pick-up of SC motion (TTL coupling), see section 10.3.2 and [P2, P5, P21].

As reported in [P2], the main o_{12} measurement recorded in-flight shows a quasi-flat sensing noise floor at frequencies above 1 Hz, which is much lower than on ground. At frequencies above 400 mHz it shows an improvement of more than a factor of one hundred.

The small peaks in the in-flight o_{12} data at 1 Hz, 2 Hz, 3 Hz, 4 Hz and 5 Hz are probably due to electrical cross-coupling from the Pulse Per Second (PPS) timing signal present on the SC.

9.2.3 Description of o_1

The o_1 measurement shows a different spectral shape than the ground measurement. To explain this difference we consider that the o_1 measurement is also an in-loop measurement of another DFACS's drag-free control loop. This loop, with unity gain frequency of about 0.2 Hz, ensures that the SC follows the x position of TM1. Therefore, it has a higher unity gain frequency than the control loop which uses o_{12}. Consequently, the o_1 spectral density is dominated by force noise of the SC, which originates mainly from the thrusters, and the gain of the drag-free control loop which suppresses this noise [P17].

The lines around 1.5 mHz and its multiples, and probably the feature around 70 mHz as well, are associated to the thrusters [P16]. This idea is also supported by the discussion in [P19]. When comparing the amplitude of this feature in o_1 and o_{12}, we find that the ratio of the two amplitudes is slightly higher than what we could attribute to common-mode

rejection [P21]. However, the feature around 70 mHz is also observed by a capacitive position sensor of TM1 (not shown here, for details about this sensor, we refer to [P24]). This is also confirmed during a period when the OMS served as an out-of-loop sensor, while the control was switched to the independent but less sensitive capacitive sensing of the GRS. Another important test was performed during Disturbance Reduction System (DRS) operations, when the main cold gas thrusters were in standby mode, while another set of thrusters was used to control the SC [P19]. We find that the interferometric readouts show no feature at 70 mHz for two selected and comparable timespans. Consequently, a platform jitter originating from the cold gas thrusters is a more likely reason, and the OMS does not cause this artifact.

9.2.4 Description of DWS measurements

The angular DWS measurements, presented in figure 9.3, have very similar characteristics towards frequencies above 1 Hz. The low frequency behavior has been analyzed in [P17] and shows a combination of star tracker noise, TM torque noise, capacitive sensing noises, and SC force noise, since DWS has been used as an in-loop sensor for the DFACS. As can be expected by design, the differential channels show more than an order of magnitude common-mode rejection of those contributions.

We find that the high-frequency sensitivity, limited by the OMS, reached even below $100\,\mathrm{prad}/\sqrt{\mathrm{Hz}}$ during the mission, more than a factor 200 better than required.

The ground measurements show comparable characteristics to the longitudinal data but had ample margin to their requirement.

The visible noise floor also depends on the RIN coupling and can be modulated by TM rotations. This led to specific experiments investigating the RIN coupling in-flight, see chapter 13.

9.2.5 Comment on the difference between ground and in-flight measurements

The results of the on-ground test campaign reported in [60], visible in figure 9.2, showed a measured performance of around (3 to 8) $\mathrm{pm}/\sqrt{\mathrm{Hz}}$ around 10 mHz, a significantly higher noise level than observed during science operations.

During the ground tests, Earth's gravity did not allow for free-falling TMs under DFACS control as in-flight. Therefore, the TMs were replaced with fixed mirrors whose attitude and longitudinal position were hand-aligned. The alignment resulted in a somewhat non-optimal phase offset between X12 and the reference interferometer, and a typically lower contrast than what was achieved in flight, resulting in some of the noise contributions being higher than in flight conditions.

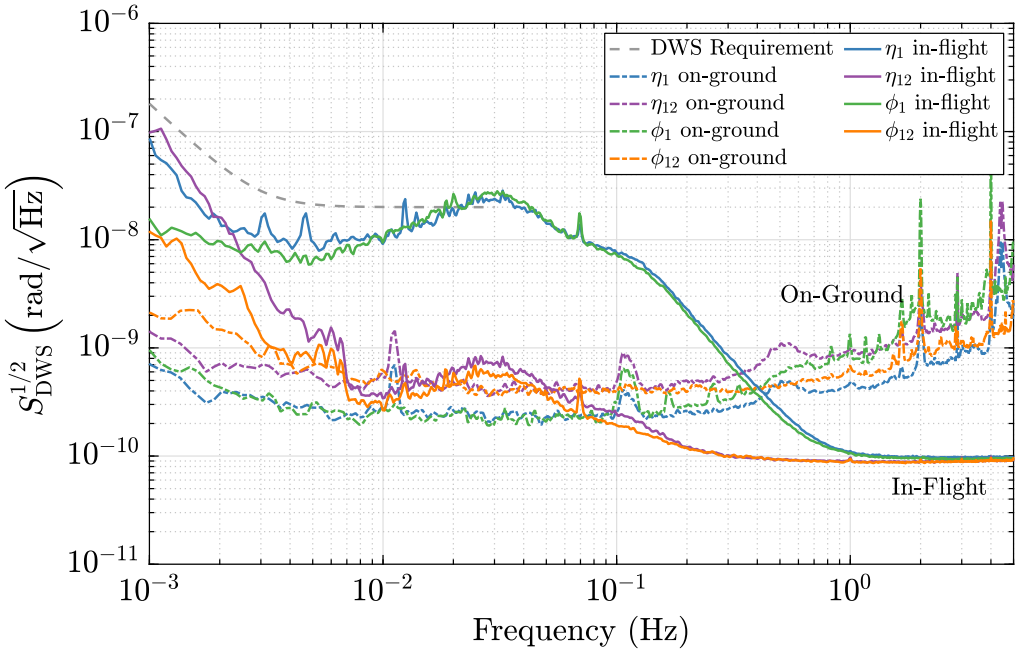

Figure 9.3 Comparison of on-ground and in-flight angular DWS TM readouts and the noise requirement. The spectral shape is similar to $o_{1,12}$ but has contributions from real TM movements (independently validated by low frequency ($<$ mHz) capacitive sensing), SC jitter, star tracker noise and OMS sensing noise. This figure applies the same LPSD algorithm as in figure 9.2. Reprint from [P3].

However, this does not explain all of the extra noise. The reason may be that the two separated mirrors, rigidly connected via individual Piezo-electric Transducers (PZTs), may not have been strictly stable to pm level. These individual mounts may also explain the difference between the o_1 and o_{12} noise levels above 30 mHz because of possible acoustic or seismic couplings that could cancel to some extent in the differential measurement. The origin of the feature in o_1 just above 100 mHz is discussed in more detail in [61]. However, the on-ground noise spectrum was never fully explained. Since the performance had been below the requirements, further investigations were not given high priority.

Moreover, as is shown in the following, the in-flight noise spectrum is well modeled (see the discussion below).

We present our noise model in sections 10.1 and 10.2 and apply it to selected in-flight data under various conditions in chapter 11. A complete mission overview is given afterwards in chapter 12.

Chapter 10
OMS noise models

10.1 Longitudinal noise model

Here an overview of the noise sources with respect to the longitudinal measurements for the interferometers is given. This model is based on pre-flight noise characterizations and in-flight observations from the LPF team mainly in Hannover (AEI) and Glasgow university [62]. It contains noises directly associated with the OMS, e.g. from the laser, readout system, thermal effects and others.

Their propagation is modeled according to the on-board processing: All the longitudinal signals are constructed using 8 QPD segments. They are combined by applying balanced detection (subtracting complementary out-of-phase quadrants from the two output ports at the recombination BS) and complex addition of the balanced segments. This leads to scaling factors due to the channel combinations, depending on the correlation properties for a given noise. Most derivations regarding the on-board processing can be found in [41, 46, 63]. A brief overview is given in appendix B. Typically, the inverse carrier to noise density is used to compute phase noise from vector-like noise contributions in the raw heterodyne signal as derived in equation (7.20).

10.1.1 Laser Frequency Noise

Laser frequency fluctuations couple directly into the phase measurement as described by [64, 65]

$$\delta\varphi = 2\pi\frac{\Delta L}{c}\delta\nu. \tag{10.1}$$

In this equation, $\delta\varphi$ are phase fluctuations measured in radian and ΔL is the path length mismatch between the reference and the measurement beam, c denotes the speed of light and $\delta\nu$ represents the laser frequency fluctuations measured in Hz.

The Frequency interferometer was particularly sensitive to frequency noise due to its intentionally large pathlength mismatch $\Delta L_F - \Delta L_R = 382\,\mathrm{mm}$ and was therefore used to estimate its contribution to $S_{o_{12}}$. By using equation (10.1) expressed as an ASD and accounting for the fact that the telemetry data from the X12 and Frequency interferometer

had the Refererence interferometer signal subtracted we find the corresponding displacement noise

$$S^{1/2}_{o_{12},\mathrm{freq}} = \frac{\lambda}{4\pi}\frac{\Delta L_{12} - \Delta L_R}{\Delta L_F - \Delta L_R} S^{1/2}_{\Psi_\mathrm{F}} =: H_{o_{12}} \cdot S^{1/2}_{\Psi_\mathrm{F}}. \tag{10.2}$$

For the data in figure 11.1 the maximum frequency noise $S^{1/2}_{\Psi_\mathrm{F}}$ was $(270 \pm 13)\,\mu\mathrm{rad}/\sqrt{\mathrm{Hz}}$ at 0.38 Hz. The coupling coefficient $H_{o_{12}}$ was estimated by a dedicated experiment on the same day, giving $H_{o_{12}} = (82 \pm 1)\,\mathrm{pm/rad}$. This corresponds to a path length mismatch $\Delta L_{12} - \Delta L_R$ of 368 µm in June 2016, and (from another experiment) around 329 µm in January 2017. This analysis has been performed by S. Paczkowski [66]. The values have been used to obtain the respective frequency noise contributions in chapter 11.

We also experienced periods of slightly increased laser frequency noise, during which it dominated the o_{12} measurement at frequencies between approximately (0.2 to 1) Hz, causing the higher noise levels (bimodal distribution) visible in figure 12.1 and [66].

10.1.2 Shot-Noise

In the given context, we understand shot-noise as statistical fluctuations of the incident photons on a QPD and the resulting photo current, which then cause a phase noise. This noise occurs uncorrelated on every PD segment and therefore enters both in the longitudinal and angular readout signals. The phase noise in the longitudinal readout of interferometer $K \in \{\mathrm{X12}, \mathrm{X1}, \mathrm{R}, \mathrm{F}\}$ converted to an equivalent differential TM displacement noise, is estimated by

$$S^{1/2}_{K,\mathrm{shot}} = \frac{\lambda}{2\pi C_K}\sqrt{\frac{e}{2\Sigma_K \frac{U_\mathrm{ADC}}{R_\mathrm{TIA}}}}\,, \tag{10.3}$$

where C_K denotes the measured contrast and e the elementary charge. In-flight measurements provide us with a corresponding product term $\Sigma_K = 2\varepsilon_K(P_{K,m} + P_{K,r})$, which represents the normalized photo current in the interferometer, with ε_K being the effective photodiode responsivity and $P_{K;m,r}$ denotes the power of the measurement and reference beam. We computed the shot-noise trace in figure 11.1 by an uncorrelated sum of the contributing noises from the X12 and R interferometer using C_K and Σ_K telemetry as well as the full range of the Analogue to Digital Convertor (ADC) converter $U_\mathrm{ADC} = 5\,\mathrm{V}$ and the effective transimpedance $R_\mathrm{TIA} = 6640\,\Omega$. The resulting noise level of $2.3\,\mathrm{fm}/\sqrt{\mathrm{Hz}}$ can likewise be found if typical values are used instead of telemetry data: $\Sigma_K \approx 1.2, C_K > 95\,\%, P_K \approx 1.2\,\mathrm{mW}$ and $0.7\,\mathrm{A/W} < \varepsilon_K < 1\,\mathrm{A/W}$.

10.1.3 PM Noise

The PM was the system that processed the photocurrent from the photodiode segments and produced an estimate of the phase of the 1 kHz heterodyne signal. Each channel of the system consisted of a transimpedance amplifier, a low-pass filter, an ADC operating

at 50 kHz to digitize the signal, and a digital processing system that performed the demodulation to calculate the phase.

The dominant noise sources are the equivalent input current noise and the quantization noise of the ADCs. Using LISO [67], the circuit was modeled (by G. Heinzel) to give an equivalent input current noise of $S_{I_{\mathrm{elec}}}^{1/2} = 17\,\mathrm{pA}/\sqrt{\mathrm{Hz}}$. The remaining input current noise is attributed to the ADC and was estimated from ground measurements as $S_{I_{\mathrm{ADC}}}^{1/2} = 102\,\mathrm{pA}/\sqrt{\mathrm{Hz}}$. From this the total input current noise $S_{I_{\mathrm{tot}}}$ is calculated and the equivalent displacement noise derived using

$$S_{K,\mathrm{PM}}^{1/2} = \frac{\lambda}{\pi C_K} \frac{S_{I_{\mathrm{tot}}}^{1/2}}{2\Sigma_K \frac{U_{\mathrm{ADC}}}{R_{\mathrm{TIA}}}} \,. \tag{10.4}$$

The total PM noise contribution in the o_{12} readout is computed by an uncorrelated sum of the contributing noises from the X12 and R interferometer. This gives an expected PM noise level of $28.7\,\mathrm{fm}/\sqrt{\mathrm{Hz}}$, which is the most significant contribution to the OMS noise budget at frequencies $> 200\,\mathrm{mHz}$ in the lower frequency noise state.

10.1.4 Laser RIN

This noise model directly follows from part II and table 7.1. As described before, RIN describes intensity fluctuations of a laser beam normalized by its mean. RIN results in instrument noise via three different mechanisms: a time varying direct force on the TMs (i.e. radiation pressure noise); coupling to phase noise at the heterodyne frequency ($1f_{\mathrm{het}}$-coupling); and coupling to phase noise at twice the heterodyne frequency ($2f_{\mathrm{het}}$-coupling).

The radiation pressure noise is suppressed well below the total noise by a power control loop, and the $1f_{\mathrm{het}}$-coupling by the use of balanced detection (i.e. by subtracting the correlated data retrieved from the A and B diodes).

The $2f_{\mathrm{het}}$-coupling is common mode in the X12 and R-interferometers. This time there is no cancellation due to balanced detection. However, in normal operations, the control of the separation of the two TMs ensures that the path length difference $d_{o_{12}}$ between those interferometers is kept close to zero (e.g. $d_{o_{12}} \approx 0.3\,\mathrm{nm}$ in figure 11.1), which suppresses the effect described by

$$S_{o_{12},\mathrm{RIN}}^{1/2} = \frac{\lambda}{4\pi}\sqrt{2}r\left|\sin\left(\frac{4\pi}{\lambda}d_{o_{12}}\right)\right|, \tag{10.5}$$

where r is the RIN level of the laser at $2f_{\mathrm{het}}$. The factor $2 \cdot 2\pi$ is due to the on-board calibration to TM displacement.

Investigations of RIN coupling have been performed over a variety of operating conditions throughout the mission, see chapters 12 and 13. From these, the estimated RIN in the frequency band above 0.8 Hz is approximately white, and varies with time within the

range $r = (1.8 \times 10^{-6}$ to $5.0 \times 10^{-6})\,\mathrm{Hz}^{-1/2}$, probably due to variations in laser operating conditions. In total, well controlled RIN noise proved to be an insignificant OMS noise due to choosing an optimal interferometric operating point (in the argument of the minimizing sine factor), contributing no more than $2.4\,\mathrm{fm}/\sqrt{\mathrm{Hz}}$ during normal operation.

10.1.5 Thermally driven noise

With regards to intrinsic low frequency noise of the OMS, there are 3 main thermally driven optical path length changes on the OB: the windows between the bench and the TMs [68], the expansion of the Zerodur baseplate, and the transmission through the beamsplitters.

The dominant effect is likely the change in refractive index of the fused silica beamsplitters. The design (as explained by D. Robertson) minimises this effect by balancing the number of optical transmissions in each arm of each interferometer. However, this relies on a common thermal environment for all the relevant optics so that common mode rejection occurs.

We estimate an upper limit of thermally driven noise by taking the modeled thermal coupling, using an observed thermal measurement at 1.17 mHz and a conservative projection to higher frequencies [P15], and assuming no common mode rejection. This noise model reads

$$S_{o_{12},\mathrm{thermal}}(f) = \left(7.86 \times 10^{-9} \times f\right)^{-2.5}, \quad \left[\frac{\mathrm{m}^2}{\mathrm{Hz}}\right]. \tag{10.6}$$

Other thermo-elastic induced noise was estimated to be below this level [69].

10.1.6 Processing Doppler error

On the processing side, an analytically predictable phase error (calculated by G. Heinzel in [62], see also [70]) in the SBDFT-derived phase was found in the case of non-negligible phase shift occurring during one time segment (10 ms). If the changes are fast enough, they produce an equivalent frequency shift of the heterodyne signal. Since the SBDFT is always evaluated at the fixed heterodyne bin, sufficiently fast signals drift measurably out of this bin, resulting in a non-symmetric Fourier transform. We call this effect "Doppler error". It depends on the injection frequency and its offset to the heterodyne frequency for a given Fourier bin width. This error was mitigated by analytical correction formulas in the processing back end for the prototype measurements but was not visible under nominal in-flight operating conditions due to the achieved phase stability.

However, this error needed to be corrected in experiments involving fast phase injections, see section 10.1.7. Since it is not relevant for LISA which uses a different phase extraction technique, a more detailed explanation is omitted here.

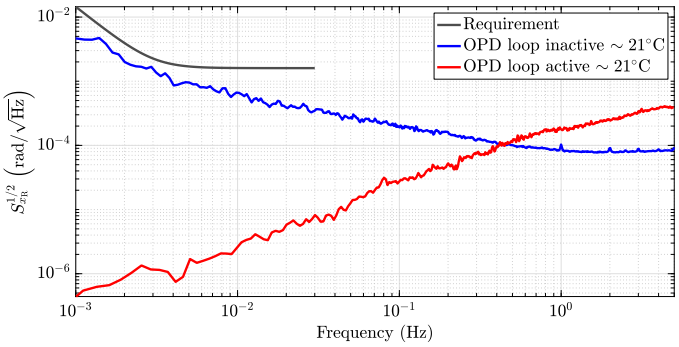

Figure 10.1 Two in-flight ASDs of the reference interferometer measurement x_R (in-loop measurement). One with inactive OPD control loop, and one in nominal configuration. The requirement is based on the significant SVN coupling measured during ground tests. Reprint from [P3], analysis by S. Paczkowski, M. Born, A. Wittchen.

10.1.7 Small Vector Noise (SVN)

This section contains both the description and a brief analysis of the in-flight SVN.

During hardware development, noise investigations in Glasgow identified an important noise source named SVN. It originates from electrical sidebands introduced by the Radio Frequency (RF) signals driving the Acousto-Optic Modulators (AOMs) which then convert into optical sidebands. These sidebands, in turn, result in a spurious interferometric signal in conjunction with fluctuations of the differential pathlength between the two fibers that deliver the light to the OB. [70].

This coupling was mitigated by design in two ways: via a stringent requirement on the spectral purity of the AOM driving frequencies and via the so called Optical Pathlength Difference (OPD) control loop, using piezos behind the AOMs as optical pathlength actuators. As an important part of the on-ground noise model, the loop behavior and remaining level of SVN in-flight was also investigated.

For characterizing the suppression of SVN we deliberately applied triangular path length differences through the OPD actuators. This appears in the x_R measurement, which, under nominal operating conditions, is used as an in-loop measurement of the OPD control loop.

In general, in-flight, the path length difference fluctuations in the fibers were below the requirement, see figure 10.1. The in-flight data shown here is from 2016-06-11/12 (inactive loop) and 2016-06-02 (active loop). The OB temperature sensors report temperatures around 21 °C for the two periods of in-flight data. The blue trace in this figure is the ASD of the reference interferometer measurement x_R when the OPD loop was inactive. The level of fluctuations is most likely due to a relatively stable thermal environment of the SC. This was not the case for the on-ground measurements. With an activated OPD control loop the noise in x_R is comparable to the example shown in red in figure 10.1.

By comparing these two measurements, we find that the control loop suppresses the noise at frequencies below 0.4 Hz and increases the noise above this frequency. We believe the OPD actuator is adding noise at high frequencies but the details are still not understood,

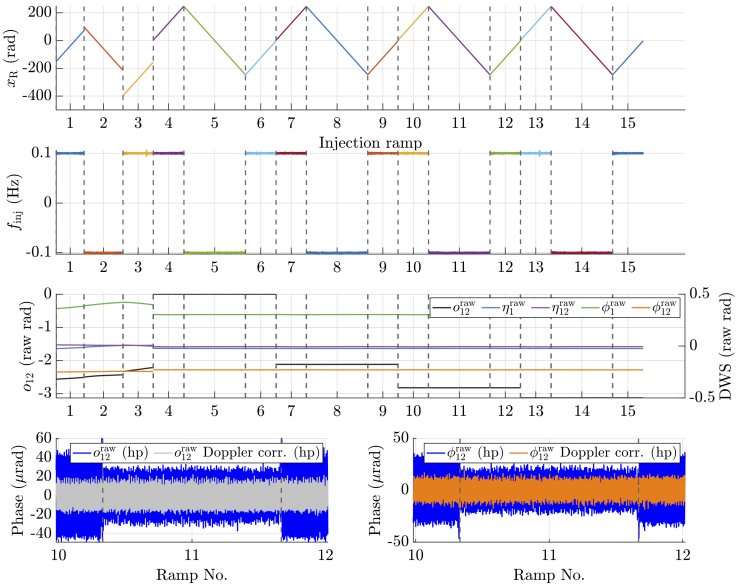

Figure 10.2 SVN experiments during the mission (see text). First panel: injected phase ramps in the reference interferometer. Second panel: Corresponding injection frequencies (derivatives). Third panel: differential displacement and TM orientation in uncalibrated radian. Last row: Effect of the Doppler correction. Reprint from [P3].

see also [71]. We observed that the piezo-controlled loop exhibits spikes at around its actuation frequency of 100 Hz which are aliased down to lower frequencies. This OPD actuator contributes its own noise and often leads to increased noise towards the end of the 10 Hz spectrum.

The related discrepancy to the designed unity gain frequency was already noted before launch and was attributed either to a change in noise level between different measurement times or a different control loop response when operated under fully closed-loop conditions [41]. In addition, a few dedicated OPD loop characterization experiments are under study. Nonetheless, the requirement on the noise in x_R is fulfilled and the SVN contribution is minimized.

To measure the remaining SVN sideband strengths directly, a set of experiments that deliberately amplified this coupling have been performed and analyzed. The impact of SVN was modeled following [70]: For a given OPD injection at frequency f_{inj}, this model considers two small contributing vectors; one at the frequency $(1f_{\mathrm{inj}})$, and one at twice the frequency $(2f_{\mathrm{inj}})$. Like any other additive vector noise the magnitude of the coupling depends on the differential phase when subtracting correlated measurements and behaves therefore similar to RIN. For o_{12}^{raw} the model reads in time-domain

$$\begin{aligned} N_{\mathrm{X12,SVN}} = &\left(k_1 \sin\left(\frac{x_R + x_{12}}{2}\right) + k_2 \cos\left(\frac{x_R + x_{12}}{2}\right)\right) \sin\left(\frac{o_{12}^{\mathrm{raw}}}{2}\right) \\ &+ \left(k_3 \sin\left(x_R + x_{12}\right) + k_4 \cos\left(x_R + x_{12}\right)\right) \sin(o_{12}^{\mathrm{raw}}). \end{aligned} \tag{10.7}$$

The in-flight experiments aimed at estimating the sideband strengths k_i. These experiments are detailed in figure 10.2. “Fast” phase ramps were injected through the OPD loop and

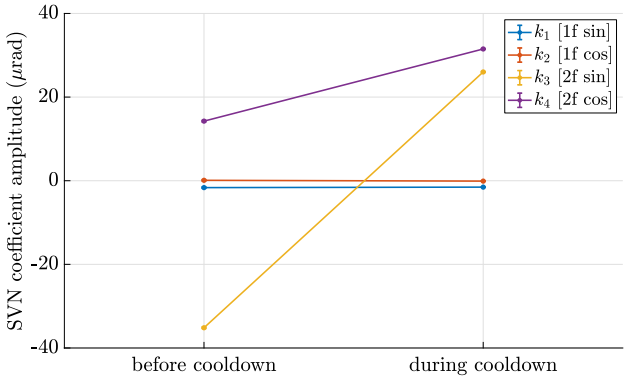

Figure 10.3 Averaged SVN coefficient fit results before (ramps 1–3) and during cooldown (ramps 4–15). These are the only ramp injections during the nominal mission, so for most of the time we apply the "before cooldown" coefficients to estimate the SVN contribution. We suspect a phase rotation during cooldown in the k_3 coefficient – the total sideband strength remains approximately the same. Reprint from [P3].

resulted in sinusoidal phase noise in the raw phase signals. One experiment took place before, and one during the cooldown of the SC in the beginning of 2017. The top panel shows the phase ramp injections through the OPD, next we display the stable injection frequencies and the raw offset of the readouts, since those control the strength of the coupling. The last row shows the effect of the Doppler correction on the data with an exemplary zoom on ramp 11 (with highpass). The data stems from January (before cooldown) and February 2017 (during cooldown). One ramp was in the order of 5 to 10 minutes.

When analyzing this experiment, we had to correct for the "Doppler error", due to the fast phase changes (see section 10.1.6). We were able to calculate and remove this effect, that leads to wrong amplitude estimates, see also the bottom panels of figure 10.2 and [70]. It was calculated here specifically for the flight PM and estimated based on the limited telemetry. However, the Doppler error is not relevant in nominal operations, when the phase changes are much slower.

From fitting the SVN noise model to these injections in all channels with appropriate Signal to Noise Ratio (SNR), we found a similar set of coupling vector amplitudes for the different operating conditions, while likely only their phase relation changes.

The main findings are that the 1f-SVN contributions are below $|2\,\mu\text{rad}|$, while the 2f-SVN coefficients reach almost $|40\,\mu\text{rad}|$, see figure 10.3.

These sidebands are further minimized by the sine factor of the differential phase during the mission, because the nominal offsets are almost zero for o_{12}. For the rotational degrees-of-freedom the contributions are slightly higher due to the DWS alignments.

For example, with an o_{12} offset of 10 nm we estimate a contribution of around $0.1\,\text{fm}/\sqrt{\text{Hz}}$ at 1 Hz.

Overall, the measurements and experiments confirm that SVN was well mitigated. However, in principle we cannot differentiate between RIN and SVN for a given nominal measurement (that does not include a fast phase change in x_R), since both show similar common mode

suppression. Based on the strong suppression from the SVN analysis presented here, we attribute most of the remaining vector noise to RIN, which then takes values in the range of its expected behavior from ground measurements [71].

10.1.8 Summary of the longitudinal noise model

To summarize, our OMS noise model for the noise power in units of PSD consists of the uncorrelated sum of

- X12 PM noises (shot-noise, ADC noise and electronic noise that depend reciprocally on the X12 contrast and power)
- XR PM noises (shot-noise, ADC noise and electronic noise that depend reciprocally on the XR contrast and power)
- XF frequency noise to o_{12} coupling
- RIN to o_{12} coupling
- SVN to o_{12} coupling
- Thermally driven noise on the OB as a conservative upper limit neglecting common-mode effects
- (Not from the sensor: Indirect contributions, see section 10.3)

The same holds true for the X1 interferometer by adjusting the inputs accordingly.

10.2 Angular DWS noise model

We also characterize the angular measurements using DWS, for which pairs of balanced quadrants are subtracted (top and bottom, left and right), resulting in a slightly lower SNR compared to the longitudinal data.

As described in section 3.2, DWS uses calibration coefficients from ground measurements, that calibrate from the “raw” optical wavefront phase difference to TM angle.

10.2.1 DWS model contributions

The angular noise model is similar to the longitudinal cases. Differences arise from the different calibration factors, the missing subtraction of the XR interferometer readout, the good suppression of frequency noise (almost identical path-lengths between quadrants) and the different channel combinations. The parameters are described in detail in section 10.1. In short, we have inputs of the contrast C, the elementary charge e, the normalized average total power per interferometer Σ, the voltage range of the ADC, U_{ADC}, and the effective transimpedance R_{TIA}.

For DWS readout $\gamma \in \{\phi_1, \phi_{12}, \eta_1, \eta_{12}\}$ in a corresponding interferometer $K \in \{\mathrm{X12}, \mathrm{X1}\}$ we find the shot-noise

$$S^{1/2}_{K,\mathrm{shot,DWS}} = \frac{4}{C_K}\sqrt{\frac{e}{2\Sigma_K \frac{U_{\mathrm{ADC}}}{R_{\mathrm{TIA}}}}}, \tag{10.8}$$

and the PM noise ($S^{1/2}_{I_{\mathrm{tot}}}$ describes the noise current produced by electronics and ADCs)

$$S^{1/2}_{K,\mathrm{PM,DWS}} = \frac{8 S^{1/2}_{I_{\mathrm{tot}}}}{2 C_K \Sigma_K \frac{U_{\mathrm{ADC}}}{R_{\mathrm{TIA}}}}. \tag{10.9}$$

The level of RIN at twice the heterodyne frequency is described by the power fluctuations over its mean power (at that frequency), expressed as an ASD called r, and contributes a phase error given by

$$S^{1/2}_{\gamma^{\mathrm{raw}},\mathrm{RIN}} = \sqrt{2} r \left|\sin\left(\gamma^{\mathrm{raw}}\right)\right|. \tag{10.10}$$

Here, γ^{raw} is the uncalibrated phase of the electrical current in units of radian (i.e. representing wavefront differences).

The coupling N_{SVN} of SVN to the phase readout is modeled by a linear combination of the corresponding sidebands with strengths k_i as described in section 10.1.7, adjusted and estimated for DWS given the available data:

$$\begin{aligned} N_{K,\gamma^{\mathrm{raw}},\mathrm{SVN}} = {} & \left(k_1 \sin(x_K) + k_2 \cos(x_K)\right) \sin(\gamma^{\mathrm{raw}}/2) \\ & + \left(k_3 \sin(2x_K) + k_4 \cos(2x_K)\right) \sin(\gamma^{\mathrm{raw}}). \end{aligned} \tag{10.11}$$

Note that the longitudinal measurements x_K that enter the equation above are used to approximate the unavailable quadrant phase data. We have to assume here that the beams are well-aligned and thus wavefront tilts cancel in the longitudinal channel combinations.

These sidebands have been estimated to be below $|k_i| < 40\,\mu\mathrm{rad}$ by the dedicated experiments discussed before. We call the resulting noise power $S_{K,\gamma^{\mathrm{raw}},\mathrm{SVN}}$.

The total noise model for each DWS channel is a combination that reflects the data processing with the calibration factors g_i (inverse of $\mathrm{rad_{el.}}/\mathrm{rad_{opt.}}$ from section 3.2).

10.2.2 Summary of the angular noise model

Similar to the longitudinal noise model, we add the different noises based on their correlation properties and scaling due to on-board processing (see section 3.2). Here it is important to use the "raw" phase measurements where applicable. If needed, they have been recalculated from the linear combinations in on-board processing.

Therefore, the total model for DWS in the X1 interferometer reads as

$$\begin{aligned} S_{\phi_1} &= g_1^2 \left(S_{\mathrm{X1,shot,DWS}} + S_{\mathrm{X1,PM,DWS}} \right) \\ &\quad + g_1^2 \left(S_{\phi_1^{\mathrm{raw}},\mathrm{RIN}} + S_{\mathrm{X1},\phi_1^{\mathrm{raw}},\mathrm{SVN}} \right), \end{aligned} \tag{10.12}$$

$$\begin{aligned} S_{\eta_1} &= g_2^2 \left(S_{\mathrm{X1,shot,DWS}} + S_{\mathrm{X1,PM,DWS}} \right) \\ &\quad + g_2^2 \left(S_{\eta_1^{\mathrm{raw}},\mathrm{RIN}} + S_{\mathrm{X1},\eta_1^{\mathrm{raw}},\mathrm{SVN}} \right). \end{aligned} \tag{10.13}$$

The model for the calibrated X12 DWS is slightly more convoluted due to the linear combinations:

$$\begin{aligned} S_{\phi_{12}} &= (g_3 - g_1)^2 \left(S_{\mathrm{X1,shot,DWS}} + S_{\mathrm{X1,PM,DWS}} \right) \\ &\quad + g_4^2 \left(S_{\mathrm{X12,shot,DWS}} + S_{\mathrm{X12,PM,DWS}} \right) \\ &\quad + \left((g_3 - g_1) S^{1/2}_{\phi_1^{\mathrm{raw}},\mathrm{RIN}} + g_4 S^{1/2}_{\phi_{12}^{\mathrm{raw}},\mathrm{RIN}} \right)^2 \\ &\quad + \left((g_3 - g_1) S^{1/2}_{\mathrm{X1},\phi_1^{\mathrm{raw}},\mathrm{SVN}} + g_4 S^{1/2}_{\mathrm{X1},\phi_{12}^{\mathrm{raw}},\mathrm{SVN}} \right)^2, \end{aligned} \tag{10.14}$$

$$\begin{aligned} S_{\eta_{12}} &= (g_5 - g_2)^2 \left(S_{\mathrm{X1,shot,DWS}} + S_{\mathrm{X1,PM,DWS}} \right) \\ &\quad + g_6^2 \left(S_{\mathrm{X12,shot,DWS}} + S_{\mathrm{X12,PM,DWS}} \right) \\ &\quad + \left((g_5 - g_2) S^{1/2}_{\eta_1^{\mathrm{raw}},\mathrm{RIN}} + g_6 S^{1/2}_{\eta_{12}^{\mathrm{raw}},\mathrm{RIN}} \right)^2 \\ &\quad + \left((g_5 - g_2) S^{1/2}_{\mathrm{X1},\eta_1^{\mathrm{raw}},\mathrm{SVN}} + g_6 S^{1/2}_{\mathrm{X1},\eta_{12}^{\mathrm{raw}},\mathrm{SVN}} \right)^2. \end{aligned} \tag{10.15}$$

Note that the RIN and SVN here is a correlated quantity, meaning that the $|\cdot|$ operator on the sine in equation (10.10) is dropped in the model for η_{12} and ϕ_{12}.

We include no thermally driven noise in DWS since we do not have independent investigations and modeling regarding its influence.

10.3 Indirect sensor noise contributions

10.3.1 Brownian noise

Brownian force noise is not a limiting noise of the sensor, but rather the cause of real, low frequency TM motion that is detected by the optical readout. It is the most relevant source of TM acceleration noise in the mHz to 100 mHz regime and thus becomes the dominant noise at the frequencies below roughly 60 mHz, where true TM motion is larger than sensing noise.

We include a simple model based on the estimation in [P5] with a residual white differential TM acceleration noise of $S_{\mathrm{B}}^{1/2} = (5.2 \pm 0.1)\,\mathrm{fm\,s^{-2}/\sqrt{Hz}}$ yielding an equivalent path length noise in early April 2016 (after integrating twice) of

$$S_{\mathrm{B,o12}}^{1/2} = \frac{S_{\mathrm{B}}^{1/2}}{(2\pi f)^2}. \tag{10.16}$$

The level of $S_{\mathrm{B}}^{1/2}$ decreased throughout the mission [P6].

We note that this displacement noise is calculated at frequencies where control forces are not relevant.

For DWS, the TM torque noise is not solely dominated by the corresponding Brownian torque noise (which can be propagated from Δg by following [72]) and is therefore not included here due to the more complex control forces as analyzed in [P17].

10.3.2 Angular and lateral motion cross-coupling (TTL noise)

The angular and lateral motion of the three bodies (TMs and SC) involved in the X1 and X12 interferometric readouts can leak into the longitudinal measurements through misalignments between the TMs and the optical system. We often refer to this noise as TTL coupling [73].

Since the motion of the SC can always be interpreted as TM motion with respect to the SC, we can describe this leakage by the effect of TM motion on the beam path only: In the case of angular jitter of either of the TMs, the measurement beam tilts due to the reflection at the respective TM. A rotation of the TM around an arbitrary point of rotation additionally moves the TM surface in or out of the beam path. Lateral TM jitter, i.e., motion along its y- or z-axis (see coordinate system in figure 3.7), couples into the interferometric readout via static angular misalignments of the TMs with respect to the optical system. A lateral shift of a tilted TM moves its reflective surface in or out of the measurement beam path, de- or increasing its path length.

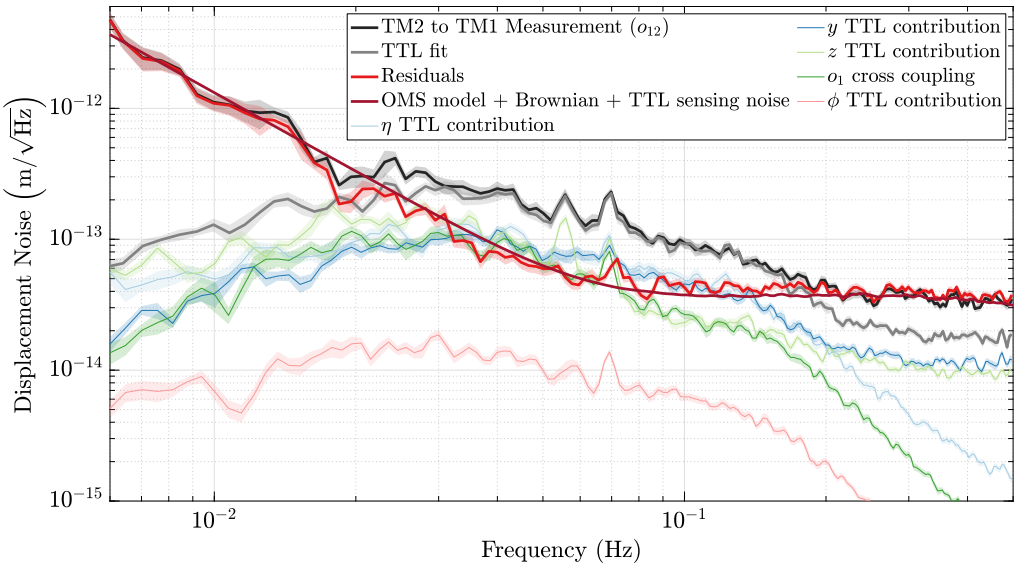

Figure 10.4 The measurement data of a nominal run (same as figure 11.1), corrected for the TTL contributions using a frequency domain fit. After the subtraction, it becomes evident that the noise level of the corrected o_{12} extends down to approximately 90 mHz. Due to the subtraction, sensing noise from multiple degrees of freedom is added to the model estimate as visible at higher frequencies in the red curves. Note that only 1 Hz data was available for y, z such that a downsampling filter reduces the visibility of the additional noise. The raising spectral shape towards lower frequencies is consistent with the measured TM displacement due to Brownian force noise. Reprint from [P3].

In both cases, the reference beam remains unchanged under this motion. Therefore, the TM motion yields an altered optical path length difference, relative angle, and relative beam offset in the X1 interferometer for X1 motion and the X12 interferometer for motions of both TMs. All these effects will change the longitudinal readout.

Changes in the relative angle due to TM angular jitter are additionally visible in DWS of the respective interferometers. However, we expect the angular motion of the SC to cancel in the X12 DWS readout due to the nearly free-fall of the TMs: The angular jitter of the SC can be interpreted as a rotation of both test masses around the center of mass of the SC by the negative SC angle. Therefore, the beam tilts due to the reflection at both TMs. Since the tilt of the second TM affects the beam inversely compared to the first TM, the beam tilt is compensated by its reflection at TM2.

During the LPF mission, TTL noise has been reduced via realignments of the TMs. In particular, rotations to new nominal positions have reduced or counteracted TTL noise contributions [P8]. The residual noise has been minimized by fitting and subtracting a linear model in post-processing [P21, P30, 74, 75].

In most of the results presented here (such as figure 9.2), this coupling is not subtracted

and is often visible as a "bump" of noise between (20 to 200) mHz. Figure 10.4 shows an example of the sensing noise after the subtraction of this effect. It has been modeled similar to the description in [P21, P30]. Here, however, we applied a fit in the displacement domain instead of acceleration, the latter used to be the nominal method during the mission. The model uses a linear combination of translational and rotational displacement estimates of the SC and corresponding coupling coefficients. We also add a cross-coupling term for o_1 that describes the amount of remaining common-mode translational jitter in o_{12} due to imperfections in the set-up.

The fit model reads

$$S_{\mathrm{TTL}} = a_{o_1} o_1 + a_\phi \bar{\phi} + a_\eta \bar{\eta} + a_y \bar{y} + a_z \bar{z}, \tag{10.17}$$

with the SC variables ϕ, η, y, z describing the motion relative to the differential TM measurement, calculated from the (detrended) TM1 and TM2 readouts, e.g. $\bar{\phi} = (\phi_2 + \phi_1)/2$, and the coupling coefficiencts a_i.

The fit has been performed in the frequency domain using an iteratively reweighted least squares method in the range (22 to 100) mHz, avoiding the influence of frequency noise, and overlapping Blackman-Harris 92 windows with 24 averages.

Our fit result is consistent with the value given in [P21], Table 1, for $\delta_{\mathrm{ifo},2}$ matching a_{o_1} for this time of the mission.

The capacitive sensors provide the y and z measurements; hence their higher sensing noise increases the noise level in the data that has TTL contributions subtracted. Our ability to estimate this additional sensing noise is limited, however, and based on the fit result at high frequencies, which is filtered due to the on-board downsampling to 1 Hz. With higher sampled data available, the SC contributions could be lowpass filtered to reduce the additional noise towards higher frequencies where the TTL contribution is not limiting.

We do not attribute the TTL noise to the sensor itself since it does not depend on properties like beam characteristics or the measurement chain but can be described independently by SC motion. Subtracting it also adds sensing noise of the measurements of the contributing degrees of freedom. Further, not all the data channels needed for the subtraction were always available with a sampling frequency of 10 Hz. For these reasons, TTL has not been included in the OMS noise model in general.

Further details of the treatment of TTL in LPF can be found in [P21, P30, 74]. For a detailed analysis of sources and physical origins we refer to [P30, 76].

Chapter 11
Sensitivity analysis

In this chapter we discuss the OMS in-orbit behavior in terms of its sensitivity and reliability in more detail. We show the performance under different operating conditions and also present our understanding of the contributing noise terms for both the longitudinal and the angular measurements.

We find that, at different frequencies, different noise sources dominate. At 20 mHz and below, the overall noise is dominated by Brownian force noise, leading to genuine differential displacement noise between the TMs, as was shown in [P5, P6]. Therefore, a comparison of the performance with the requirement is not directly possible, since OMS noise is not limiting in the (1 to 30) mHz band. A very conservative comparison of the total noise at this frequency with the requirement shows that the OMS performed at very least a factor of 20 and up to a factor of 280 better than required.

Only above 200 mHz OMS noise dominates the observed displacement noise. The most significant OMS noise sources are PM noise, laser frequency noise, shot-noise, and RIN. For nominal operations, the first two were the main contributors, while shot-noise and RIN were not limiting.

The focus lies on the calibrated TM readouts of the X1 and X12 interferometer, which are computed in-flight during the mission. They provide the angular and longitudinal TM readouts. Their sensitivity can be best modeled using data from all four interferometers. However, not all data were available for ground analysis, as many computations were solely performed on-board (as described in section 3.2). There is, for example, no continuous full set of individual QPD data, which limits the modeling accuracy.

11.1 Testing and validation of the sensing model

The performance observed during flight can be considered under various conditions that correspond to high, intermediate and low contrast. They give rise to different total noise levels in the X12 interferometer, both in terms of the longitudinal readout and the DWS signals. In the following, the same model of the underlying noise sources is used and shows good agreement with the measured noise.

The first condition (shown in sections 11.1.1 and 11.1.2) is where the alignment of the TMs is optimal. This condition is achieved in the nominal science mode. There, TM1 is in free-fall along the sensitive x-axis and TM2 is controlled to follow it in this degree of freedom. The angular orientation along ϕ and η of both TMs is controlled using the DWS signals. By choosing an appropriate working point of the DFACS controller the relative phase o_{12} of the X12 and reference interferometers is kept close to zero. In this condition, the extremely low noise of the X12 interferometer means that motion of the TM dominates any measurement below approximately 20 mHz. At higher frequencies, the measurement of the relative position of the two TMs is limited by the sensing noise in the X12 interferometer, which is dominated by a combination of RIN coupling at $2 \times f_{\mathrm{het}}$, ADC quantization noise, and frequency noise.

The second condition (shown in sections 11.1.3 and 11.1.4) corresponds to a medium-level contrast which was achieved by deliberately misaligning the TMs or by reducing one of the beam powers. Some of the noise contributions depend on the contrast. This gives us the possibility of examining the sensitivity of an interferometer as a function of contrast, and therefore of validating the intrinsic noise levels discussed above. Since the RIN (and SVN) coupling to o_{12} does not depend on the contrast but rather only on the TM position it is possible to disentangle contributions of correlated and uncorrelated noise sources.

The RIN level can also be characterized by DWS readout, where an corresponding formula depends on TM angle, rather than longitudinal position. This is further investigated in chapter 13.

The third condition under which we can study the interferometer performance is when the TMs are both mechanically grabbed (shown in section 11.1.5). In this condition, the relative motion of the two TMs is restricted to that induced by thermo-mechanical fluctuations of the grabbing fingers that hold the TMs. In addition, the alignment of the two TMs (both in attitude and longitudinally) is far from optimal, with tens of micrometer and hundreds of microradian offsets. This non-optimal alignment results in two effects: a non-zero phase offset between the X12 and reference interferometers, and a very low contrast (due to misalignment of the measurement beam's wavefront with respect to the fixed wavefront of the reference beam).

11.1.1 Noise budget under nominal conditions

Figure 11.1 shows an o_{12} measurement in nominal configuration. The noise contributions are estimated according to the noise model and show good agreement with the measurement.

Our model explains the measured noise density between (0.2 to 5) Hz. As expectecd, the measured noise is increased between (20 to 200) mHz due to TTL coupling. We find that PM noise (and within that, the ADC noise) is the dominating term in this condition.

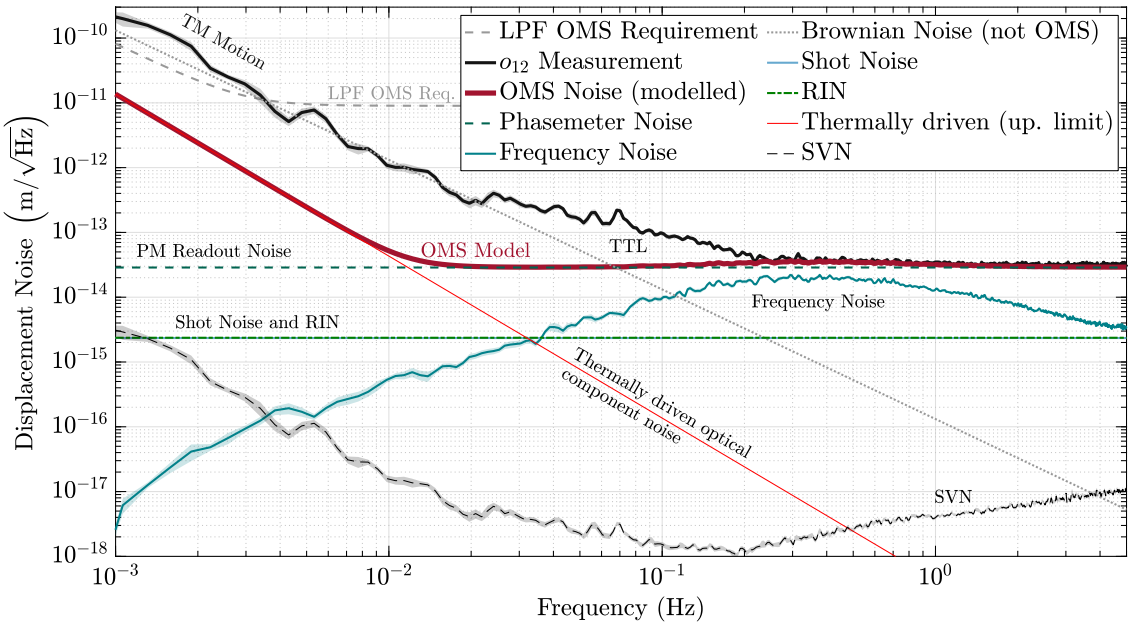

Figure 11.1 Noise model applied to an o_{12} measurement from June 1st 2016 between 18:46 UTC and 20:29 UTC in nominal configuration. Shown is the ASD computed with the same LPSD algorithm as in figure 9.2. Reprint from [P3].

This is one of the few occasions when the frequency interferometer data were transmitted to ground with 10 Hz sampling. Frequency noise causes the spectrum to increase slightly between (0.15 to 2) Hz. RIN and SVN coupling is highly suppressed due to the controlled TM position.

Below 20 mHz TM motion caused by Brownian force noise is detected. The estimate is based on the Δg measurement of April 2016 [P6]. We find that the reference interferometer has almost the same noise levels in shot and PM noise. This is expected due to its very similar design and parameters. Since the reference interferometer is subtracted, its noise adds to the combined readout o_{12}.

Figure 11.2 shows the sensitivity for DWS by example of η_1 for the same time-span as the nominal o_{12} budget plot given above. The noise model includes the described noise sources, using the appropriate coupling factors for DWS signals. We find that the noise model has slightly larger deviations from the measurements in DWS compared to the longitudinal o_{12} data. This will also become visible later in figure 12.5.

We note that η_1 is an in-loop measurement of the DFACS with a unity gain frequency of around 1 mHz. Between (0.001 to 1) Hz, the spectral shape results from a combination of angular noise from the star tracker, torque noise on TM1, capacitive sensing and SC force noise, as analyzed in [P17], and therefore in a larger band compared to o_{12}. The influence of the OMS is observed in the quasi flat sensing noise floor above 1 Hz only.

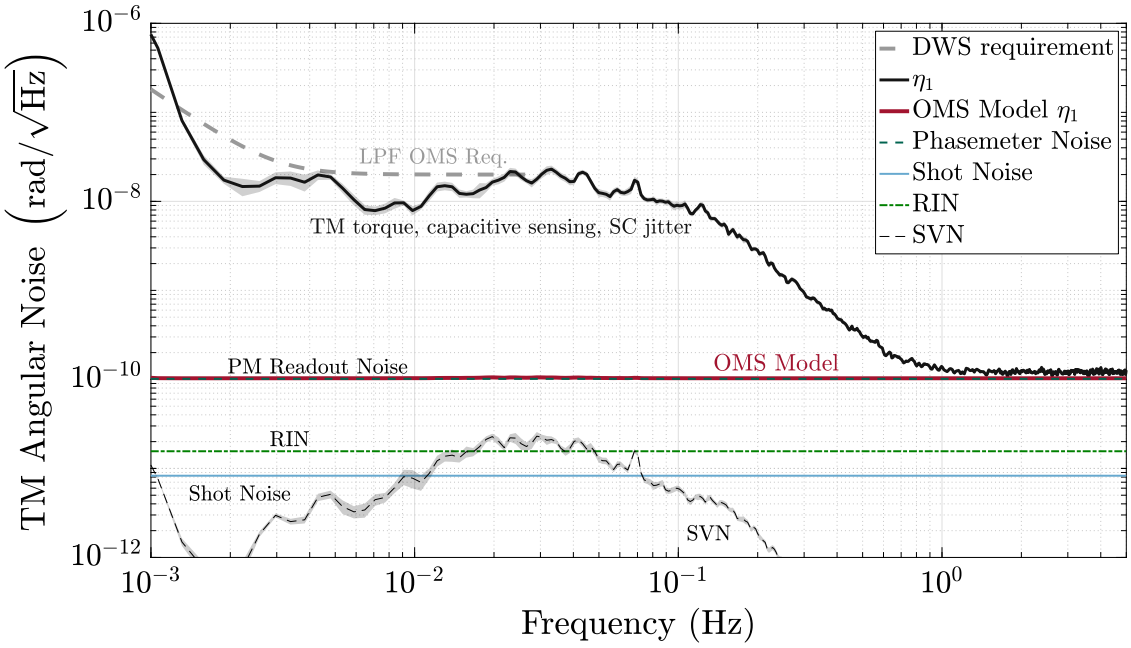

Figure 11.2 Noise model and measurement of the η_1 DWS channel (see text, same time as figure 11.1). Reprint from [P3].

11.1.2 Noise budget for o_{12} during a period of increased laser frequency noise

As explained in section 10.1.1, we observed periods of increased laser frequency fluctuations during the LPF operations. A detailed analysis is given in [66].

We show one example of the OMS noise model under these circumstances in figure 11.3. During these periods, laser frequency noise becomes the dominating noise source in the o_{12} measurement in the frequency range from approximately (0.1 to 1.5) Hz.

The model has been applied to the shown o_{12} measurement from January 2017. This measurement is comparable to figure 11.1. Please note that the SVN is not shown, since it is estimated to be below $1 \times 10^{-17}\,\mathrm{m}/\sqrt{\mathrm{Hz}}$.

As anticipated in section 10.1.1, this plot makes use of the path length mismatch $\Delta L_{12} - \Delta L_R \approx 329\,\mu\mathrm{m}$, resulting from a dedicated experiment [66] and designated analysis by S. Paczkowski.

This supports the previously stated hypothesis that the two levels of noise in o_{12} observed over the course of the mission (clearly visible in chapter 12), are indeed due to an increase in laser frequency noise.

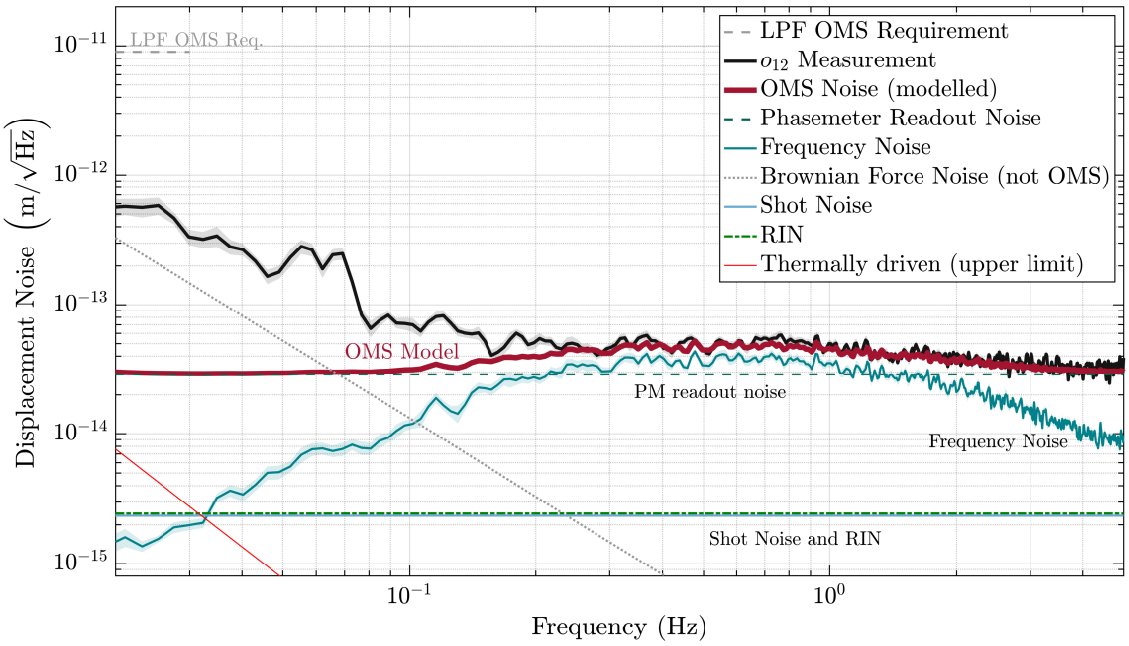

Figure 11.3 Noise model during a period of increased frequency noise (zoom-in). Reprint from [P3].

Unfortunately, this verification could only be done for the first noise runs since in the subsequent noise measurements the laser frequency noise was either not telemetered at 10 Hz or no period of increased noise was occurring in the respective noise run. However, we have found no reason to assume a different behavior at other times, given that we continue to observe periods of increased noise in the two channels at the same time over the course of the mission, and the 1 Hz data indicates an increased spectral noise power.

This contribution is also visible in the noise budget fit for the whole mission in chapter 12.

11.1.3 Noise behaviour at intermediate contrasts

The data in figure 11.4 originates from an experiment in which both TMs were commanded to a range of angular tilts, which resulted in an overall reduced contrast due to imperfectly aligned wavefronts. This experiment (2017-02-06 23:06:00 UTC – 2017-02-08 22:55:00 UTC) is explained in detail in chapter 13.

We selected stable timespans during which the measured noise floor has a flatness comparable to actual white noise. The resulting noise floor in o_{12} is estimated from a frequency average in the pseudo-flat band (1.2 to 2.8) Hz (from PSD) and plotted over the X12 contrast.

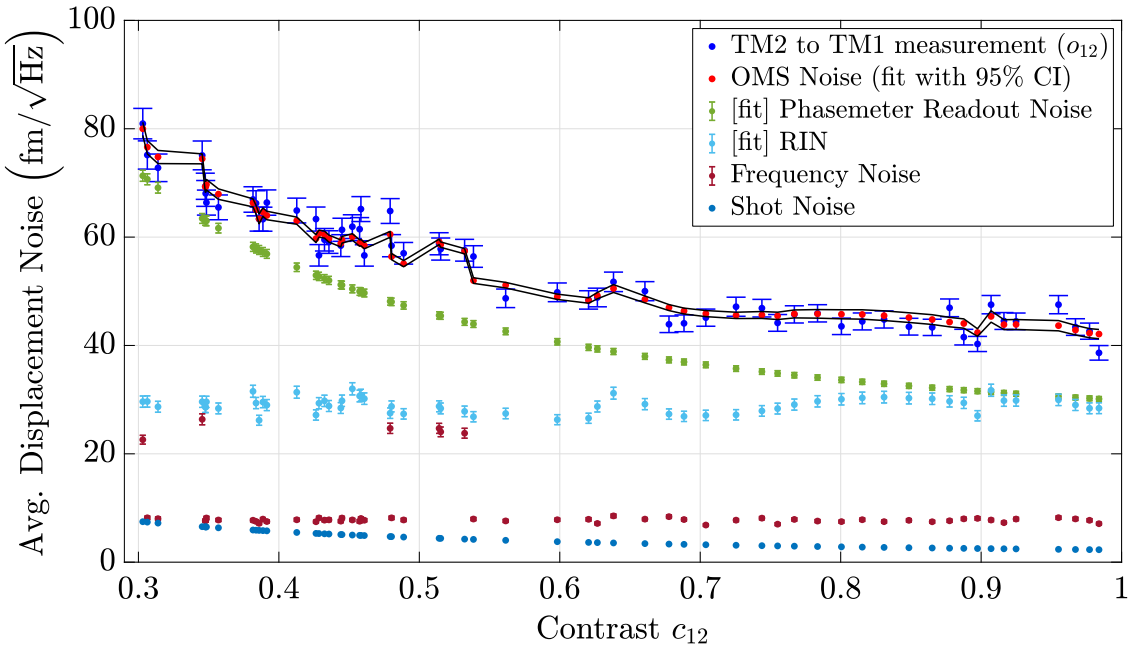

Figure 11.4 Noise model at intermediate contrasts. For this figure we fitted the noise model as stated in [P2] to an o_{12} measurement between (1.2 to 2.8) Hz with two free parameters (levels of RIN and ADC noise). Reprint from [P3].

The TM orientation also affects the RIN coupling effect to o_{12}, because a geometric piston couples TM tilt into the longitudinal path measurement of the X12 interferometer, causing the RIN coupling to vary depending on the piston crosstalk strength. The piston arises when the TM angles are controlled to certain offsets, because the rotation has its origin in the center of mass of the TM (and not at the point of reflection). This is visible in the fluctuations of the light blue RIN contribution in figure 11.4.

We can see the influence of the contrast on shot and PM noise and the variation of the two frequency noise states, whereas RIN is only coupling via the longitudinal phase offset. In this condition, RIN becomes important at high contrasts because of the phase offset and geometric piston.

The RIN value is estimated from a fit to the data and varies between this and other experiments. We also get different results depending of the type of experiment, which is still not completely understood, see chapter 14. However, the variations are small enough such that our estimates given here are sufficient to explain the good performance within requirements.

We also fit the equivalent noise current introduced by the ADC, which is likely to vary slightly compared to the ground estimate from years ago. The fit result confirms this by deviating only by about 5 %. It yields RIN $r = (2.59 \pm 0.09) \times 10^{-6}\,\sqrt{\mathrm{Hz}}$ and ADC

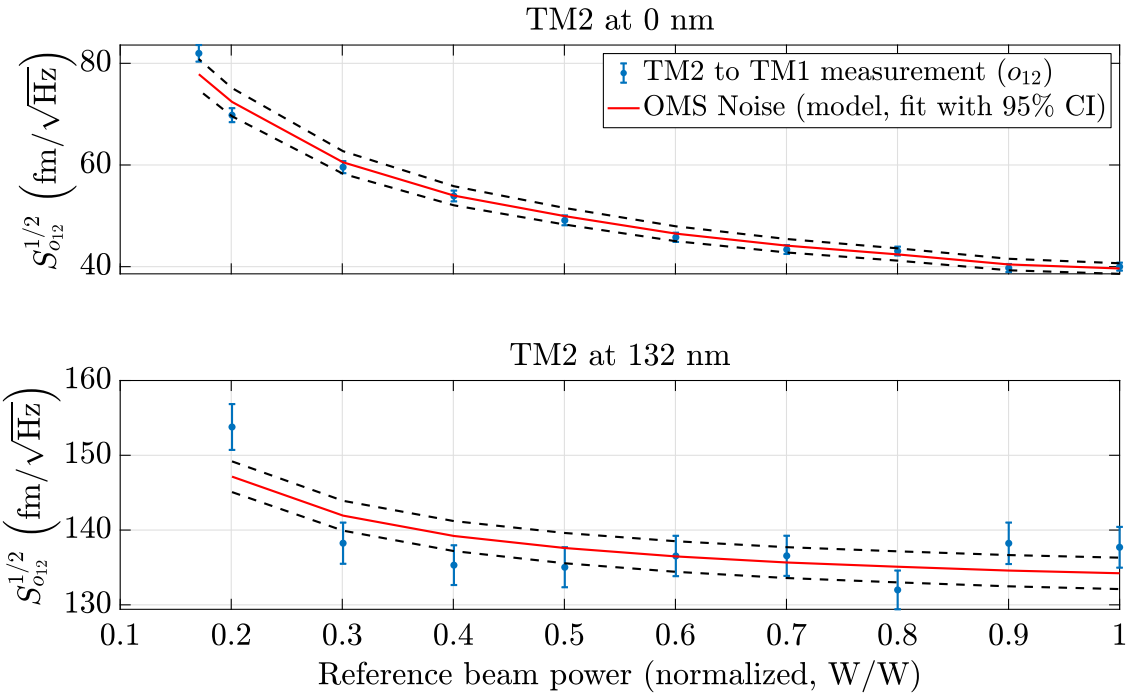

Figure 11.5 Noise behavior for varying beam powers. Top panel: The reference beam power was decreased stepwise, thus lowering the contrast. Bottom panel: Directly after lowering the reference beam power, the second TM was moved to a new (constant) position with maximal 2f-RIN coupling, and the power was increased again with the same steps in reverse. Reprint from [P3].

$S_{I_{\text{ADC}}}^{1/2} = (108.0 \pm 1.6) \times 10^{-12}\,\text{pA}/\sqrt{\text{Hz}}$. The SVN contribution is not shown, because it reaches only sub-femtometer level.

Overall, we find good agreement between the model and measurement. It explains the observed behavior for contrasts between (30 to 98) % in the X12 interferometer. Note that the contrast in the reference interferometer remained unchanged.

11.1.4 Noise behavior for varying beam powers

We also investigated the effect of unequal powers between the measurement and reference beam. Instead of changing the wavefront overlap due to TM tilts, this also lowers the strength of the heterodyne signal and thus the contrast.

The experiment (2017-06-17 08:20:00 UTC – 2017-06-17 15:00:00 UTC) consisted of stepwise reduction on the reference beam power via the power stabilization loop set-points. After reaching the lowest power, TM2 was shifted via electrostatic actuation to an 132 nm offset, increasing correlated noise sources.

Compared to section 11.1.3, this experiment also changes the noise couplings in the fixed interferometers regarding power and contrast dependent noise sources.

Figure 11.5 shows the results for the noise measurements and the model at the two TM positions. As expected, the noise increases towards lower powers due to the $1/C$ dependence. Similarly, at the offset, RIN maximizes its effect and thus exacerbates the sensitivity to above $150\,\mathrm{fm}/\sqrt{\mathrm{Hz}}$.

As in figure 11.4 we fit both the ADC noise and the RIN level using the same model from section 10.1. While the ADC yields compatible results, the RIN estimate is almost 60 % lower, yet still within sensible ranges compared to ground measurements. We applied a fit to the total data (all set-points combined) with both RIN and ADC noise contributions as free parameters. The coefficients yield RIN $r = (1.08 \pm 0.01) \times 10^{-6}\,\sqrt{\mathrm{Hz}}$ and ADC $S_{I_{\mathrm{ADC}}}^{1/2} = (110.4 \pm 2.6) \times 10^{-12}\,\mathrm{pA}/\sqrt{\mathrm{Hz}}$ and are within our previously assumed limits [P2]. In the first panel, ADC noise is dominant, while at the 132 nm offset in the second panel RIN is the major contributor.

One outlier at the lowest power has been removed, which showed particularly high and unexplained noise compared to the rest of the data. We suspect nonlinearities in the power stabilization and thermal effects causing that.

In conclusion, our model explains the observed noise behavior for two of the main parameters of the optical system – the contrast and the power ratio of the two beams for a wide parameter range.

11.1.5 Noise budget with grabbed TMs and very low contrast

In April 2017 both TMs were mechanically grabbed. The two longitudinal measurements o_1 and o_{12} and their corresponding noise models are shown in figures 11.6 and 11.7. DWS is presented in figure 11.8.

The grabbed case corresponds to a very low contrast of 0.6 % in X12 and 2 % in X1, while the contrast in the reference interferometer remains unchanged. During this measurement period, an upper limit for the RIN level of $r \approx 3 \times 10^{-6}\,\sqrt{\mathrm{Hz}}$ was estimated.

The contribution of laser frequency noise is also shown as an upper limit. This limit (by S. Paczkowski) stems from an experiment to characterize the laser frequency control loop which was executed rather shortly before this noise measurement.

In this condition the model reproduces the measured PSD down to mHz frequencies, even with very low contrast, for the longitudinal measurements. As expected while being grabbed, no TTL coupling or Brownian force noise is visible. As previously, the PM noise is dominating. The thermally driven noise, as visible at low frequencies in figures 11.6 and 11.7, suggests that the upper limit stated in [P2] and applied here is too conservative below 3 mHz. This implies that the temperature effects of the window transmission, the

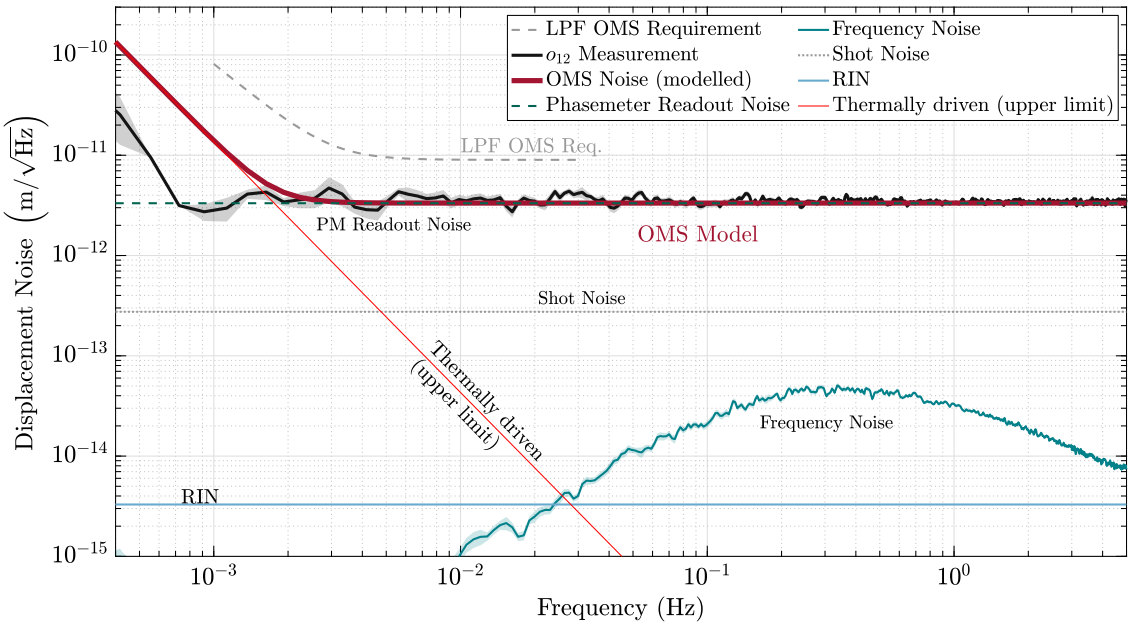

Figure 11.6 Noise model applied to an o_{12} measurement with grabbed TMs starting from 2017-04-08 19:55:00 UTC and lasting for 2 hours. Note that the SVN is not visible, since it is around $1 \times 10^{-16}\,\mathrm{m}/\sqrt{\mathrm{Hz}}$. For the RIN and laser frequency noise contribution, only an upper limit could be estimated. Reprint from [P3].

expansion of the Zerodur baseplate, or the thermal impact of the beamsplitters are less significant. Another probable explanation is the presence of common-mode rejection for the balanced beam paths. We previously excluded common-mode effects to obtain an upper limit for these thermally driven effects.

Also note that the data during the grabbed TMs case was recorded during a low temperature period (SC cooling) of about 11.5 °C on the OB.

These cases support our understanding of the sensing noise model, being nominally only visible at high frequencies, extending down to the mHz range.

The peak in o_1 around 70 mHz was already observed and discussed in figure 9.2 and section 9.2. In principle, due to grabbing, one would expect the platform jitter (and thus the peak) to be common mode and thus suppressed. Comparing with figure 9.3 we find that the peak is indeed reduced. However, we observe a drift of a few nm between TM1 and the SC, showing that the mechanical grabbing is not perfectly stable. Therefore, some residual coupling seems plausible. The same may hold true for o_{12}, where the differential mode further minimizes the coupling so that it becomes invisible.

These measurements indicate that the sensing noise floor can be well explained in all observable circumstances for both low and high contrasts and the full measurement band.

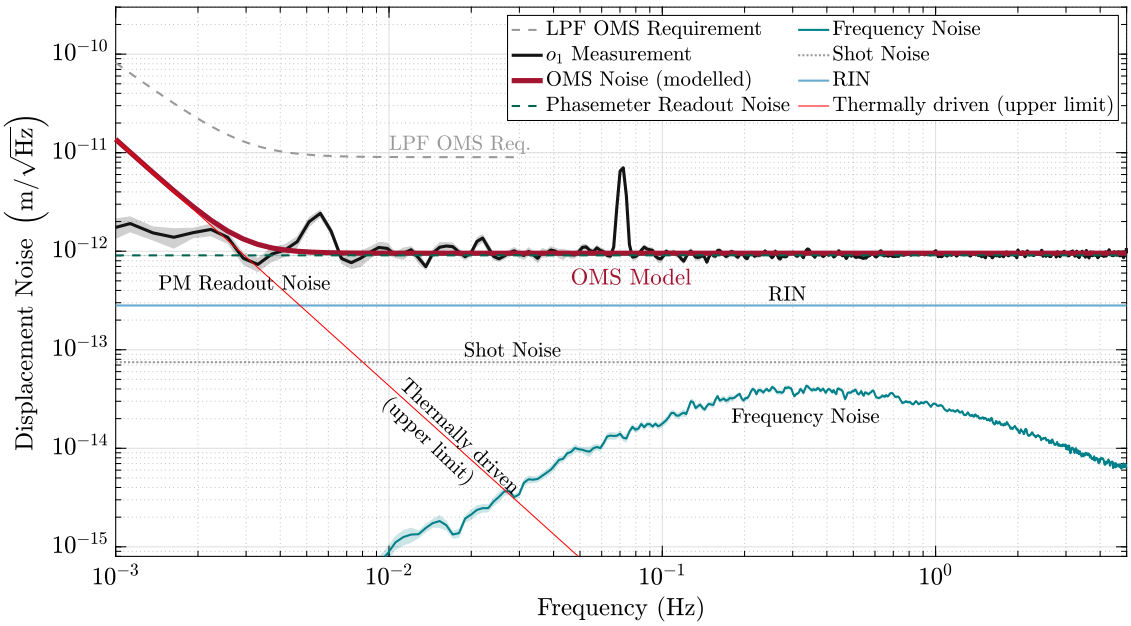

Figure 11.7 Noise model applied to an o_1 measurement with grabbed TMs. This data is recorded at the same time as the data shown in figure 11.6. Due to X1 interferometer data measuring a different TM offset and contrast, the shot-noise, RIN and frequency noise contributions differ to those of figure 11.6. However, the RIN and laser frequency noise contribution is only provided as an upper limit. Note that the SVN is not visible, since it is well below $1 \times 10^{-15}\,\mathrm{m}/\sqrt{\mathrm{Hz}}$. Reprint from [P3].

We observed variations from roughly $32\,\mathrm{fm}/\sqrt{\mathrm{Hz}}$ above 1 Hz for high contrast to $3\,\mathrm{pm}/\sqrt{\mathrm{Hz}}$ at 1 mHz for very low contrast (details see above).

For DWS, see figure 11.8, the model underestimates the noise in ϕ_{12} significantly, while still somewhat matching most of the other channels.

This data is recorded at the same time as the data shown in figures 11.6 and 11.7. We observe that the noise level is pseudo-flat in all cases down to low frequencies, but has higher magnitude for the differential angles due to the much lower contrast.

While the noise model works reasonably well for the X1 interferometer angles (yielding almost identical levels), this is not the case for the X12 interferometer angles (also almost identical levels). Especially the ϕ_{12} channel is deviating by about a factor 2 from the model. We do not know the reason for this behavior. However, we note that the model still seems to work relatively well with such low contrast that should result in questionable signal quality.

Overall, we conclude that the noise model reflects the observed behavior at frequencies where the sensing noise is expected to be limiting for most of the nominal flight operations.

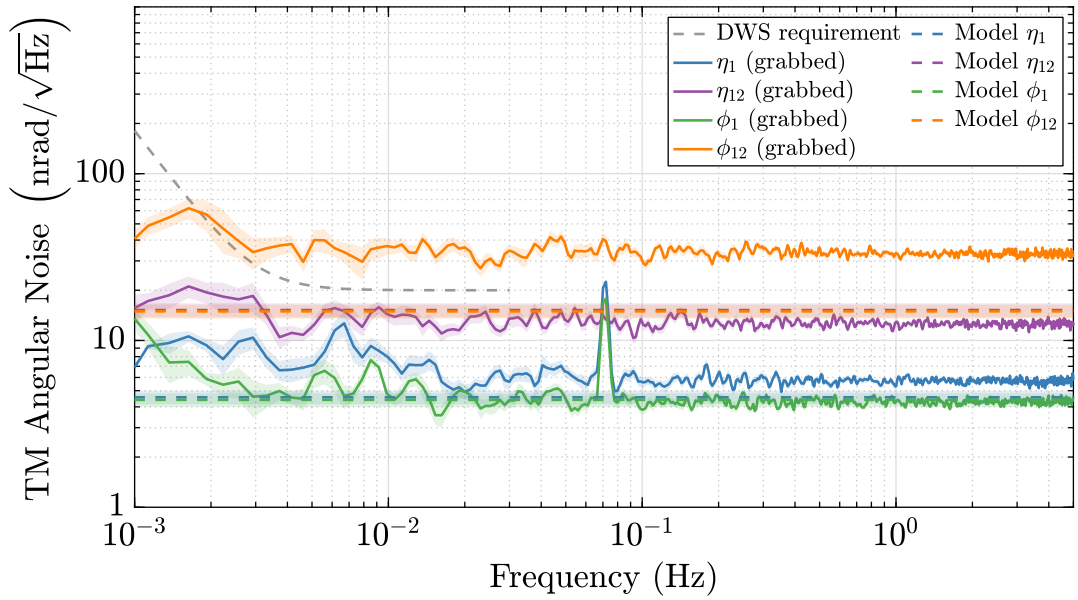

Figure 11.8 Noise model applied to DWS with grabbed TMs. Reprint from [P3].

11.1.6 Noise behavior below 1 mHz

In the nominal conditions, white Brownian force noise is dominating at mHz frequencies, with other sources of TM acceleration noise becoming dominant at even lower frequencies [P6]. Even with grabbed TMs, at frequencies $< 1\,\mathrm{mHz}$, thermo-mechanical induced motions of the structure holding the TMs is likely dominating the measurement, see also [69].

We have no indication of additional interferometer noise sources, nor of any deterioration of the performance at frequencies below 1 mHz, but we cannot completely exclude them. Based on figure 11.6 we report that even with grabbed TM we reach a sensitivity of approximately $3\,\mathrm{pm}/\sqrt{\mathrm{Hz}}$ at frequencies just below 1 mHz, which would already enable the local TM interferometry on LISA.

11.2 Limitations of the sensing noise model

Even though the model explains the observed behavior to a good degree, limitations arise mainly due to the fact that LPF, having only a limited telemetry budget, cannot provide all measurements at all times and not at the rate and resolution needed to further improve the model, as well as the fact that we measure a strong real signal at low frequencies (by design).

The physical noises are all well known contributions that depend on parameters such as contrasts and beam powers, some of which are only known after additional processing took place. For example, individual QPD data was not transmitted to ground, but just averaged channels over interferometer output ports and their quadrants. A more exact model using individual quadrant contributions is therefore unavailable.

In the high frequency range, we are likely affected by aliasing. The processing used aboard LPF employs moving average filters before decimation, which have a limited anti-alias capability. Thus, we do not always measure the flat spectrum that we understand well and the amount of aliasing cannot be assessed. In addition, we can only extrapolate the noise spectrum for frequencies below about 200 mHz and have to rely on measurements taken with grabbed TMs to indicate the correctness of the model during these relatively high noise states.

Furthermore, measurements of the frequency and reference interferometer at 10 Hz are not available for most of the noise runs, thus rendering estimation of frequency noise and SVN difficult, especially since we cannot differentiate the latter from RIN for most of the mission. At the same time, the actuator noise of the OPD is not measured independently at high frequencies, which is known to affect the spectra.

We also neglect losses arising from realistic beam combiners that are not exactly 50/50 such that the balanced detection will not be ideal.

The estimation of RIN at kHz frequencies is difficult and its level has been estimated to vary throughout the mission. This is likely due to changes in the environmental conditions and can only be observed indirectly. We have only a few more specific indirect RIN measurements that are subject to ongoing analysis.

In addition, we have a large (and difficult to estimate) uncertainty on the ADC noise contribution, which is the dominating noise term in many conditions.

Chapter 12
Long-term mission analysis

This part addresses the measurements over the course of the mission for periods where the SC was operated in nominal science mode and only noise was measured. The main results of the long-term OMS sensitivity analysis are shown in figure 12.1, including both longitudinal and angular readouts.

12.1 Data selection and analysis

We selected times during the mission where the SC was kept in nominal operating mode without (known) interfering actions. This excludes commissioning activities, experiments and spacecraft maintenance, DRS (NASA) operations and the spacecraft cooling towards the end of the mission. In a second filtering step, we split the data into 12 min long stretches and discarded segments that include glitches or transients and do not allow a stationary noise power spectrum estimation. The algorithm to filter these transients has a threshold on the amplitude change, i.e., the first derivative in time domain. We used the Median Absolute Deviation (MAD) estimator to specify an equivalent 5σ threshold [77]. From the initial 12916 segments, 140 have been discarded in o_{12} (1.1 %), 283 in η_1 (2.2 %), 112 in η_{12}, (0.9 %), 381 in ϕ_1 (2.9 %) and 331 in ϕ_{12} (2.6 %). We report that even in the presence of short-time non-stationarities the sensitivity was below $2\,\mathrm{pm}/\sqrt{\mathrm{Hz}}$ at high frequencies in the worst case (not shown here, including even more noise only measurements in different configurations). The selected and filtered times are listed in table D.1. For more information on non-stationarities and glitches during the mission see [P13, P29, 78].

Every data point in the long-term plots corresponds to those 12 min of noise measurements sampled with 10 Hz and averaged over the pseudo-flat frequency band between (1.2 to 2.8) Hz. This band has been chosen because we expect the measurement to be sensor noise limited here.

For each of the 12 minute segments the ASD is calculated using 50 % overlapping Blackmann-Harris-92 (BH92) windows with 36 averages. Every 4th bin is kept to avoid correlations between neighboring bins [79]. At 2 Hz the center bin and two surrounding bins are masked to remove the influence of on-board 1 Hz harmonics as described above.

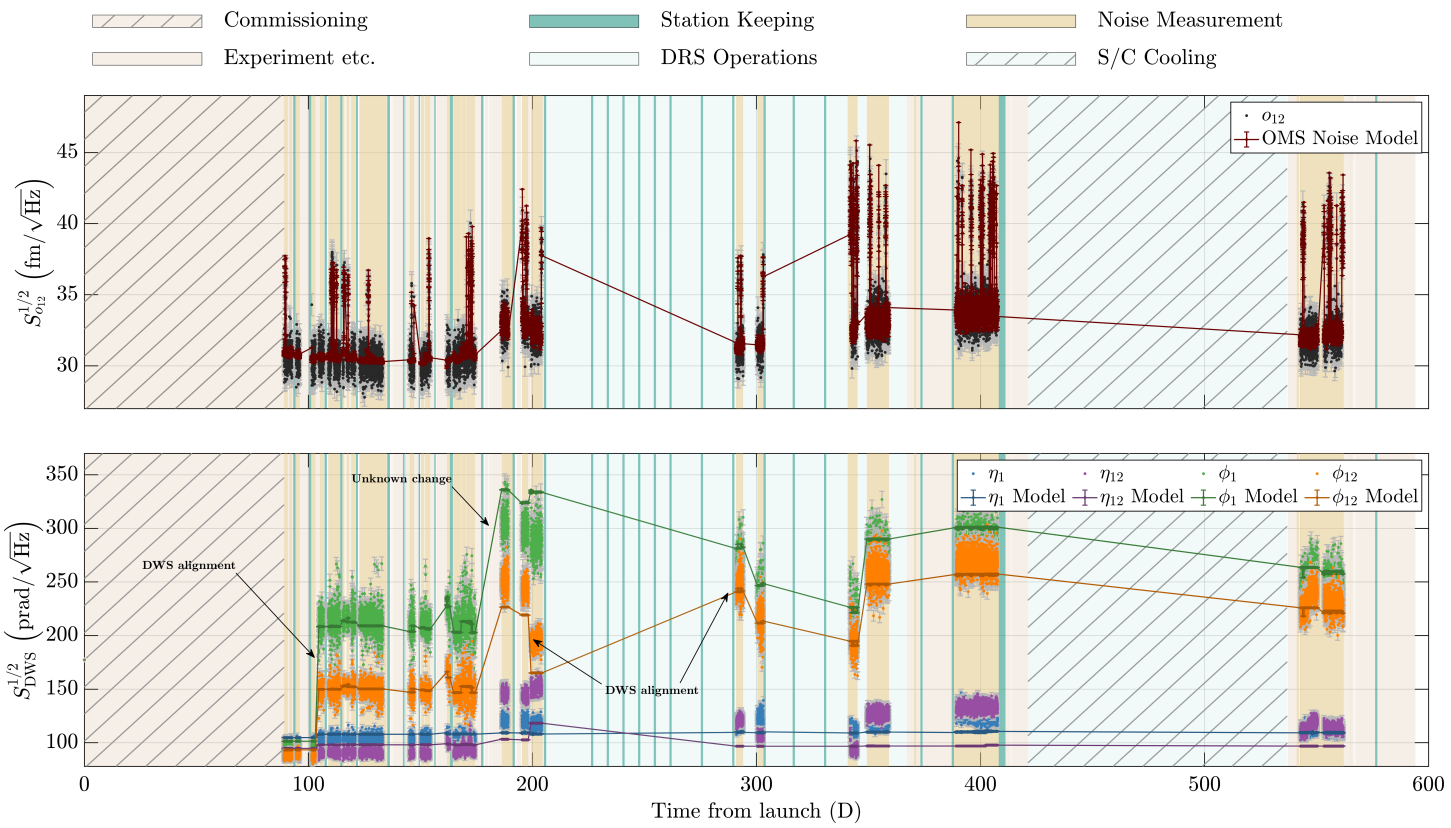

Figure 12.1 OMS sensor noise over the mission duration. Upper panel: longitudinal readout o_{12}. Lower panel: DWS channels, measuring the angular TM orientations (blue: η_1; purple: η_{12}; green: ϕ_1; orange: ϕ_{12}). The noise model estimates have solid lines, and have been fitted jointly across all channels using the model described in section 10.1 with two fit parameters per segment describing the amount of frequency noise coupling and the RIN level, for both of which we do not have independent measurements available. The solid lines increase visibility, but the model was only evaluated for the given noise data. Reprint from [P3].

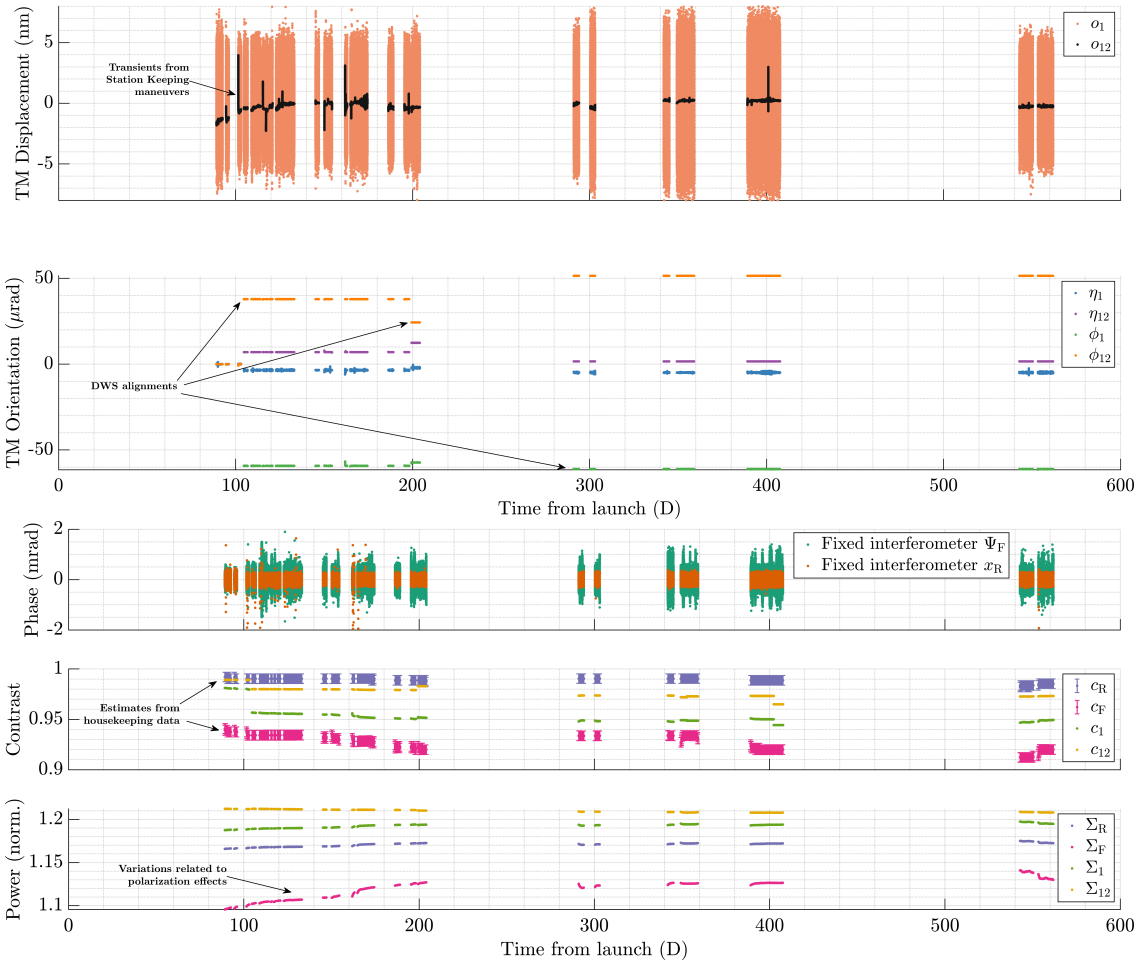

Figure 12.2 Main OMS sensor contributions to the noise model. Reprint from [P3].

However, this noise floor may be overestimated due to an imperfect anti-aliasing caused by the moving average filters used in-flight. Therefore we treat this estimation as an upper bound of the real sensor noise, as there was no access to continuous data with a higher sampling rate.

12.2 Long-term noise fit

Figure 12.1 not only shows the measured and averaged sensitivity of the OMS for the selected noise runs, but also the noise predictions by our models.

They use the data from figure 12.2. Here, the top five panels show the time series data for the relevant model contributors (first panel: longitudinal x measurements; second: DWS

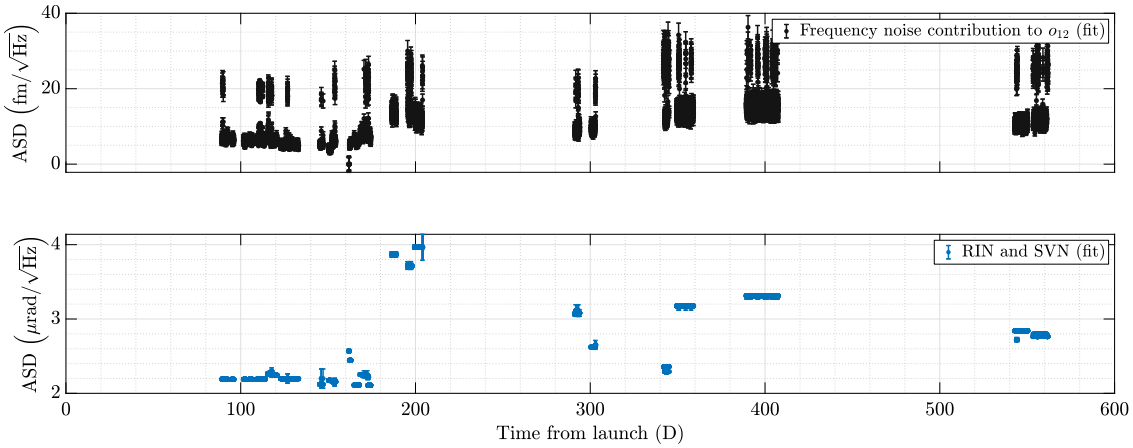

Figure 12.3 The two panels show the joint fit results for the two uncorrelated fit parameters from figure 12.1. Reprint from [P3].

measurements scaled to TM rotations; third: Reference and Frequency interferometers; fourth: contrast estimates; fifth: normalized beam powers per interferometer). For this plot the measured data channels are sampled with 1 Hz, except for the XF and XR contrast, which is estimated from ADC housekeeping data (reason for higher contrast in c_{R} than stated in [P2]). In o_{12}, remaining slow transients from necessary SC station keeping maneuvers are visible, during which the TMs were fixed by electrostatic actuation. In DWS the TMs alignments to suppress TTL noise are visible. The power measurements show variations especially in the frequency interferometer. This has mostly been explained with the presence of undesired P-polarization in the measurement beam due to a wet-dry shift in the polarizing BS within the fiber couplers [80].

As mentioned before, we fit the RIN value and the frequency noise contribution as shown in figure 12.3, the latter based on an estimate of the 1 Hz data. Since we cannot differentiate RIN from SVN here (due to high correlation), the estimate can be seen as the effective contribution from both of these.

The fit allows the RIN parameter to vary per noise run, and each noise run is divided into another set of segments, if there is a correlation between the 1 Hz frequency noise estimates and the noise level in o_{12}, to account for the two frequency noise states. Afterwards, all five data channels are jointly fitted per time segment.

While the RIN and SVN contribution are mainly determined from the DWS measurements, the frequency noise contribution estimates relies on the o_{12} data. Figure 12.2 shows the main noise model contributions for which we do have independent measurements, showing in what ranges the parameters were stable.

Note that in segment 2016-11-16 11:05:23 UTC – 2016-11-26 07:59:25 UTC the two parameters $\Sigma_{\mathrm{R}}, \Sigma_{\mathrm{F}}$ (normalized QPD powers) were not available and during 2016-12-26

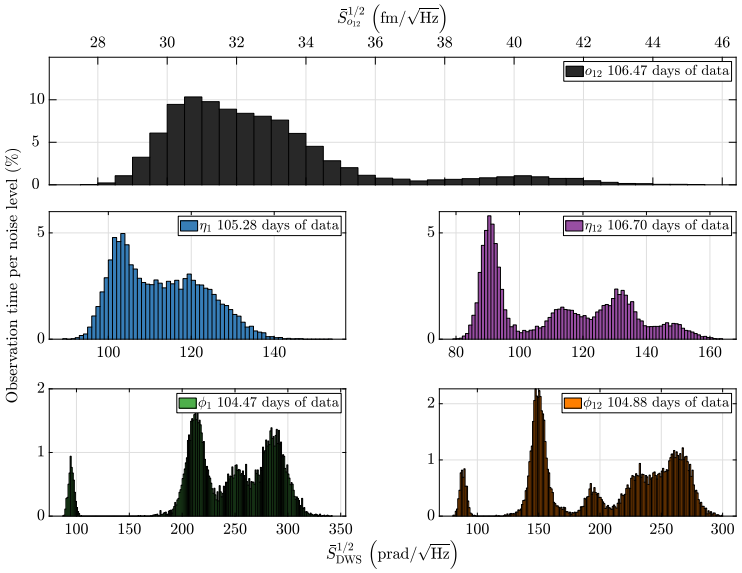

Figure 12.4 Histogram of the noise behavior over the mission shown in figure 12.1. The top plot shows the longitudinal differential readout and the lower ones are for DWS. Multimodal distributions are visible, that can be partly explained due to offset dependent noises in DWS, while in o_{12} the upper level is due to states of higher frequency noise. A detailed discussion is given in the text. Reprint from [P3].

08:14:59 UTC – 2017-01-13 19:57:57 UTC, $\Sigma_{\mathrm{R}}, \Sigma_{12}$ had some missing samples. In both cases we interpolated those for the noise model fit.

12.3 Discussion of long-term results

For o_{12}, there are more than two noise regimes apparent. However, one broad level is visible around the median and one upper level around 40 fm/$\sqrt{\mathrm{Hz}}$. The upper noise level represents 9 % of the shown data. The lower noise state has a mean of 31.9 fm/$\sqrt{\mathrm{Hz}}$.

The upper noise levels correlate in time with increased laser frequency noise due to the non-stationary (two-state) behavior of the laser. For the first three measurement timespans, the laser frequency telemetry was available at a sampling frequency of 10 Hz and we found that with the subtraction of the laser frequency noise, the periods of increased noise can be removed. At later times, the laser frequency telemetry was only available at 1 Hz which does not allow for this subtraction.

Figure 12.4 shows the histogram of the noise spectrum estimation. The y-axis shows the percentage of time spent at a specific noise level with respect to the total measurement length per observable. The bin width is 0.5 fm/$\sqrt{\mathrm{Hz}}$ for o_{12} and 1 prad/$\sqrt{\mathrm{Hz}}$ for DWS.

Based on the segment analysis defined above we find that the measurement in o_{12} varies between 27.8 fm/$\sqrt{\mathrm{Hz}}$ and 44.1 fm/$\sqrt{\mathrm{Hz}}$ with a median of $32.0^{+2.4}_{-1.7}$fm/$\sqrt{\mathrm{Hz}}$. The values are based on the 16th, 50th, and 84th percentiles of the histogram.

The DWS signals show a much broader distribution of varying modes with maxima between (86 to 290) prad/$\sqrt{\mathrm{Hz}}$. We attribute this behavior (as far as we can explain) to offset

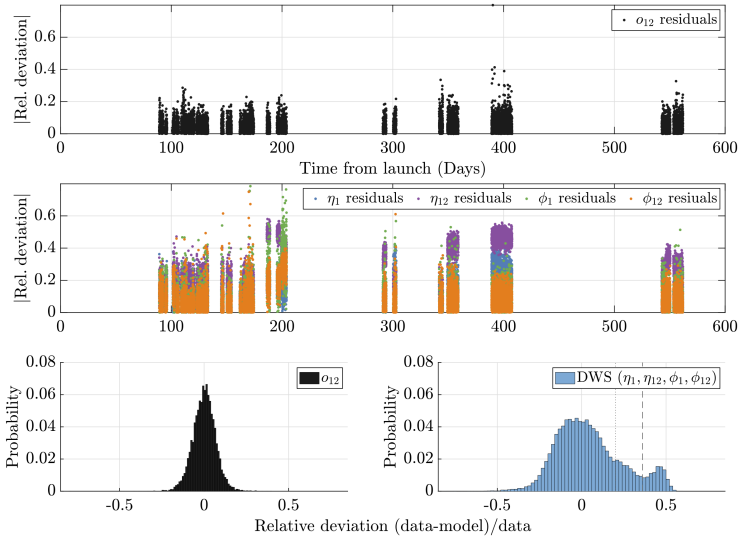

Figure 12.5 Relative residuals of the noise fit figure 12.1. The DWS panel reads blue: η_1; purple: η_{12}; green: ϕ_1; orange: ϕ_{12}. It can be seen that the model explains most of the o_{12} noise to better than 20 %. Reprint from [P3].

dependent noise couplings (such as RIN, SVN): During specific times of the mission, the TM orientation was changed, causing varying noise levels. See Section 10.1 and 11.1 for details.

In DWS, the frequency noise is highly correlated and well phase matched on all photodiode quadrants and therefore subtracts to a large degree when forming the DWS signals (by differencing the left/right, up/down quadrant phases). As expected, we see no effect from changing frequency noise levels.

The noise levels of figure 12.1 show that the OMS measurements have been much more sensitive than expected, enabling a level of investigation unpredicted at the beginning of the mission.

The models confirm that we have a good understanding of the noise (similar to what was shown in [P2]), even though we cannot explain all of the changes in the noise over the mission in DWS. The remaining discrepancy (residuals are shown in figure 12.5) between the model and the fit have been investigated to a great detail but a definite explanation could not be identified. The biggest deviation is originating from the η plane. However, a large portion is well modeled, given the intrinsic scatter per noise run of a few fm in o_{12} and tens of prad in DWS.

We deem an influence of the OB temperature rather unlikely, since it is very stable and has no correlated changes, as can be seen by comparing with the temperature data given in [P15].

The same holds true for a change in PM readout noise which is furthermore constrained by the o_{12} behavior observed during the course of the mission. A data processing error also seems not very likely since the same quadrant data is used for all the measurements

and a processing error should lead to similar noise changes in all channels which we do not observe.

Moreover, based on the observed, asymmetric change in the system noise levels in DWS (before 06.06.2016, day 186 from launch), we were searching for an explanation which is strongly suppressed in the longitudinal readout. However, the available data does not allow us to reject a hypothesis related to changing laser behavior or ghost beams.

For most laser housekeeping data, we are limited by the sampling frequency of only 0.2 Hz. Laser intensity and frequency fluctuations can only be included as estimates since no direct measurement in the required frequency ranges are available. The optical fibres should always deliver the same mode by design. The polarization of the light on the OB is known to change over the course of the mission (see [80]) and a weak correlation with changing RF amplitudes used to drive the AOMs may be present.

Even though we could observe a few periods during which the pump current and the laser temperature appear correlated to the noise in some of the observed channels, the exact mechanism from a laser setting to a change of the noise above 1 Hz is not clear It appears non-linear and no definite, repeating pattern could be found. Furthermore, in between two noise runs, we found a period where the laser heater setpoint was correlated to the noise level. However, at other times in between noise runs, we cannot confirm this observation and thus we conclude that this is not the main driver of the observed changes in noise level.

In addition, it should be noted that the DWS spectra were not always perfectly flat. This could possibly point to aliasing which is not modeled well enough or a higher influence of the OPD actuator with the observed spikes (section 10.1.7). But again, we are limited by the data rate of the telemetry. There are just a few dedicated experiments where 100 Hz data was available, which are very short and always only cover a small portion of the channels.

Since the reason for the observed changes in the DWS noise levels over the mission duration could not be found yet, we can also not estimate whether this behavior is related to any specifics of LPF and the OMS or if it is a more general aspect limiting the common-mode noise rejection in DWS compared to the much less affected longitudinal measurement.

Nonetheless, the agreement between the model and the data is good in most cases and much below any required level.

Chapter 13

DWS RIN experiments

Please note that a few introductory parts of this chapter have already been published in [P8].

During the mission, we performed a large number of experiments to characterize the different possible noise sources of the OMS. Most of them are listed in table D.2. Based on these, a detailed study of the overall sensitivity was given in chapter 11.

This chapter now focuses on the RIN coupling in DWS and addresses specifically the DWS tilt experiment in the mission extension, which was critical to validate the RIN coupling models in DWS. In these experiments, one or both TMs were commanded to a certain angular set-point through electrostatic actuation. Then, a noise measurement was recorded for a few minutes, before moving to the next set-point.

During the nominal mission, a first small experiment of this type was performed to assess the DWS noise behavior for varying TM2 angles. The procedure led to an improved understanding of RIN coupling from twice the heterodyne frequency. However, it only sampled a small parameter space of possible TM tilts and was not able to verify the whole model. The details about this previous experiment can be found in the reports about the main mission phase [P7, 63].

During the mission extension a refined version of the DWS experiment was planned. This new experiment is detailed in [P8, 63]. The idea was to increase the TM2 tilts to sample a larger phase space while simultaneously decreasing the beam walk by actuating TM1. The commanded slews sampled the phase space in a step-wise scheme from almost $(-600 \text{ to } 600)\,\mu$rad for TM2 in ϕ_2, η_2. At each set-point, the noise was measured before "masking" the B side of the PM, which was a procedure to effectively turn off balanced detection, since the whole second output port of the interferometer was disabled. Then, in this new "unbalanced" configuration the noise was also measured, before unmasking the B side again and going to the next set-point, where the procedure was repeated.

Note that some of the data from this experiment has already been used to characterize the noise model at intermediate contrasts, see figure 11.4.

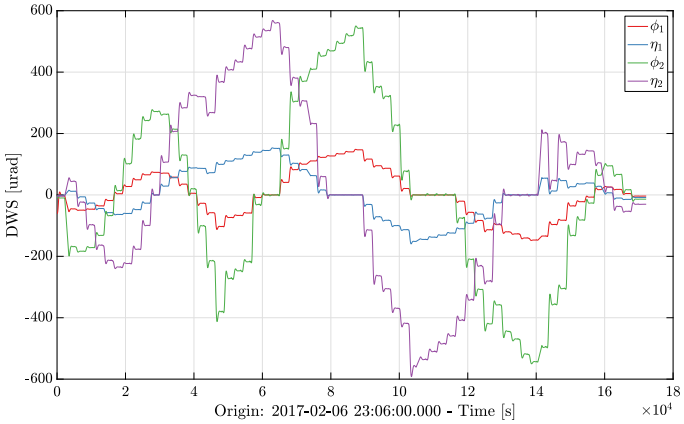

Figure 13.1 Timeseries of the second DWS experiment. Shown are the four TM angles as measured by DWS through the OMS. The different set-points of the TM angles can be observed. There is always a small overshoot until the TM settles on the new set-point. Reprint from [P8].

13.1 Experiment and contrast

The experiment was starting on 02.06.2017 at 23:00 h and lasted for about 48 h. However, due to a failure in a preceding experiment TM2 was not at its zero position, but remained rather at an offset of 275 nm. This may have had an influence on the evaluation of RIN coupling due to different beam pointing or imperfect longitudinal phase subtraction in DWS. Additionally, it is unclear at the time of writing how the performance of the DFACS controller is changing due to the slightly shifted position and its impact on the experiment, perhaps introducing slightly different actuation gains. However, the influence is expected to be negligible.

Figure 13.1 presents the measured time series of all calibrated DWS channels, scaled to TM tilts. It can be compared that the slews were much larger than in the previous experiment [P7, 63] and that both TMs were actuated in parallel. It can be seen that there always was a small overshoot before settling at a new set-point (expected from previous experiments). For very few and short segments, four data channels with a sampling frequency of 100 Hz had been requested via the so called Interferometer Data Log (IDL) for diagnostic purposes. The times at which such IDL data was taken have been masked out, because the procedure created transients in some channels. It can be concluded, that apart form the aforementioned configuration, the experiment was run as planned.

Figure 13.2 shows the impact of the experiment in the longitudinal channels. The small slews on TM1 have basically no visible impact (as o_1 is in-loop noise dominated). The more precise measurement of the differential displacement shows a varying o_{12} signal. It can be used to characterize the o_{12} noise and its dependence on the contrast, as done in figure 11.4, chapter 11. The source of the larger transients in o_{12} is still unclear, but may be related to actuation crosstalk.

The contrast in X1 and X12 is shown in figure 13.3 and in combination over the parameter space in figure 13.4. We can see that the contrast never dropped below 25 %. It stayed in the range (80.9 to 96.8) % in X1 and between (25.2 to 98.7) % in X12. This can be

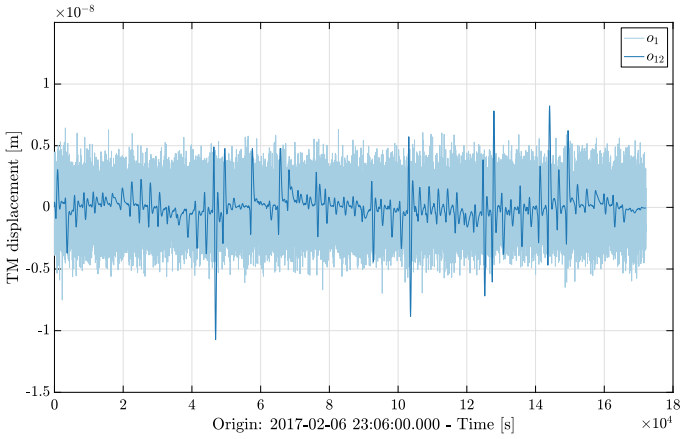

Figure 13.2 Timeseries of o_1 and o_{12}. The first measurement is dominated by noise, while the more precise data of o_{12} shows an effect of the TM slews. The mean values have been subtracted. Reprint from [P8].

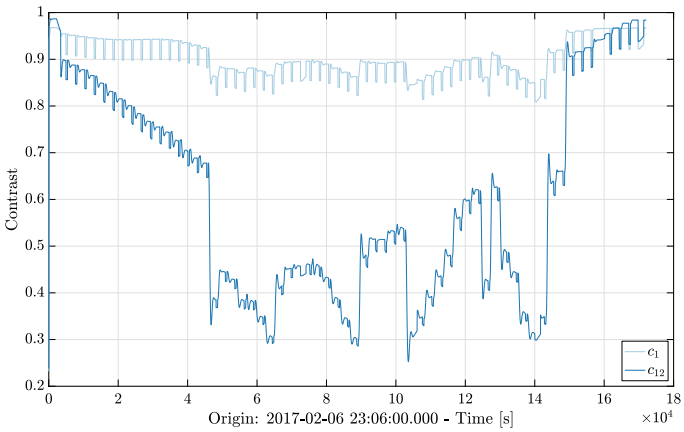

Figure 13.3 Timeseries of the contrast in both TM interferometers. Transients due to package switching have been removed. The visible small drops coincide with the masking of the B side PDs. Reprint from [P8].

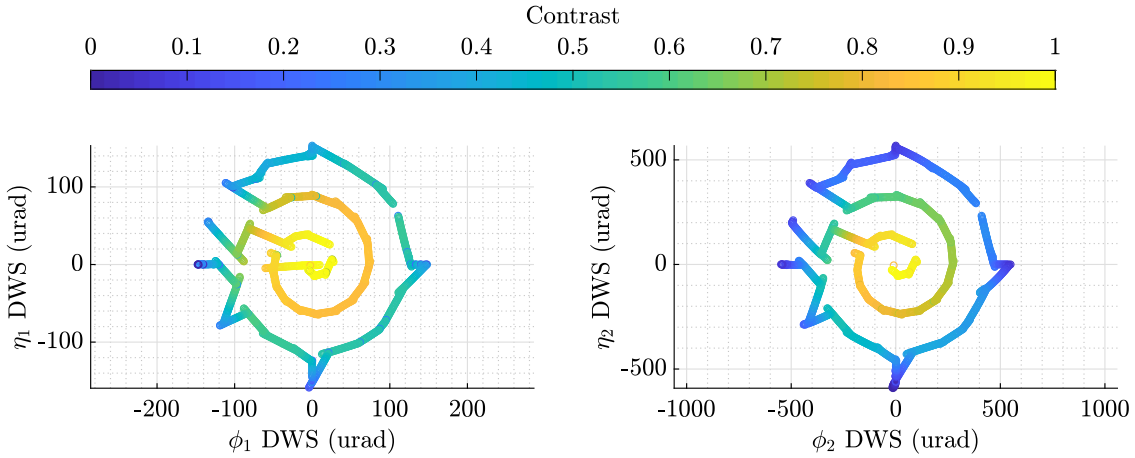

Figure 13.4 The parameter space in DWS as measured by the OMS. Segments containing transients due to package switching have been masked out. The resulting contrast stays above 25 % for the contrast in X12, and above 80 % for the X1 interferometer for the whole experiment. Reprint from [P8].

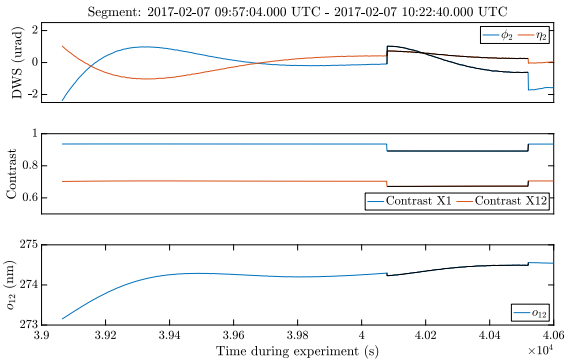

Figure 13.5 A zoomed view on of one of the set points. It can be seen that the TM did not fully stabilize until the B side diodes were masked (marked in black). Also visible are the jumps from the masking procedure. The first panel (DWS) has the segment means subtracted. The second panel shows the contrast in X1 and X12, and the third panel has the timeseries of o_{12}. Reprint from [P8].

attributed to the actuation scheme designed specifically for this experiment. The TM1 slews compensated the effect of the larger TM2 tilts which led to an overall reduced angular phase measurement on the PD12 diodes. Therefore, a very low contrast that would have caused safety procedures inside the SC stopping the experiments was avoided.

Looking closely at the segments, as given in figure 13.5, one finds that the TM2 did not completely stabilize before the B side was masked. The reason for this behavior is likely originating from residual acceleration of the actuation. The masked period is highlighted in black and shows a jump or drop in the angular and longitudinal measurements. It is in the order of 5 % for the contrast. Masking one side means losing half of the total power and also half of the signal, thus increasing the noise floor of uncorrelated PM and electronic noise by $\sqrt{2}$.

The stable segments for the following analysis have been selected by a threshold that allowed the contrast (individually for X1 and X12) to change less than $0.2\,\%\,\mathrm{s}^{-1}$. The segments have then been split up into balanced and unbalanced periods.

13.2 RIN in DWS results – Noise over tilt

The common mode subtraction property of RIN is expected to be almost identical in the longitudinal channels and DWS, since it appears as a correlated quantity. For LPF, we assume that the power levels on each quadrant are identical and that the raw, uncalibrated DWS phase is associated with the equation (see table 7.1)

$$\tilde{\phi}_{\mathrm{RIN}} = \sqrt{2}\tilde{r}\,(2f_{\mathrm{het}})\,|\sin(\varphi - \varphi_R)|, \tag{13.1}$$

for $\varphi - \varphi_R = \gamma^{\mathrm{raw}}$, and $\gamma^{\mathrm{raw}} \in \{\phi_1^{\mathrm{raw}}, \phi_{12}^{\mathrm{raw}}, \eta_1^{\mathrm{raw}}, \eta_{12}^{\mathrm{raw}}\}$, to describe the RIN to phase coupling correctly. By design, $r(t)$ appears correlated on all quadrants. Therefore, all DWS channels can be jointly analyzed.

The raw phases η_1^{raw}, ϕ_1^{raw} (from X1), and η_{12}^{raw}, ϕ_{12}^{raw} (from X12) were measured on-board. Available as telemetry were only the calibrated TM angles η_1, ϕ_1, η_2, ϕ_2 from linear

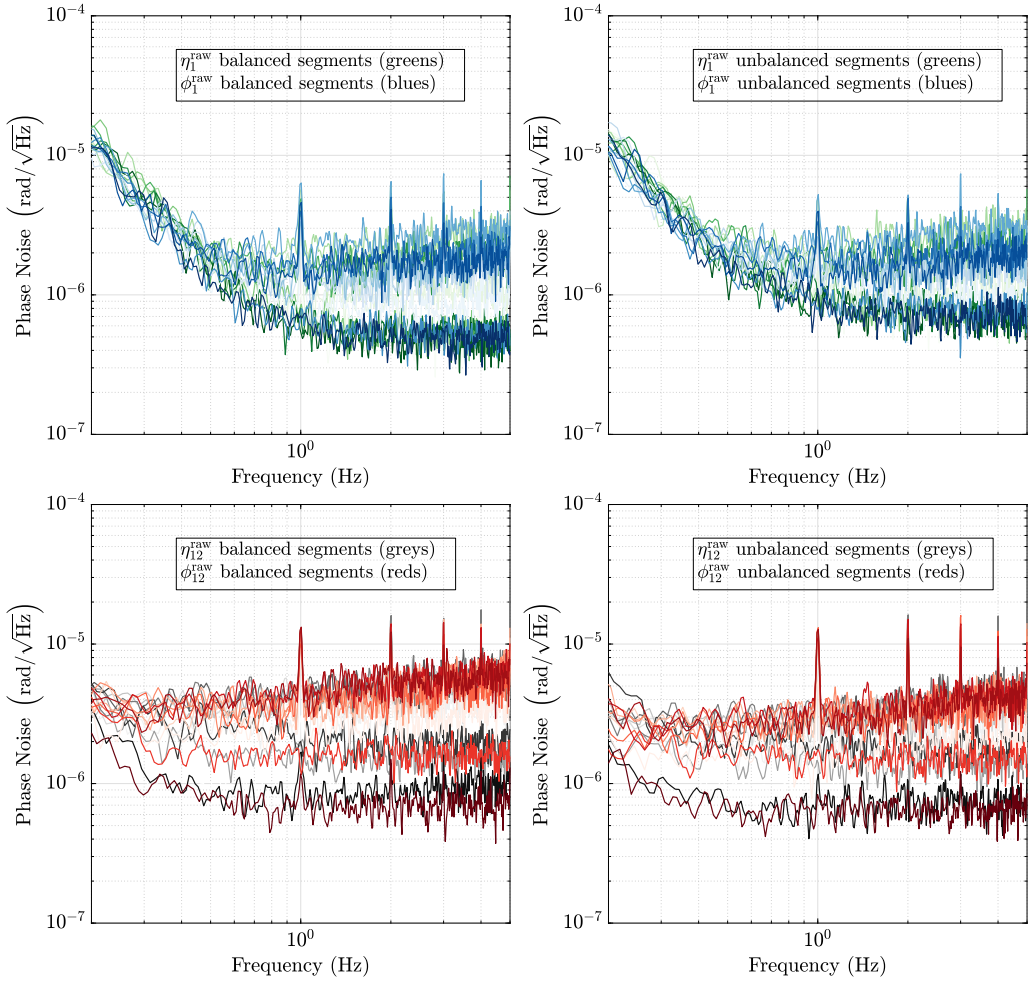

Figure 13.6 Spectral densities for some balanced and unbalanced segments. Computed with the LPSD algorithm [58], parameters see figure 9.2.

combinations of the raw phases. To use these in our model, the linear combinations are reversed. Then, all raw phases can be plotted on the same x-axis.

For analyzing individual segments, the semi-flat high frequency noise PSD average of each stable data segment can be calculated and plotted on the y-axis. Spectral components likely caused by the PPS are masked out before averaging.

However, it should be noted that, especially for DWS, we find that not all segments show a particular white noise floor. They have different gradients on them, as visible in figure 13.6. For this figure, always two directly subsequent segments have been used to allow for comparison between balanced detection and "unbalanced" segments. Every 7th segment has been chosen for this selection, plotting 18 ASD traces per panel. The low

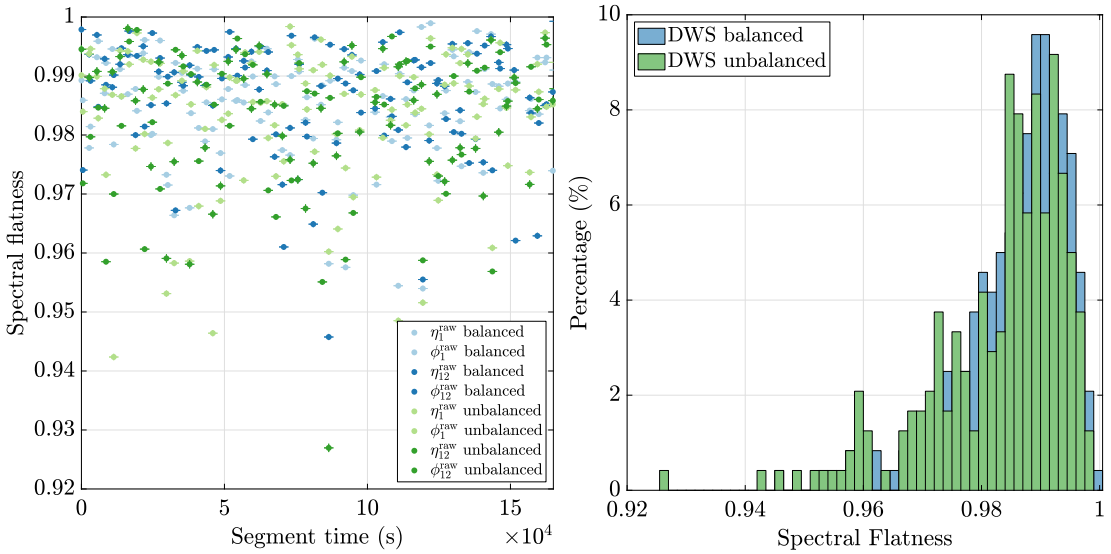

Figure 13.7 Spectral flatness for all balanced and unbalanced segments (left panel) and histogram (right panel). Computed with the Shannon-entropy algorithm [81].

frequency behavior is comparable with the analysis in section 9.2. The exact coupling of the $n \cdot 1\,\mathrm{Hz}$ PPS components is unknown [71].

It can be seen that higher noise levels associated with larger TM tilts have higher gradients in the spectral densities. For lower noise values the shape appears flat. To allow for comparison with figure 12.1, the same frequency range of (1.2 to 2.8) Hz has been chosen for the frequency averages in the following analysis. However, already visible is the increased noise floor by $\sqrt{2}$ for unbalanced detection cases when RIN is not dominant (visible in the lower ASD traces in the two top panels). In these cases the dominant noise is originating from the ADC quantization process and appears uncorrelated between quadrants.

Using a Shannon-entropy based measure of the spectral flatness, $\mathcal{F}$, with $0 \leq \mathcal{F} \leq 1$, from [81], it can be seen in figure 13.7 that most densities are actually relatively flat. No further filtering on the outliers has been performed, since we do not have independent RIN measurements or other channels that could directly explain the increasing noise. No noticeable difference between balanced and unbalanced segments, or between particular DWS channels, is present.

In figure 13.8 the overall result is shown as a plot of average phase noise over DWS “raw” phase. It combines all channels (as they should all measure the same RIN) and shows the two cases of balanced and unbalanced detection, together with a joint fit each across the 4 DWS channels for each case. The segments have been sorted after fitting. The blue points show the nominal case with balanced detection from the two BS output ports. The green points indicate segments when one PM side was disabled, so that only one BS output port was used, creating “unbalanced” segments without balanced detection. The noise model

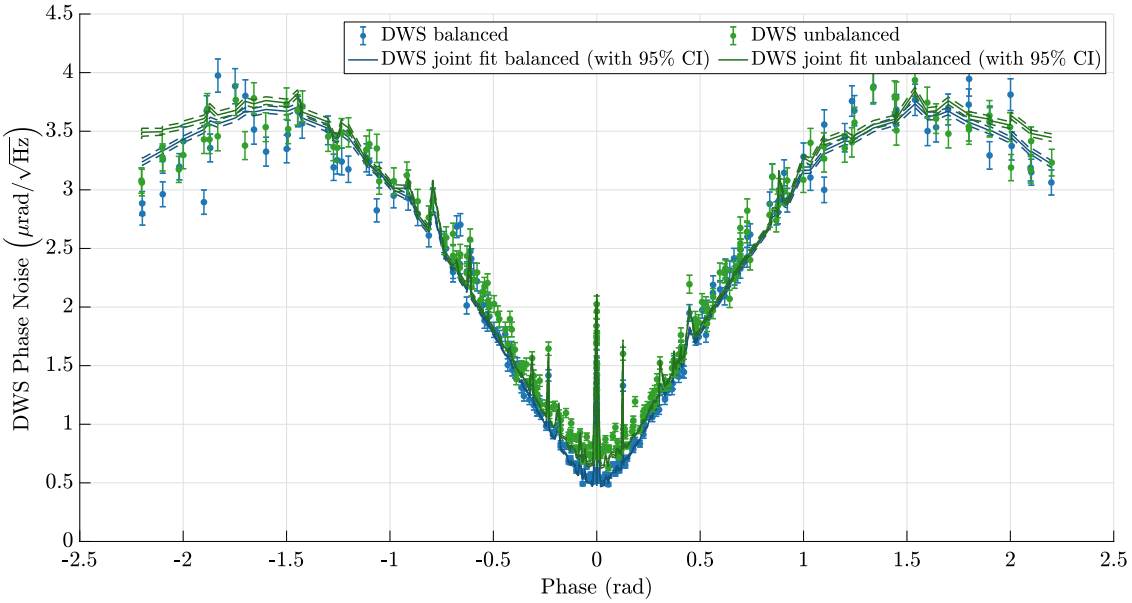

Figure 13.8 Joint fit results for all DWS channels. Balanced and unbalanced data sets are shown with noise model fits and 95 % confidence intervals.

predictions based on fit results with two free parameters (RIN level and PM noise) are also shown.

This plot shows a few interesting aspects. Firstly, the maxima of the sinusoidal RIN coupling do not visibly change much between balancing and no balancing. This strongly indicates that 1f-RIN was smaller than 2f-RIN. It should be noted that this is likely due to the specific power stabilization loop aboard LPF, targeting a heterodyne frequency of 1 kHz. For LISA with beatnotes in the MHz regime, this is not likely, see part IV.

Secondly, the noise floor around 0 rad increases by a factor $\sqrt{2}$ as expected, since balanced detection leads to a factor $1/\sqrt{2}$ for uncorrelated noises (combining 2 correlated signals with 2 uncorrelated noise sources $= \sqrt{2}/2$). Hence, the reverse is also true when balanced detection is disabled.

Thirdly, there are many points with increased noise levels around 0 rad. This occurs when one DWS channel is close to zero offset, while its adjacent plane is at a non-zero offset, thus decreasing the contrast in X1 or X12, which leads to higher noise couplings (see also section 10.2).

Furthermore, many points not directly on the sinusoidal shape are explained by the measured data included in the model, for example due to increased PM noise at low contrasts. Around the maxima, a larger spread is visible that is not completely captured by the model. This could also be related to a slightly changing laser behavior between segments, since the total experiment lasted for about 48 h, so the assumption of one

stationary RIN value is certainly not correct. However, fitting each segment individually is difficult due to the correlation between ADC and RIN and would finally lead to similar estimates for the RIN value due to the intrinsic scatter around the peaks.

The fit is using the weighted Levenberg-Marquardt nonlinear least squares algorithm [82] and the results are shown in solid lines and include the noise model as described in section 10.2 similar to figure 12.1. The solid lines are used to increase visibility, but the noise model is only evaluated at the points shown.

As described, two parameters are estimated yielding RIN (at $2f_{\mathrm{het}}$) $\tilde{r} = (2.50 \pm 0.02) \times 10^{-6}\,\sqrt{\mathrm{Hz}}$ and ADC $S_{I_{\mathrm{ADC}}}^{1/2} = (103.4 \pm 2.4) \times 10^{-12}\,\mathrm{pA}/\sqrt{\mathrm{Hz}}$ with active balanced detection, and $\tilde{r} = (2.47 \pm 0.02) \times 10^{-6}\,\sqrt{\mathrm{Hz}}$, $S_{I_{\mathrm{ADC}}}^{1/2} = (97.4 \pm 1.6) \times 10^{-12}\,\mathrm{pA}/\sqrt{\mathrm{Hz}}$ with unbalanced detection. Confidence intervals for 95 % are plotted with dashed lines and corresponding colors.

The joint fit has been chosen because the X1 DWS channels have much smaller tilts and cannot sample most of the RIN sinusoidal. Furthermore, the RIN parameter appears correlated, while the ADC coefficient is uncorrelated between channels and should be similar between interferometers, especially since the balanced and unbalanced cases show that the expected $\sqrt{2}$ difference is well met.

The aforementioned correlation between the ADC and RIN parameter appears in the fit; it is at 0.44 (balanced), and 0.51 (unbalanced). This high correlation can be understood in the way that tilting the TM changes both the contrast due to reduced beam overlap, but also increases the RIN coupling strength due to an additional phase offset.

The contribution of 1f-RIN during the unbalanced segments has not been included in the model, since it is clearly not distinguishable in the data set.

The SVN contribution has been calculated following section 10.2 and is always below a maximum of $20\,\mathrm{nrad\,Hz^{-1/2}}$ and has therefore not been included in the fit.

Figure 13.9 shows the fit results for each DWS channel individually. It can be seen that for X12, the fit catches many features of the noise distribution (for balanced and unbalanced segments) and also explains the points around zero offset. However, in X1, the DWS channels show deviations near zero offset in the unbalanced case.

It is not exactly clear where this discrepancy originates from. Different ADC noise levels are ruled out by the good fit for the balanced segments and a higher 1f-RIN contribution is unlikely due to the good fit in the X12 DWS channels, where it would also appear.

Since the estimation of the RIN value was the main priority in the presented experiment, this deviation seems interesting, yet less important for estimating the peak of the sinusoidal. Further, there is no obvious reason to exclude the X1 data set, even though it only samples a small portion of the phase range, hence the joint fit across all channels was applied. However, from the scatter in the visible data set it appears that the error of the fit is underestimated around 0 rad in the X1 channels.

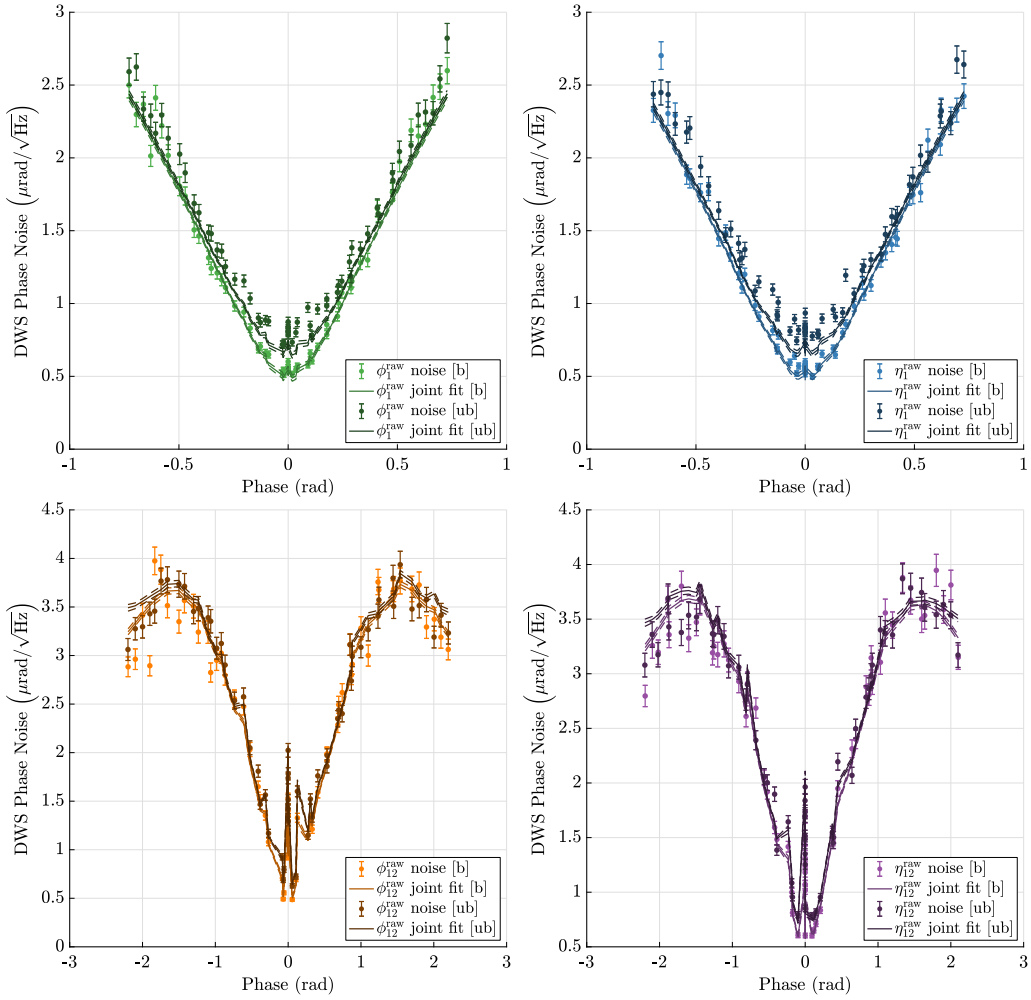

Figure 13.9 Joint fit results plotted for each DWS channel. Balanced [b] and unbalanced [ub] data are shown with their fit and 95 % confidence intervals.

Overall, the noise over phase dependency in DWS is confirmed over a wider range as before, and it supports the theory of a sinusoidal systematic in the coupling. The measurement time was relatively short (< 7 min per segment) to measure as many set-points (~ 60 per channel) as possible along this slope. Therefore, the averaging within the segments is restricted. Here, always 30 averages and BH92 windows have been used.

As indicated before with the unchanged slope maxima for both balanced and unbalanced detection, the 1f-RIN appears to be well below the 2f-RIN, as can be expected from ground characterizations with active power control loop (proprietary documents, not shown here). Therefore the RIN induced phase noise, $\tilde{\phi}_{\mathrm{RIN}}$, is dominated by 2f-RIN alone, with a sub-dominant 1f-RIN contribution that assumes equal powers in the two beams

(see table 7.1), yielding the total coupling

$$\tilde{\phi}_{\mathrm{RIN}} \approx \sqrt{\left(\frac{\sqrt{8}}{\sqrt{\eta_{\mathrm{het}}}}\tilde{r}\,(1f_{\mathrm{het}})\sin\left(\frac{\varphi-\varphi_R}{2}\right)\right)^2 + \left(\sqrt{2}\tilde{r}\,(2f_{\mathrm{het}})\sin(\varphi-\varphi_R)\right)^2} \tag{13.2}$$

$$\approx \sqrt{2}\tilde{r}\,(2f_{\mathrm{het}})\,|\sin(\varphi-\varphi_R)|, \tag{13.3}$$

approximating that 2f-RIN term dominates during the mission. This means, that we can safely assume the 1f-RIN to be at least a factor of $\sim 1/2$ smaller than 2f-RIN.

It has to be noted, however, that this experiment only gives a glimpse of the whole mission, and no direct RIN measurements are available. Since no laser degradation effects are visible, there is no reason to assume strong deviations from this behavior throughout the mission (also see RIN fit in figure 12.3).

The estimates from this experiment of $\tilde{r} = (2.50 \pm 0.02) \times 10^{-6}\,\sqrt{\mathrm{Hz}}$ (balanced) and $\tilde{r} = (2.47 \pm 0.02) \times 10^{-6}\,\sqrt{\mathrm{Hz}}$ (unbalanced) are within the previously determined boundaries $\tilde{r} < 5 \times 10^{-6}\,\sqrt{\mathrm{Hz}}$ [P2] but also add to the observed RIN discrepancy detailed in the next chapter.

Chapter 14

The RIN discrepancy

14.1 Context and overview

This thesis shows that, in LPF, the RIN to phase coupling can be observed in the longitudinal o_{12} measurement and in the angular DWS channels. Both of them are comparable in the sense that they both have a common mode subtraction: For o_{12}, it contains the correlated difference between the longitudinal x_{12} and x_{R} channel. In the case of DWS, the adjacent correlated quadrants of the QPDs are subtracted. Therefore, for a given longitudinal TM set-point ("step"), or rotation of a TM ("tilt"), they should in theory have the same coupling pattern, as described in chapter 7, and table 7.1.

In principle, both beams originate from the same laser and should contain correlated RIN. However, we do not know how much differential (uncorrelated) RIN is introduced due to the AOM modulations, which then would be uncorrelated among the beams, yet still yield correlated phase noise between interferometers. However, this again should yield comparable results, as the error would be identical in every channel.

The balanced detection is assumed to have high efficiency. For this purpose, we assume that only 2f-RIN remains after balanced detection (as supported by the previous chapter 13), and that the power levels in both interferometers are roughly equal (certainly true for DWS, true up to a deviation of 5 % for o_{12}, see Σ parameters in figure 12.2).

Therefore, the usual term (see section 10.1.4 and table 7.1)

$$\sqrt{2}\tilde{r}\,(2f_{\mathrm{het}})\,|\sin(\varphi-\varphi_R)|$$

describes the coupling under nominal conditions. Now it is either $\varphi-\varphi_R=(4\pi/\lambda)o_{12}$ or $\varphi-\varphi_R=\gamma^{\mathrm{raw}}$, with $\gamma^{\mathrm{raw}}\in\{\phi_1^{\mathrm{raw}},\phi_{12}^{\mathrm{raw}},\eta_1^{\mathrm{raw}},\eta_{12}^{\mathrm{raw}}\}$, depending on the experiment.

Overall, there have been four experiments (two during the nominal mission marked "v1", two during the extension marked "v2"; always one x-step and one DWS-tilt experiment) to characterize the RIN to phase coupling in LPF. All of them have been performed without access to an independent RIN measurement, which makes it difficult to estimate the coupling strength directly. Instead, the resulting common mode rejection can be used to fit the theory expectation to indirectly estimate the RIN strength at that moment in

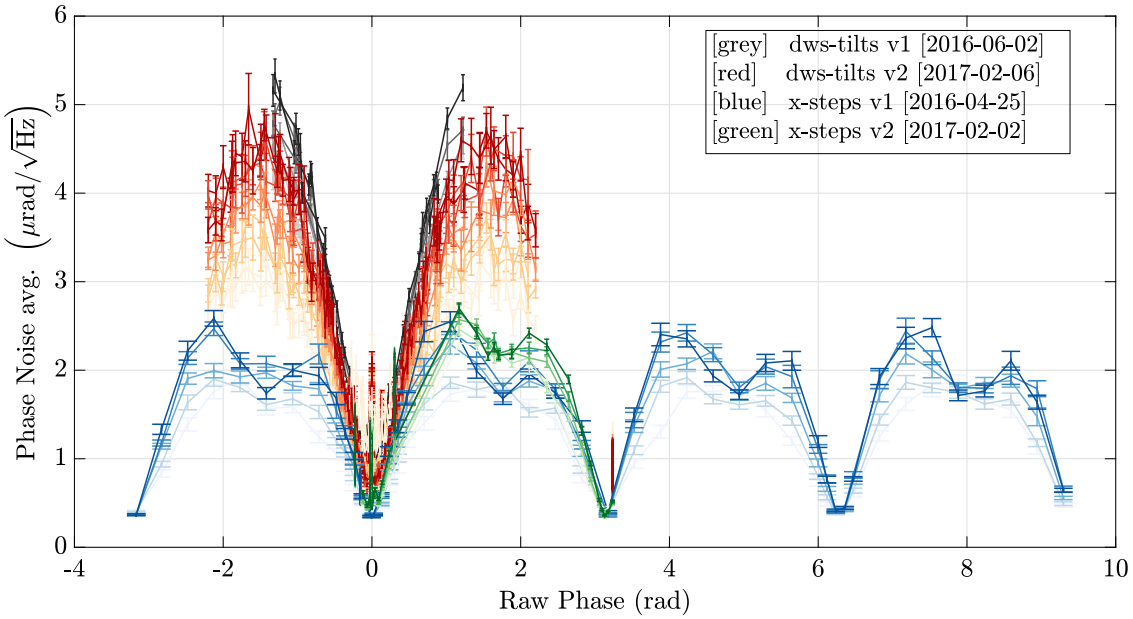

Figure 14.1 This plot shows the RIN discrepancy between longitudinal and angular experiments and also the dependency for various frequency bands (increasing by lighter to darker colors). All channels have been rescaled to (electrical) radians.

time. For this discrepancy analysis, only balanced detection is considered, which is the nominal configuration. For the few available data sets with disabled balanced detection there are comparable results (see chapter 13).

The two different experiments were run after one another over the course of the mission and have also been used to fit other channels at the same time, e.g. the o_{12} noise over contrast in figure 11.4.

Given the restrictions regarding possible TM tilts, the rotational phase-space can only be sampled up to approximately 0.7π, whereas it was possible to cross over multiple fringes in the longitudinal x-step experiments (led by A. Wittchen, see [71]).

The discrepancy of the RIN value arises between the experiments as stated in table 14.1. Shown in figure 14.1 is the difference between longitudinal shifts and angular rotations. The first DWS tilt experiment does not sample the phase space across the maxima and its results should therefore only be considered with caution. There is roughly a factor two discrepancy between the longitudinal and angular estimates. This factor is not a problem with the two models themselves, since a similar fit result was obtained for the RIN value in both DWS and o_{12} channels for data recorded at the same time (see table 14.1 4th and 5th row). The different on-board processing for longitudinal and angular channels is correctly incorporated, as can also be seen by the joint long-term mission fit across all channels in figure 12.1.

Experiment	Date (UTC)	Fit channel	RIN estimate, $\left(1 \times 10^{-6}\,\mathrm{Hz}^{-1/2}\right)$
x steps v1 ([71], figure 14.1)	2016-04-25 08:00 – 2016-04-26 08:00	o_{12}	(1.51 ± 0.01)
DWS tilts v1 (small tilts, [63], figure 14.1)	2016-06-02 08:30 – 2016-06-03 07:25	DWS	(3.2561 ± 0.0086)
x steps v2 ([71], figure 14.1)	2017-02-02 20:36 – 2017-02-04 21:36	o_{12}	(1.74 ± 0.01)
DWS tilts v2 (figure 13.8)	2017-02-06 23:06 – 2017-02-08 22:55	DWS	(2.50 ± 0.02)
DWS tilts v2 used for o_{12} vs contrast (figure 11.4)	2017-02-06 23:06 – 2017-02-08 22:55	o_{12}	(2.59 ± 0.09)
Power modulation with x step (figure 11.5)	2017-06-17 08:20 – 2017-06-17 15:00	o_{12}	(1.08 ± 0.01)

Table 14.1 RIN discrepancy across different LPF experiments.

The exact laser RIN behavior is not known and could also be non-stationary for the time-scales of these experiments. After all, the "signal" that is being estimated is a non-stationary process.

We find different results depending on the experiment and frequency range, that cannot be explained by the error bars alone. There appears to be an underlying systematic that is not understood, since the RIN estimate seems to depend on the method; either changing the overlap integral of the two beams (due to TM tilts), or changing the phase or power only (x-steps, power modulation experiment) – and not on the channel used for the analysis.

There is an added difficulty due to the presence of a suspicious yet systematic "4f" structure in the longitudinal steps, that hints at an asymmetric ghost beam or another unknown coupling, see the findings in [80], section 4.2. The apparent central dip and right-sided shoulder is especially visible when averaging over higher frequency bands.

For figure 14.1, the noise power has been averaged with 500 sample BH92 windows for the following bands

$$\begin{aligned}
&(0.6 \text{ to } 0.9)\,\mathrm{Hz}, && \text{(lighter color)}\\
&(1.2 \text{ to } 1.8)\,\mathrm{Hz}, &&\\
&(2.1 \text{ to } 2.8)\,\mathrm{Hz}, && \downarrow\\
&(3.1 \text{ to } 3.8)\,\mathrm{Hz}, &&\\
&(4.1 \text{ to } 4.8)\,\mathrm{Hz}, && \text{(darker color)}
\end{aligned}$$

to avoid the $n \cdot 1\,\mathrm{Hz}$ spikes, with the colors indicated for figure 14.1.

The spectra are flatter for smaller tilts and there seems to be aliasing from the OPD actuator steps (also compare [71]). However, this behavior cannot be fully explained with the data available from the SC. Yet, the deviations from white noise are within a few $\mu\mathrm{rad}\,\mathrm{Hz}^{-1/2}$. The RIN itself is also likely not exactly flat and may be rising towards higher frequencies, as the controller gain diminishes (visible in proprietary documents [83]).

This discrepancy, together with the 4f structure, remains unclear and it may require future investigations to understand its systematic or relate it to OMS specifics.

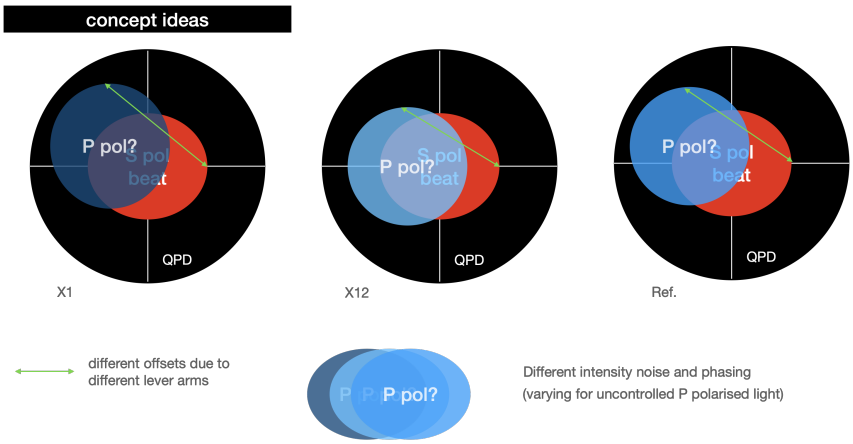

Figure 14.2 Concept of a P-polarized ghost beam with varying intensity and phasing on the QPDs of three different interferometers (X1, X12, Ref.), that could explain some of the RIN discrepancy and DWS changes. This idea was developed in collaboration with B. Kaune.

14.2 Idea for a possible explanation

Unfortunately, no direct explanation could be found. The following qualitative idea may be used for further investigations. It is conceptually depicted in figure 14.2, illustrating the coupling of an unwanted ghost beam with a certain asymmetry that changes its phasing and intensity over the course of the mission. The existence of such a parasitic beam is supported by the analysis in Section 4.2 in [80], which would then contribute to the estimated RIN on the PDs. Due to different lever arms in the interferometers, it would appear with varying pointing on different PDs and could cancel in the symmetric x dimension more strongly than in the asymmetric η plane. Therefore, this could perhaps also explain the unknown DWS noise level changes in figure 12.1 to some extent. Further, there could be spectral components beating on the diodes, potentially creating 4f interference terms on both the X12 and Reference interferometers that lead to some RIN cancellation in o_{12} only.

However, since there is no single quadrant data available for all quadrants during the mission, and also not from the ground test campaign, our knowledge is limited. Future investigations may show that this behavior was only LPF specific, if it cannot be reproduced in ground experiments. For example, the asymmetric dip structure was not visible in ground experiments using pre-flight hardware at the AEI, see Figure 12 in [P1].

14.3 Conclusion

To conclude, the indirect RIN estimation via its coupling to the longitudinal or angular phase readout stays within reasonable bounds over the whole mission (requirement $< 1 \times 10^{-5}\,\mathrm{Hz}^{-1/2}$ between (0.5 to 2) kHz, see RLU-1040 in [83]), yet an unexplained discrepancy

remains. There is also an unexpected, yet systematic, dip structure in the coupling to o_{12}. No direct verification is possible, since no independent RIN measurement is available. The unexplained behavior is not covered by the RIN model presented in this thesis. However, the observations presented in this chapter are only appearing during these specific experiments with intentional non-optimal phase offsets and do not compromise the mission performance for small TM offsets and tilts close to 0 rad due to the strong common mode subtraction, as shown in chapter 12.

Part IV

Laser Interferometer Space Antenna

Chapter 15
Overview of RIN in LISA

Please note that most content of the next three chapters has already been published in [P4] in collaboration with the co-authors.

In the following this thesis transfers all the RIN coupling heritage from the previous chapters and applies it to the full LISA mission. It gives the rationale for some of the RIN requirements stated later in chapter 18, especially for the 1f-2f-RIN bandwidth.

Analyzing RIN in LISA is naturally more complex than in LPF: Since it is a property of each laser, it propagates through the constellation into the various interferometers and generates additive power noise to the time-varying beat signals on every PD. This noise couples inevitably to the phase readout at around the heterodyne frequency and its first harmonic, as derived in part II. We show that it is one of the dominating metrology noise sources (after removal of laser frequency noise) if not carefully controlled.

1f-RIN is typically the biggest contributor, since the resulting phase noise is scaled by the ratio of the beam powers, which are, for LISA, fairly large (magnification in the long-arm (ISI) interferometers by about seven orders of magnitude). As such, its impact on the sensitivity has to be understood and mitigated.

We describe the coupling in the context of the LISA mission architecture, taking into account the constellation characteristics, possible correlations, the currently forseen optical parameters and the effects of LPF-comparable mitigation schemes.

Further, we study the impact of TDI on the RIN phase error by means of simulation and compare it with analytical expectations. We find that the coupling exhibits performance characteristics similar to that of an uncorrelated sub–1 $\mathrm{pm}/\sqrt{\mathrm{Hz}}$ noise, assuming reasonable implementation of the mitigation strategies.

Since each laser is involved in six interferometers, they can possibly add correlated noise in those interferometers. However, the RIN to phase coupling depends on the absolute beat frequency (and its harmonic), which means that RIN at different heterodyne frequencies in different interferometers can be considered uncorrelated if the beatnote frequencies are reasonably well separated, i.e., by more than the measurement band of a few Hz; this holds even if the same laser is involved. RIN from different laser sources is always considered uncorrelated, especially at MHz frequencies. This means that RIN in the

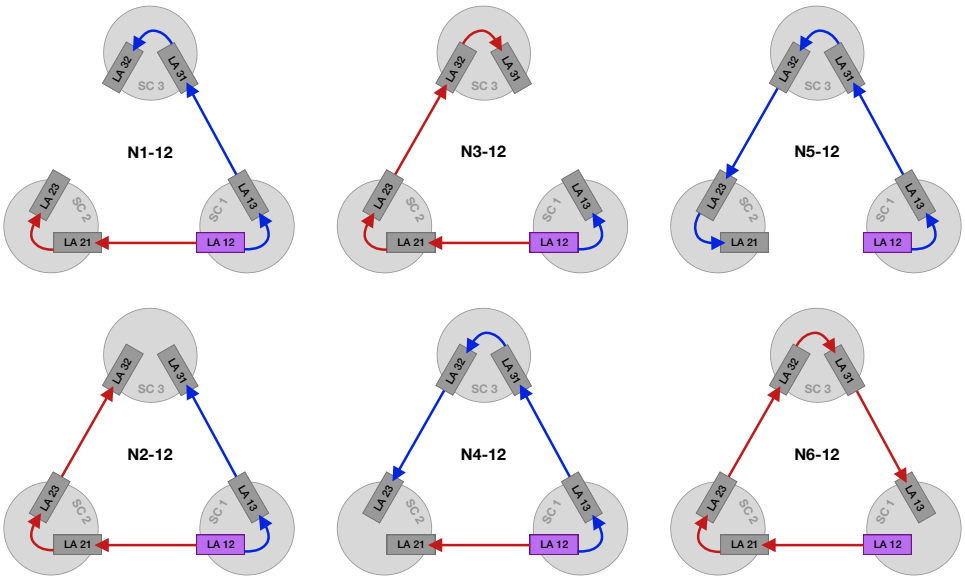

Figure 15.1 The different locking configurations, here with laser LA_{12} as the primary laser. The nominal scheme is likely N1-12 which is structurally the flattest (in a measure of locking distance from each laser to the primary laser, causing the least amount of "noise echos"). For each locking topology, the primary laser can be chosen by permutation. This image is a reprint from [30].

TMIs and Reference Interferometers (RFIs) on the same SC is correlated, while the ISIs may not have correlations. Furthermore, the ISIs are subject to orbital Doppler shifts (in the MHz range) and thus their heterodyne frequencies vary. The expected shifts can be calculated beforehand and are used to enable and optimize the interferometry and detection process. The absolute beat frequencies are technically restricted to a range of approximately (5 to 25) MHz via an (offset) frequency locking scheme of the lasers. This results in a configuration where one primary laser is locked to a cavity, while the other five lasers are locked (with MHz offsets) to the primary laser. The required offset frequencies are calculated on ground, yielding a so-called frequency plan [84]. Various possible locking topologies (with LA_{12} as the primary laser) have been identified [31, 84], as shown in figure 15.1. The locking also inevitably imprints any noise (and signal) information of the interferometers used for locking onto the locked lasers. Therefore, RIN-induced phase noise will also be added to the locked laser and propagates through the constellation into all six interferometers of that laser. Furthermore, the next laser that locks on the first locked laser will continue to carry this noise and thus have locally increased phase noise.

Figure 15.2 shows one possible schematic for the local laser control loop used for locking. Here, we assume that the error signal of the control loop has been balanced between the two interferometer output ports (current baseline), which propagates only a reduced amount of phase noise "echos" through the constellation. The exact amount of noise reduction due to balanced detection is still under review, but current design studies require

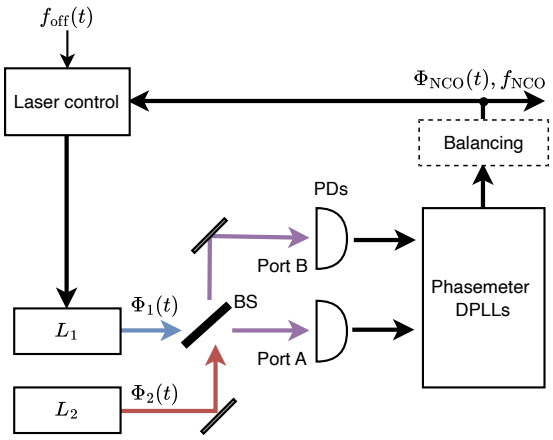

Figure 15.2 Schematic of the offset frequency locking control loop from [P4]. This represents one LISA interferometer used for locking laser L_1 to laser L_2 with a typical bandwidth of multiple kHz. The two lasers with phase evolution $\Phi_i(t)$ are brought to interference via the BS, detected on the PDs and measured in the phasemeter using the DPLLs. The two output ports are used to apply balanced detection. Then, the instantaneous (balanced) frequencies of the DPLL are used to offset lock the lasers according to the predetermined frequency planning. Any excess noise that remains in-band after balancing will be imprinted on L_1 and "echoed" throughout the constellation.

a reduction of about 90 % for 1f-RIN. During the mission, it may be necessary to adjust the balancing process due to degradation processes or frequency dependent differential signal attenuation between ports. A more detailed theoretical analysis on the balancing efficiency is given in appendix C.

We calculate and simulate these effects in the following. Luckily, TDI strongly suppresses any laser phase fluctuations in post-processing, including echoes from the locking control loops, such that the final TDI variables are unaffected by the choice of the locking topology, as previously suggested in [31, 36].

Chapter 16

RIN coupling in LISA

As mentioned before in this thesis, the key RIN properties derived in part II are almost directly applicable to LISA. In the following, the main characteristics are briefly recapped and put into context for LISA.

The RIN $n = \delta P/\langle P(t)\rangle$[1] of any laser power $P(t)$, usually expressed in ASD units of $1/\sqrt{\text{Hz}}$, causes phase noise in the LISA interferometric readout via three distinct coupling channels.

Firstly, "DC-RIN" inside the measurement band at low frequencies causes slow intensity fluctuations that lead to radiation pressure on the SCs (negligible) and TMs (not negligible). This drives the low-frequency RIN requirements and has an assumed level of $100\,\text{ppm}/\sqrt{\text{Hz}}$ at 0.1 mHz. It gives a small contribution to the TM acceleration of only about $0.35\,\text{fm/s}^2/\sqrt{\text{Hz}}$, out of a total acceleration noise allocation of roughly $10\,\text{fm/s}^2/\sqrt{\text{Hz}}$ at 0.1 mHz [19], see also chapter 18.

Secondly, 1f-RIN from around the heterodyne frequency causes additive phase noise to the main signal on the PDs.

Finally, 2f-RIN from around twice the heterodyne frequency is optically down-mixed and also produces additive noise (to first order) at the heterodyne frequency.

We focus here on the latter two mechanisms. They do not cause any direct force noise (at relevant in-band frequencies), and therefore do not generate any real TM motion signal, but cause an additive small-vector readout noise instead.

Since the RIN is a property of the laser beams, it appears correlated on all QPD segments of a single diode. In the following, we use the terms QPD and PD interchangeably, as it has no impact on our description of the RIN coupling in the longitudinal degree of freedom. For DWS, always pairs of left-right or top-bottom quadrants are used to deduce differential wavefront delays arising from angular beam alignments. Since RIN is also correlated here, the effective coupling is almost identical to the longitudinal channels, except for the intrinsic balancing. The longitudinal phase signal is lost in ideal DWS and the angular differential phase is retained.

[1] Notation slightly different to the rest of the document to remain coherent with the published article.

16.1 Theory of DPLL readout

In the next sections, we derive the RIN to phase coupling equations using the LISA-specific DPLL readout architecture (original calculation by O. Hartwig).

The DPLL depicted in figure 3.4 is a control loop that uses the error signal, Q, to adjust the total phase and frequency of an NCO. Contrary to a simple I/Q demodulation, the phase readout is not directly given by combining the I/Q channels, but instead available by digitally reading out the NCO registers.

When the loop is closed, and if we assume it to work perfectly with infinite gain in the measurement band, the error signal will be exactly equal to zero. The error signal is produced by multiplying the incoming signal (modeled as a cosine) by a sine that is perfectly in phase.

We consider an input signal $V(t)$ that has a strong main beatnote plus small additive disturbing terms, representing small-vector RIN. We write

$$V(t) = A\cos\big(\Phi(t)\big) + n(t), \tag{16.1}$$

where we assume A to be constant, and $\big|n(t)\big| \ll A$. Here, $\dot{\Phi}(t)$ is typically in the order of MHz. $n(t)$ represents our different RIN terms, but could in principle also be any other additive noise.

We assume that the phase error caused by the disturbance $n(t)$ is small, of order $\ll 1$ expressed in cycles or radian. Therefore, we consider the NCO signal used in the lock to closely follow the main beatnote, and model it as

$$U(t) = \sin\big(\Phi(t) + \varphi(t)\big), \tag{16.2}$$

where $\varphi(t) \ll 1$ accounts for the phase readout errors due to the disturbance $n(t)$. The total phase

$$\Phi_{\mathrm{NCO}}(t) = \Phi(t) + \varphi(t) \tag{16.3}$$

represents our phase readout and is available from the phasemeter phase accumulator.

The error signal is then computed by mixing the NCO signal with the input signal,

$$Q(t) = \langle V(t)U(t)\rangle, \tag{16.4}$$

where $\langle\cdot\rangle$ denotes a low-pass filter removing frequency content far away from DC. We assume that this filter is a linear operation, in the sense that $\langle aX + bY\rangle = a\langle X\rangle + b\langle Y\rangle$. A typical example for such a filter is a moving average.

The loop will adjust the phase of the NCO to drive the error signal to zero. This means we can model how the disturbance $n(t)$ affects the output of the DPLL for the closed loop by solving the equation $Q \equiv 0$ for φ; i.e., by finding the NCO phase for which the error signal vanishes.

16.1.1 Phase readout without disturbance

We first consider a scenario where there is no disturbance, i.e., $n(t) = 0$ in the above expressions. With our locking condition we get

$$Q(t) = \langle A\cos(\Phi(t))\sin(\Phi(t)+\varphi(t))\rangle \tag{16.5}$$
$$= \frac{A}{2}\langle \sin(2\Phi(t)+\varphi(t)) + \sin(\varphi(t))\rangle \tag{16.6}$$
$$= \frac{A}{2}\sin(\varphi(t)) \tag{16.7}$$
$$\approx \frac{A}{2}\varphi(t) \equiv 0 \implies \varphi(t) = 0, \tag{16.8}$$

where we used the trigonometric identity

$$\cos(a)\sin(b) = \frac{1}{2}(\sin(a+b) - \sin(a-b)) \tag{16.9}$$

and that $\varphi(t) \ll 1$. This means we simply get

$$\Phi_{\mathrm{NCO}}(t) = \Phi(t), \tag{16.10}$$

i.e., our total NCO phase is equal to the input signal phase, which is what is desired.

16.1.2 Phase readout with disturbance

Combining the previous equations, we can write

$$Q = \langle A\cos(\Phi(t))\sin(\Phi(t)+\varphi(t))\rangle + \langle n(t)\sin(\Phi(t)+\varphi(t))\rangle. \tag{16.11}$$

Using the trigonometric identities and that $\varphi(t) \ll 1$, the first term on the right-hand side becomes

$$\langle A\cos(\Phi(t))\sin(\Phi(t)+\varphi(t))\rangle \approx \frac{A}{2}\varphi(t). \tag{16.12}$$

To treat the other term, we first expand to first order in φ and then neglect the second-order term containing $\varphi(t)n(t)$, yielding

$$\langle n(t)\sin(\Phi(t)+\varphi(t))\rangle \approx \langle n(t)\sin(\Phi(t))\rangle. \tag{16.13}$$

Using this in equation (16.11), with the locking condition $Q \equiv 0$, gives the phase error induced by $n(t)$,

$$\varphi(t) \approx -\frac{2}{A}\langle n(t)\sin(\Phi(t))\rangle, \tag{16.14}$$

and the total phase readout will be given as

$$\Phi_{\mathrm{NCO}}(t) \approx \Phi(t) - \frac{2}{A}\langle n(t)\sin(\Phi(t))\rangle. \tag{16.15}$$

This means that, to first order, the disturbance is simply mixed with the main beatnote and scaled by the reciprocal beatnote amplitude.

16.2 Scaling for RIN

We now need to apply equation (16.15) to the typical photodiode detection equations adapted for heterodyne interferometry. They provide the scaling factors for A and $n(t)$ that describe the RIN coupling correctly.

We use equation (7.3) from part II, adapted for LISA, to describe the interferometer output ports A and B of the recombination beamsplitter. The amplitude transmission and reflection coefficients are labeled τ, ρ, the average beam powers P_i, the heterodyne efficiency η_{het}, and RIN n_m, n_r for a general measurement and general reference beam m, r and a certain signal power in the carrier of $\epsilon_{\mathrm{carrier}}$. We have

$$\begin{aligned} P_{\mathrm{A}} = &\underbrace{\rho^2 P_{\mathrm{m}} n_{\mathrm{m}} + \tau^2 P_{\mathrm{r}} n_{\mathrm{r}}}_{\text{1f-RIN, port A}} \underbrace{+(n_{\mathrm{m}} + n_{\mathrm{r}})\rho\tau\epsilon_{\mathrm{carrier}}\sqrt{\eta_{\mathrm{het}} P_{\mathrm{m}} P_{\mathrm{r}}}\cos\big(\Phi(t)\big)}_{\text{2f-RIN, port A}} \\ &\underbrace{+2\rho\tau\epsilon_{\mathrm{carrier}}\sqrt{\eta_{\mathrm{het}} P_{\mathrm{m}} P_{\mathrm{r}}}\cos\big(\Phi(t)\big)}_{\text{Signal, port A}}, \end{aligned} \tag{16.16}$$

and

$$\begin{aligned} P_{\mathrm{B}} = &\underbrace{\tau^2 P_{\mathrm{m}} n_{\mathrm{m}} + \rho^2 P_{\mathrm{r}} n_{\mathrm{r}}}_{\text{1f-RIN, port B}} \underbrace{-(n_{\mathrm{m}} + n_{\mathrm{r}})\rho\tau\epsilon_{\mathrm{carrier}}\sqrt{\eta_{\mathrm{het}} P_{\mathrm{m}} P_{\mathrm{r}}}\cos\big(\Phi(t)\big)}_{\text{2f-RIN, port B}} \\ &\underbrace{-2\rho\tau\epsilon_{\mathrm{carrier}}\sqrt{\eta_{\mathrm{het}} P_{\mathrm{m}} P_{\mathrm{r}}}\cos\big(\Phi(t)\big)}_{\text{Signal, port B}}. \end{aligned} \tag{16.17}$$

Here, we already see that balanced detection of the form $(P_A - P_B)/2$ is able to suppress 1f-RIN (at least to some extent depending on the scaling factors), since it appears with the same sign in both ports. However, 2f-RIN appears with opposite signs in the two ports, identical to the main signal, and therefore cannot be suppressed by balanced detection.

From these equations we can model the input signal to the DPLL using

$$V(t) = \pm A\cos\big(\Phi(t)\big) + \sum_{i=m,r} a_i n_i(t) \pm \frac{A}{2} n_i(t)\cos\big(\Phi(t)\big), \tag{16.18}$$

with the scale factor $A = 2\rho\tau\epsilon_{\mathrm{carrier}}\sqrt{\eta_{\mathrm{het}} P_{\mathrm{m}} P_{\mathrm{r}}}$, while a_i represents the scale factor for one of the 1f-RIN terms and $n_i(t)$ the RIN of one of the beams. The $\pm$ encodes output port A or B. Since the RIN between the two beams is uncorrelated (as well as 1f- and 2f-RIN per beam), we can calculate their resulting phase noise independently. In terms of spectral densities, one can build their quadratic sum for the total phase noise afterwards.

We assume a relative power stability of the lasers of around $3 \times 10^{-8}\,\mathrm{Hz}^{-1/2}$ in the relevant bandwidth (model-based estimate in the LISA noise budget), such that the resulting phase noise will be small, $\varphi(t) \ll 1$. This allows to use the previous result of equation (16.14).

Therefore, we insert $n(t) = a_i n_i(t) \pm \frac{A}{2} n_i(t)\cos(\Phi(t))$ into equation (16.14), which gives for the resulting phase noise (generated by one laser beam $i = m, r$),

$$\varphi_i(t) = \underbrace{-\frac{2a_i}{A}\langle n_i(t)\sin(\Phi(t))\rangle}_{\text{1f-RIN phasenoise}} \underbrace{\mp\frac{1}{2}\langle n_i(t)\sin(2\Phi(t))\rangle}_{\text{2f-RIN phasenoise}}. \tag{16.19}$$

We find that the noise $n(t)$ appears mixed both with $\sin(\Phi(t))$ as well as $\sin(2\Phi(t))$. This implies that noise around $\dot{\Phi}(t)$ and $2\dot{\Phi}(t)$ are down-converted to the phasemeter base band and couple into the phase accumulator. Due to the down- and up-conversion process of the mixing, only half of that noise power is actually contributing to $\varphi(t)$, since the other half is filtered out. We also see that the 2f-RIN is independent of the signal amplitude or average beampowers.

The total RIN to phase coupling must contain the RIN from both beams,

$$\varphi_{\text{tot}}(t) = \varphi_m(t) + \varphi_r(t), \tag{16.20}$$

with the corresponding coupling factors $a_m = \rho^2 P_m$, $a_r = \tau^2 P_r$ in port A and $a_m = \tau^2 P_m$, $a_r = \rho^2 P_r$ in port B.

After balanced detection, these coupling factors become

$$A = 2\rho\tau\epsilon_{\text{carrier}}\sqrt{\eta_{\text{het}} P_{\text{m}} P_{\text{r}}}, \tag{16.21}$$

$$a_m = (\rho^2 P_m - \tau^2 P_m)/2, \tag{16.22}$$

$$a_r = (\tau^2 P_r - \rho^2 P_r)/2. \tag{16.23}$$

These mixing equations are used in the simulation results presented in the next chapter to carry over any phase-correlation information correctly. They also agree with the results derived in part II for a small-vector noise approach, adjusted for LISA with its more complex phase evolution.

Each interferometer (ISI, TMI, RFI) will carry such a phase error φ_{tot} (here named by interferometer and usually scaled by $\lambda/(2\pi)$ to displacement),

$$\varphi_{\text{ISI}}(t) = \varphi_{\text{ISI},m}(t) + \varphi_{\text{ISI},r}(t), \tag{16.24}$$

$$\varphi_{\text{TMI}}(t) = \varphi_{\text{TMI},m}(t) + \varphi_{\text{TMI},r}(t), \tag{16.25}$$

$$\varphi_{\text{RFI}}(t) = \varphi_{\text{RFI},m}(t) + \varphi_{\text{RFI},r}(t), \tag{16.26}$$

where the different 1f-RIN amplitudes and total phases depend on the different interferometer optical settings (see table 16.1).

Note regarding the parameter dx_{SC} from table 16.1: It is used as a residual path offset in the RIN to phase coupling equations, and we calculate a RMS value by integrating over a frequency band from (0 to 1) Hz as in $\sqrt{(10\,\text{nm}/\sqrt{\text{Hz}})^2 \cdot 1\,\text{Hz}} = 10\,\text{nm}$. In LPF, we

Parameter	Value	Description
λ	1064 nm	Laser wavelength
f_{het}	(5 to 25) MHz	Heterodyne frequency
$n_{\text{1f, 2f}}$	$3 \times 10^{-8}\,\frac{1}{\sqrt{\text{Hz}}}$	Maximum (white) RIN ASD in the band (5 to 50) MHz, see also section 18.1
τ^2, ρ^2	0.5	BS (in power when squared as given) transmission and reflection coefficients
b	$[0.9, 0, 1]$	Balancing efficiency, i.e. matching of the 1f-RIN amplitudes in the interferometer ports
$\eta_{\text{het,ISI}}$	0.75	Heterodyne efficiency from the overlap integral in a long-arm (ISI) interferometer
$\eta_{\text{het,TMI}}$	0.82	Heterodyne efficiency from the overlap integral in a TM (TMI) interferometer
$\eta_{\text{het,RFI}}$	0.82	Heterodyne efficiency from the overlap integral in a reference (RFI) interferometer
$\epsilon_{\text{carrier}}$	0.81	Portion of power in the carrier of the beams
$P_{\text{ISI,1}}$	350 pW	Mean power of the remote laser in the long-arm interferometer (from distant SC)
$P_{\text{ISI,2}}$	1 mW	Mean power of the local laser in the long-arm interferometer
$P_{\text{TMI,1}}$	500 nW	Mean power of the adjacent laser in the TM interferometer (from adjacent bench)
$P_{\text{TMI,2}}$	500 μW	Mean power of the local laser in the TM interferometer
$P_{\text{RFI,1}}$	500 nW	Mean power of the adjacent laser in the reference interferometer (from adjacent bench)
$P_{\text{RFI,2}}$	1 mW	Mean power of the local laser in the reference interferometer
dx_{SC}	$10\,\text{nm}/\sqrt{\text{Hz}}$	Residual translational jitter of the SC, with respect to inertial space.
ϕ_{ISI}	dx_{SC}	Without noises or signals the measured phase due to residual translational jitter
ϕ_{TMI}	dx_{SC}, $[-2\pi, 2\pi]$	Limit of TMI interferometer set-point due to residual jitter or TM guidance injection
ϕ_{RFI}	0 rad	RFI interferometer phase offset

Table 16.1 Parameters of the optical chain with special relevance for the RIN to phase coupling. Where multiple numbers are stated they correspond to the different simulations performed. The values are estimates from current design studies, and are subject to minor changes. Modified reprint from [P4].

measured a RMS in x_1 of about 2 nm, and a peak-to-peak difference of about 10 nm. Also note, that for our simulations, we do not use equations (16.22) and (16.23), but instead model imperfections in the balanced detection by artificially introducing a balancing efficiency, $0 \leq b \leq 1$, and then model the residual 1f-RIN terms as

$$\varphi_{\text{1f},i}(t) = -\frac{2a_i}{A}\langle n(t)\sin(\Phi(t))\rangle \cdot (1-b), \tag{16.27}$$

while still using perfect 50/50 BSs in the simulation. More information on the balancing efficiency are also given in appendix C.

16.3 Simplified phase noise equations without correlations

If only the maximum or RMS RIN to phase coupling is required (for example for the noise level in only one interferometer), one can simplify the equations above by dropping the phase information in the mixing process. This ignores correlation properties of RIN but still gives the right level of phase noise per individual interferometer. We use the effect of the filter to select two independent noise series at the in-band sampling frequency. These two time-series $n_{1f}(t), n_{2f}(t)$ have to be scaled due to the mixing and filtering process and represent RIN from around $\dot{\Phi}$ (1f-RIN) and $2\dot{\Phi}$ (2f-RIN). The scale factors arise from simplifying $\langle n(t)\sin(\Phi(t))\rangle$, which has an ASD of approximately $\frac{1}{\sqrt{2}}\tilde{n}$, with $\tilde{n}$ as the ASD value of $n(t)$.

Therefore, if we want to replace the mixing and filtering process with an in-band, downsampled version of the $n(t)$ noise that has the correct scaling, we can use

$$\langle n(t)\sin(\Phi(t))\rangle \approx \frac{1}{\sqrt{2}} n_{1f}(t), \tag{16.28}$$

$$\langle n(t)\sin(2\Phi(t))\rangle \approx \frac{1}{\sqrt{2}}, n_{2f}(t) \tag{16.29}$$

for the 1f and 2f-RIN terms, respectively. We typically use the requirement $\tilde{n}_{1f} = \tilde{n}_{2f} = 3 \times 10^{-8}\,\mathrm{Hz}^{-1/2}$, as explained in section 18.1.

In total, that gives for one beam

$$\varphi_i(t) \approx -\frac{2a_i}{A}\frac{n_{1f}(t)}{\sqrt{2}} - \frac{1}{2}\frac{n_{2f}(t)}{\sqrt{2}}. \tag{16.30}$$

The total RIN-induced phase noise from two beams would then be the same sum as before, $\varphi_{\mathrm{tot}}(t) = \varphi_m(t) + \varphi_r(t)$, but now expressed simply by four uncorrelated noise time series with low sampling frequency and corresponding standard deviation. This can be used to set upper boundaries per interferometer level or for the locally correlated measurements (by using correlated time series for upper-boundary estimates).

16.4 Common mode rejection properties with correlations

Further, we can look at the noise properties upon subtraction of a correlated measurement. This means, for example, the subtraction of two measured total phases $\Phi_2 - \Phi_1$, where the indices 1, 2 are placeholders for any of the LISA interferometers.

We directly consider the 1f-RIN contributions (per beam i) to this difference, which can be written as

$$\begin{aligned}
&\varphi_{2,i}(t) - \varphi_{1,i}(t) \\
&= \frac{2a_i}{A}\left\langle n_i(t)\sin(\Phi_1(t))\right\rangle - \frac{2a_i}{A}\left\langle n_i(t)\sin(\Phi_2(t))\right\rangle && (16.31)\\
&= \frac{2a_i}{A}\left\langle n_i(t)\sin(\Phi_1(t)) - n_i(t)\sin(\Phi_2(t))\right\rangle && (16.32)\\
&= \frac{2a_i}{A}\left\langle 2n_i(t)\cos\left(\frac{\Phi_1(t)+\Phi_2(t)}{2}\right)\sin\left(\frac{\Phi_1(t)-\Phi_2(t)}{2}\right)\right\rangle && (16.33)\\
&= \frac{4a_i}{A}\sin\left(\frac{\Phi_1(t)-\Phi_2(t)}{2}\right)\left\langle n_i(t)\cos\left(\frac{\Phi_1(t)+\Phi_2(t)}{2}\right)\right\rangle && (16.34)\\
&\approx \frac{4a_i}{A}\sin\left(\frac{\Phi_1(t)-\Phi_2(t)}{2}\right)\frac{n_{i,1\mathrm{f}}(t)}{\sqrt{2}} && (16.35)
\end{aligned}$$

$$= \sqrt{8}\frac{a_i}{A} n_{i,1\mathrm{f}}(t) \sin\left(\frac{\Phi_1(t) - \Phi_2(t)}{2}\right). \tag{16.36}$$

In the last steps, a similar simplification regarding the downmixing and filtering process has been made as before. We can see that any common terms in the $\Phi_i(t)$ will drop out in this approach. However, this simplification only works for identical scaling amplitudes a, A in the two interferometers, otherwise numerical simulations can be used.

For 2f-RIN coupling, which is independent of scaling factors, we let $n(t) \to n(t)\cos(2\Phi_i(t))$ and get

$$\begin{aligned}
&\varphi_{2,i}(t) - \varphi_{1,i}(t) \\
&= \frac{1}{2}\left\langle n_i(t)\sin(2\Phi_1(t))\right\rangle - \frac{1}{2}\left\langle n_i(t)\sin(2\Phi_2(t))\right\rangle && (16.37)\\
&= \frac{1}{2}\left\langle n_i(t)\sin(2\Phi_1(t)) - n_i(t)\sin(2\Phi_2(t))\right\rangle && (16.38)\\
&= \frac{1}{2}\left\langle 2n_i(t)\cos(\Phi_1(t) + \Phi_2(t))\sin(\Phi_1(t) - \Phi_2(t))\right\rangle && (16.39)\\
&= \sin(\Phi_1(t) - \Phi_2(t))\left\langle n_i(t)\cos(\Phi_1(t) + \Phi_2(t))\right\rangle && (16.40)\\
&\approx \frac{n_{i,2\mathrm{f}}(t)}{\sqrt{2}}\sin(\Phi_1(t) - \Phi_2(t)). && (16.41)
\end{aligned}$$

As for both the 1f- and 2f-RIN equations, this result is only valid for phases with large commonalities with slowly varying residuals of the $\Phi_1(t) - \Phi_2(t)$ subtraction (compared to the filter bandwidth), such as in the local interferometry in LISA.

To compare these results to part II, we include two uncorrelated laser beams, and let $n(t) \to n_m(t) + n_r(t)$. We find for 1f-RIN (assuming 50/50 BSs, identical signal amplitudes, identical beam powers per beam and $\tilde{n}_m \approx \tilde{n}_r$)

$$\varphi_{1\mathrm{f}}(t) \approx \frac{\sqrt{2\left(a_m^2 + a_r^2\right)}}{A} n_{1\mathrm{f}}(t) \sin\left(\frac{\Phi_1(t) - \Phi_2(t)}{2}\right) \tag{16.42}$$

and for 2f-RIN (where the power scaling is irrelevant, but still assuming $\tilde{n}_m \approx \tilde{n}_r$)

$$\varphi_{2\mathrm{f}}(t) \approx n_{2\mathrm{f}}(t)\sin(\Phi_1(t) - \Phi_2(t)). \tag{16.43}$$

This gives the same results as derived in part II, but here assuming a DPLL phasemeter and the total phase information, without previously subtracting common-mode frequencies between interferometers. Although note, equal beam powers are not foreseen in the LISA interferometers and hence not assumed in the following analysis.

16.5 Laser locking

The required control for laser locking adds another outer loop that uses the instantaneous frequency measured by the inner DPLL, as depicted in figure 15.2. Each laser has its own phase, $\Phi_1(t), \Phi_2(t)$, such that the beatnote is represented by the total difference phase $\Phi(t) = \Phi_1(t) - \Phi_2(t)$. As before, we denote by $n(t)$ an additive noise source, in our case RIN.

From the locking condition of the DPLL, equation (16.15), we know that

$$\Phi_{\mathrm{NCO}}(t) \approx \Phi(t) - \frac{2}{A}\langle n(t)\sin(\Phi(t))\rangle.$$

The outer offset frequency locking loop has the (ideal in-band) locking condition that

$$f_{\mathrm{NCO}}(t) - f_{\mathrm{off}}(t) \equiv 0, \tag{16.44}$$

$$\iff \dot{\Phi}_{\mathrm{NCO}}(t) - f_{\mathrm{off}}(t) \equiv 0 \tag{16.45}$$

where the frequency offsets $f_{\mathrm{off}}(t)$ are predefined values calculated from the frequency planning.

This locking is assumed to be perfect (in the measurement band, within a bandwidth of $\sim 10\,\mathrm{kHz}$), such that any disturbance of the offset phase, for example due to RIN, laser frequency noise, or even gravitational-wave signals, is added sign-inverted to the laser phase (compared to the phasemeter measurement). This implies that any of those terms cancel in the respective interferometer. Note that we assume the current baseline, i.e., that the locking will use the balanced readout, such that 1f-RIN is already minimized at the input to the control loop and therefore not fully imprinted on the laser, and thus not fully canceled on the level of individual PDs. Since 2f-RIN is not canceled by balanced detection, it will be fully imprinted on the laser, i.e., it will be fully canceled on the level of individual PDs.

We can see this easily if we look at the outer loop locking equation. In the phase domain, after integrating equation (16.44) and setting the integration constant to 0, we have

$$0 \equiv \Phi_{\mathrm{NCO}}(t) - \Phi_{\mathrm{off}}(t) \tag{16.46}$$

$$\Rightarrow \Phi_{\mathrm{off}}(t) \approx \Phi(t) - \frac{2}{A}\langle n(t)\sin(\Phi(t))\rangle \tag{16.47}$$

$$\iff \Phi_{\mathrm{off}}(t) \approx \Phi_1(t) - \Phi_2(t) - \frac{2}{A}\langle n(t)\sin(\Phi_1(t) - \Phi_2(t))\rangle \tag{16.48}$$

$$\Rightarrow \Phi_1(t) = \Phi_2(t) + \Phi_{\mathrm{off}}(t) + \frac{2}{A}\langle n(t)\sin(\Phi_1(t) - \Phi_2(t))\rangle. \tag{16.49}$$

We see that the equation is implicit and cannot be solved analytically for $\Phi_1(t)$. We can iteratively solve it to first order,

$$\Phi_1(t) = \Phi_2(t) + \Phi_{\mathrm{off}}(t) + \frac{2}{A}\langle n(t)\sin([\Phi_1(t) = \dots] - \Phi_2(t))\rangle \tag{16.50}$$

$$\approx \Phi_2(t) + \Phi_{\text{off}}(t) + \frac{2}{A}\langle n(t)\sin(\Phi_{\text{off}}(t))\rangle \tag{16.51}$$

$$\approx \Phi_2(t) + \Phi_{\text{off}}(t) + \frac{2}{A}\langle n(t)\sin(\Phi(t))\rangle. \tag{16.52}$$

We expect that the effect of the loop on the input signal $\Phi_1(t)$ is very small due to $n \ll 1$, which allows the approximations in the last two equations for simulation purposes. It is assumed here that the loop will always have enough bandwidth to perfectly cancel the measured noise and imprint it on the laser phase, "echoing" it through the constellation.

As an example, we give the locking propagation equations for the baseline N1-12 locking configuration, see figure 15.1. The laser phase is locked with the phase error measured in the respective locking interferometer, and propagated with delays such that the laser phase errors can be written as

$$R_{12} = \text{Reference}, \tag{16.53}$$
$$R_{13} = \text{sign}(t_{13}) \cdot t_{13}, \tag{16.54}$$
$$R_{31} = \text{sign}(s_{31}) \cdot s_{31} + D_{31}(R_{13}), \tag{16.55}$$
$$R_{32} = \text{sign}(t_{32}) \cdot t_{32} + R_{31}, \tag{16.56}$$
$$R_{21} = \text{sign}(s_{21}) \cdot s_{21}, \tag{16.57}$$
$$R_{23} = \text{sign}(t_{23}) \cdot t_{23} + R_{21}, \tag{16.58}$$

where R_{ij} describes the RIN phase error that each laser LA_{ij} is carrying. The shorthand notation t_{ij} stands for the RIN phase error originating from RFI_{ij} and s_{ij} maps the RIN phase error from ISI_{ij}. Delays D_{ij} are defined as in figure 3.2 and the $\text{sign}(\cdot)$ represents the sign of the beat frequency in the corresponding interferometer.

16.6 RIN Correlations in LISA

In this section, we discuss possible correlations between interferometers.

First, a correlation may appear between the two ISIs sharing one same laser if the beatnote frequencies are identical at the times the measurements are combined in TDI, i.e., at multiples of the light travel time between the SC. We found that in the baseline N1-L12 configuration, these coincidences are rare events (due to the frequency planning and the arm-breathing). In any case, the overall RIN contributions in the ISIs will be completely dominated by the RIN of the local beam, due to the power ratios $\sqrt{P_{\text{ISI},1}/P_{\text{ISI},2}} \cdot n_{1\text{f}}(t) \ll \sqrt{P_{\text{ISI},2}/P_{\text{ISI},1}} \cdot n_{1\text{f}}(t)$. Thus, any potential correlation would involve one of the negligible terms, and can therefore be safely ignored.

Second, as explained before, 1f-RIN and 2f-RIN are several MHz apart due to the mission design, and thus can be considered as uncorrelated. However, the same two lasers interfere

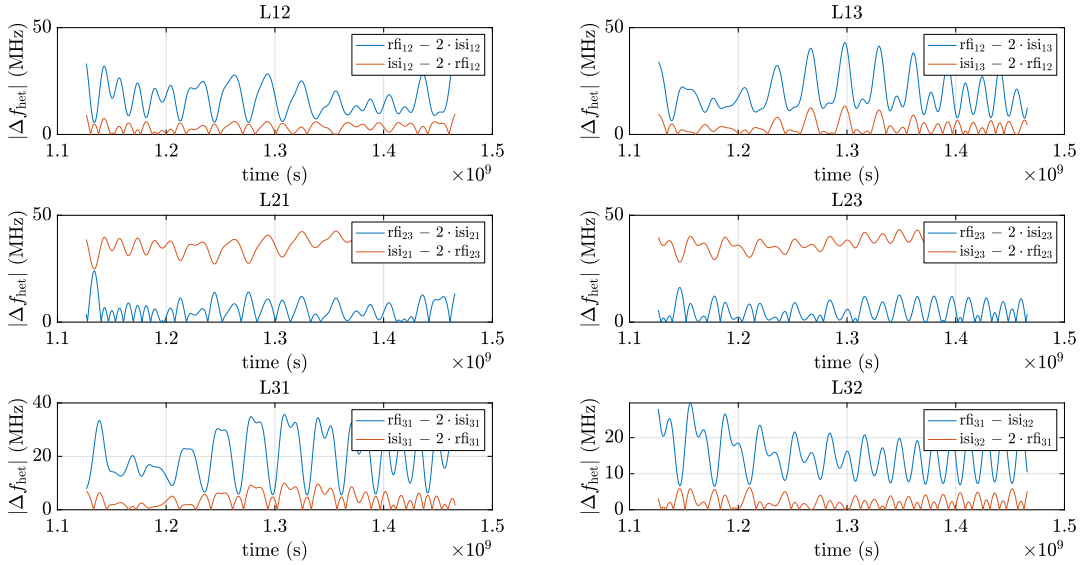

Figure 16.1 Locking beatnote differences between local and ISI interferometers per laser. It shows the rare possibility of 1f-2f-RIN correlations for the baseline configuration N1-12 for more than 10 years of data. We show pairwise absolute beat frequency differences for each laser. Only when the difference is becoming as small as a few Hz, the correlation would show up in the data. This only happens for a few hours in total for all lasers per configuration for the whole duration of more than 10 years and causes negligible extra phase noise, because 1f-RIN dominates the 2f-RIN term. The frequency plan considered here is computed for Earth-trailing orbits provided by ESA. Reprint from [P4].

in the four local TMIs and RFIs on each SC and therefore produce correlated RIN. The correlation (1f- with 1f-RIN) is not very strong, since the power ratios are inverse in the local interferometers of two adjacent MOSAs. In the case of 2f-RIN, however, there is full correlation, since it does not depend on the beam powers.

Third, we consider possible correlations between the 2 ISIs and the 4 remaining interferometers on one single SC. To minimize crosstalk in the DPLL, the frequency plan ensures that the RFIs/TMIs and the ISIs on one SC do not share the same heterodyne frequency, with a margin of about 2 MHz. Therefore, no direct correlations are expected to occur. The remaining possibility is for correlations between 1f- and 2f-RIN, e.g., if one beat is at 12 MHz and the other one at 6 MHz. This would lead to a correlation between 1f-RIN from the 12 MHz beat with 2f-RIN in the 6 MHz beat. However, this can be considered unproblematic, here again, as the 1f-RIN term is likely to be dominating. In addition, such a scenario is a rare event: even with a relatively large threshold of 50 Hz difference between the beats (compared to the ~ 4 Hz measurement band), the maximal duration involving correlated measurements across all lasers and interferometers is in the order of a few hours for over 10 years of simulated frequency plan data (shown in figure 16.1 for the baseline N1-L12 configuration). Furthermore, the frequency plan could be further

optimized to avoid such crossings, if desired.

We conclude that possible correlations can be safely neglected under the assumptions for realistic scenarios. However, the following simulations and calculations properly track correlations due to laser locking and local 2f-RIN. The results support this consideration.

16.7 Influence of TDI

TDI strongly suppresses laser phase noise by about eight orders of magnitude. For this purpose, it uses time shifted combinations of the interferometric phase measurements. As such, it also suppresses the laser locking noise "echos", since they appear in the measurements identically to the laser frequency noise that TDI is designed to suppress. Unfortunately, this process also adds other noises from the 18 interferometric measurements into the resulting TDI variables.

These noises have been studied and are now well understood (see, for example, [36]). To first order, RIN can be considered to behave like any other uncorrelated readout noise due to its properties discussed before; especially since the most significant RIN contribution appears uncorrelated in the ISIs, while the correlated appearances (TMI, RFI) produce much smaller noise contributions to the total measurement chain.

According to [36], an uncorrelated readout noise (e.g., in units of $\mathrm{m}/\sqrt{\mathrm{Hz}}$) entering all ISIs with a level of $\tilde{\varphi}$, which describes the dominant RIN contribution, has a PSD in the TDI combination X_2 of

$$S_{X_2}(\omega, \tilde{\varphi}) = 4\tilde{\varphi}^2 C_{XX}(\omega), \tag{16.59}$$

$$C_{XX}(\omega) = 16 \sin^2\left(\omega \frac{L}{c}\right) \sin^2\left(\omega \frac{2L}{c}\right), \tag{16.60}$$

where $\omega = 2\pi f$, and c is the speed of light in a vacuum.

Therefore, the dominant 1f-RIN coupling is expected to follow S_{X_2}, while the correlated terms should only appear if the 1f-RIN is completely suppressed, for example by perfect balanced detection. The latter is unrealistic in a real system, but can be used to create a complete TDI model for the coupling and to verify our understanding. It is not entirely described by S_{X_2} and needs to be modified as given in the results section.

Chapter 17
Simulations and results

17.1 Simulation architecture

To verify the validity of the analytical derivations presented in the previous chapter and track the effects of possible correlations, we implemented a time-domain simulation.

Figure 17.1 gives an overview of this simulator (currently implemented in MATLAB [85]), which has multiple stages and is able to simulate the whole LISA constellation with its 18 interferometers.

The simulation is performed in phase (time) domain to easily represent the mixing process inside the DPLL between the heterodyne signal and the sinusoidal assuming infinite gain. The laser and optical parameters are read from a configuration file and then propagated to the interferometers, where the interference phase of two beams is simulated. Then, the RIN phase error due to the mixing and demodulation process is calculated at high sampling frequency, and used as an output either for the locking scheme or directly for the output of the interferometers.

Typically, we simulate tens of thousands of seconds with a sampling frequency of 1 kHz. We use the total phase of each interferometer. Since we cannot simulate MHz frequencies directly for long time periods, we choose the offset frequencies such that all beatnote frequencies are in a range between 100 Hz and 250 Hz, instead of 5 MHz and 25 MHz. This is sufficient to accurately model the RIN coupling in the time domain, as its behavior is independent of the absolute heterodyne frequency.

We simulate laser locking, and correctly keep track of the beatnote polarities. The locking control loop is assumed to be perfect, such that the locking interferometer error signal is sign-inverted and added to the locked laser, and then propagates to all interferometers involving this laser.

Following previous considerations for the frequency planning, we assume that only local interferometers on the same SC share the same heterodyne frequency. Additionally, each laser carries its own RIN noise time series, which is propagated (and delayed where applicable) to the corresponding interferometers.

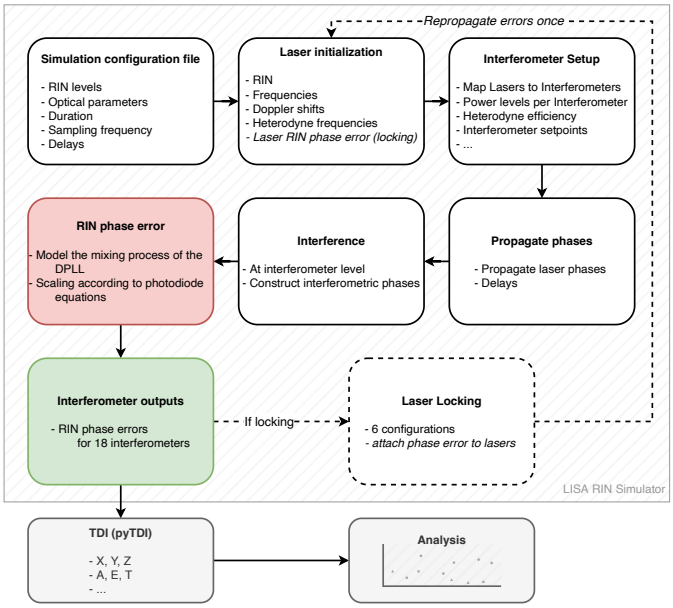

Figure 17.1 Diagram showing the different stages of the LISA RIN simulator. Reprint from [P4].

The delays, in the order of 8 s, are constant and symmetric for the two directions of each arm, but not equal between different arms. The initial assumption of unequal beatnote frequencies would not be violated for slowly-varying arm lengths due to the frequency locking, as explained above. This is especially valid for our relatively short simulations, for which the frequencies do not change much.

The RIN mixing is then applied using all beatnote phases and corresponding lasers with their RIN time series. We include a model for balanced detection with different balancing efficiencies. The RIN phase error is propagated as its own time series through the constellation, to avoid numerical problems with the large phase ramps of the beatnote phases.

The outputs are filtered and downsampled, typically to a final output sampling frequency of 10 Hz. The simulation records all 18 interferometer outputs as time-series for further analysis, e.g. calculating the ASD or checking cross-correlations.

Thanks to the pyTDI package the propagation through TDI can simply be calculated from the output as well.

17.2 Results

In this section, we present our analytical and simulated results for the LISA mission parameters from table 16.1. The main findings are summarized in table 17.1, figure 17.3 and figure 17.4. We show the expected noise levels per interferometer, local common-mode suppression, and the propagation through TDI.

Locking config.	Interferometer	1f-RIN	2f-RIN	Total ($b = 0.9$)	Total ($b = 1$)	Total ($b = 0$)
None	ISI_{ij}	8.7×10^{-12}	2.5×10^{-15}	0.87×10^{-12}	2.5×10^{-15}	8.7×10^{-12}
	TMI_{ij}	0.16×10^{-12}	2.5×10^{-15}	16.2×10^{-15}	2.5×10^{-15}	0.16×10^{-12}
	RFI_{ij}	0.22×10^{-12}	2.5×10^{-15}	22.2×10^{-15}	2.5×10^{-15}	0.22×10^{-12}
	$TMI_{ij} - RFI_{ij}$	65.6×10^{-15}	3.0×10^{-16}	6.5×10^{-15}	3.0×10^{-16}	65.6×10^{-15}
N1-12	ISI_{32}			1.5×10^{-12}	6.2×10^{-15}	15.0×10^{-12}
	ISI_{23}			1.5×10^{-12}	6.2×10^{-15}	15.0×10^{-12}
	ISI_{13}			1.2×10^{-12}	5.1×10^{-15}	12.3×10^{-12}
N2-12	ISI_{23}			1.7×10^{-12}	6.2×10^{-15}	17.4×10^{-12}
	RFI_{32}			1.5×10^{-12}	6.2×10^{-15}	15.0×10^{-12}
	RFI_{31}			1.5×10^{-12}	6.2×10^{-15}	15.0×10^{-12}
N3-12	ISI_{23}			1.7×10^{-12}	6.2×10^{-15}	17.4×10^{-12}
	ISI_{13}			1.5×10^{-12}	6.2×10^{-15}	15.0×10^{-12}
	ISI_{31}			1.5×10^{-12}	6.2×10^{-15}	15.0×10^{-12}
N4-12	ISI_{32}			1.7×10^{-12}	7.2×10^{-15}	17.4×10^{-12}
	RFI_{21}			1.5×10^{-12}	6.2×10^{-15}	15.0×10^{-12}
	RFI_{23}			1.5×10^{-12}	6.2×10^{-15}	15.0×10^{-12}
N5-12	ISI_{32}			1.7×10^{-12}	7.2×10^{-15}	17.4×10^{-12}
	ISI_{21}			1.5×10^{-12}	6.2×10^{-15}	15.0×10^{-12}
	ISI_{12}			1.5×10^{-12}	6.2×10^{-15}	15.0×10^{-12}
N6-12	ISI_{31}			2.1×10^{-12}	8.0×10^{-15}	21.2×10^{-12}
	ISI_{23}			1.7×10^{-12}	6.2×10^{-15}	17.3×10^{-12}
	RFI_{13}			1.5×10^{-12}	6.2×10^{-15}	15.0×10^{-12}

Table 17.1 Numerical simulation results of the RIN to phase coupling, based on the parameters listed in table 16.1. Reprint from [P4].

The first four rows in table 17.1 show the resulting phase noise in the unlocked case. The TMI-RFI subtraction does not yield exactly zero phase noise due to the mismatched powers. This can also be seen as the minimum in figure 17.3 for the blue trace. The following rows show the three interferometers with the largest propagated phase noise for each locking configuration. The last columns report the total phase noise assuming different balancing efficiencies (realistic case, best and worst). The laser locking is assumed to be applied to the data after balanced detection with the stated balancing efficiency. It can be seen that the locking locally increases the phase noise due to the imprint of RIN echos, and that the N1-12 scheme provides the lowest resulting total increase of noise. The numerical estimates are averages of the flat PSD in the band (0.01 to 2) Hz (using 24 averages and a Blackman-Harris92 window), from 30 000 s of data sampled with 1 kHz each. All values are given in $\mathrm{m\,Hz^{-1/2}}$. The relative standard deviation is of the order of a few %, values are rounded to the last digit.

The local correlations are visible in figure 17.2 for one SC without locking. The diagonal shows the histogram; off-diagonal elements show density plots with units of picometers. The reason for the slightly rectangular correlations between the local RFI and TMI arises from the mixing process, which contains a sinusoidal multiplication with a phase modulation (the TM setpoint) in this case. We see that the RIN-induced phase noise can

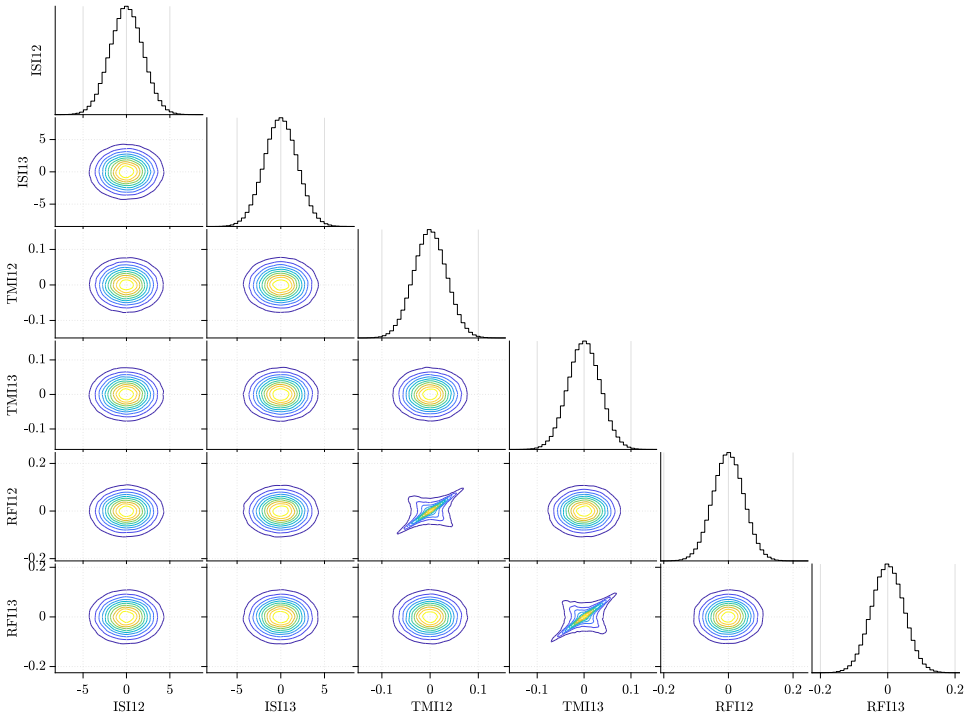

Figure 17.2 Correlations between noises of the local interferometers from figure 17.3, here for SC 1 (no locking), with 90 % balancing efficiency. The plot has been produced using [86]. Reprint from [P4].

be considered largely uncorrelated, even between adjacent local interferometers, due to the inversely distributed powers. This verifies our theoretical predictions and shows that the simulator tracks the correlations realistically.

17.2.1 1f-RIN estimates

Based on the theoretical derivation above and the optical parameters relevant for the RIN to phase coupling from the current LISA design (given in table 16.1), we estimate the expected noise levels in the three distinct interferometers without locking.

The 1f-RIN couplings are strong contributors to the phase noise in LISA. The TMI shows a 1f-RIN contribution of about $155\,\mathrm{fm}/\sqrt{\mathrm{Hz}}$, the RFI has a noise of about $220\,\mathrm{fm}/\sqrt{\mathrm{Hz}}$ and the ISI reaches even a level of $8.7\,\mathrm{pm}/\sqrt{\mathrm{Hz}}$. Assuming a balancing efficiency of 90 %, these values reduce to $15.5\,\mathrm{fm}/\sqrt{\mathrm{Hz}}$, $22\,\mathrm{fm}/\sqrt{\mathrm{Hz}}$, and $0.87\,\mathrm{pm}/\sqrt{\mathrm{Hz}}$. The correlated TMI − RFI subtraction in TDI is able to reduce the contribution of these two interferometers to about $6.5\,\mathrm{fm}/\sqrt{\mathrm{Hz}}$. Contrary to the results presented in table 7.1, a complete subtraction is not possible in LISA due to the unequal beam powers in the correlated interferometers, even if the residual translational SC jitter dx_{SC} vanishes.

In total, we get for a single link (uncorrelated ISI, two uncorrelated TMI − RFI measurements) $\sqrt{(0.87\,\mathrm{pm}/\sqrt{\mathrm{Hz}})^2 + (\sqrt{2}\cdot 6.5\,\mathrm{fm}/\sqrt{\mathrm{Hz}})^2} \approx 0.87\,\mathrm{pm}/\sqrt{\mathrm{Hz}}$, which achieves the desired noise reduction.

17.2.2 2f-RIN estimates

We find white-noise baseline estimates for 2f-RIN of about $2.5\,\mathrm{fm}/\sqrt{\mathrm{Hz}}$ in the ISI, TMI and RFI. This value is expected to be identical across the interferometers, because the coupling is independent of beam parameters, such as powers. Since it is correlated in the TMI − RFI subtraction performed in TDI, the contribution of these two interferometers is further reduced by a similar sine factor as the 1f-RIN (with twice its argument), and only adds marginal noise to the single link TM-to-TM measurement. Here, full subtraction is possible, since the noise in the correlated interferometers does not depend on the beam powers.

The total 2f-RIN noise in a single TM-to-TM link can be estimated (similarly to 1f-RIN) by $\sqrt{(2.5\,\mathrm{fm}/\sqrt{\mathrm{Hz}})^2 + (\sqrt{2}\cdot 0.3\,\mathrm{fm}/\sqrt{\mathrm{Hz}})^2} \approx 2.6\,\mathrm{fm}/\sqrt{\mathrm{Hz}}$. Therefore, the phase noise due to 2f-RIN is much weaker than the phase noise caused by 1f-RIN and essentially negligible in the noise budget for the given RIN requirement.

17.2.3 DWS

DWS uses pairs of photodiode quadrants to sense wavefront tilts between the measurement and reference beams. It is used for SC and TM angular control, since the wavefront tilts can be calibrated to yield physical TM-to-SC angles, and the angle of the SC to the incoming beam. As such, it uses the same phase readout (yet different quadrant combinations, see for example [33]) as the longitudinal channels and will therefore also be affected by RIN. The behavior is expected to be the same as in the longitudinal TMI − RFI common mode suppression (because pairs of quadrants are always combined), but with better results due to effectively equal power levels across the quadrants. Since the expected angles measured through DWS are rather small (usually much less than 1 rad for the non-calibrated quadrant phase) and the quadrants share the same correlated RIN, common-mode suppression, together with balanced detection, are expected to yield good minimization effects.

17.2.4 Contribution summary

In total, we find the quadratic sum of the 1f-RIN and 2f-RIN contributions for a single TM-to-TM link, with 90 % balancing efficiency and no laser locking, to be at a level of $0.87\,\mathrm{pm}/\sqrt{\mathrm{Hz}}$ for the longitudinal readout. This amount of noise has to be considered

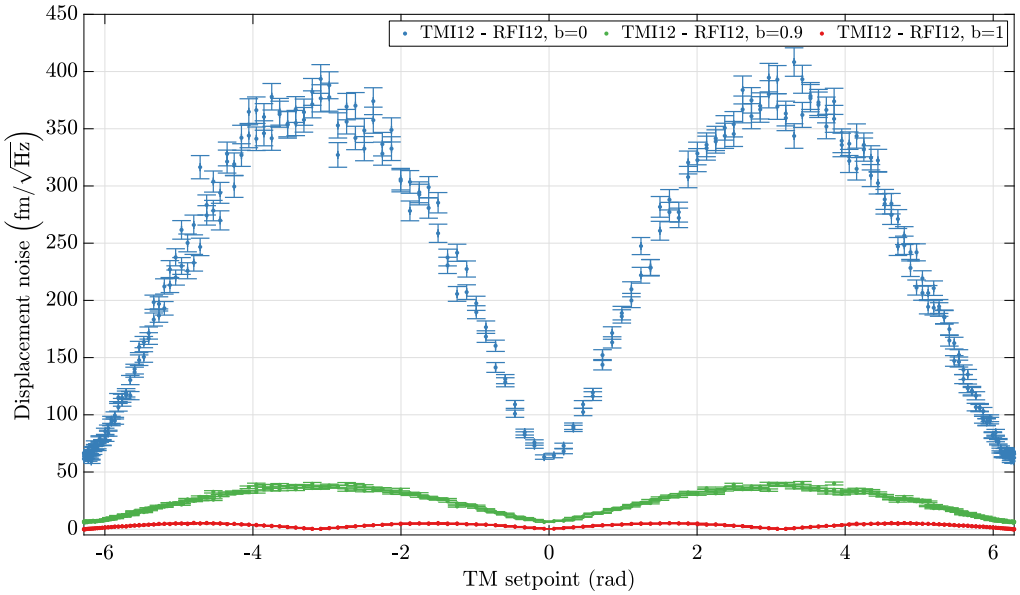

Figure 17.3 Simulated data for one local $\mathrm{TMI}_{ij} - \mathrm{RFI}_{ij}$ subtraction with different balancing efficiencies in the unlocked case. Reprint from [P4].

as an entry in the $\sim 10\,\mathrm{pm}/\sqrt{\mathrm{Hz}}$ noise budget of the total optical metrology noise. Let us note how important it is to meet the balancing requirements; if not, the total optical metrology budget would already be dominated by the RIN-induced phase noise alone.

More detailed estimates are given in table 17.1 as a summary of the expected noise ASD levels per local interferometer and the biggest local noise measurements for all locking schemes, based on the parameters of table 16.1. These have been calculated both analytically (where directly possible) and numerically simulated using the RIN simulator described above, where we disabled all other noises.

17.2.5 Local common-mode rejection

In figure 17.3, we present the local correlated behavior of the frequency-averaged RIN phase error in the $\mathrm{TMI}_{ij} - \mathrm{RFI}_{ij}$ subtraction. This shows the properties of the RIN phase error, following the expected sinusoidal shape. For perfect 1f-RIN subtraction ($b = 1$), only 2f-RIN remains. The different noise floors are due to the unmatched power levels in the two interferometers. For these simulations, a slow sine injection from $[-2\pi, 2\pi]$ has been injected to mimic TM motion for 30 000 s of data sampled at 1 kHz. Each point shown here corresponds to the total measurement having been cut into 100 s segments, and their flat PSDs averaged between 1 and 3 Hz.

The results follow the expected theoretical pattern (also agrees with table 17.1) and show the common-mode rejection for a differential phase (labeled TM setpoint here) between

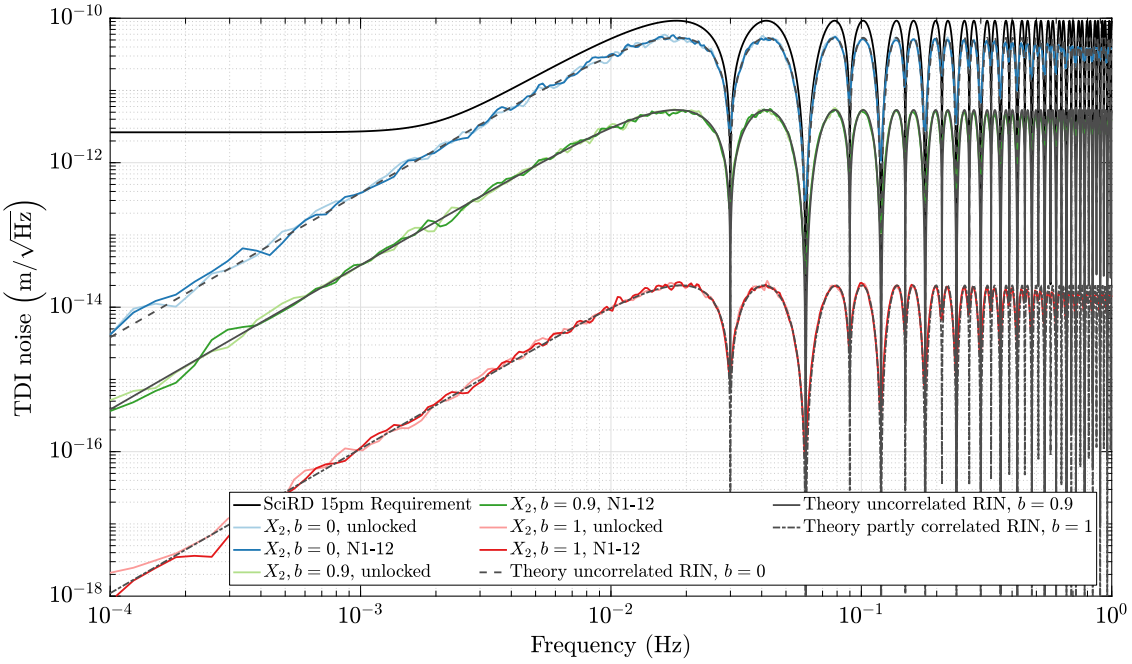

Figure 17.4 Propagation of the RIN phase error through TDI, with a simulation duration of 1×10^5 s and $f_s = 1000$ Hz. This plot has been produced with PyTDI [87] and the lpsd algorithm [58]. The theoretical expectations are plotted without the usual relaxation towards lower frequencies. Modified reprint from [P4].

the two interferometers. The theoretical pattern is described in part II. An important observation is that even for the correlated subtraction on the same MOSA, the noise cannot be fully reduced due to the unequal beam powers. Note that this rejection would be even weaker if two interferometers from adjacent optical benches would be used in the subtraction, due to the even more unequal beam powers. Figure 17.2 shows the measured correlations from this simulation.

Similar effects have been observed in LPF and on ground [P1]. During the mission, a set-point close to 0 rad may be chosen to minimize the noise.

17.2.6 Propagation through TDI

Having simulated all interferometers with and without locking, the phase outputs need to be propagated through TDI, similar to the real mission data. For this purpose we are using the software package PyTDI [87].

In figure 17.4, we show the results with different balancing efficiencies for the baseline locking configuration (N1-12), and compare these scenarios to the case of unlocked lasers. We also overlay the analytical expectations given below. As expected, we find that TDI

suppresses the additional noises due to laser locking. We see that the RIN phase error resembles a pure ISI uncorrelated readout noise, with the transfer function given in equation (16.59). The relevant noise level is given by

$$\tilde{\varphi} = \tilde{\varphi}_{\mathrm{ISI}} \approx (1-b) \cdot 8.7 \, \frac{\mathrm{pm}}{\sqrt{\mathrm{Hz}}}, \tag{17.1}$$

with the condition that the ISIs dominate, and $b < 1$. The residual 2f-RIN terms of $2.5\,\mathrm{fm}/\sqrt{\mathrm{Hz}}$ only have to be considered for perfect balanced detection ($b = 1$, see below), when the correlated noise in the TMI and RFI also becomes relevant.

A more detailed (yet still simplified) upper bound for the total noise after TDI can be estimated by adding the transfer function of the individual interferometer contributions, assuming the TMI and RFI add uncorrelated noise only. This leads to $\sqrt{2}$ smaller noise than the maximal possible contribution due to their correlation, but assuming good suppression due to the $\sin(dx_{\mathrm{SC}})$ factor (as relevant in the TMI-RFI subtraction through TDI), this would still be a reasonably high upper bound that reduces the required estimation effort drastically. The total RIN propagation after TDI would then follow (using the results from [36]),

$$S_{X_2} = S_{X_2,\mathrm{ISI}} + S_{X_2,\mathrm{TMI}} + S_{X_2,\mathrm{RFI}}, \tag{17.2}$$

where

$$S_{X_2,\mathrm{ISI}} = 4 C_{XX}(\omega) \cdot \tilde{\varphi}^2_{\mathrm{ISI}}, \tag{17.3}$$

$$S_{X_2,\mathrm{RFI}} = 4 C_{XX}(\omega) \cdot \tilde{\varphi}^2_{\mathrm{RFI}}, \tag{17.4}$$

$$S_{X_2,\mathrm{TMI}} = C_{XX}(\omega) \left(3 + \cos\left(\omega \frac{2L}{c}\right)\right) \cdot \tilde{\varphi}^2_{\mathrm{TMI}}. \tag{17.5}$$

The noise levels according to the results from the derivation in the previous sections,

$$\tilde{\varphi}_{\mathrm{IFO}} = \frac{\lambda}{2\pi} \sqrt{\left((1-b) \cdot a_{\mathrm{IFO,1f}} \cdot \tilde{n}_{\mathrm{1f}}\right)^2 + \left(\frac{1}{2}\tilde{n}_{\mathrm{2f}}\right)^2}. \tag{17.6}$$

This translates for the three distinct interferometers (assuming 50/50 beamsplitters) to

$$a_{\mathrm{ISI,1f}} = \frac{1}{\eta_{\mathrm{carrier}}} \sqrt{\frac{P^2_{\mathrm{ISI},1} + P^2_{\mathrm{ISI},2}}{2\eta_{\mathrm{het,ISI}} P_{\mathrm{ISI},1} P_{\mathrm{ISI},2}}}, \tag{17.7}$$

$$a_{\mathrm{RFI,1f}} = \frac{1}{\eta_{\mathrm{carrier}}} \sqrt{\frac{P^2_{\mathrm{RFI},1} + P^2_{\mathrm{RFI},2}}{2\eta_{\mathrm{het,RFI}} P_{\mathrm{RFI},1} P_{\mathrm{RFI},2}}}, \tag{17.8}$$

$$a_{\mathrm{TMI,1f}} = \frac{1}{\eta_{\mathrm{carrier}}} \sqrt{\frac{P^2_{\mathrm{TMI},1} + P^2_{\mathrm{TMI},2}}{2\eta_{\mathrm{het,TMI}} P_{\mathrm{TMI},1} P_{\mathrm{TMI},2}}}, \tag{17.9}$$

such that we find for the noise levels

$$\tilde{\varphi}_{\text{ISI}} \approx (1-b) \cdot 8.7 \, \frac{\text{pm}}{\sqrt{\text{Hz}}}, \tag{17.10}$$

$$\tilde{\varphi}_{\text{RFI}} \approx (1-b) \cdot 220 \, \frac{\text{fm}}{\sqrt{\text{Hz}}}, \tag{17.11}$$

$$\tilde{\varphi}_{\text{TMI}} \approx (1-b) \cdot 155 \, \frac{\text{fm}}{\sqrt{\text{Hz}}}, \tag{17.12}$$

which is clearly dominated by the ISI terms.

However, in the limit of $b \to 1$, the 2f-RIN contributions and their correlations become relevant. Then, the RIN residual is expected to be dominated by the sum of uncorrelated contributions in the ISIs and the fully correlated contribution among the local interferometers (TMI and RFI) in the two adjacent MOSAs. This special case of 2f-RIN correlation is not discussed in the literature, hence we give the derivation here.

If we assign the same noise to all local interferometers on one spacecraft ($\text{RFI}_{ij} = \text{RFI}_{ik} = \text{TMI}_{ij} = \text{TMI}_{ik} = n_{i,\text{2f-RIN}}$) and perform a derivation (calculated by M. Staab) similar to that presented in [36] (assuming equal arm lengths), we recover the following residual in X_2,

$$X_{2,\text{2f-RIN,corr.}} = (1-D^2)^2(1-D^4)\varphi_{1,\text{2f-RIN}}, \tag{17.13}$$

with the propagation delay D as defined in [36]. We note that only the RIN contribution of SC1 remains in X_2, while those of the other two SC cancel. We compute the PSD by taking the Fourier transform of the previous equation and calculating the expectation value of the squared magnitude, yielding

$$S_{X_2,\text{2f-RIN,corr.}} = 4\sin^2\left(\omega\frac{L}{c}\right) C_{XX}(\omega) \cdot \tilde{\varphi}^2_{\text{2f-RIN}}, \tag{17.14}$$

where $\tilde{n}_{\text{2f-RIN}}$ is the equal level of 2f-RIN in all interferometers and the usual TDI transfer function is modulated by an additional sine squared factor. This causes a faster roll-off of the PSD towards low frequencies and is thus only relevant at the maxima of the TDI transfer function. The sum of the uncorrelated ISI RIN $S_{X_2,\text{ISI}}$ term for $b = 1$ and the locally correlated 2f-RIN $S_{X_2,\text{2f-RIN,corr.}}$ term is plotted in figure 17.4 and agrees well with the simulation result.

In a nutshell, the simulated noise propagations through TDI are in very good agreement with the theoretical predictions, and the correlations do not have any significant influence under realistic circumstances.

Chapter 18

RIN requirements for LISA

Please note that this chapter contains sections in exact wording from an unpublished, internal technical note that was prepared in collaboration with C. Bode and T. Schwarze [53].

For the context of this thesis with regards to the LISA mission, this section presents an overview of the current recommended RIN laser requirements. They are based on the previous section regarding the 1f- and 2f-RIN coupling in LISA, and also based on investigations with a PM prototype at the AEI (the latter was carried out by C. Bode and T. Schwarze).

In general, the RIN requirement for LISA has to cover a large frequency range. It reaches from the low in-band frequency of around 0.1 mHz up to high frequencies of 3 GHz. Multiple frequency bands have been identified due to corresponding dominant coupling mechanisms and dependencies, as presented in the following section. The requirement regarding the heterodyne frequency range for 1f- and 2f-RIN coupling is driven by the goal to stay below an induced displacement noise of $1\,\mathrm{pm}/\sqrt{\mathrm{Hz}}$ to render its importance almost negligible. This is in accordance to the missions' metrology budget (see equation (3.1) in section 3.1). It would require 100 uncorrelated noise sources of this strength to violate the $10\,\mathrm{pm}/\sqrt{\mathrm{Hz}}$ requirement. As this thesis shows, a requirement of $3 \times 10^{-8}\,\mathrm{Hz}^{-1/2}$ above 3 MHz, together with a balancing efficiency of 0.9, reaches that goal, leaving a margin of about 13 %.

18.1 Recommended RIN requirements for LISA

The requirements are stated in table 18.1. The columns with the bold header are the actual requirements, the column in the middle gives the numerically integrated value of $\tilde{s}_{\mathrm{RIN}}$ for δ_{pp} (peak-to-peak value), based on the assumption of a white noise $\tilde{s}_{\mathrm{RIN}}$. This may differ from the actual δ_{pp} requirement for the reasons stated in the given reference.

The reasoning for the different frequency ranges is explained in the following.

DC-RIN: The requirement is coming from an allocation from the performance model [88] due to radiation pressure effects. It contains a margin for δ_{pp} with a factor of 3 due to thermal issues. The presence of an unexpected coupling in the PM is still under investigation, see [53].

kHz-RIN: This requirement is also from electrical tests with the protoype PM. The investigation was not completed for all frequencies due to an experimental limitation, therefore a margin factor of 3 for both RIN and δ_{pp} requirements was used [53].

1f-2f-RIN: This thesis describes this coupling in detail. No safety margin is applied to the requirement due to the uncertainty in related quantities (beam powers, RIN balancing efficiency requirement) and the knowledge that anything below $3 \times 10^{-8}\,\sqrt{\mathrm{Hz}}$ is unlikely feasible. The goal is to remain below $1\,\mathrm{pm}/\sqrt{\mathrm{Hz}}$, which is possible with 90 % balancing efficiency.

Furthermore, the maximum allowable δ_{pp} magnitude of distortions will be set as follows. In order not to saturate the photoreceivers, a maximum of 10% of power of the signal is allowed for the distorting signal. This is most critical for the ISI, where the ratio between signal and distortion coming from the local laser is worst. Note that absolute power is not of primary interest, as by design weaker signals will be amplified more in the photoreceivers. Dependent on the phase relationship between carrier and sidebands, both could add up towards saturation. Hence, we conservatively impose the 10% requirement onto the carrier only. The safety margin for δ_{pp} is 17 %, basically by rounding down to a requirement of $1 \times 10^{-4}\,\sqrt{\mathrm{Hz}}$:

$$2\epsilon_{\mathrm{carrier}}\sqrt{\eta_{\mathrm{Het,ISI}} P_{\mathrm{ISI},2} P_{\mathrm{ISI},1}} \cdot 0.1 \overset{!}{\geq} \frac{P_{\mathrm{ISI},2} \cdot \delta_{\mathrm{pp}}}{2}, \tag{18.1}$$

resulting in a value of $\delta_{\mathrm{pp}} \leq 1.17 \times 10^{-4}$. To add some margin, we suggest a requirement of $\delta_{\mathrm{pp}} \leq 1 \times 10^{-4}$. The frequency band includes some margin to the enforced (5 to 25) MHz heterodyne frequency band (due to frequency planning [84]), and is extended to twice the maximum heterodyne frequency (due to 2f-RIN coupling).

HF-RIN: No direct coupling is expected in this frequency range. However, aliasing effects due to imperfect anti-aliasing filters may cause additional noise components in the 1f-2f-RIN band. Distortions to the low power sidebands shall be suppressed well enough. Therefore the distortions shall only reach 10 % of the sideband beat powers. This, together with a damping factor for aliasing, leads to the given requirements for δ_{pp}. No additional margin applied. See [53].

The frequency shape for DC-RIN is given by

$$u(f) = \sqrt{1 + \left(\frac{0.1\,\mathrm{mHz}}{f}\right)^2}. \tag{18.2}$$

Frequency range	$\tilde{s}_{\mathrm{RIN}}(f)$ $[1/\sqrt{\mathrm{Hz}}]$ **(shall be $\leq$)**	δ_{pp} ($\tilde{s}_{\mathrm{RIN}}$ int.)	$\boldsymbol{\delta_{\mathrm{pp}}}$ **(shall be $\leq$)**	Reference
$(2 \times 10^{-5}$ to $1 \times 10^{2})$ Hz	$1 \times 10^{-4} \times u(f)$	(0.03)	1×10^{-2}	DC-RIN goal, section 18.3
$(1 \times 10^{-4}$ to $1 \times 10^{2})$ Hz ↪ Req. due to PM:	$1 \times 10^{-4} \times u(f)$ 2×10^{-3}	(0.03)	1×10^{-2}	DC-RIN, section 18.3 ↪ PM, [53]
$(1 \times 10^{2}$ to $3 \times 10^{6})$ Hz	2×10^{-6}	(1×10^{-2})	1×10^{-2}	kHz-RIN, [53]
$(3 \times 10^{6}$ to $60 \times 10^{6})$ Hz	3×10^{-8}	(6.4×10^{-4})	1×10^{-4}	1f-2f-RIN, section 17.2
$(60 \times 10^{6}$ to $3 \times 10^{9})$ Hz	3×10^{-8}	(4.6×10^{-3})	1×10^{-3}	HF-RIN, [53]

Table 18.1 RIN requirements for LISA. In gray, the DC-RIN requirement is extended to a low-frequency goal. Note that for DC the PM coupling leads to a less stringent requirement than the requirement derived from radiation pressure effects. The peak-to-peak value δ_{pp} is explained in section 18.2.

18.2 Note regarding the peak-to-peak value

In the table, a requirement for the maximum peak-to-peak amplitude δ_{pp} for distortions is given. These are calculated under the assumption that the distortion contains the noise of the full respective frequency band with bandwidth f_{B}. For the assumption of white noise this can be simplified to (factors $\sqrt{2}$ to convert from RMS to amplitude, 2 for peak-to-peak):

$$\delta_{\mathrm{pp}} = 2\sqrt{2}\sqrt{f_{\mathrm{B}}\tilde{r}^2} = \sqrt{8 f_{\mathrm{B}}}\tilde{r}. \tag{18.3}$$

In some cases (when explicitly stated), the calculated values for δ_{pp} are overridden by stricter requirements from additional considerations. Due to the lack of models for the coupling of DC-RIN and kHz-RIN, results of an electrical PM test are shown. These were used to derive coupling factors empirically. For 1f-RIN and 2f-RIN, the formulas from table 7.1 in combination with the parameters given in table 16.1 are applied to obtain estimates on the coupling.

Finally, the results are merged to give a requirement for RIN through the full spectrum in table 18.1.

18.3 Note regarding DC-RIN

Please note that radiation pressure noise on the TMs due to the effects of low frequency "DC-RIN" are not a central part of this thesis. They are well understood from LPF, see [89]. The following information is given for completeness.

The most stringent requirement for RIN in the measurement band is derived from slow power fluctuations causing radiation pressure effects on the TMs. This effect couples

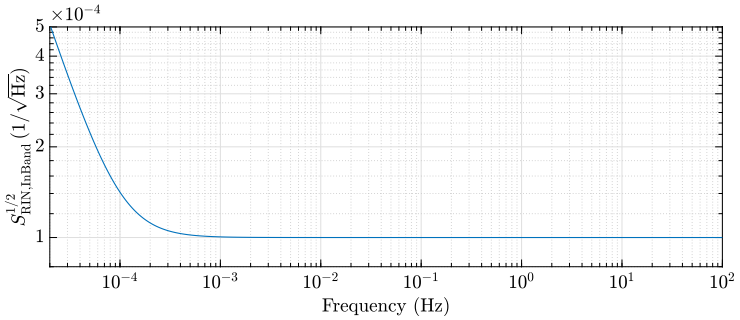

Figure 18.1 Requirement on RIN due to radiation pressure noise on the TMs.

directly via the TM acceleration noise. In-band power fluctuations cause force noise on the TM that in turn causes true test TM motion.

The description is found in reference [88, p. 85]. It considers an acceleration noise allocation from laser radiation pressure noise S_g^{LRP} of

$$S_g^{\mathrm{LRP}} \leq \left[1\,\mathrm{fm/s^2/Hz^{1/2}}\right]^2 \left(\frac{0.1\,\mathrm{mHz}}{f}\right)^2 + \left[0.5\,\mathrm{fm/s^2/Hz^{1/2}}\right]^2. \tag{18.4}$$

Furthermore it gives an estimate for the expected radiation pressure noise from RIN of

$$\begin{aligned} S_g^{\mathrm{LASER}} &\approx \left(\frac{2P_{\mathrm{TM}}}{M_{\mathrm{TM}}c}\right)^2 S_{\mathrm{RIN,InBand}} \\ &\approx \left[0.35\,\mathrm{fm/s^2/Hz^{1/2}}\right]^2 \times \left(\frac{P_{\mathrm{TM}}}{1\,\mathrm{mW}}\right)^2 \frac{S_{\mathrm{RIN,InBand}}}{\left(100\,\mathrm{ppm/Hz^{1/2}}\right)^2}. \end{aligned} \tag{18.5}$$

where, as a reminder, P_{TM} is the laser power incident on the TM, and $S_{\mathrm{RIN,InBand}}$ corresponds to $\tilde{r}^2$. Also, 100 % reflection is assumed.

It is stated further, that a RIN of 100 ppm/Hz$^{1/2}$ should be possible at 0.1 mHz with intensity control performed with a power monitor PD on the OB, with a second "out-of-loop" PD readout employed as a diagnostic.

An upper bound for a RIN slope to fulfill the acceleration noise allocation S_g^{LRP} is then given as

$$S_{\mathrm{RIN,InBand}}\,(f) \approx \left(100\,\mathrm{ppm/Hz^{1/2}}\right)^2 \cdot \left[1 + \left(\frac{0.1\,\mathrm{mHz}}{f}\right)^2\right], \tag{18.6}$$

and its square root ($=\tilde{s}_{\mathrm{RIN,DC}}(f)$) is plotted in figure 18.1. Note that the plot shows the goal for the frequency ranges down to 2×10^{-5} Hz, whereas the requirement starts at 1×10^{-4} Hz.

Part V

Concluding remarks

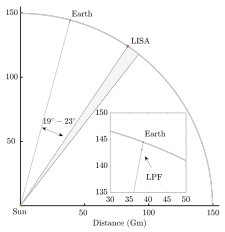

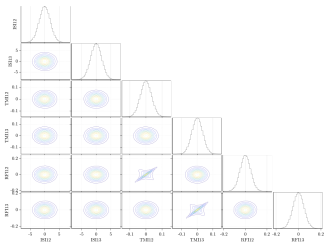

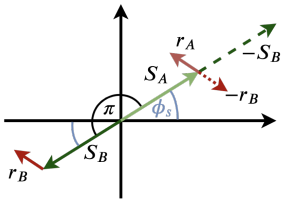

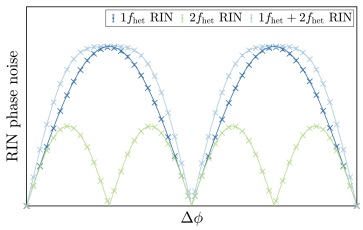

Chapter 19
Summary & Conclusion

This thesis shows the influence of laser RIN in the phase readout of heterodyne interferometers with particular focus on the LPF and LISA missions.

These two missions have (had) particularly stringent requirements due to the tremendous measurement challenge in space. Therefore, every noise source must be characterized and its influence investigated. The LPF mission was an ideal and unique laboratory to test and extend the understanding of high-precision optical metrology in space. The legacy from design, construction, testing, operations, modeling, and analysis tasks continues to deliver valuable contributions for the development of LISA.

As RIN is a critical source of phase noise, a detailed analysis aligned with the two missions is a relevant objective. Therefore, this thesis acts as an envelope for the findings published in [P1–P4] while adding more context and details from the LPF mission.

The theoretical coupling has been described in great detail and simplified equations have been derived, simulated, and tested with good agreement. The effect of balanced detection and common mode rejection properties are of interest as they allow mitigation of this noise to a large extent. While RIN coupling from around the heterodyne frequency was well known previously, a widely unknown coupling from two times the heterodyne frequency is described. It now yields a complete picture of this mechanism. While the 1f-RIN coupling depends on the beam powers, it can be mitigated by employing balanced detection. However, this is impossible for 2f-RIN, and the coupling does not depend on the beam powers.

The very successful LPF mission allowed a detailed study of this coupling. However, its OMS is a complex system that needed to be characterized in great detail to isolate the RIN behavior from the other noise sources. Therefore, a complete mission sensitivity analysis for varying operational conditions was necessary to verify the overall noise model with its RIN contribution. The in-flight measurement sensitivity was much better than the original requirements and reached $32.0^{+2.4}_{-1.7}\mathrm{fm}/\sqrt{\mathrm{Hz}}$ in o_{12}, and around $100\,\mathrm{prad}/\sqrt{\mathrm{Hz}}$ in the angular degrees of freedom, at frequencies where the OMS was dominating above 200 mHz. The analysis showed that the RIN contribution can be well modeled, and a fit to the mission data allowed the verification of the laser performance. The implementation of balanced detection and operating the TM phase offset close to zero allowed strong mitigation of the

RIN contributions in-flight to a level below $5 \times 10^{-6}\,\mathrm{Hz}^{-1/2}$, corresponding to $2.4\,\mathrm{fm}/\sqrt{\mathrm{Hz}}$ in o_{12}.

The overall models include contributions from the measurement system (ADC quantization noise, electronic noise) and laser noises (RIN, frequency noise, shot-noise), and are given for longitudinal and angular measurement channels. For example, in the differential TM to TM measurement o_{12}, this model explains the observed sensitivity in the frequency range (1.2 to 2.8) Hz to better than 20 % of relative deviation for most of the nominal mission. This analysis increases the confidence in understanding the system and paves the way for the more complex LISA design.

The analysis of experiments aiming directly at measuring the RIN to phase coupling in the longitudinal and angular phase channels shows a good agreement with the models. However, there are two remaining discrepancies. One regarding the RIN value over time and across different channels, and one due to the unexpected dip structure in the longitudinal data. However, this thesis shows that the general behavior agrees with the expectations and that the coupling only has little impact due to the nominally small offsets in the nominal mission configuration.

For LISA, a firm theoretical understanding of the constellation and its RIN propagation was developed. For testing the laser locking and the resulting noise levels, a mission simulator was built that verified the models. Using the current requirements and optical design parameters, the RIN induced phase error in the main science measurements without balanced detection reaches a large contribution of around $9\,\mathrm{pm}/\sqrt{\mathrm{Hz}}$. However, with the mitigation due to efficient balancing requirements and local common mode rejection, much lower (and less worrying) sub-pm noise levels are realistic. For LISA, 1f-RIN dominates (and is intensified) due to the unequal beam powers in the interferometers, while 2f-RIN is orders of magnitude below.

Due to the orbital motion and resulting Doppler shifts, as well as the frequency planning and offset locking of the lasers, RIN can be modeled as an uncorrelated noise source at ISI level and follows the known transfer functions through TDI.

Overall, this thesis shows that RIN to phase coupling is well understood. Its observation in LPF led to better modeling of the effect in the LISA constellation, allowing to set requirements for the lasers of $3 \times 10^{-8}\,\mathrm{Hz}^{-1/2}$ for (3 to 60) MHz, and for the balancing efficiency of 90 %. This ensures that the coupling can be well controlled within the bounds of the missions' sensitivity budget.

Chapter 20
Outlook

This thesis gives a comprehensive overview of the RIN coupling in LPF and LISA. As often is the case in such complex systems, a few open questions remain that could lead to further investigations.

Firstly, there is a small potential coupling of DC-RIN through the PM that was observed in electrical ground tests. The theoretical understanding of the underlying mechanism only allows for a second-order effect through the multiplicative channel, yet internal couplings within the DPLL are suspected. Further testing may be required to identify its characteristics.

Secondly, the RIN discrepancy between the longitudinal and angular degrees of freedom, in combination with the change of overlap integral and the unexplained 4f structure, remains intriguing. There is, for example, the tilt-dynamics optical bench simulator (TDOBS) experiment at the AEI that could be used to further investigate the RIN coupling on the ground.

Thirdly, an ongoing effort exists to characterize and ensure balancing efficiency requirements for LISA. Ground testing and more advanced simulations (including frequency dependent photoreceiver responses), that should be included in the overall mission instrument simulator and performance model, could increase understanding and help with risk assessments regarding quadrant failures or balanced detection degradation effects.

Furthermore, the described coupling mechanisms should be considered for future geodesy or gravity space missions employing a similar optical TM readout, see for example the ideas in [90].

Part VI

Appendix

Appendix A

Amplitude noise from additive vector noise

In the following a derivation for amplitude noise from an additive noise source is given using the same approach as in part II. A signal phasor S at frequency $\omega_s = 2\pi f_s$ and a small additive phasor V with frequency $\omega_v = 2\pi(f_s + \epsilon)$,

$$S = se^{i(\omega_s t + \phi_s)}, \quad V = ve^{i(\omega_v t + \phi_v)} \tag{A.1}$$

result in phasor R,

$$R = S + V = re^{i(\omega_s t + \phi_r(t))}, \tag{A.2}$$

with

$$r^2 = s^2 + v^2 + 2sv\cos(2\pi\epsilon t + \phi_s - \phi_v), \tag{A.3a}$$

$$\phi_r = \arg\left(e^{i\phi_s} + \frac{v}{s}e^{i(2\pi\epsilon t + \phi_v)}\right). \tag{A.3b}$$

We are interested in the amplitude variations of r, called γ, due to the presence of V. We assume $v \ll s$ and drop the v^2 term:

$$r^2 = s^2 + v^2 + 2sv\cos(2\pi\epsilon t + \phi_s - \phi_v) \tag{A.4a}$$

$$\approx s^2\left(1 + 2\frac{v}{s}\cos(2\pi\epsilon t + \phi_s - \phi_v)\right) \tag{A.4b}$$

We can further expand

$$r = s\sqrt{1 + 2\frac{v}{s}\cos(2\pi\epsilon t + \phi_s - \phi_v)} \tag{A.5a}$$

$$\approx s\left(1 + \frac{v}{s}\cos(2\pi\epsilon t + \phi_s - \phi_v)\right) \tag{A.5b}$$

$$= s + \underbrace{v\cos(2\pi\epsilon t + \phi_s - \phi_v)}_{=\gamma} \tag{A.5c}$$

The variance or squared RMS value is

$$\gamma_{\mathrm{RMS}}^2 = \frac{v^2}{2}. \tag{A.6}$$

We can immediately extend this result for a phasor at a frequency $f_s - \epsilon$. Such a phasor would end up at $-\epsilon$ in the resulting phase spectrum, and be folded to $+\epsilon$ in a typical one-sided spectral calculation. This is important for the notion of bandlimited noise around the signal, as it is present in real measurement systems. There, both sides of the signal contain a certain level of noise, that is uncorrelated between each other.

Using these considerations, we model the noise as follows: We assume bandlimited, white noise with a PSD value $n_0(f)$ and total noise power $NP = \int_B n_0(f)df \approx 2n_0B$, equally distributed left and right of the signal.

We already showed in the previous calculation, that noise at a frequency $f_s \pm \epsilon$ ends up at frequency ϵ in the one-sided phase spectrum. Therefore we can represent the noise for one particular frequency on the left and right side of the signal by sine phasors $N_{1,2}$ with the white noise amplitude n_0 in a band of $b = 1\,\mathrm{Hz}$. Both sine representations follow a uniform random phase distribution, since they represent uncorrelated noise:

$$N_{1,2} = \sqrt{2n_0b}\cos(\omega_{1,2}t + \psi_{1,2}), \tag{A.7}$$

with $\omega_{1,2} = 2\pi(f_s \pm \epsilon)$ and equal noise power $N_{1,2,\mathrm{rms}}^2 = n_0b$. So, the total noise power measured in a PSD of the resulting phase at frequency ϵ would be $N_{1,\mathrm{RMS}}^2 + N_{2,\mathrm{RMS}}^2 = 2n_0b = 2N_{1,2,\mathrm{RMS}}^2$. figure 7.4 shows a graphical representation.

We can simplify even further and use only one single sine representation for both phasors left and right with additional scaling, since their noise power ends up at the same frequency. This leads to a noise vector N with representation

$$N = \sqrt{2}\sqrt{2n_0b}\cos(2\pi(f_s + \epsilon)t + \psi),\ N_{\mathrm{RMS}}^2 = 2n_0b. \tag{A.8}$$

In the end, this is true for all frequencies in a bandwidth B that defines the sampling frequency of the output phase signal. Therefore, it is enough to propagate a general noise amplitude in this way to describe the whole resulting amplitude spectrum over the bandwidth B.

We can now describe the resulting amplitude noise from a general additive white noise process using equation (A.5): A signal S with amplitude s and an additive small noise N with amplitude $\sqrt{2}\sqrt{2n_0b}$ at frequencies $f_s \pm \epsilon$ will lead to amplitude deviations of the form

$$\gamma \approx \sqrt{2}\sqrt{2n_0b}\cos(2\pi\epsilon t + \phi_s - \psi). \tag{A.9}$$

Calculating the variance we find

$$\gamma_{\mathrm{RMS}}^2 = \frac{4n_0b}{2} = 2n_0b, \tag{A.10}$$

which gives in units of an ASD by dividing by $b = 1\,\mathrm{Hz}$ and taking the square root

$$\tilde{\gamma} = \sqrt{2}\sqrt{n_0}. \tag{A.11}$$

This result is true for any frequency ϵ. Therefore the frequency dependence was dropped and the result describes the whole output spectrum (for white noise).

This result is true for any small additive phase noise. Therefore we can calculate for an approximately white noise source around a strong carrier signal the resulting amplitude noise $\tilde{\gamma}$ with the following formula

$$\tilde{\gamma} = \sqrt{2} \cdot \text{Noise ASD}, \quad \left[\frac{\mathrm{rad}}{\sqrt{\mathrm{Hz}}}\right]. \tag{A.12}$$

Appendix B

Signal processing and noise propagation

This chapter gives a brief overview of the scaling factors for propagating noises through an interferometric readout due to typical processing steps.

B.1 Noise sources and their propagation

For the purpose of propagating noise sources through a readout system, it is advisable to organize them in two classes: correlated and uncorrelated, since they obtain different scaling factors. The correlated noises are generally treated like the correlated signal, while uncorrelated noises depend on the amount of channels used (except for shot-noise, see below).

Typically, the following noise sources (among many others) can be considered. First, laser beam noise (usually correlated) with

- Laser frequency noise – cancels largely in DWS,
- Laser intensity noise (due to 1f-RIN and 2f-RIN) – larger in LISA than on LPF due to unequal powers,
- Sideband Small Vector Noise (LPF),
- Pointing Noise, SC jitter,
- Straylight.

Second, readout noise (uncorrelated) with

- Shot-noise,
- ADC Noise,
- Electric circuit noise (TIA etc.),
- Phasemeter noise,
- Aliasing (in LPF, but better filters in LISA).

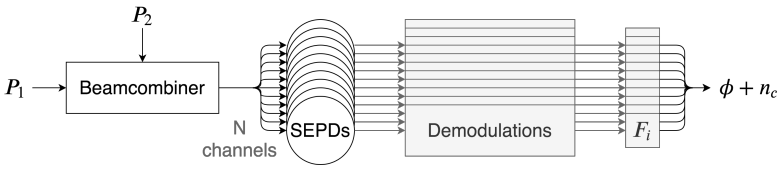

Figure B.1 Illustration of the measurement chain when distributing the optical signal on N channels and recombining complex signal amplitudes afterwards.

The usual processing involves balanced detection and QPDs for using DWS, which implies to split the optical beam power onto N segments, that may then be further processed with individual demodulations resulting in complex signal phasors F, that are being recombined before extracting the phase (with some resulting noise n_c), as shown in figure B.1. Recalling equation (7.20),

$$\tilde{\phi}_n = \frac{\text{Noise ASD}}{\text{Signal RMS}}, \quad \left[\frac{\text{rad}}{\sqrt{\text{Hz}}}\right]$$

one can easily calculate the following dependency on N, starting from a single quadrant, assuming the same level of noise on all N quadrants. Then the final combined noise n_c (after complex valued channel combinations) has the same level (in ASD) as the single quadrant, scaled by

- PD electronic noise: $\sim N^{1/2}$ (uncorrelated)
- ADC noise: $\sim N^{1/2}$ (uncorrelated)
- Shot-noise: $\sim N^0$ (uncorrelated)
- Frequency noise: $\sim N^0$ (correlated)
- RIN 1f: $\sim N^0$ (correlated)
- RIN 2f: $\sim N^0$ (correlated)

The shot-noise is the most interesting of the uncorrelated noise sources, since it depends on the (average) beam current I on a certain segment $\sim \sqrt{2eI}$, while the signal is also scaled by the current, such that the dependency on N cancels. The other noise sources behave as expected.

B.2 Example for DWS in LISA

Here, a simple processing architecture is assumed. We consider an example for redundant balanced detection and constructing DWS signals (see figure B.2):

- Redundant balanced detection ⇒ 16 QPD segments
- Redundant DWS

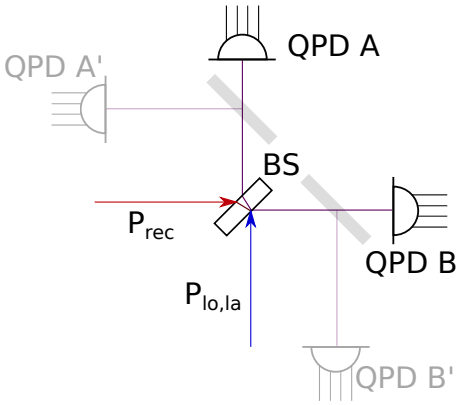

Figure B.2 Schematic of redundant balanced detection. Two beams with powers P_i are brought to interference and then split up onto eight quadrants per BS output port. SEPD Single-Element-Photodiode.

- Different signal processing/tracking architectures are possible, see [33]

Here, only a simple signal architecture is assumed, starting from a single quadrant noise $\tilde{\phi}_n$ being traced through the processing:

1. Propagate every segment through the PM: phase demodulation resulting in complex phasors F (see equation (7.1a)), carrying noise.
2. Combine always 4 phasors for balanced detection. For uncorrelated noises: Reduces total noise by $\sqrt{4}/4 = 1/2$, correlated noises retain their scaling.
3. Add always 2 balanced segments into typical (up,down,left,right) pre-DWS combinations. For uncorrelated noises: Reduces total noise by $\sqrt{2}/2 = 1/\sqrt{2}$
4. Build raw DWS signals (subtracting up-down, right-left). Uncorrelated noises: Increase total noise with factor $\sqrt{2}$ Correlated noises: Partial subtraction depending on DWS phase.

Appendix C
Balancing efficiency

In this appendix a more detailed description of balanced detection is given.

Balanced detection is a processing method to reduce the coupling of 1f-RIN and coherent straylight into the phase measurement.

This chapter looks at how well the subtraction works, i.e. if there are noise residuals remaining and on which system parameters they depend. The goal is to define a factor describing the quality of balanced detection. We call this factor the *balancing efficiency*. It is supposed to describe the reduction of phase noise (as opposed to the reduction of raw noise current) for a given noise source.

The principal idea is to subtract both output ports of the last recombination BS in an interferometer. To show the method using a very simplified model let the output powers in port A, P_A, and in port B, P_B, both contain the signal s and noise n. For 1f-RIN and specific straylight being represented by n, the important characteristic is that the signal has a $e^{i\pi} = -1$ phase difference between the two ports, whereas n (for this class of noises) does not have alternating signs:

$$P_A = s + n, \tag{C.1}$$
$$P_B = -s + n. \tag{C.2}$$

Therefore we can reduce the noise by subtracting the two ports, ideally giving

$$P_{\text{bal}} = \frac{P_A - P_B}{2} = s, \tag{C.3}$$

thus removing the noise terms in principle. The division by 2 preserves the signal amplitude that is measured in one port. This method is called *balanced detection*.

An important aspect is that 1f-RIN and coherent straylight have their own balancing efficiencies, allowing to study the trade-off for reduction of one noise source with respect to a potential increase of the other, see appendix C.5.

Previous work on balancing efficiency and RIN was carried out in [52]. To the authors understanding, they focused on power noise in the case that the local oscillator is much stronger than the measurement beam.

In the context of LISA, balanced detection is mainly needed to minimize the strong 1f-RIN coupling in the long-arm interferometer, whereas the dominant noise in the local interferometers may arise from backscattered straylight.

In the LISA performance budget [88] we currently assume a reduction of phase noise by 90 %, leaving 10 % phase noise residuals. For that case, the (in this chapter defined) balancing efficiency would equal 90 %, matching the currently used formalism.

Using the PD heterodyne equations from part II, the detected power is converted into electrical current by the PD responsivities R_a, R_b, passes through analogue electronics with gains g_a, g_b and picks up certain delays d_a, d_b, yielding processed data streams per channel C_A and C_B

$$C_A = d_a g_a R_a P_A = c_a P_A, \tag{C.4}$$
$$C_B = d_b g_b R_b P_B = c_b P_B, \tag{C.5}$$

with $c_i = d_i g_i R_i$. Delays are ignored in the following, which would lead to frequency dependent balancing.

For *balanced detection*, we subtract the two output channels such that $\Delta C = (C_A - C_B)/2$. Assuming that both channels have identical processing ($c_a = c_b$) and that the overlap integrals give the same result on both diodes ($\phi_a = \phi_b = \phi, \eta_a = \eta_b = \eta$) we find

$$\Delta C = \frac{c_a}{2}\left[P_1(\rho^2 - \tau^2) + P_2(\tau^2 - \rho^2) + 4\rho\tau\sqrt{P_1 P_2}\sqrt{\eta}\cos(2\pi f_{\mathrm{het}} t - \varphi_L - \phi)\right]. \tag{C.6}$$

If $\rho^2 = \tau^2$ also holds true, only the signal remains

$$\Delta C = c_a 2\rho\tau\sqrt{P_1 P_2}\sqrt{\eta}\cos(2\pi f_{\mathrm{het}} t - \varphi_L - \phi), \tag{C.7}$$

which is the intention of balanced detection.

We see, that for the DC terms to cancel completely, we need to ensure that both

- $\rho^2 = \tau^2$ **and**
- $c_a = c_b$ holds true.

The other possibility (after reordering the terms) is that

- $P_1 = P_2$ **and**
- $c_a = c_b$ holds true,

but this second option is very unlikely to be true for any interferometer in LISA.

Focusing on the first set of conditions, but assuming one of them does not hold true, say $\rho^2 \neq \tau^2$, it may still be desirable to adjust c_a and c_b in such a way that at least one of the DC terms is strongly suppressed. For example, if the offending noise is scaled by the powers and $P_1 \gg P_2$, then suppression of the P_1 term may take priority.

We can assume that one channel has adjustable gains, such that $c_b = \alpha c_a$ (there could be analogue gains or digital factors after the ADC), whereas the reflection and transmission coefficients ρ, τ are fixed by design with certain manufacturing tolerances.

In a mission like LISA it is important to monitor BS coefficients, beam powers and PD responsivities in order to adjust the gains in case of long-term degradation effects.

The following equation has to be minimized to suppress DC terms, or any noise that scales with them (see 1f-RIN)

$$P_1 c_a(\rho^2 - \alpha\tau^2) + P_2 c_a(\tau^2 - \alpha\rho^2) \stackrel{!}{=} \min. \tag{C.8}$$

This basically means, for a set of powers $\{P_1, P_2\}$ and $\{\rho^2, \tau^2\}$ we can calculate α such that the residuals are at minimum.

In the next sections the analysis is extended to include noise terms.

C.1 RIN coupling in the absence of balanced detection

To quantitatively describe the improvement by balanced detection (which we will name balancing efficiency) we need to compare it to an artificially computed total phase noise without balancing for reference.

In the absence of balanced detection, the two ports measure the following signal and 1f-RIN contributions (see part II)

$$\text{Port A:} \quad s_{\mathrm{A,rms}} = c_a \rho\tau\sqrt{2\eta_a P_1 P_2}, \quad r_a = c_a(\rho^2 P_1 r_1 + \tau^2 P_2 r_2) \tag{C.9}$$

$$\text{Port B:} \quad s_{\mathrm{B,rms}} = c_b \rho\tau\sqrt{2\eta_b P_1 P_2}, \quad r_b = c_b(\tau^2 P_1 r_1 + \rho^2 P_2 r_2) \tag{C.10}$$

That means, if we go over to spectral densities with $r_i \to \tilde{r}_i(f)$ we can calculate the inverted carrier-to-noise density to estimate the phase error (again see part II)

$$\tilde{\phi} = \frac{\text{Noise ASD}}{\text{Signal RMS}}, \quad \left[\frac{\text{rad}}{\sqrt{\text{Hz}}}\right]. \tag{C.11}$$

Common factors such as c_i cancel, since they are present in all terms. So, we measure the 1f-RIN phase noise of

$$\text{Port A:} \quad \tilde{\phi}_a = \frac{\tilde{r}_a}{s_{\mathrm{A,rms}}} = \frac{\rho^2 P_1 \tilde{r}_1 + \tau^2 P_2 \tilde{r}_2}{\rho\tau\sqrt{2\eta_a P_1 P_2}} \tag{C.12}$$

$$\text{Port B:} \quad \tilde{\phi}_b = \frac{\tilde{r}_b}{s_{\mathrm{B,rms}}} = \frac{\tau^2 P_1 \tilde{r}_1 + \rho^2 P_2 \tilde{r}_2}{\rho\tau\sqrt{2\eta_b P_1 P_2}} \tag{C.13}$$

individually (note that the sum in the nominator has to be calculated linearly for correlated 1f-RIN and quadratically for uncorrelated 1f-RIN). This means, if $\rho \neq \tau$, we may measure different phase errors, even if $\eta_a = \eta_b$.

To artificially combine both channels after demodulation, one could for example average the two output phases. Then, the total noise would be (with $\eta_a = \eta_b = \eta$, $\rho^2 + \tau^2 = 1$)

$$\tilde{\phi}_{a+b} = \frac{\tilde{\phi}_a + \tilde{\phi}_b}{2} = \frac{P_1\tilde{r}_1 + P_2\tilde{r}_2}{2\rho\tau\sqrt{2\eta P_1 P_2}}. \tag{C.14}$$

To compare this result, we can look at the total 1f-RIN present in the system in combination with the total signal amplitude available. This leads to a BS independent coupling factor, which is found by using

$$\text{Total:} \quad s_{\text{rms}} = \sqrt{2\eta_b P_1 P_2}, \quad r = P_1 r_1 + P_2 r_2, \tag{C.15}$$

yielding a nominal 1f-RIN coupling coefficient of

$$\tilde{\phi} = \frac{P_1\tilde{r}_1 + P_2\tilde{r}_2}{\sqrt{2\eta P_1 P_2}}. \tag{C.16}$$

We see that for $\rho\tau = 0.5$ the two equations equation (C.14) and equation (C.16) agree. The equality is quite good for well-manufactured BSs with only percentage-level deviations from an ideal 50/50 splitting, e.g. $\sqrt{0.47}\sqrt{0.53} = 0.4991$. For a BS with a 30/70 ratio, the total noise in equation (C.14) would increase by approximately 11 %.

C.2 Balanced detection in the presence of 1f-RIN

C.2.1 Phasor picture of balanced detection regarding 1f-RIN

To aid the analysis a phasor sketch is given in figure C.1. It is based on the assumption that for 1f-RIN terms the π phase shift from the BS cancels when measuring the power and their phasing is kept identical between the ports. For the analysis we always assume that the 1f-RIN phasors have identical phasing (e.g. their respective phase is identical) and thus allow 1f-RIN subtraction. Only the vector lengths, which are affected by system parameters, can be made equal (at least up to an optimum value) using adjustable gains in the detection chain.

In equation (C.6) we introduce 1f-RIN by substituting $P_i \to r_i P_i$ yielding

$$\Delta C_{1\text{f}} = \frac{1}{2}\left[P_1 r_1 c_a(\rho^2 - \alpha\tau^2) + P_2 r_2 c_a(\tau^2 - \alpha\rho^2)\right] \tag{C.17}$$

which is residual 1f-RIN in ΔC. The addition of the two $r_i P_i$ terms has to be performed quadratically, if $r_1 \neq r_2$ are uncorrelated, or linearly, if $r_1 = r_2 = r$ are correlated.

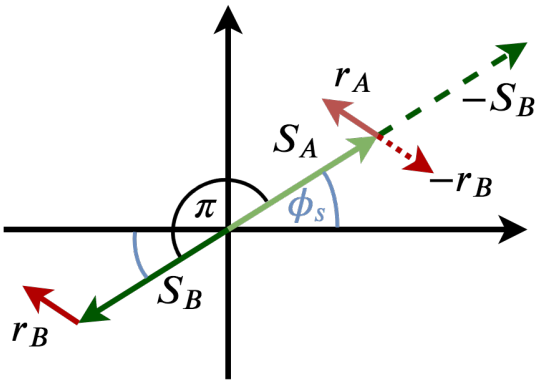

Figure C.1 Phasor representation of balanced detection. The dashed lines represent the phasors from port B after balanced detection. Ideally, the two RIN contributions are then completely in-phase and identical in magnitude, allowing perfect subtraction.

The signal RMS amplitude in the combined ports is (assuming equal overlap integrals and $c_b = \alpha c_a$) according to equation (C.6)

$$\Delta C_{\mathrm{s,rms}} = \frac{1}{2}\rho\tau c_a\sqrt{2\eta P_1 P_2}(1+\alpha) \tag{C.18}$$

So, the resulting phase error is

$$\Delta\tilde{\phi} = \frac{\Delta\tilde{C}_{\mathrm{1f}}}{\Delta C_{\mathrm{s,rms}}} \tag{C.19}$$

$$= \frac{\sqrt{\langle\left[P_1\tilde{r}_1(\rho^2-\alpha\tau^2)+P_2\tilde{r}_2(\tau^2-\alpha\rho^2)\right]^2\rangle}}{\rho\tau\sqrt{2\eta P_1 P_2}(1+\alpha)}, \tag{C.20}$$

which represents the 1f-RIN induced phase error in the case of correlated RIN.

The squaring and averaging action ensures positive results.

C.2.2 Correlated 1f-RIN between beams

Starting with equation (C.17), we set $r_1 = r_2 = r$ for correlated RIN. Therefore the addition between P_1 and P_2 terms can be performed linearly and we can solve

$$\Delta C_{\mathrm{1f,corr.}} = \frac{c_a r}{2}\left[P_1\rho^2 + P_2\tau^2 - \alpha\left(P_1\tau^2 + P_2\rho^2\right)\right] \stackrel{!}{=} 0 \tag{C.21}$$

$$\Rightarrow \alpha_{\mathrm{best}} = \frac{P_1\rho^2 + P_2\tau^2}{P_1\tau^2 + P_2\rho^2} \tag{C.22}$$

$$\Rightarrow \alpha_{\mathrm{best}} = \frac{P_{\mathrm{A,mean}}}{P_{\mathrm{B,mean}}}. \tag{C.23}$$

This choice of α_{best} reduces the 'raw' noise. However, the goal is to reduce the phase noise, which is not necessarily the same (but it is in this case).

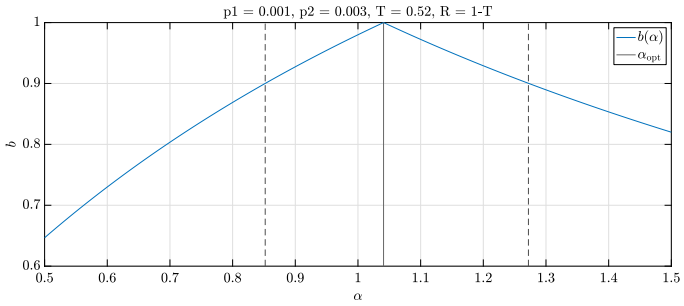

Figure C.2 Example for the balancing efficiency depending on parameter α in the case of correlated RIN. The dashed lines mark the region above 90 % balancing efficiency.

Therefore, we look into the optimization of the resulting 1f-RIN phase error

$$\Delta\tilde{\phi}_{\text{corr.}} = \frac{\left|P_1(\rho^2 - \alpha\tau^2) + P_2(\tau^2 - \alpha\rho^2)\right|}{\rho\tau\sqrt{2\eta P_1 P_2}(1+\alpha)}\tilde{r}(1f) \stackrel{!}{=} \min, \tag{C.24}$$

which gives an α_{opt} that is in agreement with $\alpha_{\text{best}} = \alpha_{\text{opt}}$.

We define the balancing efficiency $b = 1 - (\text{1f-RIN(balanced)}/\text{1f-RIN(unbalanced)})$, and find

$$(1-b) = \frac{\text{1f-RIN, balanced}}{\text{1f-RIN, unbalanced}} = \frac{\Delta\tilde{\phi}}{\tilde{\phi}_{a+b}} \tag{C.25}$$

$$= 2\frac{\left|P_1(\rho^2 - \alpha\tau^2) + P_2(\tau^2 - \alpha\rho^2)\right|}{(P_1+P_2)(1+\alpha)} \tag{C.26}$$

$$= 2\frac{\left|P_1\rho^2 + P_2\tau^2 - \alpha\left(P_1\tau^2 + P_2\rho^2\right)\right|}{(P_1+P_2)(1+\alpha)} \tag{C.27}$$

The interval $\alpha \in \{\alpha_{\min}, \alpha_{\max}\}$ is given for the condition $b \geq y$, with y being the worst allowed balancing efficiency, for example 90 %.

Example for correlated 1f-RIN. Assume the following parameters

$$P_1 = 1\,\text{mW},\ P_2 = 3\,\text{mW}, \tag{C.28}$$

$$\rho^2 = 0.48,\ \tau^2 = 0.52, \tag{C.29}$$

we find the coupling completely suppressed for $\alpha = 1.041$, meaning that $b = 1$. A balancing efficiency of at least $b = 0.9$ can be achieved for $\alpha \in \{0.852, 1.272\}$, see figure C.2.

C.2.3 Uncorrelated 1f-RIN between beams

In the case that $r_1 \neq r_2$ uncorrelated, the addition has to be performed as a quadratic sum:

$$\Delta C_{\mathrm{1f,uncorr.}} = \frac{c_a}{2}\left[\sqrt{P_1^2 r_1^2(\rho^2-\alpha\tau^2)^2 + P_2^2 r_2^2(\tau^2-\alpha\rho^2)^2}\right] \stackrel{!}{=} \min \tag{C.30}$$

$$\Rightarrow \alpha_{\mathrm{best}} = \frac{\rho^2\tau^2\left(P_1^2 r_1^2 + P_2^2 r_2^2\right)}{P_1^2 r_1^2 \tau^4 + P_2^2 r_2^2 \rho^4}, \tag{C.31}$$

and for $r_1 \approx r_2 = r$ we get

$$\Rightarrow \alpha_{\mathrm{best}} = \frac{\rho^2\tau^2\left(P_1^2 + P_2^2\right)}{P_1^2\tau^4 + P_2^2\rho^4}. \tag{C.32}$$

Here again, α_{best} only minimizes the raw noise produced by 1f-RIN.

The relevant reduction of phase coupling is analyzed in the following: We need to calculate the phase noise and find the optimal α_{opt} ensuring a minimum. The procedure ($\Delta C_{\mathrm{s,rms}}$ as before) yields

$$\Delta\tilde{\phi}_{\mathrm{uncorr.}} = \frac{\Delta\tilde{C}_{\mathrm{1f,uncorr.}}}{\Delta C_{\mathrm{s,rms}}} \tag{C.33}$$

$$= \frac{1}{\rho\tau(1+\alpha)}\sqrt{\frac{P_1^2\tilde{r}_1^2(\rho^2-\alpha\tau^2)^2 + P_2^2\tilde{r}_2^2(\tau^2-\alpha\rho^2)^2}{2\eta P_1 P_2}} \stackrel{!}{=} \min. \tag{C.34}$$

Again, the phase noise minimization also incorporates the difference in the signal amplitudes compared to α_{best} in equation (C.30), yielding

$$\alpha_{\mathrm{opt}} = \frac{P_1^2 r_1^2\rho^2 + P_2^2 r_2^2\tau^2}{P_1^2 r_1^2\tau^2 + P_2^2 r_2^2\rho^2} \tag{C.35}$$

Here, the unbalanced case holds as a reference and is given by equation (C.14), if the nominator is quadratically combined:

$$\tilde{\phi}_{a+b,\mathrm{uncorr.}} = \frac{\sqrt{P_1^2\tilde{r}_1^2 + P_2^2\tilde{r}_2^2}}{2\rho\tau\sqrt{2\eta P_1 P_2}} \tag{C.36}$$

In this case, the balancing efficiency b turns out to be

$$(1-b) = \frac{\text{1f-RIN, balanced}}{\text{1f-RIN, unbalanced}} = \frac{\Delta\tilde{\phi}_{\mathrm{uncorr.}}}{\tilde{\phi}_{a+b,\mathrm{uncorr.}}} \tag{C.37}$$

$$= \frac{2\sqrt{P_1^2 r_1^2(\rho^2-\alpha\tau^2)^2 + P_2^2 r_2^2(\tau^2-\alpha\rho^2)^2}}{(\alpha+1)\sqrt{P_1^2 r_1^2 + P_2^2 r_2^2}} \tag{C.38}$$

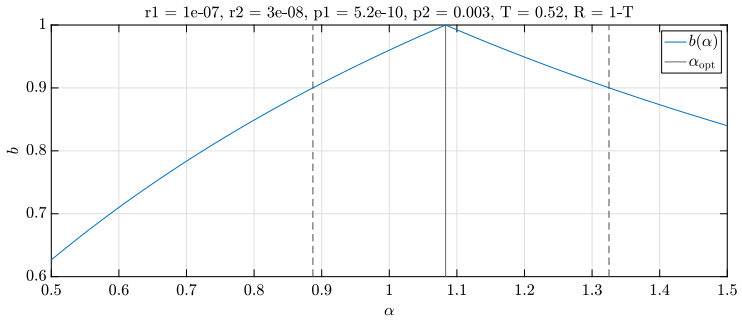

Figure C.3 Example for the balancing efficiency depending on parameter α in the case of uncorrelated RIN. The dashed lines mark the region above 90 % balancing efficiency. Because the power mismatch is so large, we basically reduce the problem to the linear optimization for correlated RIN.

Example 1 for uncorrelated RIN. Assume the following parameters

$$P_1 = 519\,\mathrm{pW},\ P_2 = 3\,\mathrm{mW}, \tag{C.39}$$
$$\rho^2 = 0.49,\ \tau^2 = 0.51, \tag{C.40}$$
$$\tilde{r}_1 = 1 \times 10^{-7}\,\sqrt{\mathrm{Hz}},\ \tilde{r}_2 = 3 \times 10^{-8}\,\sqrt{\mathrm{Hz}}, \tag{C.41}$$

we get optimization parameters (not identical)

$$\alpha_{\mathrm{best}} = 1.08333333333327 \tag{C.42}$$
$$\alpha_{\mathrm{opt}} = 1.08333333333328 \tag{C.43}$$

as presented in figure C.3. It can be seen that a balancing efficiency of 1 appears possible.

Example 2 for uncorrelated RIN. However, if we assume the following worse-case parameters

$$P_1 = 3\,\mathrm{mW},\ P_2 = 3\,\mathrm{mW}, \tag{C.44}$$
$$\rho^2 = 0.4,\ \tau^2 = 0.6, \tag{C.45}$$
$$\tilde{r}_1 = 1 \times 10^{-7}\,\sqrt{\mathrm{Hz}},\ \tilde{r}_2 = 5 \times 10^{-8}\,\sqrt{\mathrm{Hz}}, \tag{C.46}$$

we get a larger discrepancy in the optimization parameters

$$\alpha_{\mathrm{best}} = 0.75 \tag{C.47}$$
$$\alpha_{\mathrm{opt}} = 0.79 \tag{C.48}$$

as presented in figure C.4. Here, it is not possible to suppress the RIN coupling as much, as the balancing efficiency has a maximum at 84 %.

Note: In example 2, setting $\rho^2 = 0.01$, $\tau^2 = 0.99$, the result gives a significant discrepancy

$$\alpha_{\mathrm{best}} = 0.01, \tag{C.49}$$
$$\alpha_{\mathrm{opt}} = 0.26. \tag{C.50}$$

In such a case, the maximal balancing efficiency achievable is 21.6 %.

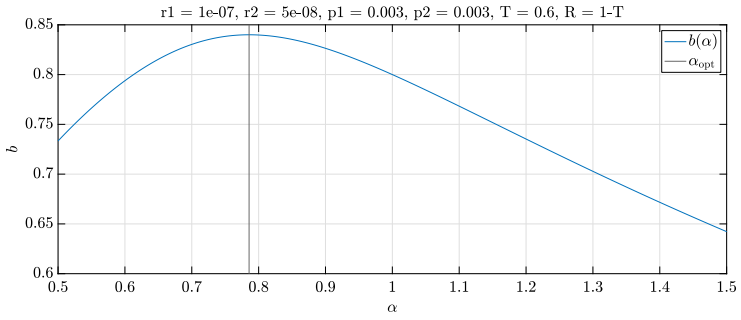

Figure C.4 Example for the balancing efficiency depending on parameter α in the case of uncorrelated RIN. Here it is impossible to reach 90 % of balancing efficiency.

C.2.4 Balanced detection and modulated beams

In the case that the beams are modulated (as it is the case for LISA) additional sidebands appear and the signal RMS amplitudes get an additional factor $\epsilon_{\text{carr}} < 1$.

This leads to a lower signal power and therefore more phase noise, since the overall 1f-RIN level stays the same. However, it does not affect the balancing efficiency, since the signal amplitude is assumed to be affected in the same way for both balanced and unbalanced detection.

The optimal gain parameter in the measurement chain α_{opt} also remains unchanged.

C.3 Balanced detection and coherent straylight

In the context of LISA, we assume coherent, backscattered light with a somewhat fixed phase for the analysis. As opposed to 1f-RIN, we only look at straylight entering the recombination BS at one specific port, and with the same frequency as the original beam.

Given a signal phasor s, and a coherent (at the same frequency) noise phasor n, where the amplitude of the noise vector is much smaller than the signal amplitude, we have a phase deviation of

$$\Delta\phi = \frac{n_{\text{amplitude}}}{s_{\text{amplitude}}} |\sin\Big(n_{\text{phase}} - s_{\text{phase}}\Big)| \leq \frac{n_{\text{amplitude}}}{s_{\text{amplitude}}} \tag{C.51}$$

We focus on the maximal phase error given by the above upper bound and neglect phase instabilities of the backscattered light for now.

For this kind of backscattered straylight we distinguish two cases:

1. Straylight entering the beamsplitter with the same frequency as the beam in the other input port → This effect can be reduced with balanced detection.
2. Straylight entering the BS with the same frequency as the beam in the same input port → Unfortunately, this effect cannot be reduced by balanced detection, but it is expected to be secondary with atto-level powers in the ghost beam.

C.3.1 Case I: Backreflected light from the backlink fibre in the TM and Reference interferometers

We model the input beams E_1, E_2 and the backscattered beam E_b as follows

$$E_1 = \sqrt{P_1} e^{i(\omega_1 t - \phi)}, \tag{C.52}$$
$$E_2 = \sqrt{P_2} e^{i\omega_2 t}, \tag{C.53}$$
$$E_b = \sqrt{P_b} e^{i(\omega_1 t - \phi_b)}, \tag{C.54}$$
$$\omega_1 = \omega_2 + \omega_{\text{het}} \tag{C.55}$$

The beamsplitter output is

$$\begin{pmatrix} E_A \\ E_B \end{pmatrix} = \begin{pmatrix} \rho & \tau \\ \tau & -\rho \end{pmatrix} \begin{pmatrix} E_1 \\ E_2 + E_b \end{pmatrix}, \tag{C.56}$$

which is squared and integrated over the PD surface to yield the optical powers (here we ignore the overlap integrals assuming perfect alignment)

$$P_A = \rho^2 P_1 + \tau^2 P_2 + \tau^2 P_b + 2\rho\tau\sqrt{P_1 P_b}\cos(\phi_b - \phi) \tag{C.57}$$
$$+ 2\rho\tau\sqrt{P_1 P_2}\cos(\omega_{\text{het}} t - \phi) + 2\tau^2\sqrt{P_2 P_b}\cos(\omega_{\text{het}} t - \phi_b) \tag{C.58}$$
$$P_B = \tau^2 P_1 + \rho^2 P_2 + \rho^2 P_b - 2\rho\tau\sqrt{P_1 P_b}\cos(\phi_b - \phi) \tag{C.59}$$
$$- 2\rho\tau\sqrt{P_1 P_2}\cos(\omega_{\text{het}} t - \phi) + 2\rho^2\sqrt{P_2 P_b}\cos(\omega_{\text{het}} t - \phi_b) \tag{C.60}$$

We assume that the phasemeter is only sensitive to terms with frequencies near the heterodyne frequency, thus leaving only

$$P_A = 2\rho\tau\sqrt{P_1 P_2}\cos(\omega_{\text{het}} t - \phi) + 2\tau^2\sqrt{P_2 P_b}\cos(\omega_{\text{het}} t - \phi_b), \tag{C.61}$$
$$P_B = -2\rho\tau\sqrt{P_1 P_2}\cos(\omega_{\text{het}} t - \phi) + 2\rho^2\sqrt{P_2 P_b}\cos(\omega_{\text{het}} t - \phi_b). \tag{C.62}$$

To calculate a nominal reference for the case of no balancing, we artificially compute the maximal phase error for each port according to equation (C.51) and artificially average them, as follows

$$\Delta\phi_{\text{A,max}} = \frac{\tau}{\rho}\sqrt{\frac{P_b}{P_1}}, \tag{C.63}$$
$$\Delta\phi_{\text{B,max}} = \frac{\rho}{\tau}\sqrt{\frac{P_b}{P_1}}, \tag{C.64}$$
$$\Rightarrow \Delta\phi_{\text{A+B,max}} = \frac{\Delta\phi_{\text{A,max}} + \Delta\phi_{\text{B,max}}}{2} = \frac{1}{2\rho\tau}\sqrt{\frac{P_b}{P_1}}. \tag{C.65}$$

This will serve as a reference for the definition of the balancing efficiency.

The processing chain gives (as described in the beginning)

$$C_A = d_a g_a R_a P_A = c_a P_A, \tag{C.66}$$
$$C_B = d_b g_b R_b P_B = c_b P_B, \tag{C.67}$$

with $c_i = d_i g_i R_i$. Again, delays are ignored in the following. This leads to frequency independent balancing.

For *balanced detection*, we subtract the two output channels such that $\Delta C = (C_A - C_B)/2$,

$$\Delta C = \frac{1}{2}\left[(c_a\tau^2 - c_b\rho^2)2\sqrt{P_2 P_b}\cos(\omega_{\text{het}}t - \phi_b) + (c_a + c_b)2\rho\tau\sqrt{P_1 P_2}\cos(\omega_{\text{het}}t)\right] \tag{C.68}$$
$$= \frac{c_a}{2}\left[(\tau^2 - \alpha\rho^2)2\sqrt{P_2 P_b}\cos(\omega_{\text{het}}t - \phi_b) + (1+\alpha)2\rho\tau\sqrt{P_1 P_2}\cos(\omega_{\text{het}}t)\right] \tag{C.69}$$

We assume further that $c_b = \alpha c_a$ as before.

Using equation (C.51) we get

$$n_{\text{amplitude}} = \frac{c_a}{2}(\tau^2 - \alpha\rho^2)2\sqrt{P_2 P_b}, \tag{C.70}$$
$$s_{\text{amplitude}} = \frac{c_a}{2}(1+\alpha)2\rho\tau\sqrt{P_1 P_2} \tag{C.71}$$
$$\Rightarrow \Delta\phi_{\max} = \frac{n_{\text{amplitude}}}{s_{\text{amplitude}}} \tag{C.72}$$
$$= \frac{(\tau^2 - \alpha\rho^2)}{\rho\tau(1+\alpha)}\sqrt{\frac{P_b}{P_1}} \stackrel{!}{=} 0, \tag{C.73}$$
$$\Rightarrow \alpha_{\text{opt}} = \frac{\tau^2}{\rho^2} \tag{C.74}$$

This is a different condition than for RIN.

Now we can define the balancing efficiency b

$$(1-b) = \frac{|\Delta\phi_{\max}|}{\Delta\phi_{\text{A+B,max}}} \tag{C.75}$$
$$= \frac{2|\tau^2 - \alpha\rho^2|}{1+\alpha}. \tag{C.76}$$

Exemplary study for the LISA backlink. It is interesting, that for coherent straylight being backscattered from the backlink fiber, the actual power of the signal and backscattered beams are only influencing the induced phase error with $\sim\sqrt{P_b/P_1}$, whereas the balancing efficiency (and the optimal gain to compensate for the mismatch) is independent on these.

To consider optical components beyond the recombination BS, only the combined differential transmissions and combined reflections after the recombination BS need to be taken

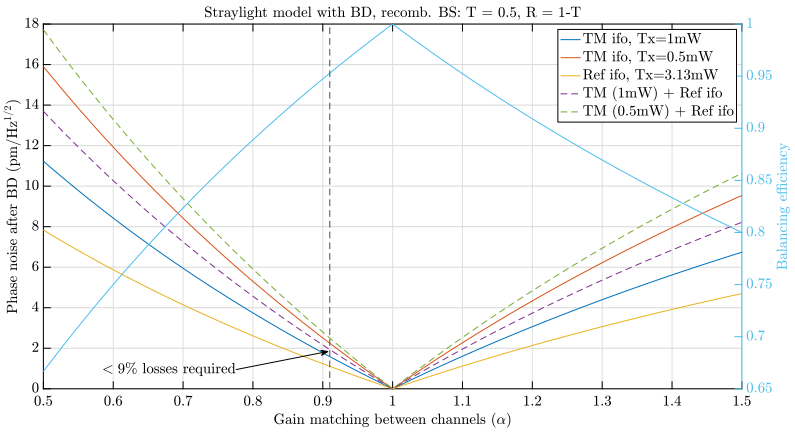

Figure C.5 Example for phase noise reduction due to balanced detection for backscattered straylight. The differential gain mismatch should be below 9 % to reach the goal of $2\,\mathrm{pm}/\sqrt{\mathrm{Hz}}$.

into account between the output channels. Those then need to be balanced with gains such that α_{opt} is met to maximize the balancing efficiency. That means, from this preliminary analysis, the balancing efficiency for this type of backscattered coherent straylight can be calibrated by knowing the optical and electrical losses and adjusting the gains.

For example in the TM interferometer, if we assume a backscattered straylight ghost beam induced displacement noise of $\approx 39\,\mathrm{pm}/\sqrt{\mathrm{Hz}}$, and in the reference interferometer of $\approx 23.5\,\mathrm{pm}/\sqrt{\mathrm{Hz}}$, then one processing channel would need to compensate for the mismatch compared to the other channel. This could include electrical gains or losses g_e and optical gains or losses g_o in each of the processing channels. For standard balancing, you need to compare two of these channels, such that we can call the ratio of the $g_o g_e$ product in port A to the one in port B still α similar as to how it was introduced before. α can be seen as the combined gain matching between two channels after the recombination BS.

Therefore, we can plot this phase noise over its matching ratio α, see figure C.5.

And for a 2nd case, if we assume differential $\pm 2\,\%$ variations due to BS coatings, $\pm 0.1\,\%$ due to AR coatings, $\pm 1\,\%$ due to polarization filters, then we have a maximal differential loss of $0.96 \times 0.998 \times 0.98 = 0.939$. And further for the worst case assuming a maximal differential splitting of already 52/48 at the recombination BS we achieve rather a result like figure C.6.

Which implies that we can still compensate for that by increasing the electrical gain in the channel with the optical losses, but that requires the corresponding knowledge, and/or calibration to the lowest measurable noise.

It also implies, that if we had this amount of losses in one channel compared to the other, it requires the corresponding electrical gain to compensate to stay below $2\,\mathrm{pm}/\sqrt{\mathrm{Hz}}$ in any case. If we had the same losses in both channels (or at least some common losses), this would improve the situation of course.

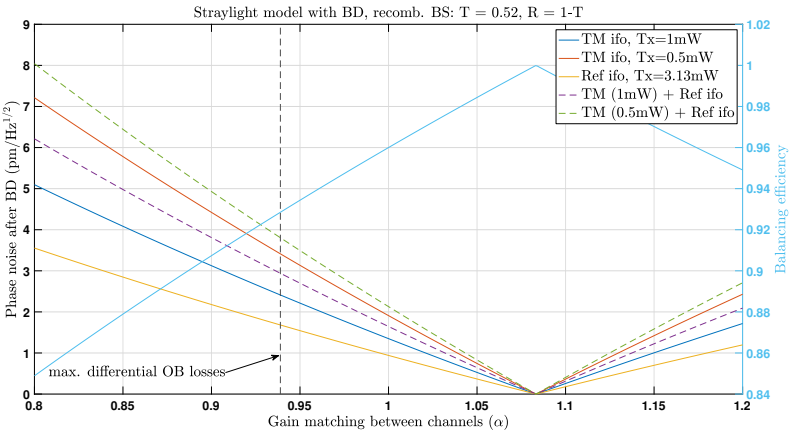

Figure C.6 Example for phase noise reduction due to balanced detection for backscattered straylight. Worst case scenario with additional optical losses and an imperfect recombination BS. Here we need to actively compensate for the losses in one channel.

C.3.2 Case II: 2nd order backscattering in the same input port as the original beam

Here the backscattered light takes the same path as the beam coming from the fibre and continues to go all the way back laser where it is backreflected to the interferometers, taking the same path as the local main beam.

We model the input beams E_1, E_2 and the backscattered beam E_b as follows

$$E_1 = \sqrt{P_1} e^{i(\omega_1 t - \phi)}, \tag{C.77}$$
$$E_2 = \sqrt{P_2} e^{i\omega_2 t}, \tag{C.78}$$
$$E_b = \sqrt{P_b} e^{i(\omega_1 t - \phi_b)}, \tag{C.79}$$
$$\omega_1 = \omega_2 + \omega_{\text{het}} \tag{C.80}$$

The beamsplitter output is

$$\begin{pmatrix} E_A \\ E_B \end{pmatrix} = \begin{pmatrix} \rho & \tau \\ \tau & -\rho \end{pmatrix} \begin{pmatrix} E_1 + E_b \\ E_2 \end{pmatrix}, \tag{C.81}$$

which is squared and integrated over the PD surface to yield the optical powers (here we ignore the overlap integrals assuming perfect alignment)

$$P_A = \rho^2 P_1 + \tau^2 P_2 + \rho^2 P_b + 2\rho^2 \sqrt{P_1 P_b} \cos(\phi_b - \phi) \tag{C.82}$$
$$+ 2\rho\tau \sqrt{P_1 P_2} \cos(\omega_{\text{het}} t - \phi) + 2\rho\tau \sqrt{P_2 P_b} \cos(\omega_{\text{het}} t - \phi_b) \tag{C.83}$$
$$P_B = \tau^2 P_1 + \rho^2 P_2 + \tau^2 P_b + 2\tau^2 \sqrt{P_1 P_b} \cos(\phi_b - \phi) \tag{C.84}$$
$$- 2\rho\tau \sqrt{P_1 P_2} \cos(\omega_{\text{het}} t - \phi) - 2\rho\tau \sqrt{P_2 P_b} \cos(\omega_{\text{het}} t - \phi_b) \tag{C.85}$$
$$\tag{C.86}$$

If we only look at the terms near the heterodyne frequency we find

$$P_A = 2\rho\tau \sqrt{P_1 P_2} \cos(\omega_{\text{het}} t - \phi) + 2\rho\tau \sqrt{P_2 P_b} \cos(\omega_{\text{het}} t - \phi_b) \tag{C.87}$$

$$P_B = -2\rho\tau\sqrt{P_1 P_2}\cos(\omega_{\text{het}}t - \phi) - 2\rho\tau\sqrt{P_2 P_b}\cos(\omega_{\text{het}}t - \phi_b) \tag{C.88}$$

and we can easily recognize that in this case balanced detection is *not* possible, since the signs are not alternating between the signal and the noise terms. The reason is that the noise is multiplicatively mixed through the port where the light with the same frequency enters.

C.4 Balancing efficiency summary

This section summarizes the results of the previous sections. In general, the balancing quality depends on (as already partly stated in [52])

- the noise correlation in the two beams
- whether the two interfering beam powers are the same
- whether the BS coefficients are 50/50 (for a lossy BS we don't have π phase difference)
- whether the PD responsivities R_a, R_b are identical
- whether the gains g_a, g_b in the electrical/PM chain are matching
- unequal delays in the processing chain of the two ports that let the signals drift out of the π phasing

The ideal balancing conditions are given by

- Lossless BS, $c_a\tau^2 = c_b\rho^2 \wedge c_a\rho^2 = c_b\tau^2 \Rightarrow \rho^2 = \tau^2 \wedge g_a R_a = g_b R_b \Rightarrow$ BD ✓
- If $\rho^2 \neq \tau^2$ we can partially remove 1f-RIN by tuning the gains, depending on the correlation and other parameters
- For straylight, only light originating from the local beam that is backreflected from the fiber and enters the BS on the same way as the light coming from the fiber can be canceled. Here, the condition is also met for $\rho^2 = \tau^2 \wedge g_a R_a = g_b R_b$
- Second order coherent straylight as described in case II, appendix C.3.2, cannot be subtracted like 2f-RIN.

We find the balancing efficiencies and optimization parameters for the different noises as follows, always assuming that a tune-able gain $c_b = \alpha c_a$ is available:

For **correlated 1f-RIN**, the balancing efficiency can be derived from equation (C.25) as

$$b_{\text{1f,corr.}} = 1 - \frac{2\left|P_1\rho^2 + P_2\tau^2 - \alpha\left(P_1\tau^2 + P_2\rho^2\right)\right|}{(P_1 + P_2)(1+\alpha)}, \tag{C.89}$$

$$\alpha_{\text{opt}} = \frac{P_1\rho^2 + P_2\tau^2}{P_1\tau^2 + P_2\rho^2}. \tag{C.90}$$

For **uncorrelated 1f-RIN**, the balancing efficiency can be derived from equation (C.37) as

$$b_{\text{1f,uncorr.}} = 1 - \frac{2\sqrt{P_1^2 r_1^2(\rho^2 - \alpha\tau^2)^2 + P_2^2 r_2^2(\tau^2 - \alpha\rho^2)^2}}{(\alpha+1)\sqrt{P_1^2 r_1^2 + P_2^2 r_2^2}}, \tag{C.91}$$

$$\alpha_{\text{opt}} = \frac{P_1^2 r_1^2 \rho^2 + P_2^2 r_2^2 \tau^2}{P_1^2 r_1^2 \tau^2 + P_2^2 r_2^2 \rho^2}. \tag{C.92}$$

For **coherent straylight** as described in case I, appendix C.3.1, the balancing efficiency can be defined as

$$b_{\text{stray}} = 1 - \frac{2|\tau^2 - \alpha\rho^2|}{1+\alpha}, \tag{C.93}$$

$$\alpha_{\text{opt}} = \frac{\tau^2}{\rho^2}. \tag{C.94}$$

C.5 Trade-off between 1f-RIN and straylight reduction

In a practical sense, looking at the balancing efficiencies for 1f-RIN and straylight reduction, one wants to select a gain parameter α that minimises both 1f-RIN and backscattered straylight up to a certain requirement. For example, both noises shall be suppressed by at least 90 %, narrowing the range of possible α setpoints.

Example study. Assume the following parameters

$$P_1 = 1\,\text{mW},\ P_2 = 3\,\text{mW}, \tag{C.95}$$

$$\rho^2 = 0.45,\ \tau^2 = 0.55, \tag{C.96}$$

$$\tilde{r}_1 = 1 \times 10^{-7}\,\sqrt{\text{Hz}},\ \tilde{r}_2 = 3 \times 10^{-8}\,\sqrt{\text{Hz}}. \tag{C.97}$$

The resulting balancing efficiencies for straylight and 1f-RIN are presented in figure C.7. Here, it is possible to reach an overall balancing efficiency of 90 % for both noises. As can be seen, $\alpha = 1$ is a good trade-off here.

In general, $\alpha = 1$ always seems to ensure the maximal balancing efficiency for both noises at the same time and represents the intersection point for both curves, since

$$b_{\text{1f,corr.}}(\alpha = 1) = 1 - \left|(\rho^2 - \tau^2)\right|, \tag{C.98}$$

$$b_{\text{stray}}(\alpha = 1) = 1 - \left|(\rho^2 - \tau^2)\right|. \tag{C.99}$$

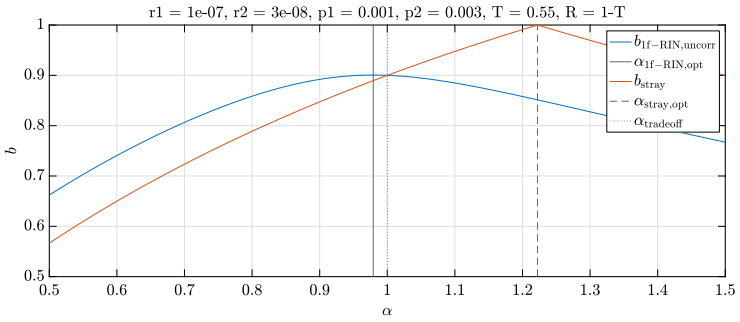

Figure C.7 Example for the balancing efficiency depending on parameter α in the case of uncorrelated 1f-RIN and backscattered straylight. Here it is impossible to reach 90 % of balancing efficiency in both cases for $\alpha = 1$.

Importance of a trade-off study with absolute noise magnitudes. It should be noted that the balancing efficiency does not include the absolute magnitude of the noise. Therefore it may be favorable to only suppress 70 % of straylight such that 99 % of 1f-RIN can be suppressed, because the overall 1f-RIN contribution may be much higher, or vice versa. It could be necessary to perform a trade-off study for the LISA instrument design to derive requirements for the precision of the gain adjustments.

Trade-off study for LISA. Note: The BS coefficients of 48/52 are assumed to be somewhat worst case.

Long-Arm interferometer parameters:

$$P_1 = 330\,\mathrm{pW},\ P_2 = 3\,\mathrm{mW}, \tag{C.100}$$
$$\rho^2 = 0.48,\ \tau^2 = 0.52, \tag{C.101}$$
$$\tilde{r}_1 = 6 \times 10^{-8}\,\sqrt{\mathrm{Hz}},\ \tilde{r}_2 = 3 \times 10^{-8}\,\sqrt{\mathrm{Hz}}, \tag{C.102}$$

Test-Mass interferometer parameters:

$$P_1 = 1\,\mathrm{mW},\ P_2 = 5\,\mu\mathrm{W}, \tag{C.103}$$
$$\rho^2 = 0.48,\ \tau^2 = 0.52, \tag{C.104}$$
$$\tilde{r}_1 = 3 \times 10^{-8}\,\sqrt{\mathrm{Hz}},\ \tilde{r}_2 = 3 \times 10^{-8}\,\sqrt{\mathrm{Hz}}, \tag{C.105}$$

Reference interferometer parameters:

$$P_1 = 3.1\,\mathrm{mW},\ P_2 = 5\,\mu\mathrm{W}, \tag{C.106}$$
$$\rho^2 = 0.48,\ \tau^2 = 0.52, \tag{C.107}$$
$$\tilde{r}_1 = 3 \times 10^{-8}\,\sqrt{\mathrm{Hz}},\ \tilde{r}_2 = 3 \times 10^{-8}\,\sqrt{\mathrm{Hz}}, \tag{C.108}$$

The resulting balancing efficiencies are shown in figure C.8. It can be seen that the balancing is always sufficient enough to enable high suppression of one of the two noises while keeping the other noise suppressed by at least 90 %. It appears useful to have adjustable gains with a dynamic range of at least a bit more than 10 %.

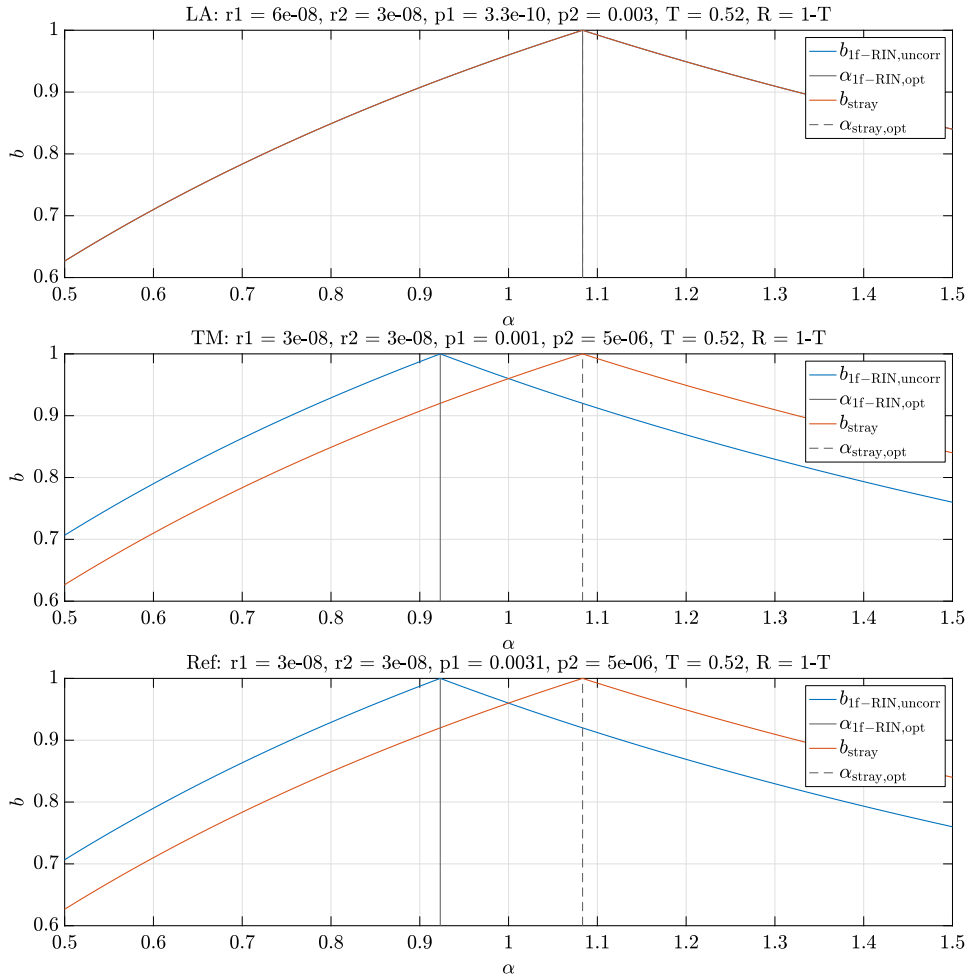

Figure C.8 Shown is the balancing efficiency $b(\alpha)$ in the case of uncorrelated 1f-RIN and backscattered straylight in a simulation of the situation in the LISA interferometers. From top to bottom: Long-Arm, TM & Reference interferometer. Here it is possible to reach 90 % of balancing efficiency even if the other straylight noise term needs to be suppressed by more than 99 %.

Appendix D
Noise runs and OMS experiments

A list of the noise runs for long-term analysis of the OMS and a table with dedicated OMS experiments from the mission. Commissioning activities are not listed. The experiments are from the LPF OMS team.

Nr.	Start (UTC)	End (UTC)	Nr.	Start (UTC)	End (UTC)
1	2016-03-01 08:05:00	2016-03-02 23:59:59	16	2016-05-16 00:00:00	2016-05-19 04:59:59
2	2016-03-03 15:00:00	2016-03-04 20:59:58	17	2016-05-19 11:30:00	2016-05-21 10:59:58
3	2016-03-06 18:15:00	2016-03-08 08:00:00	18	2016-05-21 15:30:00	2016-05-23 13:59:59
4	2016-03-13 16:30:00	2016-03-15 06:59:59	19	2016-05-23 17:03:00	2016-05-25 16:43:59
5	2016-03-16 20:00:00	2016-03-18 23:59:59	20	2016-06-06 11:05:00	2016-06-09 07:59:58
6	2016-03-21 02:00:00	2016-03-26 07:59:59	21	2016-06-15 13:35:00	2016-06-18 07:58:59
7	2016-03-27 14:00:00	2016-03-28 07:59:58	22	2016-06-19 13:00:00	2016-06-24 07:59:59
8	2016-03-29 08:00:00	2016-03-30 07:59:59	23	2016-09-19 05:00:55	2016-09-21 12:59:33
9	2016-03-31 08:00:00	2016-04-02 01:59:59	24	2016-09-21 13:45:00	2016-09-22 05:55:58
10	2016-04-04 00:00:00	2016-04-14 07:59:59	25	2016-09-28 13:35:00	2016-10-01 07:55:58
11	2016-04-26 08:04:00	2016-04-28 07:59:59	26	2016-11-09 00:45:19	2016-11-12 07:58:20
12	2016-05-01 08:05:00	2016-05-02 23:54:58	27	2016-11-16 11:05:00	2016-11-26 07:59:59
13	2016-05-03 08:00:00	2016-05-05 15:29:59	28	2016-12-26 08:00:00	2017-01-13 19:57:59
14	2016-05-13 00:50:00	2016-05-13 07:29:59	29	2017-05-28 23:43:55	2017-06-05 14:59:00
15	2016-05-13 08:30:00	2016-05-14 07:59:58	30	2017-06-08 12:00:45	2017-06-17 02:55:58

Table D.1 Selected and filtered "noise runs" for the long-term noise behavior analysis of the OMS, see chapter 12. Reprint from [P3].

Nr.	Experiment	Start (UTC)	End (UTC)	Description
1	Engineering days	2016-03-14 08:00:00	2016-03-17 20:00:00	Sinusoidal injections to the lateral Degree-of-Freedom (DOF) of both TMs at different set-points and final TM realignments for TTL suppression.
2	Thermal stability experiments	2016-03-16	2017-06-17	Experiments testing various OMS components, see [P15], given for completeness.
3	Single quadrant investigations 1	2016-04-23 13:30:00	2016-04-23 13:50:22	Attempt to characterize limited number of single quadrants with short 100 Hz segments.
4	Longitudinal step experiment 1	2016-04-25 08:00:00	2016-04-26 08:00:00	Longitudinally shift TM2 to different set-points to analyse noise behaviour and fit RIN.
5	Single quadrant investigations 2	2016-04-25 12:50:02	2016-04-25 13:40:22	Attempt to characterize limited number of single quadrants with short 100 Hz segments.
6	Beam power modulation	2016-05-30 08:00:00	2016-05-31 08:00:00	Modulation of reference beam, during thermal experiments.
7	Beam power modulation	2016-05-31 20:00:00	2016-06-01 16:00:00	Modulation of measurement beam.
8	OPD loop characterisation experiment	2016-06-01 16:35:08	2016-06-01 17:05:30	Estimate controller transfer function and open-loop transfer function.
9	Frequency loop characterisation experiment	2016-06-01 17:35:10	2016-06-01 18:06:00	Estimate transfer functions from laser frequency modulation.
10	Frequency loop open	2016-06-02 00:42:00	2016-06-02 05:40:00	Data to compare to ground and closed-loop measurement.
11	DWS angular tilt experiment 1	2016-06-02 08:30:00	2016-06-03 07:25:00	Tilt TM2 to different angular set-points to analyse noise behaviour and fit RIN.
12	OPD loop open	2016-06-11 12:02:31	2016-06-12 00:00:59	Data to compare to ground and closed-loop measurement.
13	Single quadrant investigations 3	2016-06-12 15:10:00	2016-06-12 16:30:21	Attempt to characterize limited number of single quadrants with short 100 Hz segments.
14	OPD loop characterisation experiment	2016-06-13 04:35:05	2016-06-13 05:32:05	Estimate controller transfer function and open-loop transfer function.
15	Frequency loop characterisation experiment	2016-06-13 06:05:10	2016-06-13 06:55:49	Estimate transfer functions from laser frequency modulations.
16	Beam power modulation	2016-06-13 21:27:30	2016-06-14 21:27:30	Modulation of reference beam, during thermal experiments.
17	Path length mismatch experiment	2016-06-14 21:20:00	2016-06-15 06:42:00	Estimate the path length mismatch from laser frequency modulations.
18	Frequency loop open	2016-06-15 02:53:00	2016-06-15 05:29:59	Data to compare to ground and closed-loop measurement.
19	OPD loop open	2016-07-07 10:57:01	2016-07-07 11:20:20	Data to compare to ground and closed-loop measurement.
20	OPD loop open	2016-07-07 11:23:00	2016-07-07 11:44:27	Data to compare to ground and closed-loop measurement.
21	DWS de-risk with large tilts	2017-01-17 07:00:00	2017-01-18 07:25:00	Tilt TM1 and TM2 to large angular set-points in preparation for DWS tilt 2 experiment, check for too low contrast.
22	SVN experiment 1	2017-01-18 06:27:05	2017-01-18 06:53:32	Injection of phase ramps via the OPD loop to measure SVN.
23	Short cross-talk experiment	2017-01-21 00:30:00	2017-01-21 05:30:00	Sinusoidal injections to the lateral DOF of both TMs at one set-point.
24	Beam power modulation	2017-01-21 08:00:00	2017-01-22 10:30:00	Multiple modulations and counter modulation experiments with varying depths.
25	Frequency loop characterisation experiment	2017-01-22 10:35:10	2017-01-22 11:26:49	Estimate transfer functions from laser frequency modulations.
26	Path length mismatch experiment	2017-01-22 12:05:00	2017-01-22 14:59:00	Estimate the path length mismatch from laser frequency modulations.
27	Frequency loop open	2017-01-22 16:45:00	2017-01-23 02:59:59	Data to compare to ground and closed-loop measurement.
28	SVN experiment 2	2017-02-02 20:35:00	2017-02-04 21:30:00	Injection of phase ramps via the OPD loop to measure SVN, with longitudinal offsets.
29	Longitudinal step experiment 2	2017-02-02 20:36:00	2017-02-04 21:36:00	Longitudinally shift TM2 to different set-points to analyse noise behaviour and fit RIN. Includes OPD ramps at offsets for SVN analysis and unbalanced segments.
30	Long cross-talk experiment	2017-02-04 21:00:00	2017-02-06 23:00:00	Series of short cross-talk experiments performed at different set-points of the various DOFs.
31	DWS angular tilt experiment 2	2017-02-06 23:06:00	2017-02-08 22:55:00	Tilt TM1 and TM2 to different angular set-points to analyse noise behaviour and fit RIN. Includes unbalanced segments.
32	Frequency loop characterisation experiment	2017-04-06 22:30:08	2017-04-06 23:50:42	Estimate transfer functions from laser frequency modulations.
33	Reference beam power modulation	2017-06-17 08:20:00	2017-06-17 15:00:00	Steps to lower the reference beam power, shift TM2 and increase the power again.
34	OPD loop open	2017-06-25 16:43:10	2017-06-25 17:55:10	Data to compare to ground and closed-loop measurement.
35	Direct RIN measurement at $2f$	2017-07-11 00:00:00	2017-07-12 03:32:00	Attempt to measure 2f-RIN directly by shifting the SBDFT to 2 kHz.

Table D.2 List of OMS specific experiments during the LPF mission. More details on most of these can be found in [P7, P8]. Reprint from [P3].

Curriculum Vitae

Personal Data

Name: Lennart Wissel
Date of Birth: 24.03.1990 (Gehrden, Germany)
Email: lennart.wissel@aei.mpg.de

Education

2017 – present	**PhD Candidate** Max Planck Institute for Gravitational Physics (Albert-Einstein-Institut), Leibniz Universität Hannover.
2016 – 2017	**LISA Pathfinder Mission Operations** Scientist on duty (AEI), data analyst at European Space Operations Centre (ESOC), Darmstadt.
2014 – 2015	**University of Birmingham** ERASMUS, enrolled in physics and computer sciences
2013 – 2017	**Leibniz Universität Hannover, M.Sc. in Physics** *Master thesis:* "In-orbit performance and behaviour of the LISA Pathfinder Optical Metrology System", Institute for Gravitational Physics, Leibniz Universität Hannover
2010 – 2014	**Leibniz Universität Hannover, B.Sc. in Physics** *Bachelor thesis:* "Setup of a fiber-based laser system for characterising AlGaAs mirror coatings for a highly stable reference resonator", Institute for Quantum Optics
2009 – 2010	**Voluntary Year of Social Service** Regionssportbund Hannover e.V.
2002 – 2009	**Hannah-Arendt-Gymnasium Barsinghausen** Graduated with Abitur in 2009

Bibliography

Main publications

P1. Wissel, L., Wittchen, A., Schwarze, T. S., Hewitson, M., Heinzel, G. & Halloin, H. Relative-Intensity-Noise Coupling in Heterodyne Interferometers. *Phys. Rev. Applied* **17,** 024025. https://link.aps.org/doi/10.1103/PhysRevApplied.17.024025 (2 Feb. 2022).

P2. Armano, M. *et al.* Sensor Noise in LISA Pathfinder: In-Flight Performance of the Optical Test Mass Readout. *Phys. Rev. Lett.* **126,** 131103. https://link.aps.org/doi/10.1103/PhysRevLett.126.131103 (13 Apr. 2021).

P3. Armano, M. *et al.* Sensor noise in LISA Pathfinder: An extensive in-flight review of the angular and longitudinal interferometric measurement system. *Phys. Rev. D* **106,** 082001. https://link.aps.org/doi/10.1103/PhysRevD.106.082001 (8 Oct. 2022).

P4. Wissel, L., Hartwig, O., Bayle, J., Staab, M., Fitzsimons, E., Hewitson, M. & Heinzel, G. Influence of Laser Relative-Intensity Noise on the Laser Interferometer Space Antenna. *Phys. Rev. Appl.* **20,** 014016. https://link.aps.org/doi/10.1103/PhysRevApplied.20.014016 (1 July 2023).

Further publications with the author

P5. Armano, M. *et al.* Sub-Femto-g Free Fall for Space-Based Gravitational Wave Observatories: LISA Pathfinder Results. *PHYSICAL REVIEW LETTERS* **116.** ISSN: 0031-9007. https://link.aps.org/doi/10.1103/PhysRevLett.116.231101 (JUN 7 2016).

P6. Armano, M. *et al.* Beyond the Required LISA Free-Fall Performance: New LISA Pathfinder Results down to 20 mu Hz. *PHYSICAL REVIEW LETTERS* **120.** ISSN: 0031-9007. https://link.aps.org/doi/10.1103/PhysRevLett.120.061101 (FEB 5 2018).

P7. Heinzel, G. *et al. LPF final report for the German contribution to the nominal mission* tech. rep. (Max Planck Institute for Gravitational Physics (Albert Einstein Institute), Hannover, 2018). https://www.tib.eu/de/suchen/id/TIBKAT%3A1030758840.

P8. Audley, H. *et al. LISA Pathfinder mission extension report for the German contribution, Laser Interferometer Space Antenna LISA* tech. rep. (Hannover, 2020). https://www.tib.eu/de/suchen/id/TIBKAT%3A1692401564.

P9. Armano, M. *et al.* Analysis of the accuracy of actuation electronics in the Laser Interferometer Space Antenna Pathfinder. *REVIEW OF SCIENTIFIC INSTRUMENTS* **91.** ISSN: 0034-6748. https://doi.org/10.1063/1.5140406 (APR 1 2020).

P10. Bortoluzzi, D. *et al.* In-flight testing of the injection of the LISA Pathfinder test mass into a geodesic. *Advances in Space Research* **67,** 504–520. ISSN: 0273-1177. https://www.sciencedirect.com/science/article/pii/S0273117720306384 (2021).

P11. Armano, M. *et al. LISA Pathfinder* in *Lepton Photon Interactions at High Energies* (), 185–204. https://www.worldscientific.com/doi/abs/10.1142/9789811207402_0013.

P12. Armano, M. *et al.* Novel methods to measure the gravitational constant in space. *PHYSICAL REVIEW D* **100.** ISSN: 2470-0010. https://link.aps.org/doi/10.1103/PhysRevD.100.062003 (SEP 20 2019).

P13. Thorpe, J. I. *et al.* Micrometeoroid Events in LISA Pathfinder. *ASTROPHYSICAL JOURNAL* **883.** ISSN: 0004-637X. https://dx.doi.org/10.3847/1538-4357/ab3649 (SEP 20 2019).

P14. Armano, M. *et al.* LISA Pathfinder Performance Confirmed in an Open-Loop Configuration: Results from the Free-Fall Actuation Mode. *PHYSICAL REVIEW LETTERS* **123.** ISSN: 0031-9007. https://link.aps.org/doi/10.1103/PhysRevLett.123.111101 (SEP 11 2019).

P15. Armano, M. *et al.* Temperature stability in the sub-milliHertz band with LISA Pathfinder. *MONTHLY NOTICES OF THE ROYAL ASTRONOMICAL SOCIETY* **486,** 3368–3379. ISSN: 0035-8711. https://doi.org/10.1093/mnras/stz1017 (JUL 2019).

P16. Armano, M. *et al.* LISA Pathfinder micronewton cold gas thrusters: In-flight characterization. *PHYSICAL REVIEW D* **99.** ISSN: 2470-0010. https://link.aps.org/doi/10.1103/PhysRevD.99.122003 (JUN 28 2019).

P17. Armano, M. *et al.* LISA Pathfinder platform stability and drag-free performance. *PHYSICAL REVIEW D* **99.** ISSN: 2470-0010. https://link.aps.org/doi/10.1103/PhysRevD.99.082001 (APR 16 2019).

P18. Armano, M. *et al.* Forbush Decreases and $<$ 2 Day GCR Flux Non-recurrent Variations Studied with LISA Pathfinder. *ASTROPHYSICAL JOURNAL* **874.** ISSN: 0004-637X. https://dx.doi.org/10.3847/1538-4357/ab0c99 (APR 1 2019).

P19. Anderson, G. *et al.* Experimental results from the ST7 mission on LISA Pathfinder. *PHYSICAL REVIEW D* **98.** ISSN: 2470-0010. https://link.aps.org/doi/10.1103/PhysRevD.98.102005 (NOV 14 2018).

P20. Armano, M. *et al.* Precision charge control for isolated free-falling test masses: LISA Pathfinder results. *PHYSICAL REVIEW D* **98.** ISSN: 2470-0010. https://link.aps.org/doi/10.1103/PhysRevD.98.062001 (SEP 11 2018).

P21. Armano, M. *et al.* Calibrating the system dynamics of LISA Pathfinder. *PHYSICAL REVIEW D* **97.** ISSN: 2470-0010. https://link.aps.org/doi/10.1103/PhysRevD.97.122002 (JUN 12 2018).

P22. Armano, M. *et al.* Measuring the Galactic Cosmic Ray flux with the LISA Pathfinder radiation monitor. *ASTROPARTICLE PHYSICS* **98,** 28–37. ISSN: 0927-6505. https://www.sciencedirect.com/science/article/pii/S0927650517303250 (MAR 2018).

P23. Armano, M. *et al.* Characteristics and Energy Dependence of Recurrent Galactic Cosmic-Ray Flux Depressions and of a Forbush Decrease with LISA Pathfinder. *ASTROPHYSICAL JOURNAL* **854.** ISSN: 0004-637X. https://dx.doi.org/10.3847/1538-4357/aaa774 (FEB 20 2018).

P24. Armano, M. *et al.* Capacitive sensing of test mass motion with nanometer precision over millimeter-wide sensing gaps for space-borne gravitational reference sensors. *PHYSICAL REVIEW D* **96.** ISSN: 2470-0010. https://link.aps.org/doi/10.1103/PhysRevD.96.062004 (SEP 26 2017).

P25. Armano, M. *et al. LISA Pathfinder: First steps to observing gravitational waves from space* in *11TH INTERNATIONAL LISA SYMPOSIUM* **840** (2017). https://dx.doi.org/10.1088/1742-6596/840/1/012001.

P26. Armano, M. *et al. LISA Pathfinder closed-loop analysis: a model breakdown of the in-loop observables* in *11TH INTERNATIONAL LISA SYMPOSIUM* **840** (2017). https://doi.org/10.15488/9810.

P27. Armano, M. *et al. Laser Frequency Noise Stabilisation and Interferometer Path Length Differences on LISA Pathfinder* in *11TH INTERNATIONAL LISA SYMPOSIUM* **840** (2017). https://dx.doi.org/10.1088/1742-6596/840/1/012004.

P28. Armano, M. *et al.* Spacecraft and interplanetary contributions to the magnetic environment on-board LISA Pathfinder. *MONTHLY NOTICES OF THE ROYAL ASTRONOMICAL SOCIETY* **494,** 3014–3027. ISSN: 0035-8711. https://doi.org/10.1093/mnras/staa830 (MAY 2020).

P29. Armano, M. *et al.* Transient acceleration events in LISA Pathfinder data: Properties and possible physical origin. *Phys. Rev. D* **106,** 062001. https://link.aps.org/doi/10.1103/PhysRevD.106.062001 (6 Sept. 2022).

P30. Armano, M. *et al.* Tilt-to-length coupling in LISA Pathfinder: A data analysis. *Phys. Rev. D* **108,** 102003. https://link.aps.org/doi/10.1103/PhysRevD.108.102003 (10 Nov. 2023).

P31. Armano, M. *et al.* LISA Pathfinder. *arXiv e-prints.* https://doi.org/10.48550/arXiv.1903.08924 (2019).

References

1. Schleicher, A., Ziegler, T., Schubert, R., Brandt, N., Bergner, P., Johann, U., Fichter, W. & Grzymisch, J. In-orbit performance of the LISA Pathfinder drag-free and attitude control system. *CEAS Space Journal* **10,** 471–485 (Dec. 2018).
2. LIGO collaboration. *LIGO facts* https://www.ligo.caltech.edu/page/facts. Accessed: 18.01.2024.
3. Einstein, A. Näherungsweise Integration der Feldgleichungen der Gravitation. *Sitzungsberichte der Königlich Preussischen Akademie der Wissenschaften,* 688–696 (Jan. 1916).
4. Einstein, A. Über Gravitationswellen. *Sitzungsber. Preuss. Akad. Wiss. Berlin (Math. Phys.)* **1918,** 154–167 (1918).
5. Levine, J. Early Gravity-Wave Detection Experiments, 1960-1975. *Physics in Perspective (PIP)* **6,** 42–75 (Apr. 2004).
6. Abbott, B. P. *et al.* Observation of Gravitational Waves from a Binary Black Hole Merger. *Phys. Rev. Lett.* **116,** 061102. https://link.aps.org/doi/10.1103/PhysRevLett.116.061102 (6 Feb. 2016).
7. Miller, M. C. & Yunes, N. The new frontier of gravitational waves. *Nature* **568,** 469–476 (2019).
8. Misner, C. W., Thorne, K. S. & Wheeler, J. A. *Gravitation* (ed Misner, C. W., Thorne, K. S., & Wheeler, J. A.) (1973).
9. Hulse, R. A. & Taylor, J. H. Discovery of a pulsar in a binary system. *The Astrophysical Journal* **195,** L51–L53 (1975).
10. Weisberg, J. M. & Taylor, J. H. Gravitational radiation from an orbiting pulsar. *General Relativity and Gravitation* **13,** 1–6 (1981).
11. Boyle, M. *et al.* The SXS collaboration catalog of binary black hole simulations. *Classical and Quantum Gravity* **36,** 195006. https://dx.doi.org/10.1088/1361-6382/ab34e2 (Sept. 2019).
12. Fischer, N., Pfeiffer, H. & Buonanno, A. *Black Hole Binary Merger* https://www.aei.mpg.de/213678/a-signal-like-none-before. Accessed: 18.01.2024.
13. Bond, C., Brown, D., Freise, A. & Strain, K. Interferometer techniques for gravitational-wave detection. *Living Reviews in Relativity* **19** (Feb. 2017).

14. Nitz, A. H., Kumar, S., Wang, Y.-F., Kastha, S., Wu, S., Schäfer, M., Dhurkunde, R. & Capano, C. D. 4-OGC: Catalog of Gravitational Waves from Compact Binary Mergers. *The Astrophysical Journal* **946,** 59. https://dx.doi.org/10.3847/1538-4357/aca591 (Mar. 2023).
15. Castelvecchi, D. Here come the waves. *Nature* **556,** 164–168 (2018).
16. Abbott, B. P. *et al.* GW170817: Observation of Gravitational Waves from a Binary Neutron Star Inspiral. *Phys. Rev. Lett.* **119,** 161101. https://link.aps.org/doi/10.1103/PhysRevLett.119.161101 (16 Oct. 2017).
17. *The Gravitational Wave Spectrum* https://science.gsfc.nasa.gov/663/research/index.html. Accessed: 11.01.2023.
18. Martynov, D. V. *et al.* Sensitivity of the Advanced LIGO detectors at the beginning of gravitational wave astronomy. *Phys. Rev. D* **93,** 112004. https://link.aps.org/doi/10.1103/PhysRevD.93.112004 (11 June 2016).
19. Amaro-Seoane, P. *et al. Laser Interferometer Space Antenna* 2017. https://arxiv.org/abs/1702.00786.
20. Isoyama, S., Fujita, R., Chua, A. J. K., Nakano, H., Pound, A. & Sago, N. Adiabatic Waveforms from Extreme-Mass-Ratio Inspirals: An Analytical Approach. *Phys. Rev. Lett.* **128,** 231101. https://link.aps.org/doi/10.1103/PhysRevLett.128.231101 (23 June 2022).
21. Agazie, G. *et al.* The NANOGrav 15 yr Data Set: Constraints on Supermassive Black Hole Binaries from the Gravitational-wave Background. *The Astrophysical Journal Letters* **952,** L37. https://dx.doi.org/10.3847/2041-8213/ace18b (Aug. 2023).
22. Buikema, A. *et al.* Sensitivity and performance of the Advanced LIGO detectors in the third observing run. *Phys. Rev. D* **102,** 062003. https://link.aps.org/doi/10.1103/PhysRevD.102.062003 (6 Sept. 2020).
23. Abbott, B. P. *et al.* Multi-messenger Observations of a Binary Neutron Star Merger*. *The Astrophysical Journal Letters* **848,** L12. https://dx.doi.org/10.3847/2041-8213/aa91c9 (Oct. 2017).
24. Bailes, M. *et al.* Gravitational-wave physics and astronomy in the 2020s and 2030s. *Nature Reviews Physics* **3,** 344–366. ISSN: 2522-5820. https://doi.org/10.1038/s42254-021-00303-8 (May 2021).
25. Ganapathy, D. *et al.* Broadband Quantum Enhancement of the LIGO Detectors with Frequency-Dependent Squeezing. *Phys. Rev. X* **13,** 041021. https://link.aps.org/doi/10.1103/PhysRevX.13.041021 (4 Oct. 2023).
26. Punturo, M. *et al.* The Einstein Telescope: a third-generation gravitational wave observatory. *Classical and Quantum Gravity* **27,** 194002. https://dx.doi.org/10.1088/0264-9381/27/19/194002 (Sept. 2010).

27. Littenberg, T. B. & Cornish, N. J. Prototype global analysis of LISA data with multiple source types. *Phys. Rev. D* **107,** 063004. https://link.aps.org/doi/10.1103/PhysRevD.107.063004 (6 Mar. 2023).

28. ISA Science Study Team. LISA Science Requirements Document ESA-L3-EST-SCI-RS-001-i1.0. https://www.cosmos.esa.int/web/lisa/lisa-documents/ (2018).

29. Hartwig, O. & Bayle, J.-B. Clock-jitter reduction in LISA time-delay interferometry combinations. *Phys. Rev. D* **103,** 123027. arXiv: 2005.02430 [astro-ph.IM] (2021).

30. Bayle, J.-B. & Hartwig, O. Unified model for the LISA measurements and instrument simulations. *Phys. Rev. D* **107,** 083019. https://link.aps.org/doi/10.1103/PhysRevD.107.083019 (8 Apr. 2023).

31. Hartwig, O. *Instrumental modelling and noise reduction algorithms for the Laser Interferometer Space Antenna* PhD thesis (Leibniz U., Hannover, 2021).

32. Gerberding, O., Sheard, B., Bykov, I., Kullmann, J., Delgado, J. J. E., Danzmann, K. & Heinzel, G. Phasemeter core for intersatellite laser heterodyne interferometry: modelling, simulations and experiments. *Classical and Quantum Gravity* **30,** 235029. https://dx.doi.org/10.1088/0264-9381/30/23/235029 (Nov. 2013).

33. Heinzel, G., Álvarez, M. D., Pizzella, A., Brause, N. & Delgado, J. J. E. Tracking Length and Differential-Wavefront-Sensing Signals from Quadrant Photodiodes in Heterodyne Interferometers with Digital Phase-Locked-Loop Readout. *Phys. Rev. Applied* **14,** 054013. https://link.aps.org/doi/10.1103/PhysRevApplied.14.054013 (5 Nov. 2020).

34. Abich, K., Abramovici, A., Amparan, B., Baatzsch, A., Okihiro, B. B., Barr, D. C., Bize, M. P., Bogan, C., Braxmaier, C., Burke, M. J., *et al.* In-Orbit Performance of the GRACE Follow-on Laser Ranging Interferometer. *Phys. Rev. Lett.* **123,** 031101. https://link.aps.org/doi/10.1103/PhysRevLett.123.031101 (3 July 2019).

35. Estabrook, F. B., Tinto, M. & Armstrong, J. W. Time-delay analysis of LISA gravitational wave data: Elimination of spacecraft motion effects. *Phys. Rev. D* **62,** 042002. https://link.aps.org/doi/10.1103/PhysRevD.62.042002 (4 July 2000).

36. Nam, D. Q., Lemiere, Y., Petiteau, A., Bayle, J.-B., Hartwig, O., Martino, J. & Staab, M. *TDI noises transfer functions for LISA* 2022. https://arxiv.org/abs/2211.02539.

37. Robertson, D. *3OB "As Built" OptoCAD Model - S2-UGL-TN-3045* tech. rep. (Institute for Gravitational Research, University of Glasgow, 2013).

38. G. Hechenblaikner and others. Digital Laser Frequency Control and Phase-Stabilization Loops in a High Precision Space-Borne Metrology System. *IEEE Journal of Quantum Electronics* **47,** 651–660 (May 2011).

39. Antonucci, F. *et al.* The LISA Pathfinder mission. *Classical and Quantum Gravity* **29,** 124014 (2012).

40. Audley, H. *et al.* The LISA Pathfinder interferometry—hardware and system testing. *Classical and Quantum Gravity* **28,** 094003. http://stacks.iop.org/0264-9381/28/i=9/a=094003 (2011).

41. Audley, H. *Preparing for LISA Pathfinder operations : characterisation of the optical metrology system* PhD thesis (Leibniz Universität Hannover, 2014).

42. Heinzel, G., Braxmaier, C., Schilling, R., Rudiger, A., Robertson, D., Plate, M. T., Wand, V., Arai, K., Johann, U. & Danzmann, K. Interferometry for the LISA technology package (LTP) aboard SMART-2. *Classical and Quantum Gravity* **20,** S153–S161. ISSN: 0264-9381 (2003).

43. Heinzel, G. *et al.* The LTP interferometer and phasemeter. *Classical and Quantum Gravity* **21,** S581–S587. ISSN: 0264-9381. https://dx.doi.org/10.1088/0264-9381/21/5/029 (2004).

44. Braxmaier, C. *et al.* in *Gravitational Wave and Particle Astrophysics Detectors* (eds Hough, J. & Sanders, G. H.) 164–173 (2004). ISBN: 0-8194-5432-X.

45. Van Veggel, A.-M. A. & Killow, C. J. Hydroxide catalysis bonding for astronomical instruments. *Advanced Optical Technologies* **3,** 293–307. https://doi.org/10.1515/aot-2014-0022 (2014).

46. Heinzel, G. *LPF interferometer noise* Technical note S2-AEI-TN-3076 (Albert Einstein Institut Hannover, 2016).

47. Lough, J. *et al.* First Demonstration of 6 dB Quantum Noise Reduction in a Kilometer Scale Gravitational Wave Observatory. *Phys. Rev. Lett.* **126,** 041102. https://link.aps.org/doi/10.1103/PhysRevLett.126.041102 (4 Jan. 2021).

48. Ghosh, S., Sanjuan, J. & Mueller, G. Arm locking performance with the new LISA design. *Classical and Quantum Gravity* **39,** 115009. https://dx.doi.org/10.1088/1361-6382/ac69a4 (May 2022).

49. Nery, M. T., Venneberg, J. R., Aggarwal, N., Cole, G. D., Corbitt, T., Cripe, J., Lanza, R. & Willke, B. Laser power stabilization via radiation pressure. *Opt. Lett.* **46,** 1946–1949. https://opg.optica.org/ol/abstract.cfm?URI=ol-46-8-1946 (Apr. 2021).

50. Cullen, T., Aronson, S., Pagano, R., Nery, M. T., Cain, H., Cripe, J., Cole, G. D., Sharifi, S., Aggarwal, N., Willke, B. & Corbitt, T. Passive laser power stabilization via an optical spring. *Opt. Lett.* **47,** 2746–2749. https://opg.optica.org/ol/abstract.cfm?URI=ol-47-11-2746 (June 2022).

51. Shortt, B., Mondin, L., McNamara, P., Dahl, K., Lecomte, S. & Duque, P. LISA laser system and European development strategy. **11180** (eds Sodnik, Z., Karafolas, N. & Cugny, B.) 138–151. https://doi.org/10.1117/12.2535932 (2019).

52. Stierlin, R., Bättig, R., Henchoz, P. .-. & Weber, H. P. Excess-noise suppression in a fibre-optic balanced heterodyne detection system. *Optical and Quantum Electronics* **18,** 445–454. ISSN: 1572-817X. http://dx.doi.org/10.1007/BF02041170 (Nov. 1986).

53. Wissel, L., Vorndamme, C. & Schwarze, T. *RIN requirements for LISA* Technical note LISA-AEI-TN-xxxx (AEI, 2020).

54. Wanner, G. & Heinzel, G. Analytical description of interference between two misaligned and mismatched complete Gaussian beams. *Appl. Opt.* **53,** 3043–3048. http://ao.osa.org/abstract.cfm?URI=ao-53-14-3043 (May 2014).

55. Gerberding, O. *Phase readout for satellite interferometry* PhD thesis (Leibniz University Hannover, 2014). https://www.repo.uni-hannover.de/handle/123456789/8308.

56. Rice, S. O. Mathematical analysis of random noise. *The Bell System Technical Journal* **23,** 282–332. ISSN: 0005-8580 (July 1944).

57. Robins, W. P. *Phase Noise in Signal Sources* https://digital-library.theiet.org/content/books/te/pbte009e (Institution of Engineering and Technology, 1984).

58. Tröbs, M. & Heinzel, G. Improved spectrum estimation from digitized time series on a logarithmic frequency axis. *Measurement* **39,** 120–129. https://www.sciencedirect.com/science/article/pii/S026322410500117X (2006).

59. Heinzel, G., Rüdiger, A. & Schilling, R. Spectrum and spectral density estimation by the Discrete Fourier Transform (DFT), including a comprehensive list of window functions and some new flat-top windows. https://hdl.handle.net/11858/00-001M-0000-0013-557A-5 (2002).

60. Cervantes, F. G. *et al. LISA Technology Package Flight Hardware Test Campaign* 141–150. ISBN: 978-1-58381-816-9 (2013).

61. Kersten, M. *Test Report on OMS Performance Parameter Characterization During OSTT - S2-ASD-TR-3155* tech. rep. (Astrium, 2012).

62. Heinzel, G., Wand, V., Garcia, A., Guzman, F., Steier, F., Killow, C., Robertson, D., Ward, H., Killow, C., Robertson, D. & Ward, H. *Investigation of noise sources in the LTP interferometer* Technical note S2-AEI-TN-3028 (Albert Einstein Institut Hannover, 2005).

63. Wissel, L. *In-orbit performance and behaviour of the LISA Pathfinder Optical Metrology System* MA Thesis (Leibniz Universität Hannover, 2017).

64. Billing, H. *et al.* An argon laser interferometer for the detection of gravitational radiation. *Journal of Physics E: Scientific Instruments* **12,** 1043–1050. https://doi.org/10.1088%2F0022-3735%2F12%2F11%2F010 (Nov. 1979).

65. Robertson, D. *et al.* LTP interferometer - noise sources and performance. *Classical and Quantum Gravity* **22,** S155–S163. ISSN: 0264-9381 (2005).

66. Paczkowski, S. *Laser Frequency Stabilisation and Interferometer Path Length Differences during the LISA Pathfinder Satellite Mission* PhD thesis (Leibniz Universität Hannover, 2021).

67. Heinzel, G. *Electronic Noise in Interferometers* in *Gravitational Wave Detection II* (eds Kawamura, S. & Mio, N.) **32** (Japan Universal Academy Press, Jan. 2000), 83.

68. Nofrarias, M., Marin, A. F. G., Lobo, A., Heinzel, G., Ramos-Castro, J., Sanjuan, J. & Danzmann, K. Thermal diagnostic of the optical window on board LISA Pathfinder. *Classical and Quantum Gravity* **24,** 5103–5121. ISSN: 0264-9381 (2007).

69. Gibert, F. *et al.* Thermo-elastic induced phase noise in the LISA Pathfinder spacecraft. *Classical and Quantum Gravity* **32,** 045014. https://doi.org/10.1088%2F0264-9381%2F32%2F4%2F045014 (Jan. 2015).

70. Monsky, A. *Understanding interferometric drag-free sensors in space using intelligent data analysis tools* PhD thesis (Leibniz U., Hannover, 2010).

71. Wittchen, A. *Relative intensity noise in the LISA Pathfinder interferometer - experiments on ground and in space* PhD thesis (Hannover, 2021). https://www.tib.eu/de/suchen/id/TIBKAT%3A1795473649.

72. Cavalleri, A., Ciani, G., Dolesi, R., Heptonstall, A., Hueller, M., Nicolodi, D., Rowan, S., Tombolato, D., Vitale, S., Wass, P. J. & Weber, W. J. Increased Brownian Force Noise from Molecular Impacts in a Constrained Volume. *Phys. Rev. Lett.* **103,** 140601. https://link.aps.org/doi/10.1103/PhysRevLett.103.140601 (14 Sept. 2009).

73. Hartig, M.-S., Schuster, S. & Wanner, G. Geometric tilt-to-length coupling in precision interferometry: mechanisms and analytical descriptions. *Journal of Optics.* http://iopscience.iop.org/article/10.1088/2040-8986/ac675e (2022).

74. Wanner, G. & Karnesis, N. Preliminary results on the suppression of sensing cross-talk in LISA Pathfinder. *Journal of Physics: Conference Series* **840,** 012043. https://doi.org/10.1088%2F1742-6596%2F840%2F1%2F012043 (May 2017).

75. Paczkowski, S., Giusteri, R., Hewitson, M., Karnesis, N., Fitzsimons, E. D., Wanner, G. & Heinzel, G. Postprocessing subtraction of tilt-to-length noise in LISA. *Phys. Rev. D* **106,** 042005 (2022).

76. Hartig, M.-S. & Wanner, G. Tilt-to-length coupling in LISA Pathfinder: Analytical modeling. *Phys. Rev. D* **108,** 022008. https://link.aps.org/doi/10.1103/PhysRevD.108.022008 (2 July 2023).

77. Leys, C., Ley, C., Klein, O., Bernard, P. & Licata, L. Detecting outliers: Do not use standard deviation around the mean, use absolute deviation around the median. *Journal of Experimental Social Psychology* **49,** 764–766. ISSN: 0022-1031. https://www.sciencedirect.com/science/article/pii/S0022103113000668 (2013).

78. Baghi, Q., Korsakova, N., Slutsky, J., Castelli, E., Karnesis, N. & Bayle, J.-B. Detection and characterization of instrumental transients in LISA Pathfinder and their projection to LISA. *Phys. Rev. D* **105,** 042002. https://link.aps.org/doi/10.1103/PhysRevD.105.042002 (Feb. 2022).

79. Vitale, S. *et al.* Data series subtraction with unknown and unmodeled background noise. *Phys. Rev. D* **90,** 042003. http://link.aps.org/doi/10.1103/PhysRevD.90.042003 (Aug. 2014).

80. Kaune, B. *In-orbit stability analysis of the LISA pathfinder optical metrology: photoreceivers and polarisation.* PhD thesis (Leibniz Universität Hannover, 2021).

81. Madhu, N. Note on measures for spectral flatness. *Electronics letters* **45,** 1195–1196 (2009).

82. Seber, G. & Wild, C. *Nonlinear Regression* ISBN: 9780471725305. https://books.google.de/books?id=YBYlCpBNo_cC (Wiley, 2005).

83. Kayser-Threde. *LA PFM Function and Performance Test Report, Hanover-Tests* tech. rep. (Kayser-Threde, 2010).

84. Heinzel, G. *LISA Frequency Planning - LISA-AEI-INST-TN-002 1.0* tech. rep. (Albert Einstein Institute, 2018).

85. MATLAB. *version 9.13.0.2399474 (R2022b) Update 7* (The MathWorks Inc., Natick, Massachusetts, 2022).

86. Adler, W. *cornerplot* https://github.com/wtadler/cornerplot. 2022.

87. Staab, M., Bayle, J.-B. & Hartwig, O. *PyTDI* version 1.2.1. July 2022. https://doi.org/10.5281/zenodo.6867012.

88. LIG. *LISA Performance Model and Error Budget* Technical note LISA-LCST-INST-TN-003. Available at https://atrium.in2p3.fr/33984a34-5b35-415f-aaeb-f79448f71c2e (LIG, 2019).

89. Castelli, E. *LISA Pathfinder noise performance results: disturbances in the sub-mHz frequency band and projection to LISA* PhD thesis (Trento U., 2020).

90. Dávila Álvarez, A. *et al.* A simplified gravitational reference sensor for satellite geodesy. *Journal of Geodesy* **96,** 70 (2022).

Declaration

Hereby, I declare that some parts of this thesis have already been published in peer-reviewed science journals by myself and co-authors. Individual sections and illustrations are similar or identical, and paragraphs have been reused with exact wording or modifications. All these sources have been clearly referenced.

Pages containing exact or only slightly modified wording from my contributions to those publications are:

- Pages 12 – 15, [P4],
- Pages 16 – 21, [P2, P3],
- Pages 25 – 26, 29 – 53, [P1],
- Pages 57 – 95, [P2, P3],
- Pages 97 – 100, [P8],
- Pages 115 – 139, [P4].

They partially include contributions from collaborative work with the co-authors. Those contributions have been indicated in the respective sections.

Further, I hereby assure that I have independently written the presented work, and used no sources or aids other than those specified.

Hannover, 02.02.2024 _____

Lennart Wissel

Colophon

This document was typeset using a modified version of the book class of the KOMA-Script LaTeXpackage developed by Markus Kohm.

Most analysis scripts were produced using Matlab with the ltpda add-on or python, with extensive use of numpy and scipy. Also the MCMC package emcee and the LPSD algorithm have been used.

Some figures utilize either the diagram application draw.io or the component library developed by A. Franzen. Plots were usually generated using Matlab and exported using the script export_fig. For selecting colors, the colorbrewer library has often been used. Figures not created by the author are marked as such, with references provided in their caption. Mission logos provided by ESA.

The author expresses his gratitude to everyone providing free software and promoting open science.